frontiers | Research Topics

Adhesive hydrogels: Design, fabrication, and bio-applications

Edited by
Qihui Zhou, Yong Liu, Tengbo Yu and Mohamed S. Hasanin

Published in
Frontiers in Bioengineering and Biotechnology

ISSN 1664-8714
ISBN 978-2-8325-3641-4
DOI 10.3389/978-2-8325-3641-4

About Frontiers

Frontiers is more than just an open access publisher of scholarly articles: it is a pioneering approach to the world of academia, radically improving the way scholarly research is managed. The grand vision of Frontiers is a world where all people have an equal opportunity to seek, share and generate knowledge. Frontiers provides immediate and permanent online open access to all its publications, but this alone is not enough to realize our grand goals.

Frontiers journal series

The Frontiers journal series is a multi-tier and interdisciplinary set of open-access, online journals, promising a paradigm shift from the current review, selection and dissemination processes in academic publishing. All Frontiers journals are driven by researchers for researchers; therefore, they constitute a service to the scholarly community. At the same time, the *Frontiers journal series* operates on a revolutionary invention, the tiered publishing system, initially addressing specific communities of scholars, and gradually climbing up to broader public understanding, thus serving the interests of the lay society, too.

Dedication to quality

Each Frontiers article is a landmark of the highest quality, thanks to genuinely collaborative interactions between authors and review editors, who include some of the world's best academicians. Research must be certified by peers before entering a stream of knowledge that may eventually reach the public - and shape society; therefore, Frontiers only applies the most rigorous and unbiased reviews. Frontiers revolutionizes research publishing by freely delivering the most outstanding research, evaluated with no bias from both the academic and social point of view. By applying the most advanced information technologies, Frontiers is catapulting scholarly publishing into a new generation.

What are Frontiers Research Topics?

Frontiers Research Topics are very popular trademarks of the *Frontiers journals series*: they are collections of at least ten articles, all centered on a particular subject. With their unique mix of varied contributions from Original Research to Review Articles, Frontiers Research Topics unify the most influential researchers, the latest key findings and historical advances in a hot research area.

Find out more on how to host your own Frontiers Research Topic or contribute to one as an author by contacting the Frontiers editorial office: frontiersin.org/about/contact

Adhesive hydrogels: Design, fabrication, and bio-applications

Topic editors

Qihui Zhou — University of Health and Rehabilitation Sciences, China
Yong Liu — University of Chinese Academy of Sciences, China
Tengbo Yu — Qingdao Municipal Hospital, China
Mohamed S. Hasanin — National Research Centre, Egypt

Citation

Zhou, Q., Liu, Y., Yu, T., Hasanin, M. S., eds. (2023). *Adhesive hydrogels: Design, fabrication, and bio-applications*. Lausanne: Frontiers Media SA.
doi: 10.3389/978-2-8325-3641-4

Table of contents

frontiers | Frontiers in Bioengineering and Biotechnology

TYPE Editorial
PUBLISHED 21 September 2023
DOI 10.3389/fbioe.2023.1290228

OPEN ACCESS

EDITED AND REVIEWED BY
Hasan Uludag,
University of Alberta, Canada

*CORRESPONDENCE
Qihui Zhou,
qihuizhou@uor.edu.cn
Yong Liu,
y.liu@ucas.ac.cn
Mohamed Sayed Hasanin,
sido_sci@yahoo.com
Tengbo Yu,
ytb8912@163.com

RECEIVED 07 September 2023
ACCEPTED 11 September 2023
PUBLISHED 21 September 2023

CITATION
Zhou Q, Liu Y, Hasanin MS and Yu T (2023), Editorial: Adhesive hydrogels: design, fabrication, and bio-applications. *Front. Bioeng. Biotechnol.* 11:1290228. doi: 10.3389/fbioe.2023.1290228

Editorial: Adhesive hydrogels: design, fabrication, and bio-applications

Qihui Zhou[1]*, Yong Liu[2]*, Mohamed Sayed Hasanin[3]* and Tengbo Yu[4]*

[1]School of Rehabilitation Sciences and Engineering, University of Health and Rehabilitation Sciences, Qingdao, China, [2]Wenzhou Institute, University of Chinese Academy of Sciences, Wenzhou, China, [3]Cellulose and Paper Department, National Research Centre, Cairo, Egypt, [4]Qingdao Hospital, Qingdao Municipal Hospital, University of Health and Rehabilitation Sciences, Qingdao, China

KEYWORDS

adhesive hydrogels, biomaterials, biomedical applications, disease treatment, tissue repair and regeneration

Editorial on the Research Topic
Adhesive hydrogels: design, fabrication, and bio-applications

Adhesive hydrogels have been appealing as emerging biomedical materials for high demand for fundamental research and practical biomedical applications owing to inherent self-adhesiveness, flexible structure, dynamic mechanical properties, and near-physiological environment (Hao et al., 2022; Li et al., 2022; Mei et al., 2022). The integrated adhesion between the hydrogel interface and surrounding tissues is one of the most critical interactions that offer overall robustness and reliability during specific environment (Duan et al., 2023b; Han et al., 2023; Zeng et al., 2023). Based on their unique (bio) physicochemical features above, adhesive hydrogels have been applied in numerous indications, including implant scaffolds in tissue engineering, hemostasis, mucosal adhesives to extend the administration site time, and bio-adhesives in place of wounds to reduce infection (Hao et al., 2022; Ko and Liao, 2023; Zhao et al., 2023). In addition, therapeutic cells and drug molecules can be transported by adhesive hydrogels and released at the injury site to enhance efficacy (Duan et al., 2023a; Zhang et al., 2023). Adhesive hydrogels perform suitably in clinical investigations for soft tissue regeneration, anti-exudation, medicine distribution, and other applications. This Research Topic focuses on the recent advances regarding adhesive hydrogels and their biomedical applications, aiming to provide a reference for researchers in related fields. We have collected nine original research articles.

These groundbreaking materials, the result of meticulous design considerations and inventive processes for fabrication, have the potential to redefine bio-applications and change medical technology. This takes us on an expedition into the fascinating world of adhesive hydrogels, exploring their sophisticated production processes, varied design, and an incredible range of revolutionary bio-application they provide. In original research articles on this Research Topic about the regulation of biomaterial base Adhesive hydrogel for tissue repair and regeneration, Zhu et al. developed an adhesive hydrogel for loading of conditioned medium (CM) based on Gel-MA (CM/Gel-MA), which was greatly adhesive and favors the stable retention of CM. CM/Gel-MA boosted the activity of endometrial stromal cells (ESCs), promoting cell proliferation and reducing α-SMA, collagen I, CTGF, E-cadherin,

and IL-6 expression to reduce the inflammatory response and inhibit fibrosis. CM/Gel-MA hydrogel prevented uterine adhesion (IUA) through physical barriers from adhesive hydrogel and functional promotion from CM. Qu et al. prepared a hyaluronic acid (HA) and *Bletilla striata* polysaccharide (BSP) based dissolving microneedle patches (MNs) to mediate mesoporous polydopamine nanoparticles (MPDA) loaded with Triamcinolone acetonide (TA) as the transmucosal delivery system to treat oral mucositis (OM). A@MPDA-HA/BSP MNs possessed well-arranged microneedles, good penetration efficiency, quick dissolution in 3 min, excellent biocompatibility, and anti-inflammatory effects. MNs decreased oral ulcer area and inflammatory factor levels such as TNF-α and CD31. Yang et al. introduced an innovative method using oxidized regenerated cellulose and fibrin glue to prevent air leakage following lung segmentectomy. Their approach revealed efficacy in an *ex vivo* porcine lung model, suggesting a potential alternative to existing methods. Li et al. proposed a novel hydrogel-based method for enumerating fetomaternal hemorrhage, a critical factor in preventing newborn hemolytic diseases. Their approaches offer a clinically applicable prenatal diagnosis technique, addressing the limitations of traditional methods.

In contrast, biomaterials have been commonly used in antimicrobial/cancer applications. For antimicrobial research, Wei et al. addressed the challenges of cytotoxicity in silver nanoparticles by developing a coating technique using polydopamine. This approach enhanced antibacterial properties and biocompatibility, presenting a promising route for diverse medical applications. In addition, Hajizadeh et al. presented a solution for capturing haemin using albumin-based cryogels, showcasing higher binding capacity and reaction rates compared to conventional approaches. Their work has potential implications for preventing alloimmunization. Wang et al. explored shape-memory fibers for tissue regeneration, particularly in the osteogenic differentiation of stem cells. They demonstrate enhanced shape recovery and mechanical properties by manipulating fiber structure and programming parameters, offering new avenues for biomaterial applications.

In conclusion, the original research papers in this Research Topic indicate adhesive hydrogels broadly impact tissue healing, regeneration, drug delivery, and infection control. Researchers from Sweden and China cooperate to usher in a new biomedical era, stressing the significance of the accomplishment globally. These groundbreaking findings demonstrate the dynamic potential of adhesive hydrogels, revolutionizing healthcare and allowing improved cures and treatments.

Author contributions

QZ: Conceptualization, Funding acquisition, Resources, Supervision, Writing–original draft. YL: Conceptualization, Writing–review and editing. MH: Writing–review and editing. TY: Writing–review and editing.

Acknowledgments

The Research Topic Editors deeply acknowledge the authors of all contributions composing this Research Topic. They also acknowledge all the reviewers' constructive comments and engagement and the editorial support from Frontiers throughout the publication process.

Conflict of interest

The authors declare that the research was conducted in the absence of any commercial or financial relationships that could be construed as a potential conflict of interest.

Publisher's note

References

Duan, N., Mei, L., Hu, L., Yin, X., Wei, X., Li, Y., et al. (2023a). Biomimetic, injectable, and self-healing hydrogels with sustained release of ranibizumab to treat retinal neovascularization. *ACS Appl. Mater. Interfaces* 15, 6371–6384. doi:10.1021/acsami.2c17626

Duan, N., Zhang, L.-N., Bohara, R., Martin-Saldaña, S., Yang, F., Zhao, Y.-Y., et al. (2023b). Adhesive hydrogels in osteoarthritis: from design to application. *Mil. Med. Res.* 10, 4. doi:10.1186/s40779-022-00439-3

Han, Z., Deng, L., Chen, S., Wang, H., and Huang, Y. (2023). Zn2+-Loaded adhesive bacterial cellulose hydrogel with angiogenic and antibacterial abilities for accelerating wound healing. *Burn. Trauma* 11, tkac048. doi:10.1093/burnst/tkac048

Hao, Y., Yuan, C., Deng, J., Zheng, W., Ji, Y., and Zhou, Q. (2022). Injectable self-healing first-aid tissue adhesives with outstanding hemostatic and antibacterial performances for trauma emergency care. *ACS Appl. Mater. Interfaces* 14, 16006–16017. doi:10.1021/acsami.2c00877

Ko, A., and Liao, C. (2023). Hydrogel wound dressings for diabetic foot ulcer treatment: status-quo, challenges, and future perspectives. *BMEMat* 2, e12037. doi:10.1002/bmm2.12037

Li, M., Liang, Y., Liang, Y., Pan, G., and Guo, B. (2022). Injectable stretchable self-healing dual dynamic network hydrogel as adhesive anti-oxidant wound dressing for photothermal clearance of bacteria and promoting wound healing of MRSA infected motion wounds. *Chem. Eng. J.* 427, 132039. doi:10.1016/j.cej.2021.132039

Mei, L., Zhang, D., Shao, H., Hao, Y., Zhang, T., Zheng, W., et al. (2022). Injectable and self-healing probiotics-loaded hydrogel for promoting superbacteria-infected wound healing. *ACS Appl. Mater. Interfaces* 14, 20538–20550. doi:10.1021/acsami.1c23713

Zeng, J., Sun, P., Zhao, Y., Fang, X., Wu, Z., and Qi, X. (2023). Bone mesenchymal stem cell-derived exosomes involved co-delivery and synergism effect with icariin via mussel-inspired multifunctional hydrogel for cartilage protection. *Asian J. Pharm. Sci.* 18, 100799. doi:10.1016/j.ajps.2023.100799

Zhang, D., Mei, L., Hao, Y., Yi, B., Hu, J., Wang, D., et al. (2023). A hydrogel-based first-aid tissue adhesive with effective hemostasis and anti-bacteria for trauma emergency management. *Biomater. Res.* 27, 56. doi:10.1186/s40824-023-00392-9

Zhao, Y., Yi, B., Hu, J., Zhang, D., Li, G., Lu, Y., et al. (2023). Double cross-linked biomimetic hyaluronic acid-based hydrogels with thermo-stimulated self-contraction and tissue adhesiveness for accelerating post-wound closure and wound healing. *Adv. Funct. Mater.* 33, 2300710. doi:10.1002/adfm.202300710

frontiers | Frontiers in Bioengineering and Biotechnology

TYPE Original Research
PUBLISHED 14 November 2022
DOI 10.3389/fbioe.2022.1072393

OPEN ACCESS

EDITED BY
Chaoyong Liu,
Beijing University of Chemical Technology, China

REVIEWED BY
Zhanzhan Zhang,
Tianjin Medical University, China
Yangzhouyun Xie,
Yale University, United States

*CORRESPONDENCE
Zhuo Ao,
aoz@nanoctr.cn
Dong Han,
dhan@nanoctr.cn

†These authors have contributed equally to this work

SPECIALTY SECTION
This article was submitted to Biomaterials, a section of the journal Frontiers in Bioengineering and Biotechnology

RECEIVED 17 October 2022
ACCEPTED 31 October 2022
PUBLISHED 14 November 2022

CITATION
Li Z, Xiang J, Zhang Q, Zhao M, Meng Y, Zhong J, Li T, Jia L, Li K, Lu X, Ao Z and Han D (2022), An engineered hydrogel with low-dose antitumor drugs enhances tumor immunotherapy through tumor interstitial wrap. *Front. Bioeng. Biotechnol.* 10:1072393. doi: 10.3389/fbioe.2022.1072393

An engineered hydrogel with low-dose antitumor drugs enhances tumor immunotherapy through tumor interstitial wrap

Zhongxian Li[1,2†], Jiawei Xiang[1,2†], Qiang Zhang[3], Mingyuan Zhao[1,2], Yuan Meng[1,2], Jie Zhong[1,2], Tingting Li[4], Lanxin Jia[2,5], Kai Li[4], Xi Lu[4], Zhuo Ao[1*] and Dong Han[1,2,4*]

[1]CAS Center for Excellence in Nanoscience, National Center for Nanoscience and Technology, Beijing, China, [2]University of Chinese Academy of Sciences, Beijing, China, [3]Hebei Key Lab of Nano-Biotechnology, Hebei Key Lab of Applied Chemistry, Yanshan University, Qinhuangdao, China, [4]College of Life Sciences, Bejing University of Chinese Medicine, Beijing, China, [5]CAS Key Laboratory of Bio-Inspired Materials and Interfacial Science, Technical Institute of Physics and Chemistry, Chinese Academy of Sciences, Beijing, China

Stimulating immunogenic cell death (ICD) is the key to tumor immunotherapy. However, traditional chemoradiotherapy has limited effect on stimulating immunity and often requires repeated administration, which greatly reduces the tumor-killing effect. In this article, we created a sodium alginate hydrogel sustained-release system containing low-dose doxorubicin (Dox) and immune adjuvant R837, which were injected into the interstitial space to wrap around the tumor *in situ*, achieving a sustained release and long-lasting immune response. Cooperating with immune checkpoint blockade, Dox induced ICD, activated dendritic cells (DCs) and converted immunosuppressive M2-type tumor-associated macrophages (TAM) to tumor-killing M1-type TAMs. Simultaneously, it greatly promoted T cell proliferation and infiltration, and reduced tumor immunosuppressive factors, triggering a robust immune response to suppress tumors *in vivo*. In conclusion, this anti-tumor strategy based on interstitial injection can achieve continuous local immune stimulation by low-dose chemotherapy drugs, providing a potential approach for tumor immunotherapy.

KEYWORDS

immunogenic cell death, interstitial administration, hydrogel, tumor immunotherapy, tumor microenvironment

Introduction

As a process of activating the immune system and triggering a robust immune response to promote the tumor necrosis, tumor immunotherapy includes immune checkpoint inhibitors, adoptive cellular therapy, and tumor vaccines (Zhang et al., 2019; Zhang and Zhang, 2020). It is a beneficial supplement to traditional surgery, and chemoradiotherapy, significantly improving anti-tumor efficiency and prolonging patient survival (Waldman et al., 2020).

Dying tumor cells can produce damage-associated molecular patterns (DAMPs) that are exposed on the cell surface, promote DC maturation, then T cells and memory T cells are recruited, which infiltrate into tumors and trigger tumor immunogenic cell death (ICD) (Kroemer et al., 2013; Galluzzi et al., 2020; Jin and Wang, 2021). Initiation of ICD can convert tumor environment from a "cold" (immunosuppressive) state into a "hot" (immune-responsive) state, which causes tumor regression of both *in situ* and distant metastases (Dewan et al., 2009; Zhao et al., 2022).

Although chemotherapy or radiotherapy can induce the ICD process (Krysko et al., 2012; Rios-Doria et al., 2015), their immune responses are not strong enough. Thus, additional auxiliary stimulation is often needed to amplify the immune response, such as breaking the reactive oxygen species balance in tumor tissues (Aboelella et al., 2021), cold tumor heating (Mansurov et al., 2020), scaled delivery of chemotherapy drugs (Wang et al., 2021; Zhang et al., 2021), photothermal drug combined therapy (Liu et al., 2022a) so as to enhance the anti-tumor effect and shorten the cycle of chemotherapy. However, these strong stimuli inevitably trigger side effects of cancer immune responses, such as myelosuppression, lymphopenia, and other inflammatory responses (Kepp et al., 2020; Banstola et al., 2021; Kroemer et al., 2022). Due to the highly immunosuppressive and heterogeneous microenvironment of tumors, the ability to release tumor-associated antigens is weakened, and a timely and effective immune response cannot be generated, resulting in continuous tumor growth (Ngambenjawong et al., 2017; Duan et al., 2018; Musetti and Huang, 2018). Therefore, ICD with lower stimulation to enhance the immune response and modulate the immune system to improve the tumor microenvironment is crucial for more efficient tumor immunotherapy.

In previous studies, it has been found that interstitial fluid filled space enables flattened connections between functional structures in organisms, which show promise for improving disease pathophysiology (Foster and McVey Neufeld, 2013; Budden et al., 2017; Liu et al., 2022b). Interstitial drug delivery showed the effects of activating and recruiting immune cells for better clearance of parasites resident in organs, and accelerated pathological recovery (Zhang et al., 2020a). From the damaged area to the tumor area, the liquid metal moved through and wrapped around the tumor, separating the tumor from the surrounding normal vessel supply (Hu et al., 2018; Cao et al., 2020). With the help of interstitial drug delivery, the toxicity caused by intravenous administration can be avoided, and low-dose chemotherapy drugs can be wrapped around the tumor tissues and released slowly, providing a sustained tumor-killing effect (Xu et al., 2020). This can ensure the possibility for the efficient presentation of tumor antigens from dying tumor cells to lymph node DCs (Zhang et al., 2020b). However, in the current tumor therapy, there are few studies on using the interstitial structure to assist in enhancing the immune response to achieve anti-tumor therapy. Therefore, developing a novel drug delivery strategy *via* the interstitial route to trigger ICD will bring inspiration for tumor immunotherapy.

Here, we prepared an injectable sodium alginate hydrogel as a sustained-release system carrying the hydrophobic immune adjuvant R837 and low-dose Dox. The drug-loaded hydrogel was injected into the interstitial space around the tumor tissues, which produced an effective wrap against tumor growth, invasion and metastasis. Firstly, the interstitial blocking restricts the nutrition supply in tumor sites from normal tissues, which physically limited tumor growth. What's more, the gel slowly released Dox to inhibit tumor growth while triggering an immune response, and low-dose Dox was enough to induce ICD with low system toxicity, while the supplement loading of R837 in the hydrogel can effectively amplify the immunogenicity. We obtained a better anti-tumor efficacy when combined with immune checkpoint inhibitor, aPD-L1. Wrapping tumor tissues by the interstitial route can inhibit tumor invasion and metastasis, Dox induced ICD can achieve rapid antigen presentation. R837 adjuvant could better stimulate tumor immunotherapy, greatly promote T cell infiltration and activation, and significantly reduce immunosuppressive factors in tumor microenvironment (Lei et al., 2022; Wang et al., 2022). Therefore, this anti-tumor strategy based on interstitial injection with low-dose chemotherapeutic drugs, enhancing immune response, provides a feasible solution for tumor immunotherapy.

Materials and methods

Materials, animals and antibodies

Sodium alginate was purchased from Sigma-Aldrich (United States); anhydrous calcium chloride was purchased from Xilong Chemical; doxorubicin was purchased from Rhawn Co., Ltd. (Shanghai, China); IMIQUIMOD (R837) was purchased from Macklin Biochemical Co., Ltd. (Shanghai, China); Durvalumab (anti-PD-L1) was purchased from Merck, Inc. (United States); Viability/Cytotoxicity Assay Kit was purchased from Mei5 Biotechnology Co., Ltd.; TNF-α Elisa Kit and IL-6 Elisa Kit was purchased from MEIMIAN Inc. (Jiangsu, China); Cell Counting Kit-8 was purchased from Beijing Solarbio Science & Technology Co., Ltd. (Beijing, China); Anti-mouse CD45-Alexa Fluor® 700, anti-CD80-Percp, anti-CD11b-FITC, anti-CD80-FITC, anti-H-2Kd-PE, anti-CD83-FITC, anti-CD206-APC, anti-F4/80-APC, anti-CD86-PE, anti-CD3-FITC, anti-CD4-Percp, anti-CD8-PE were purchased from BioLegend, Inc. (United States).

The murine melanoma cell line B16F10 was obtained from the Cell Bank of the Chinese Academy of Sciences (Shanghai, China). B16F10 cells were cultured in RPMI 1640 medium supplemented with fetal bovine serum (FBS, 10%, v/v, Gibco, United States) and antibiotic-antifungal solution (1%, v/v, Gibco, United States), 37°C and 5% CO_2 atmosphere. All experiments were performed using cells in logarithmic growth phase. Eight-week-old male C57BL/6 mice were obtained from Beijing Vital River Laboratory Animal Technology Co., Ltd. (Beijing, China).

All animal handling procedures followed ethics committee guidelines of National Center for Nanoscience and Technology.

Gelling amount

At room temperature, 375 mg of sodium alginate powder was dissolved in 30 ml of 0.9% sodium chloride injection, and stirred overnight to fully dissolve the sodium alginate to prepare a 12.5 mg/ml sodium alginate solution. Take 2 ml of the prepared 12.5 mg/ml sodium alginate solution and add it to a 5 ml capacity vial. Calcium chloride solutions with concentrations of 2, 3, 4, 4.5, 5, 5.5, and 6 mg/ml was prepared with anhydrous calcium chloride, and the solvent was 0.9% sodium chloride injection. Finally, 0.5 ml of calcium chloride solution was added to sodium alginate solution while stirring. Invert each bottle and observe the minimum calcium chloride concentration required for gel formation.

Preparation of Alg-Dox-R837 hydrogel system

We took 2 ml of the 12.5 mg/ml sodium alginate solution prepared by the above method which was accompanied by Dox and R837, and added 0.5 ml of 5 mg/ml calcium chloride solution. Finally, the mixture was stirred so that the final Dox concentration was 0.5 mg/ml and the concentration of R837 was 1 mg/ml to form a stable Alg-Dox-R837 hydrogel system. Subsequent drug-laden hydrogel systems were prepared in the same way.

Morphological characterization

The surface morphologies of Alg, Alg-Dox and Alg-Dox-R837 xerogel samples were characterized by SEM (Hitachi S4800 + EDS, Hitachi, Japan). The xerogels were first dehydrated by a freeze-drying device, and after sample preparation, platinum was coated with ion sputter coater (Lab 18, Lesker). The image of the gel morphology was observed at an accelerating voltage of 10 kV. The composition of the elements on the surface of the gel was observed utilizing energy spectroscopy.

Rheological testing of drug-loaded hydrogels and injectability

Alg, Alg-Dox and Alg-Dox-R837 hydrogel samples were determined using a dynamic mechanical rheological stress meter (Haake MARS3, Thermo Electron, GmbH) at 25 °C with an angular frequency range of 0.1–100 rad/s viscoelastic properties.

An appropriate amount of the hydrogel was drawn into a 1 ml syringe, and the hydrogel was patterned on the cardboard by squeezing the syringe plunger to verify its injectability.

In vitro release of Dox from hydrogel systems

We took 1 ml of Alg-Dox-R837 hydrogel prepared according to the above method, placed it in a dialysis bag with a molecular weight of 5 kDa, and transferred it to 50 ml of 0.9% NaCl injection solution. At multiple time points, 2 ml of dialysate was removed and the corresponding optical density (OD) was measured at 484 nm using a UV spectrophotometer to calculate the release of Dox.

Drug distribution in hydrogel drug delivery systems

After 1 week of adaptive feeding of C57BL/6 mice, melanoma cells named B16F10 cells ($1*10^6$ cells per mouse), were subcutaneously inoculated on the right back. On the 7th day after inoculation, Alg, Dox, and Alg-Dox were injected into the peritumoral stroma. After 48 h, the tumor tissues of the mice in each group were collected, embedded in OCT, and the frozen tissues were serially sectioned at 5 μm with a cryostat, and the frozen sections were placed on glass slides. The penetration and distribution of Dox in it were observed by optical microscope and fluorescence microscope.

The paraffin-embedded tissue sections were stained with immunofluorescence by deparaffinization, antigen retrieval, permeation, and blocking in 5% serum albumin. Fluorescently conjugated primary antibodies were incubated overnight at 4°C to label the peritumoral stroma with α-SMA. Dox has spontaneous light. Nuclei were stained with DAPI for 10 min. The sections were examined under fluorescence microscope.

Cell-killing of drug-loaded hydrogel to B16F10 cells

The proliferation-inhibitory effect of hydrogels on B16F10 was assessed by CCK8 assay analysis. B16F10 cells were seeded in 96-well plates at $3*10^3$ cells per well for 24 h. Discard the old medium. Add Dox loaded with gradient concentrations (0–100 μg/ml) sodium alginate hydrogel mixed with cell culture medium (10% drug loaded hydrogel, 9% fetal bovine serum, 81% DMEM medium, 1% double antibody), each concentration was set to three parallel wells, after a total of 24 h and 48 h incubation, PBS was added to wash once. Add 100 μL of 10% CCK-8 medium to each well, place in a cell incubator to

incubate for 4 h and use a multi-mode microplate detection system to read the absorbance at 450 nm wavelength.

Live and dead staining of cells

To visualize dead and live cells after different treatments, fluorescence images of cells were acquired by propidium iodide (PI) and acetoxymethyl ester (AM) staining. First, $5*10^5$ B16F10 cells were inoculated into confocal dishes and allowed for 24 h to adhere. Each group was administered according to Blank (without any treatment), Alg, Dox, Alg-Dox, Alg-R837, and Alg-Dox-R837groups, and incubated for 24 h. The cells were taken out and stained, and then placed under a confocal microscope (UltraVIEW VoX, PerkinElmer Instruments Shanghai Co., Ltd.) to observe and record at 405nm, 488nm and 563 nm.

In vitro activation of dendritic cells

To verify the role of drug-loaded hydrogels in immunity. The expression of immune molecules (CD80, MHCII) in DC2.4 cells after direct co-incubation with drugs was studied by ultrasensitive nanoflow cytometry (Attune NxT, Thermo Fisher Scientific Co., Ltd.), and related inflammatory factors (IL-6, TNF-α) were quantified by ELISA.

In order to simulate the actual drug onset process and study the effect of B16F10 tumor cell apoptosis on the activation of immune response, a transwell system was also introduced. Blank group (top layer without any treatment, not even B16F10 cells), and B16F10 cells treated with Alg, Dox, Alg-Dox, Alg-R837, Alg-Dox-R837 for 24 h were placed in the dishes. The residues obtained of B16F10 cells by different treatment methods are placed in transwell insert, and DC2.4 cells were incubated in the transwell chamber. The expression of immune molecules was detected after co-incubating again for 24 h.

Antitumor efficacy in mice

Adaptive rearing of C57/BL6 mice was subcutaneously inoculated with $1*10^6$ B16F10 cells on the right back for 1 week. When the tumor volume reached 100 mm^3 at day 7, mice were randomly divided into six therapeutic groups ($n = 6$), which were recorded as control group, Dox group, Alg-Dox group, Alg-Dox-R837 group, aPD-L1 group and Alg-Dox-R837+aPD-L1 group. They were weighed every 2 days, and the tumor growth on the back was observed.

Then, mice were immunized with one dosage of 100 μL of saline or 100 μL of saline with Dox alone or 100 μL gel of Alg-Dox, or gel of Alg-Dox-R837, with or without Dox pretreatment by interstitial injection at day 0. A single dose of gel loaded Dox interstitial injection pretreatment was administrated 2 days before the first immunization and the concentration was equivalent to 2.5 mg/kg body weight according to previous report. After pre-treatment, mice were treated with aPD-L1 immunotherapy at a dose of 2 mg/kg every 3 days. 14 days later, the mice were euthanized, the tumors were dissected and weighed, the weight and size of the tumors were observed, and the serum was collected.

In vivo anti-tumor efficacy evaluation

Tumor length and width were measured every 2 days for each treatment group, and tumor volume was calculated based on the equation $0.5\times \text{length} \times \text{width}^2$. Representative tumor tissues were photographed on day 15 after treatment. Mice were sacrificed when the tumor volume exceeded 1,500 mm^3. The body weight of the mice was recorded every 2 days from the time of treatment.

After 14 days of administration, the tumor tissue, liver and kidney organs of mice in each group were collected, fixed with 4% paraformaldehyde, dehydrated with gradient ethanol, embedded in paraffin, sectioned (thickness 5 μm), stained with H&E, and observed diseases of organs under an inverted microscope.

Detection by flow cytometry

After treatment, immune cells were isolated from tumor tissues or tumor draining lymph nodes of each group of mice ($n = 6$) for immune response analysis. Typically, tumor draining lymph node DCs were isolated using RPMI 1640, cell filters (70 μm, BD FALCON), and stained with anti-CD45, anti-CD83, anti-CD80, and anti-MHCII. Finally, cells were washed once with cell staining buffer and analyzed by flow cytometry (BD FACS Calibur, United States).

Tumor-associated macrophages (TAM) and cytotoxic T lymphocytes (CTL) were isolated from tumor tissues using RPMI 1640, collagenases I and III (1 mg/ml), red blood cell lysis buffer, and cell filters (70 μm, BD FALCON). Then, each sample was divided into two samples for TAM and CTL analysis respectively. For TAM analysis, samples were stained with anti-CD45, anti-F4/80, anti-CD86, and anti-CD206. For CTL analysis, samples were stained with anti-CD3, anti-CD8, and anti-CD4. Then, cells were flushed with cell staining buffer and analyzed by flow cytometry (BD FACS Calibur, United States).

ELISA for TNF-α and IL-6 level

Cell medium supernatant and serum were collected and the secreted levels of TNF-α and IL-6 were determined by ELISA according to the manufacturer's instructions. Then, the absorbance values of the samples at 450 nm were recorded with a fluorescent plate reader (Perkin-Elmer).

Statistical analysis

Data are shown as mean ± SD (standard deviation) with at least three independent replicates. Statistical analyses were performed using a paired/unpaired two-sample Student's t-test with GraphPad Prism 9.0 software; P-value < 0.05 was considered as significant (ns, no significance; *: $p < 0.05$; **: $p < 0.01$; ***: $p < 0.001$).

Results and discussion

Preparation and characterization of Alg-Dox-R837

The hydrogel for immunity inducing was prepared *via* simple mixing of alginate solution and Ca^{2+} solution. Based on the coordination between Ca^{2+} and carboxyl groups in alginate (Alg), Alg-Ca^{2+} hydrogel with an ionically cross-linked network could be obtained by simply mixing Alg solution with Ca^{2+} (Shu et al., 2021; Sun et al., 2021). The Ca^{2+} solution with different concentrations was added to the Alg solution (10 mg/ml) so as to determine the gel-forming conditions (Figure 1A). When the Ca^{2+} concentration was 1 mg/ml, a stable hydrogel system can be formed. The hydrophobic R837 was mixed with a low dose of Dox in the hydrogel solution. The optimal concentration of Ca^{2+} (1 mg/ml), Dox (0.5 mg/ml), and R837 (1 mg/ml) was chosen to synthesize Alg-Dox-R837 hydrogel (Figure 1B). Furthermore, the hydrogel exhibited excellent injectable properties, which can be easily extruded from a syringe and can be written into arbitrary patterns (e.g., NCNST logo) (Figure 1C). To verify the drug loading uniformity, the structure of the hydrogel was characterized by scanning electron microscopy, and the structure of the hydrogel did not change significantly after loading with Dox and R837, indicating that drugs were uniformly dispersed in the Alg-Ca^{2+} hydrogel system with strong loading capacity (Figure 1D). The energy spectrum shows the existence and good distribution of C, Ca, Na, Cl, and O element in the lyophilized Alg-Dox-R837 hydrogel, indicating that the combination of sodium alginate and calcium chloride for the preparation of the hydrogel was successful and feasible (Figure 1E). To examine the change in the mechanical properties of the hydrogel before and after the drug loading, the storage modulus (G′) and loss modulus (G″) of the hydrogel was measured. The results showed that with the incorporation of Dox and R837, both the G′ value and G″ value of the gel increased at the same time, indicating that the addition of drugs would increase the strength of the hydrogel. Meanwhile, the gel loaded with Dox and R837 showed more obvious shear thinning effect, which also demonstrated that the Alg-Dox-R837 hydrogel had excellent injectable properties (Figure 1G). What's more, the experiment of Dox release was a necessary test to see whether the resulting material would be used in biomedical applications. The Dox release of Alg-Dox-R837 hydrogel system in 0.9% sodium chloride injection system was shown in Figure 1H. About 40% of Dox was released at 96 h. Overall, the release rate of Dox was decreased greatly and the release time of Dox is prolonged, so that it was convenient to realize the long-term release of low-dose amounts of Dox to kill tumor cells, then achieve the purpose of triggering ICD.

Subcutaneous interstitial administration of gel to achieve tumor wrapped

To verify the wrap of Alg-Dox-R837 hydrogel by subcutaneous interstitial injection around tumor sites (Figure 2A), we observed the frozen section of the tissue after the tumor stroma-wrapped hydrogel was wrapped in optimal cutting temperature compound (OCT). Alg-Dox-R837 hydrogel (red) was tightly distributed in the interstitial space around the tumor (black), achieving effective tumor wrap, which might block the formation of tumor blood vessels and the delivery of nutrients to the tumor (Figure 2B). To verify the release efficiency and infiltration of Dox in tumor tissues, α-SMA was subjected to fluorescence localization, which is positively and highly expressed in peritumoral tissue. Compared with pure Dox solution injected, the Alg-Dox-R837 hydrogel system exhibited a large amount of DOX infiltration and released into tumor tissue (Figure 2C), which would promote Dox to kill tumor cells effectively. The permeability of the drug was calculated from the fluorescence area. The results showed that the drug permeability of the free Dox group had a large error range, and the average permeability was 10.8%, which may due to the free Dox was metabolized faster in the body. In contrast, the error range in the Alg-Dox-R837 interstitial administration group was smaller, and the average permeability was 26.7%, indicating that Dox based on the gel carrier could enter the tumor tissue stably and had a higher level of Dox accumulated in the tumor tissues (Figure 2D).

In vitro tumor cell killing and activation of dendritic cells

The inhibitory effect of Dox-loaded hydrogel on melanoma cell B16F10 was evaluated by CCK-8 test. Based on the cell viability value of the group without Dox, the hydrogel containing different concentrations of Dox (0–100 μg/ml) showed obvious anti-tumor effects after cells were incubated for 24 h and 48 h. With the increase of Dox concentration, the inhibitory effect of the drug loaded hydrogel system on the proliferation of B16F10 cells became more obvious. After 24 h and 48 h incubation, the IC50 of the drug-loaded hydrogel system for B16F10 was 4.33 μg/ml and 0.13 μg/ml. The results showed that the drug-loaded hydrogel system could continuously and effectively inhibit the activity of B16F10 cells (Figure 3A).

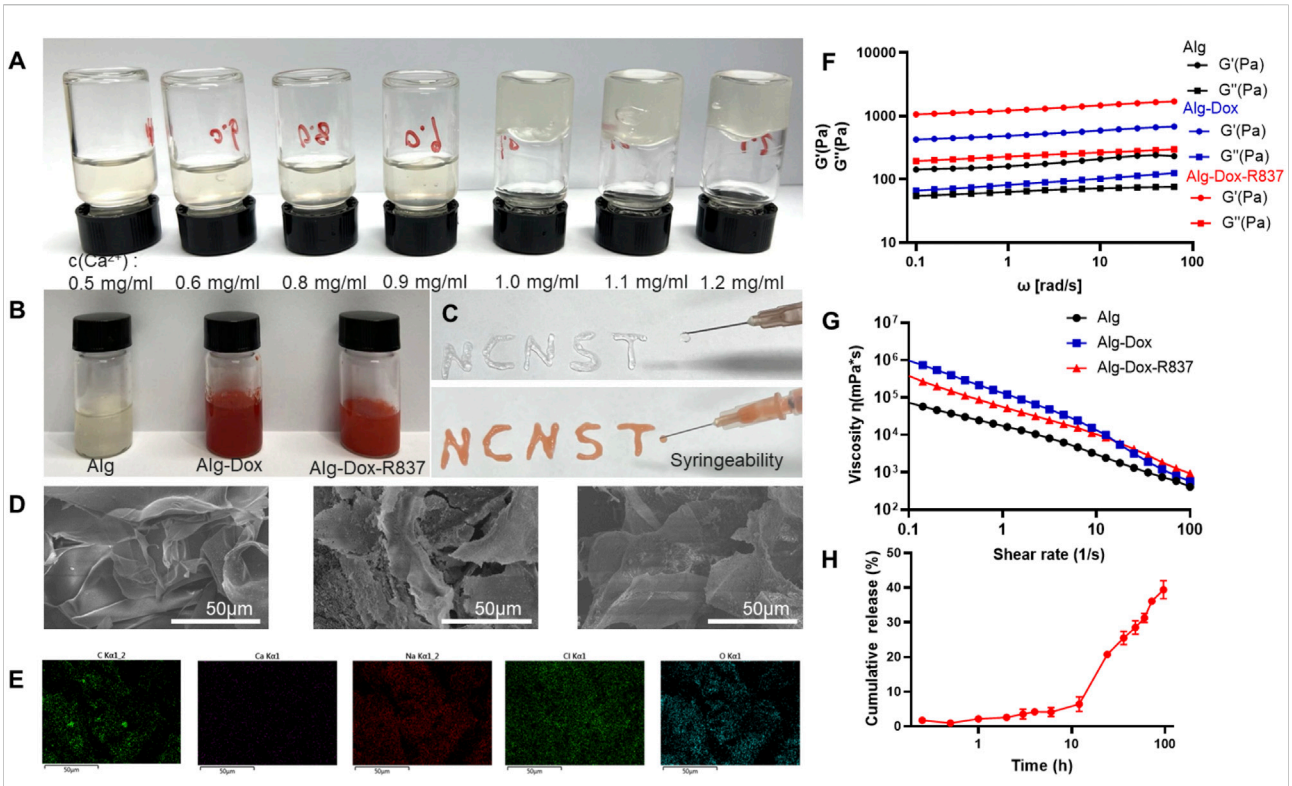

FIGURE 1
Characterization of Alg-Dox-R837 hydrogel **(A)** Gel formation with different Ca^{2+} concentrations; **(B)** Gel images with different components; **(C)** Alg-Dox-R837 formed "NCNST"; **(D)** Morphological characterization of hydrogel with different compositions (scale bar: 50 μm); **(E)** Elemental energy spectrum distribution of Alg-Dox-R837; **(F)** Loss modulus and storage modulus of Alg, Alg-Dox and Alg-Dox-R837; **(G)** Viscosity *versus* shear rate for Alg, Alg-Dox and Alg-Dox-R837; **(H)** *In vitro* sustained release profile of Dox in Alg-Dox-R837 gel.

To further verify the killing effect of the drug-loaded hydrogel on cells, we did cell live and dead staining. The results showed that Alg was safer for cells, and the proportion of apoptotic cells was low, indicating the biosafety of the hydrogel. The R837 adjuvant had no obvious killing effect on B16F10 cells. Dox has a certain killing effect on B16F10 cells, but due to the fast metabolism of Dox, the proportion of apoptotic cells is low. Alg-Dox and Alg-Dox-R837 showed a strong cell-killing effect due to their slow-release effect of Dox, while Alg-Dox and Alg-Dox-R837 showed no significant difference in cell-killing intensity (Figure 3B).

To verify the function of Alg-Dox-R837 in the immune response, costimulatory molecule expression and cytokine secretion in DC 2.4 cells were measured. We used flow cytometry to determine the expression of cell surface markers (MHCII and CD80) and used ELISA to quantify the levels of IL-6 and TNF-α in the supernatant of DCs after different treatments to verify the effect of DCs activation. The results showed that Alg itself could not increase the DC2.4 expression levels of MHCII and CD80, that is, Alg showed negligible effect on activating DCs. However, after adding an appropriate amount of R837 adjuvant and Dox, the expressions of MHCII and CD80 on the DC surface were significantly increased (Figure 3C&D), showing obvious DC activation. Mature DCs process phagocytic antigens and produce a number of pro-inflammatory cytokines to promote an immune response, which is presented to T lymphocytes, elicits humoral or cellular immunity. The results showed the levels of inflammatory factors (TNF-α, IL-6) in the cell culture medium were increased (Figure 3E&F). The Alg-Dox-R837 group had the most obvious activation effect on DCs.

At the same time, B16F10 was cultured in the upper layer of transwell plate, and after different drug treatments, the effect of B16F10 cells and their residues on DCs was observed (Figure 3G). The results showed that when DCs were in contact with B16F10 cells, the CD80 and MHCII expression of DC markers would slightly increase, indicating that DCs were activated to a certain extent. The Dox-treated groups, such as the Dox, Alg-Dox, and Alg-Dox-R837 groups, showed significant increases in the expression levels of surface markers MHCII and CD80 (Figure 3H). It showed that a small amount of killed tumor cells could effectively promote the maturation of DCs, thereby activating a strong immune response.

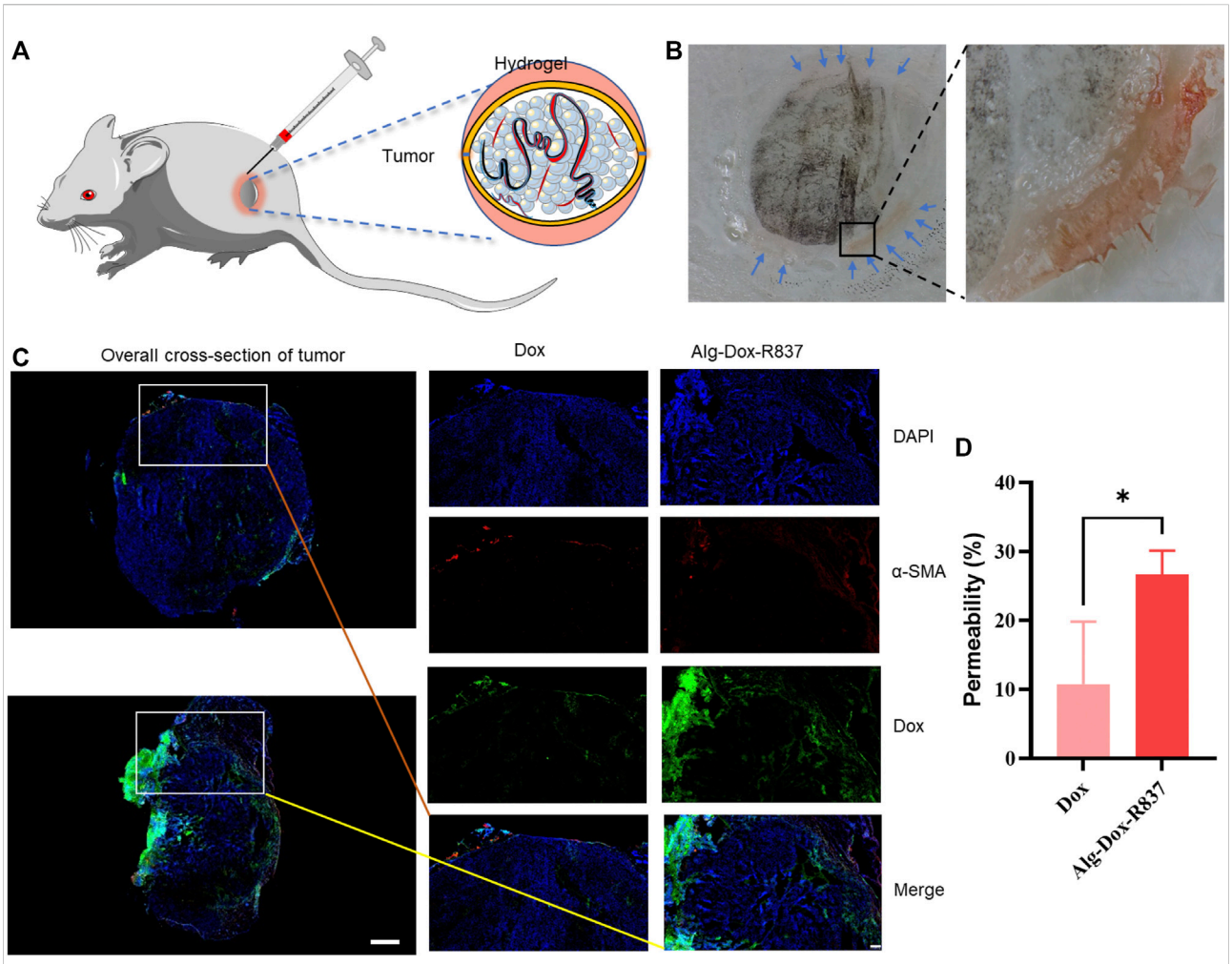

FIGURE 2
Subcutaneous interstitial administration of gel to achieve tumor wrap **(A)** Schematic diagram of interstitial injection of hydrogel to achieve tumor wrap; **(B)** Cryosection imaging of gel-wrapped tumor (black: melanoma, red: Alg-Dox -R837 gel); **(C)** Localized fluorescence imaging (scale bar: 200 μm) and overall cross-section imaging (scale bar: 1,000 μm) of Dox in tumors after treatments; **(D)** Permeability of tumor-to-stromal.

In vivo antitumor efficacy

In order to verify the antitumor effect of the Alg-Dox-R837 hydrogel system *in vivo*, we established a melanoma (B16F10) mouse model. After 7 days of modeling, the hydrogel was injected into the interstitium to wrap the tumor (Figure 4A). Following treatment, changes in tumor volume of mice were recorded daily (Figures 4B,D). The results showed that the tumor tissue of the mice in the untreated group grew rapidly. After interstitial administration of Dox alone, the growth of melanoma tumor tissue in mice was not significantly inhibited. This is because the metabolic rate of Dox is fast, and it is difficult to achieve significant therapeutic effect with lower frequency administration of Dox. At the same time, the single aPD-L1 administration group also did not exert a significant therapeutic effect. After administration of Alg-Dox, because Alg can slowly release Dox to kill melanoma, it makes up the disadvantage of the fast metabolism of Dox, which produces a certain inhibitory effect on tumor proliferation, and the volume growth of tumor tissue is slowed down to a certain extent. However, in the Alg-Dox-R837 group, the inhibitory effect on the tumor was more significant due to the immune activation effect of the R837 adjuvant. After the interstitial wrap of Alg-Dox-R837 hydrogel for 2 days, the injection of aPD-L1 through the lower extremity interstitium showed the strongest immune response and anti-tumor effect, and the tumor tissue volume of this group remained low level. After 14 days of treatment, the mice in each group were dissected, and it was found that the average melanoma volume of the mice in the Alg-Dox-R837+aPD-L1 group was the smallest, even some mice no longer detected tumor tissue, indicating that the interstitial immune response can effectively treat melanoma *in situ*

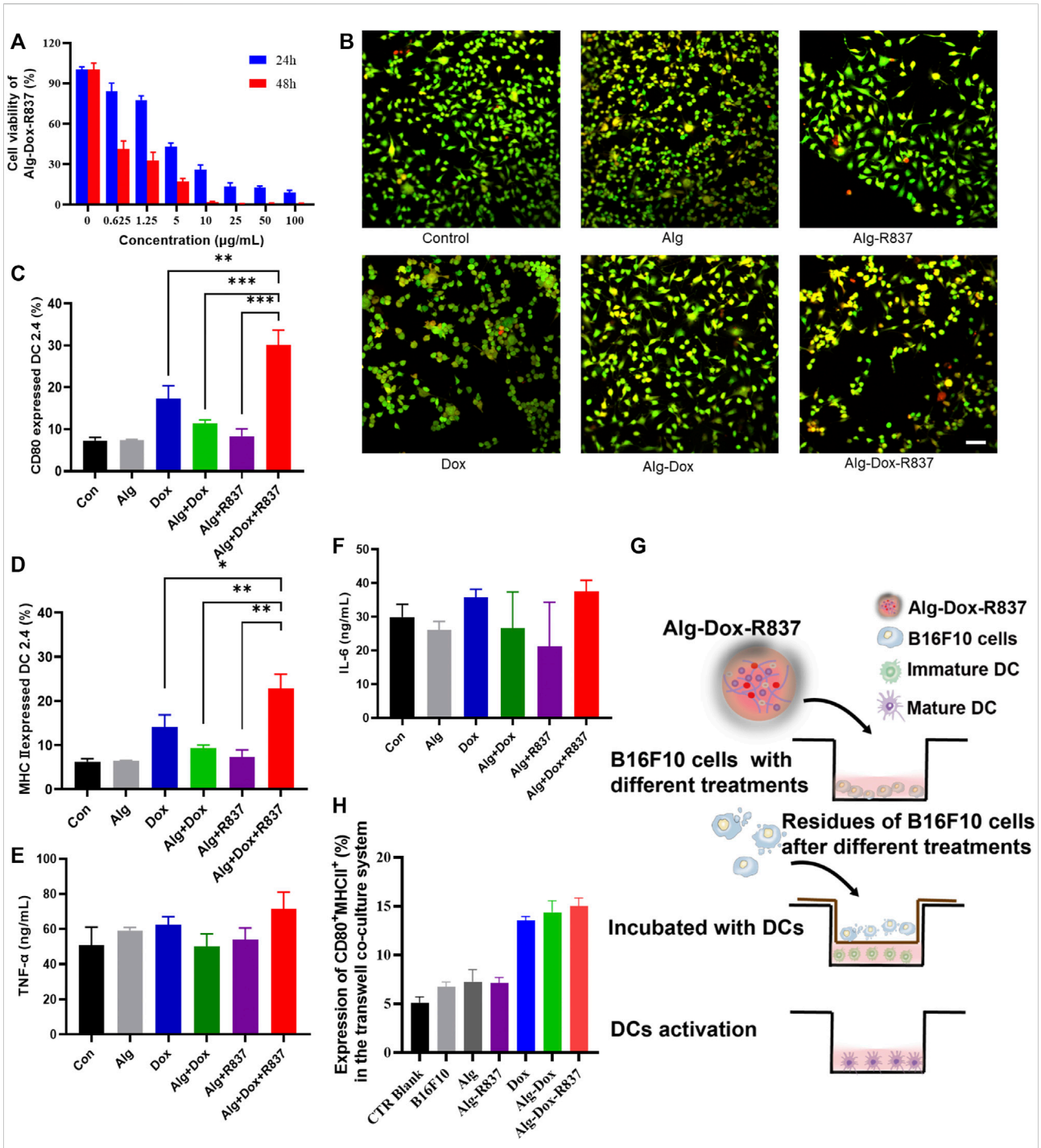

FIGURE 3
In vitro cell killing and activation of dendritic cells **(A)** Killing effect of Alg-Dox-R837 on B16F10; **(B)** Fluorescence images of dead and live cells after different treatments obtained by calcein AM and PI staining (scale bar: 70 μm); **(C,D)** The expression of DC surface markers CD80 and MHCII was assessed by flow cytometry; **(E,F)** The secretion of TNF-α and IL-6 in the culture supernatant of DC was measured by ELISA; **(G)** Schematic representation of B16F10 residue-induced DC activation after various treatments assessed using the transwell system. B16F10 cell residues with different treatments were placed in the transwell insert, and DC2.4 cells were cultured in the transwell chamber; **(H)** The expression of DC2.4 surface markers (CD80 and MHCII) in the transwell co-culture system was assessed by flow cytometry analysis.

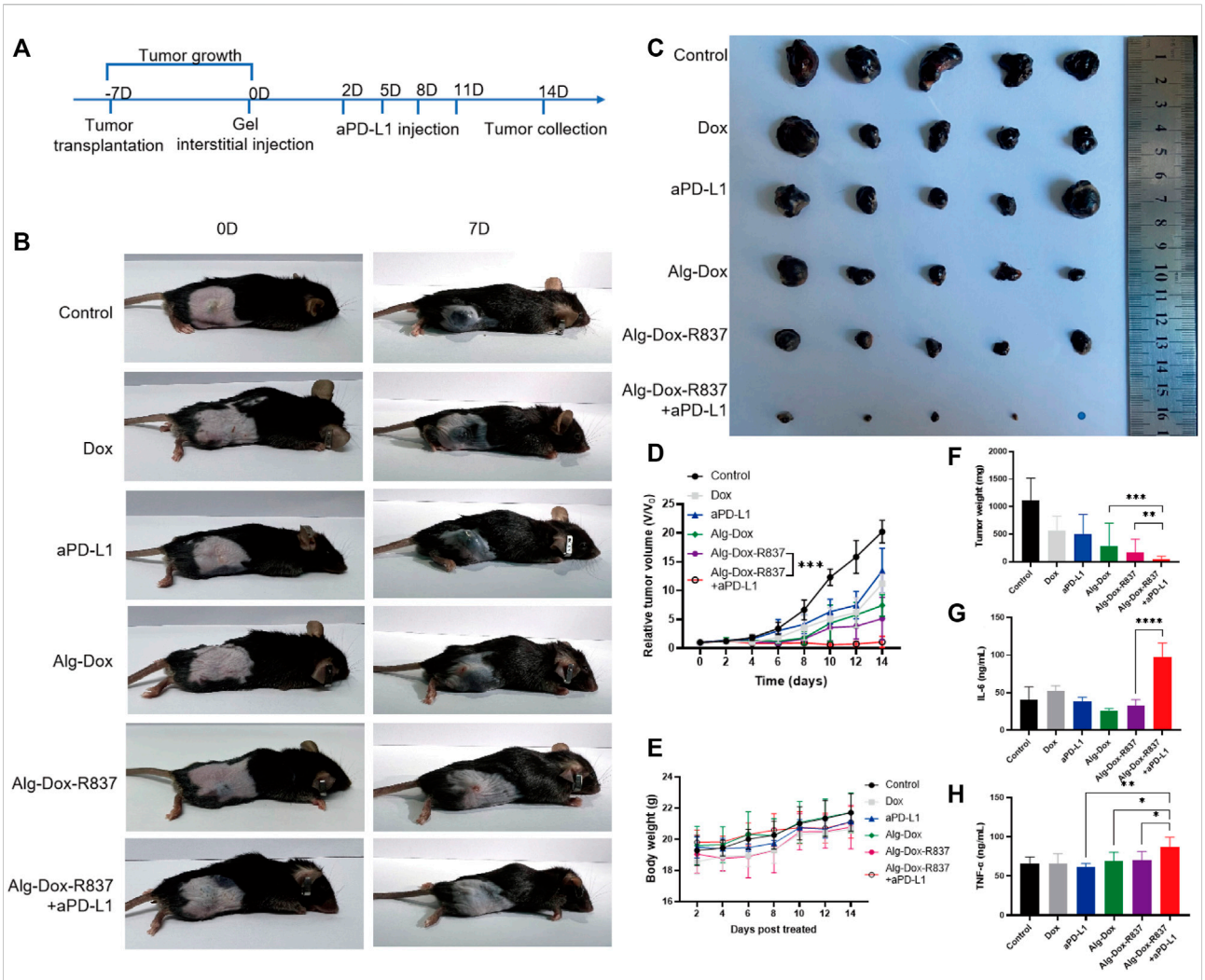

FIGURE 4
In vivo antitumor efficacy **(A)** Dosing schedule of interstitum-based chemo-immunotherapy *in vivo*; **(B)** Tumor image after 14 days of treatment in mice; **(C)** Image of isolated tumor after 14 days; **(D)** Treatment time curve of relative tumor volume during 14 days; **(E)** Curve of body weight with different treatments; **(F)** Weight of isolated tumor after 14 days of treatment; **(G)** Secreted IL-6 in mice serum after 14 days of treatment; **(H)** Secreted TNF-α in mice serum after 14 days of treatment.

(Figures 4C,F). The body weight changes of the mice in each group were monitored within 14 days. The results showed that the average body weight of the mice in each group increased generally within 14 days, indicating that the strategy of interstitial administration did not adversely affect the life quality of the mice (Figure 4E).

After 14 days of treatment, the serum of each group was collected for the detection of IL-6 and TNF-α. As shown in Figures 4G,H, the levels of serum inflammatory factors in the Alg-Dox administration group, Alg-Dox-R837 administration group and Alg-Dox-R837+aPD-L1 group increased, and the content of inflammatory factors in the serum of the mice was the highest in the Alg-Dox- R837+aPD-L1 administration group. It shows that the administration of interstitial hydrogel can significantly induce the immune response, achieving the purpose of safe and efficient tumor treatment.

After 14 days of administration, tumor tissue and major metabolic organs (liver and kidney) were collected for hematoxylin and eosin (H&E) staining (Figure 5). As shown in the figure, compared with the control group, slight necrosis of tumor cells was observed in the Dox, Alg-Dox, and Alg-Dox-R837 administration groups, indicating that the administration methods of Dox, Alg-Dox, and Alg-Dox-R837 have certain anti-tumor effect. The effect of single administration of aPD-L1 group was not obvious. However, extensive tumor tissue necrosis was observed in the Alg-Dox-R837+aPD-L1 group. In addition, the tumor tissue area in this group significantly shrank after administration, and the tumor tissue sections were surrounded

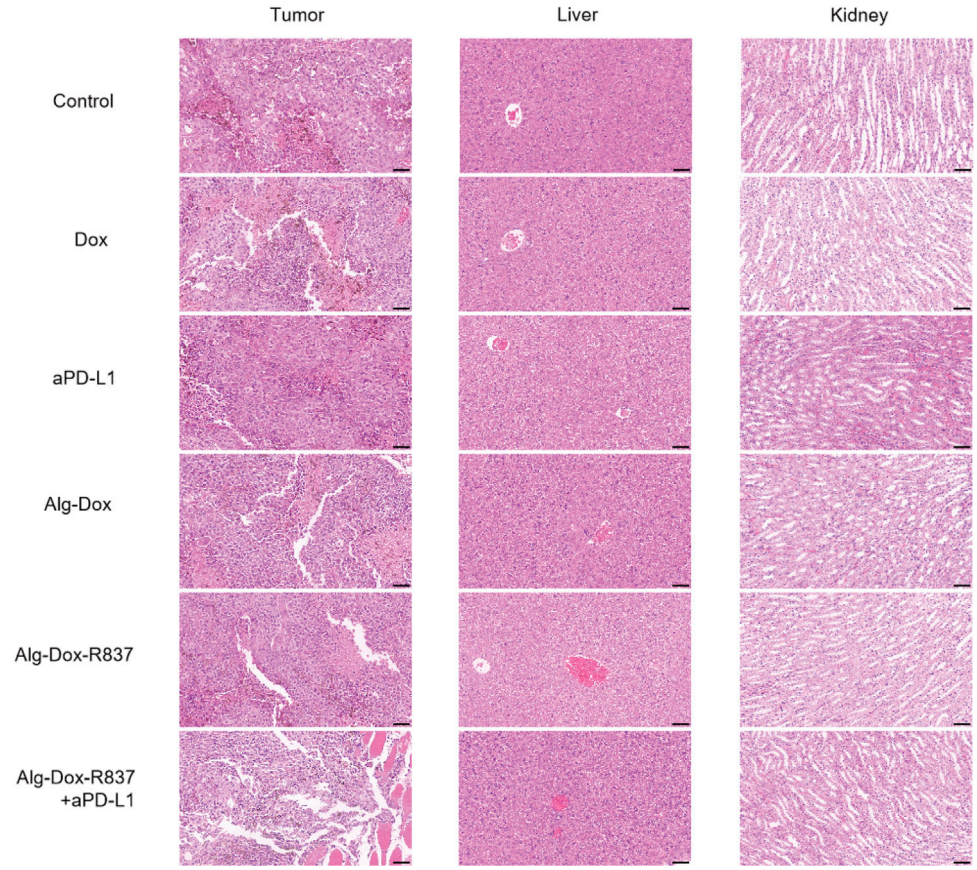

FIGURE 5
HE-stained images of major metabolic organs (liver and kidney) and tumor tissue after 14 days of drug administration in mice (scale bar: 50 μm).

by large pieces of normal muscle cells, indicating that the interstitial drug administration strategy can effectively inhibit the growth and invasion of tumor tissue. What's more, there was no significant difference in pathological damage between the liver and kidney of the mice in administration groups and the control group, indicating that the interstitial administration had no obvious toxic or side effects on metabolic organs such as liver and kidney.

Remodeling of the tumor microenvironment

Altering the tumor microenvironment to suppress tumorigenesis is as important as direct tumor killing, and here we examined macrophage polarization in mice tumor tissues after administration by cellular markers (Cossarizza et al., 2021). As shown in the figure (Figures 6A,B), we observed that when only Dox, Alg-Dox, aPD-L1, and Alg-Dox-R837 were administered, the M1 or M2 cell marker values of macrophages in tumor tissues of mice (M1: $F4/80^{+}CD86^{+}$, M2: $F4/80^{+}CD206^{+}$) did not change significantly in each group, indicating that these administration groups had little effect on the polarization direction of macrophages. However, in the combined administration group of Alg-Dox-R837+aPD-L1, the M1 cell marker value increased, and the M2 cell marker value decreased, showing a more significant transformation of macrophages to the M1 type. At the same time, we detected and compared the changes of helper T cell ($CD3^{+}CD4^{+}$) and killer T ($CD3^{+}CD8^{+}$) cell markers in tumor tissues of mice in each group (Figure 6C&D). The results showed that the contents of $CD4^{+}$ T cells and $CD8^{+}$ T cell markers in the mice after administration increased to a certain extent, and the combined administration group that was administered Alg-Dox-R837+aPD-L1 detected the highest levels. It showed that the combined administration strategy of Alg-Dox-R837+aPD-L1 could significantly change the tumor microenvironment, promote the transformation of macrophages to the M1 type, and induce the increase of $CD4^{+}T$ and $CD8^{+}T$ cells in tissues, and a stronger T cell immune response would be stimulated for antitumor therapy. However, the analysis of the activation status of DC cells in the lymph nodes of mice (Figure 6E) showed that, except for the Alg-

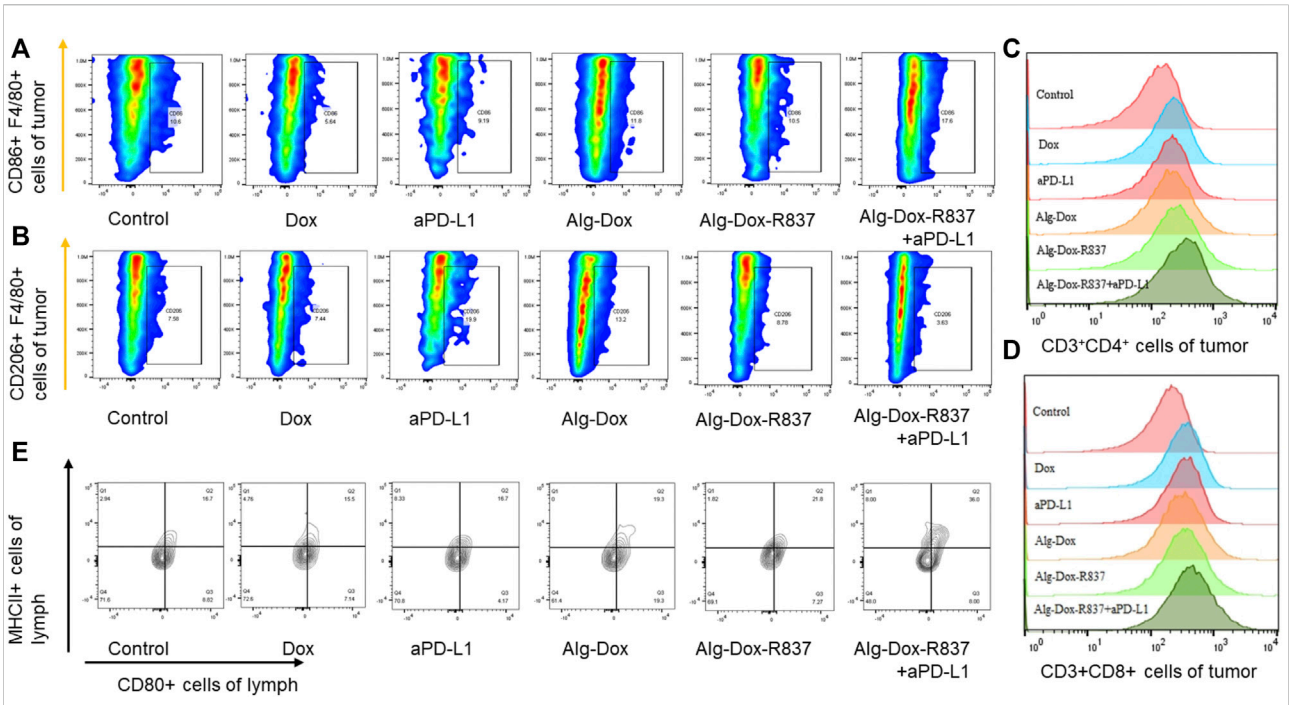

FIGURE 6
Remodeling of the tumor microenvironment **(A)** Changes in the number of M1-type macrophages ($F4/80^+CD86^+$); **(B)** Changes in the number of M2-type macrophages ($F4/80^+CD206^+$); **(C)** Changes in the number of helper T cells ($CD3^+CD4^+$) after treatment; **(D)** Changes in the number of killer T cells ($CD3^+CD8^+$) after treatment; **(E)** After treatment, the activation of DC cells in lymph nodes.

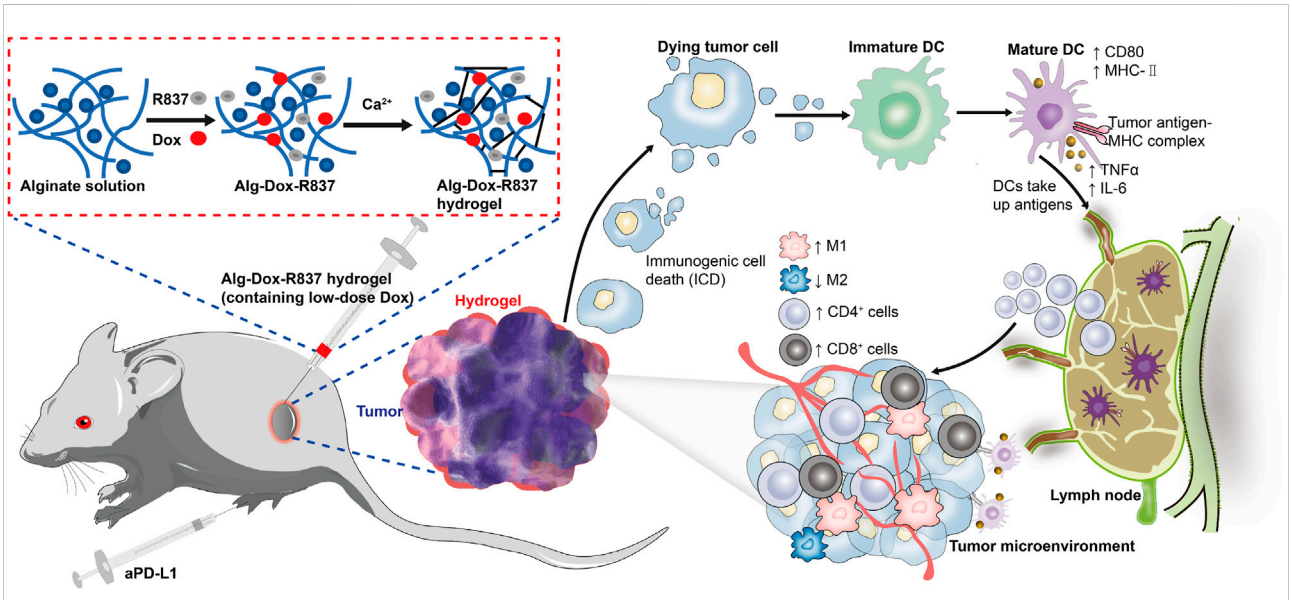

FIGURE 7
Schematic illustration of the mechanism of tumor immunotherapy by an engineered hydrogel through tumor interstitial wrap.

Dox-R837+aPD-L1 group, various administration methods had little effect on the activation status of DC cells. After administration of Alg-Dox-R837+aPD-L1, the amounts of cell markers MHCII and CD80 in CD83-expressing cells (dendritic cells) was significantly increased. It showed that this mode of administration inhibited the invasion and metastasis of the tumor wrapped, and enhanced antigen presentation to promote the maturation of DCs in the lymph nodes (Figure 7).

Conclusion

In conclusion, a sodium alginate hydrogel system was prepared and the target drugs (Dox and R837) were incorporated into it. The results showed that the hydrogel system had good gel formation and good biocompatibility. After injection into the interstitial space around the tumor, it could slowly release Dox to kill tumor cells, activate and recruit more immune cells to generate an immune response with the help of R837, and finally produce a strong anti-tumor immune effect.

It has been reported that there are not negligible immune cells in the interstitium, which undertake important immune functions. However, there are few reports on the immune cell response and application of interstitial distribution. In this work, a hydrogel system was designed, embedded in the interstitial tissue and directly acting on the surrounding environment. The immune response of interstitial cells was successfully induced, the further development of melanoma was suppressed, and the tumor cells were successfully killed. It showed significance for the future interstitial administration to induce subcutaneous immune response, thereby reducing system toxicity and enhancing efficacy of therapeutic drugs.

Data availability statement

The original contributions presented in the study are included in the article/supplementary material, further inquiries can be directed to the corresponding authors.

Ethics statement

The animal study was reviewed and approved by National Center for Nanoscience and Technology. Written informed consent was obtained from the owners for the participation of their animals in this study.

Author contributions

DH and ZA designed the research. ZL and JX performed drug synthesis. ZL, QZ, MZ, YM, JZ, TL, LJ, KL, and XL conducted the animal experiments, ZL and JX analyzed the data, ZL, JX, and QZ wrote the manuscript. All authors have read and approved the final submitted manuscript.

Funding

This work was supported by the Key Research Program of CAS (QYKJZD-SSW-SLH02) and the Key Research Program of Frontier Sciences of CAS (ZDBS-LY-SLH036).

Conflict of interest

The authors declare that the research was conducted in the absence of any commercial or financial relationships that could be construed as a potential conflict of interest.

Publisher's note

All claims expressed in this article are solely those of the authors and do not necessarily represent those of their affiliated organizations, or those of the publisher, the editors and the reviewers. Any product that may be evaluated in this article, or claim that may be made by its manufacturer, is not guaranteed or endorsed by the publisher.

References

Aboelella, N. S., Brandle, C., Kim, T., Ding, Z. C., and Zhou, G. (2021). Oxidative Stress in the Tumor Microenvironment and Its Relevance to Cancer Immunotherapy. *Cancers (Basel)* 13, 986–1009. doi:10.3390/cancers13050986

Banstola, A., Poudel, K., Kim, J. O., Jeong, J. H., and Yook, S. (2021). Recent progress in stimuli-responsive nanosystems for inducing immunogenic cell death. *J. Control. Release* 337, 505–520. doi:10.1016/j.jconrel.2021.07.038

Budden, K. F., Gellatly, S. L., Wood, D. L. A., Cooper, M. A., Morrison, M., and Hugenholtz, P., (2017). Emerging pathogenic links between microbiota and the gut-lung axis. *Nat. Rev. Microbiol.* 15, 55–63. doi:10.1038/nrmicro.2016.142

Cao, Y. P., Hu, X. J., Zhang, Q., Hua, W. D., Hu, N., and Nie, Y. F., (2020). Intervaginal space injection of a liquid metal can prevent breast cancer invasion and better-sustain concomitant resistance. *Mat. Chem. Front.* 4, 1397–1403. doi:10.1039/c9qm00753a

Cossarizza, A., Chang, H. D., Radbruch, A., Abrignani, S., Addo, R., and Akdis, M., (2021). Guidelines for the use of flow cytometry and cell sorting in immunological studies (third edition). *Eur. J. Immunol.* 51, 2708–3145. doi:10.1002/eji.202170126

Dewan, M. Z., Galloway, A. E., Kawashima, N., Dewyngaert, J. K., Babb, J. S., and Formenti, S. C., (2009). Fractionated but not single-dose radiotherapy induces an immune-mediated abscopal effect when combined with anti-CTLA-4 antibody. *Clin. Cancer Res.* 15, 5379–5388. doi:10.1158/1078-0432.ccr-09-0265

Duan, J., Wang, Y., and Jiao, S. (2018). Checkpoint blockade-based immunotherapy in the context of tumor microenvironment: Opportunities and challenges. *Cancer Med.* 7, 4517–4529. doi:10.1002/cam4.1722

Foster, J. A., and Mcvey Neufeld, K.-A. (2013). Gut–brain axis: How the microbiome influences anxiety and depression. *Trends Neurosci.* 36, 305–312. doi:10.1016/j.tins.2013.01.005

Galluzzi, L., Vitale, I., Warren, S., Adjemian, S., Agostinis, P., and Martinez, A. B., (2020). Consensus guidelines for the definition, detection and interpretation of immunogenic cell death. *J. Immunother. Cancer* 8, e000337. doi:10.1136/jitc-2019-000337

Hu, N., Cao, Y. P., Ao, Z., Han, X. X., Zhang, Q., and Liu, W. T., (2018). Flow behavior of liquid metal in the connected fascial space: Intervaginal space injection in the rat wrist and mice with tumor. *Nano Res.* 11, 2265–2276. doi:10.1007/s12274-017-1848-0

Jin, M. Z., and Wang, X. P. (2021). Immunogenic cell death-based cancer vaccines. *Front. Immunol.* 12, 697964. doi:10.3389/fimmu.2021.697964

Kepp, O., Marabelle, A., Zitvogel, L., and Kroemer, G. (2020). Oncolysis without viruses - inducing systemic anticancer immune responses with local therapies. *Nat. Rev. Clin. Oncol.* 17, 49–64. doi:10.1038/s41571-019-0272-7

Kroemer, G., Galassi, C., Zitvogel, L., and Galluzzi, L. (2022). Immunogenic cell stress and death. *Nat. Immunol.* 23, 487–500. doi:10.1038/s41590-022-01132-2

Kroemer, G., Galluzzi, L., Kepp, O., and Zitvogel, L. (2013). Immunogenic cell death in cancer therapy. *Annu. Rev. Immunol.* 31, 51–72. doi:10.1146/annurev-immunol-032712-100008

Krysko, D. V., Garg, A. D., Kaczmarek, A., Krysko, O., Agostinis, P., and Vandenabeele, P. (2012). Immunogenic cell death and DAMPs in cancer therapy. *Nat. Rev. Cancer* 12, 860–875. doi:10.1038/nrc3380

Lei, H., Kim, J. H., Son, S., Chen, L., Pei, Z., and Yang, Y., (2022). Immunosonodynamic therapy designed with activatable sonosensitizer and immune stimulant imiquimod. *ACS Nano* 16, 10979–10993. doi:10.1021/acsnano.2c03395

Liu, G., Wang, H., Shi, C., Chen, G., Wang, Y., and Huang, W., (2022a). Confining isolated photosensitizers to relieve self-aggregation and potentiate photodynamic efficacy for synergistic cancer therapy. *Chem. Commun.* 58, 10813–10816. doi:10.1039/d2cc03446h

Liu, W. T., Cao, Y. P., Zhou, X. H., and Han, D. (2022b). Interstitial fluid behavior and diseases. *Adv. Sci. (Weinh).* 9, e2100617. doi:10.1002/advs.202100617

Mansurov, A., Ishihara, J., Hosseinchi, P., Potin, L., Marchell, T. M., and Ishihara, A., (2020). Collagen-binding IL-12 enhances tumour inflammation and drives the complete remission of established immunologically cold mouse tumours. *Nat. Biomed. Eng.* 4, 531–543. doi:10.1038/s41551-020-0549-2

Musetti, S., and Huang, L. (2018). Nanoparticle-Mediated remodeling of the tumor microenvironment to enhance immunotherapy. *ACS Nano* 12, 11740–11755. doi:10.1021/acsnano.8b05893

Ngambenjawong, C., Gustafson, H. H., and Pun, S. H. (2017). Progress in tumor-associated macrophage (TAM)-targeted therapeutics. *Adv. Drug Deliv. Rev.* 114, 206–221. doi:10.1016/j.addr.2017.04.010

Rios-Doria, J., Durham, N., Wetzel, L., Rothstein, R., Chesebrough, J., and Holoweckyj, N., (2015). Doxil synergizes with cancer immunotherapies to enhance antitumor responses in syngeneic mouse models. *Neoplasia* 17, 661–670. doi:10.1016/j.neo.2015.08.004

Shu, G., Zhu, W., Jiang, Y. Z., Li, X. W., Pan, J. B., and Zhang, X. N., (2021). Persistent luminescence immune hydrogel for photodynamic-immunotherapy of tumors *in vivo*. *Adv. Funct. Mat.* 31, 2104472. doi:10.1002/adfm.202104472

Sun, L., Shen, F., Tian, L., Tao, H., Xiong, Z., and Xu, J., (2021). ATP-responsive smart hydrogel releasing immune adjuvant synchronized with repeated chemotherapy or radiotherapy to boost antitumor immunity. *Adv. Mat.* 33, e2007910. doi:10.1002/adma.202007910

Waldman, A. D., Fritz, J. M., and Lenardo, M. J. (2020). A guide to cancer immunotherapy: from T cell basic science to clinical practice. *Nat. Rev. Immunol.* 20, 651–668. doi:10.1038/s41577-020-0306-5

Wang, X., Shi, Z., Luo, J., Zeng, Y., He, L., and Chen, L., (2022). Ultrasound improved immune adjuvant delivery to induce DC maturation and T cell activation. *J. Control. Release* 349, 18–31. doi:10.1016/j.jconrel.2022.06.054

Wang, Y., Zhang, Z., Zheng, C., Zhao, X., Zheng, Y., and Liu, Q., (2021). Multistage adaptive nanoparticle overcomes biological barriers for effective chemotherapy. *Small* 17, e2100578. doi:10.1002/smll.202100578

Xu, W. L., Shi, B. J., Li, S. L., Yu, F. X., Guo, L. N., and Li, M., (2020). Targeted inhibition of myeloid-derived suppressor cells in the tumor microenvironment by low-dose doxorubicin to improve immune efficacy in murine neuroblastoma. *Chin. Med. J.* 134, 334–343. doi:10.1097/cm9.0000000000001234

Zhang, Q., Ao, Z., Hu, N., Zhu, Y., Liao, F., and Han, D. (2020a). Neglected interstitial space in malaria recurrence and treatment. *Nano Res.* 13, 2869–2878. doi:10.1007/s12274-020-2946-y

Zhang, Y. N., Poon, W., Sefton, E., and Chan, W. C. W. (2020b). Suppressing subcapsular sinus macrophages enhances transport of nanovaccines to lymph node follicles for robust humoral immunity. *ACS Nano* 14, 9478–9490. doi:10.1021/acsnano.0c02240

Zhang, Y., and Zhang, Z. (2020). The history and advances in cancer immunotherapy: Understanding the characteristics of tumor-infiltrating immune cells and their therapeutic implications. *Cell. Mol. Immunol.* 17, 807–821. doi:10.1038/s41423-020-0488-6

Zhang, Z., Wang, Q., Liu, Q., Zheng, Y., Zheng, C., and Yi, K., (2019). Dual-locking nanoparticles disrupt the PD-1/PD-L1 pathway for efficient cancer immunotherapy. *Adv. Mat.* 31, e1905751. doi:10.1002/adma.201905751

Zhang, Z., Yue, Y. X., Xu, L., Wang, Y., Geng, W. C., and Li, J. J., (2021). Macrocyclic-amphiphile-based self-assembled nanoparticles for ratiometric delivery of therapeutic combinations to tumors. *Adv. Mat.* 33, e2007719. doi:10.1002/adma.202007719

Zhao, H., Xu, J., Wang, Y., Sun, C., Bao, L., and Zhao, Y., (2022). A photosensitizer discretely loaded nanoaggregate with robust photodynamic effect for local treatment triggers systemic antitumor responses. *ACS Nano* 16, 3070–3080. doi:10.1021/acsnano.1c10590

frontiers | Frontiers in Bioengineering and Biotechnology

TYPE Original Research
PUBLISHED 28 November 2022
DOI 10.3389/fbioe.2022.1072153

OPEN ACCESS

EDITED BY
Yong Liu,
University of Chinese Academy of Sciences, China

REVIEWED BY
Semra Akgönüllü,
Hacettepe University, Turkey
Ankur Sood,
Yeungnam University, South Korea

*CORRESPONDENCE
Solmaz Hajizadeh,
Solmaz.hajizadeh@tbiokem.lth.se

SPECIALTY SECTION
This article was submitted to Biomaterials, a section of the journal Frontiers in Bioengineering and Biotechnology

RECEIVED 17 October 2022
ACCEPTED 17 November 2022
PUBLISHED 28 November 2022

CITATION
Hajizadeh S, Dicko C and Bülow L (2022), Interaction of haemin with albumin-based macroporous cryogel: Adsorption isotherm and fluorescence quenching studies.
Front. Bioeng. Biotechnol. 10:1072153.
doi: 10.3389/fbioe.2022.1072153

Interaction of haemin with albumin-based macroporous cryogel: Adsorption isotherm and fluorescence quenching studies

Solmaz Hajizadeh*, Cedric Dicko and Leif Bülow

Division of Pure and Applied Biochemistry, Department of Chemistry, Lund University, Lund, Sweden

Albumin-based cryogels for capturing haemin were synthesised by crosslinking different biomolecules, bovine serum albumin (BSA) and ovalbumin (OVA). The impact of the protein and coupling agent concentrations on cryogel's mechanical properties, swelling ratios and polymerisation yields, as well as autoclaving as a post-treatment on the cryogel, were studied. We found that BSA (50 mg/ml) and the crosslinker (*N*-(3-dimethylaminopropyl)-*N*′-ethylcarbodiimide hydrochloride, 46 mg/ml) formed a cryogel with optimum physical characteristics at a comparatively low protein concentration. The cryogel's mechanical stability was increased using a double-layer cryogel approach by crosslinking the BSA proteins at subzero temperature inside an acrylamide and hydroxyethyl methacrylate premade cryogels. Batch binding and kinetic adsorption isotherms of haemin on the cryogels were assessed to evaluate their binding capacity toward the porphyrin molecule. The results showed that single-layer cryogels (BSA and OVA) had a higher capacity (~0.68 mg/ml gel) and higher reaction rate constant towards haemin adsorption than double-layer gels. In contrast, the double-layer cryogels had higher mechanical strength than single-layer gels. The experimental results suggested that the cryogels followed the Freundlich model and the pseudo-second-order isotherm for batch adsorption and kinetics, respectively. The interaction between haemin and the gels was studied by fluorescence quenching. We found between 1.1 and 1.6 binding sites for different cryogels.

KEYWORDS

haemin, albumin, macroporous network, double-layer cryogel, adsorption isotherm, binding sites

Introduction

Human haemoglobin (Hb) comprises four subunits, two alpha and two beta units, each carrying one haem molecule (Ahmed et al., 2020). Haem, Fe^{2+} protoporphyrin IX is crucial in transporting oxygen in the bloodstream. The interaction between haem and globin is stable under physiological conditions, and the iron atoms are kept in the ferrous state by intracellular methemoglobin reductases and $O_2^{\circ-}$ (Hargrove et al., 1997). However, under the autooxidation effect, Fe^{2+} transforms to Fe^{3+} and changes to methemoglobin

(Hebbel et al., 1988). Under such conditions, haem can escape from its protein cavity. Released haem (haematin) is an inflammatory-inducing molecule due to its ability to generate reactive oxygen species (ROS). ROS can alter membrane permeability and human erythrocytes (Graça-Souza et al., 2006) and is recognised as a damage-associated molecular pattern, DAMP. References to haem cytotoxicity can be found elsewhere (Wagener et al., 2001; Aich et al., 2015). In a functioning body, free haem uptake is facilitated by specific serum transport proteins (globin, albumin and haemopexin) and distributed according to their concentrations, affinities for haem, and rates of clearance from the circulation (Morgan et al., 1976). However, in patients (Fontanellas et al., 1994), blood transfusion bags (Vijayan et al., 2022) or when designing haemoglobin-based oxygen carriers (HBOCs) (Bialas et al., 2019), the free haem ions should be removed by other means and methods, such as filtration or dialysis (Fontanellas et al., 1994; Coronel et al., 2003), to minimise their side effects. However, these methods have a few limitations, such as fouling and low efficiency when dealing with suspensions and complex mixtures. Thus, an alternative solution is needed.

In this study, a new class of materials, known as cryogels, was introduced to deplete haem from a solution or suspension. Cryogel (from the Greek word kryos, meaning ice) is a subcategory of hydrogels. The gel material results from the cryotropic gelation (cryogelation) technique that allows forming macroporous polymeric networks with interconnected channels and controlled porosities (Plieva et al., 2004). During cryogelation, the polymer/monomer solution is frozen at a low temperature to create unfrozen and frozen phases. The polymerisation occurs in the unfrozen domains where the concentrations of the chemicals are remarkably high, and the ice crystals (frozen phase) act as porogens. The final product is a permanent macroporous structure where the geometry of the ice crystals determines its final pore size (Hajizadeh et al., 2012). The advantage of cryogels over hydrogels or other polymeric membranes is their large interconnected pores, which allow efficient mass transfer and good flow properties. Since the introduction of cryogels in the 1970s, many different synthetic monomers/polymers, biological molecules and particles have been used to form cryogels (Aragão Börner et al., 2014; Agarwal et al., 2021; Jones et al., 2021). These materials are found in many different applications ranging from separation and purification (Hajizadeh et al., 2021) to biomedical applications (Henderson et al., 2013) and environmental applications (Jain and Kumar, 2013; Berillo et al., 2021).

Porous albumin-based cryogels are popular in various biomedical applications due to their biocompatibility and biodegradability (Kirsebom et al., 2013). In this study, serum albumin protein from bovine and ovalbumin were crosslinked to form a macroporous cryogel for capturing free haemin molecules from an aqueous solution. The suggested material is a potentially good candidate in biomedical and biotechnology applications for removing haem frommixtures. However, the drawback of these materials is their low mechanical stability, making them soft, unsteady and challenging to handle. This issue has been addressed in this study by forming a double-layer cryogel. Double-layer cryogel refers to forming one type of cryogel inside another premade macroporous gel. The binding capacity and kinetics of the different gels were evaluated and discussed, as well as the number of their binding sites.

Materials

Bovine serum albumin (BSA ≥98%, heat shock fraction), haemin, ovalbumin (OVA ≥98%), acrylamide (Am), *N*,*N*′-methylenebis (acrylamide) (MBAm, 99%), *N*,*N*,*N*′,*N*′-tetramethylethylenediamine (TEMED ≥99%), ammonium persulfate (APS ≥98.0%), 2-hydroxyethyl methacrylate (HEMA ≥99%), sodium hydrogen phosphate, sodium dihydrogen phosphate, sodium hydroxide (NaOH), and *N*-(3-dimethylaminopropyl)-*N*′-ethylcarbodiimide hydrochloride (EDC) were all purchased from Merck (Sigma-Aldrich, Burlington, MA, United States) and applied as received.

Methods

Single-layer albumin-based cryogel synthesis

BSA cryogels were synthesised by crosslinking the protein using EDC, as reported elsewhere (Rodionov et al., 2016). Briefly, different masses of BSA powder were dissolved in water to prepare some solution at various concentrations (Table 1). The solutions were cooled in an ice bath. The appropriate amount of crosslinker (EDC) was then added to the BSA solutions and stirred using a magnet while standing in an ice bath. Aliquots (0.25 ml) of the solutions were transferred into precooled glass tubes (i.d. 7 mm) and frozen at −16°C in a cryostat for 2 days. Once the reaction was completed, the gels were thawed at room temperature and washed with water to remove unreacted chemicals.

OVA cryogels were prepared with the same procedure mentioned above, except that the OVA molecule was used instead of BSA proteins. The BSA and OVA cryogels were kept in water at 4°C and henceforth referred to as BSA-CG and OVA-CG, respectively.

Double-layer cryogel synthesis

To synthesise the double-layer cryogels, Am or HEMA monomers were used as the main building block for the primary cryogel. The preparation of cryogel using radical

TABLE 1 Formation conditions, polymerisation yield, swelling rate and mechanical properties of the BSA cryogel.

BSA (mg/ml)	EDC (mg/ml)	Molar ratio COOH/ECD/NH_2	Yield (%)	Swelling rate (%)	Hardness (N)	Compressibility (N mm)
30	37	1: 5.5: 0.6	51.50 ± 1.4	15.78 ± 1.0	—	—
40	37	1: 4: 0.6	46.80 ± 1.7	20.85 ± 3.2	0.94 ± 0.16	0.51 ± 0.13
50	31	1: 2.4: 0.6	40.93 ± 2.5	20.52 ± 1.6	3.55 ± 0.89	1.94 ± 0.47
50	37	1: 3.2: 0.6	52.34 ± 0.9	14.35 ± 2.6	1.1 ± 0.02	0.61 ± 0.02
50	46	1: 3.9: 0.6	53.73 ± 1.3	15.43 ± 1.9	1.49 ± 0.06	0.27 ± 0.04
50	56	1: 4.6: 0.6	45.37 ± 6.8	16.84 ± 2.8	5.25 ± 4.38	2.9 ± 2.4
50	62	1: 5.3: 0.6	44.04 ± 0.4	12.18 ± 1.5	1.41 ± 0.83	0.76 ± 0.45

polymerisation has been reported elsewhere (Hajizadeh, 2012). The monomer concentration of monomers was kept at 6%, and the molar ratio between Am (or HEMA) and MBAm was 6: 1. An activator, TEMED (1% of total monomer volume), was added to the mixture. Then, the solution was degassed under negative pressure to remove any soluble oxygen while the solution was cooled in an ice bath for a minimum of 5 min. Ammonium persulfate (APS) solution (500 μL, 1% of total monomer volume) as an initiator was added to the monomer mixture in the final step. Aliquots (0.25 ml) of the solution were transferred into glass tubes (i.d. 7 mm) and frozen at −12°C in a liquid cryostat overnight. The gels were thawed at room temperature, washed with water to remove all the unreacted monomers, and dried at 60°C. The gels are henceforth referred to as Am-CG and HEMA-CG for the Am and HEMA cryogels, respectively.

The procedure to prepare the second layer inside the primary cryogel is similar to the formation of the single-layer cryogel, as mentioned earlier, with a few minor changes. A dried Am-CG (HEMA-CG) was placed inside glass tubes (i.d. 7 mm). BSA and EDC concentrations were kept at 50 and 46 mg/ml, respectively. The cooled mixture of protein and crosslinker (0.25 ml) was added to the glass tube over the dried Am-CG (or HEMA-CG). After the gel absorbed the solution, the glass tube was sealed and placed inside the cryostat for 2 days at −16°C. The new cryogels are referred to as Am-BSA-CG (HEMA-BSA-CG) based on the type of the first layer of cryogel. The gels were kept in water at 4°C.

Characterisation of cryogels

The polymerisation yield for each cryogel was calculated based on the equation below:

$$Y\,(\%) = \frac{W_1}{W_0} \times 100 \tag{1}$$

where W_0 and W_1 are the theoretical weight and the measured dry weight of the cryogels, respectively. All gels were dried in an oven at 60°C overnight.

The swelling degree was calculated using Eq. 2:

$$S = \frac{W_2 - W_1}{W_1} \tag{2}$$

where W_1 and W_2 are the weights of the dried and swollen cryogels, respectively. The gels were swollen in a water solution, and the excess water was blotted away using filter papers.

Scanning electron microscopy (SEM) was used to study the morphology of the macroporous gels. The middle section of the cryogel was cut transversally into thin discs (1–2 mm thick) and freeze-dried. The discs were sputtered with gold: palladium (40: 60, to a thickness of 15 nm) and imaged using a JEOL JSM-80 5600 LV microscope (Tokyo, Japan).

Thermo Nicolet 6700 FTIR spectrometer equipped with a single bounce diamond ATR and a DTGS detector (Thermo Fisher-Scientific Inc. United States) was used to study Fourier-transform infrared spectroscopy (FTIR) spectra of the different cryogels. Different cuts were made from each gel's top, middle and bottom sections for FTIR analysis.

A texture analyser (XT2i, Stable Micro Systems, Godalming, England) and Exponent v.5.0.9.0 software (Godalming, England) were used to assess the mechanical stability and the data analysis, respectively. The texture analyser had a 2 kg load cell, and the compressive force was applied at a constant rate of 0.5 mm/s. The wet cryogels (stored in a water solution overnight) were placed on a metal plate and compressed up to 50% of their original height. The compression test was performed in triplicate. Young's modulus was extracted as follows (Eq. 3):

$$E = \frac{\sigma}{\varepsilon} = \frac{F/A_0}{\Delta l/l_0} \tag{3}$$

where E is Young's modulus (Pa), F is the force applied to the object (N), A_0 is the cross-sectional area of the cryogel on which the force is applied (m^2), Δl is the change in length under compression, and l_0 is the original height of the object. The hardness and compressibility of the material can also be extracted from force-time graph data. Hardness is a force required to attain a given deformation, and compressibility explains the work

required to deform the product under the first compression cycle (Jones et al., 1997).

To study the effect of sterilisation on the protein cryogel characterisation, wet BSA-CG was autoclaved for 20 min at 121°C and then refrigerated.

Batch binding adsorption

For the batch adsorption experiment, a stock solution of haemin (6 mg/ml) was prepared in phosphate buffer (0.1 M, pH 7.4). Haemin is soluble in alkaline solutions, e.g., NaOH and organic solvents such as dimethyl sulfoxide (DMSO). The powder was first dissolved in a low volume (~1 ml) of NaOH solution (0.01 M) to make the stock solution and then diluted with phosphate buffer (0.1 M, pH 6). If needed, the final pH was adjusted to 7.4 by adding NaOH droplets (6 M).

Two millilitres of different haemin concentration solutions (0.1, 0.2, 0.4, 0.8, 0.16, 0.32, 0.65, 1.3 mg/ml) were prepared from the stock solution using phosphate buffer (0.1 M, pH 7.4) in Eppendorf tubes. In each tube, a wet cryogel was added and gently shaken on a rocking table at room temperature for 24 h. After binding, the supernatants were measured by a NanoPhotometer Pearl ultraviolet-visible (UV-Vis) spectrophotometer (Munich, Germany) at 390 nm wavelength to determine the remaining haemin concentration in the solution (ε_{390} = 34.4×10^4 M^{-1} cm^{-1}). To calculate the nonspecific binding, each gel was washed with 2 ml carbonate buffer (0.1 M, pH 9) overnight on a rocking table at room temperature. The amount of the adsorbed haemin on the gel was calculated by the depletion method using Eq. 4:

$$Q = \frac{\left(C_i - C_{eq} - C_w\right)V}{v} \tag{4}$$

where Q is the capacity of the cryogel (mg of haemin/mL of gel), C_i, C_{eq}, and C_w are the haemin initial, equilibrium concentrations in solution and concentration in wash solution (mg/ml), respectively. V is the volume of the haemin solution (ml) in contact with the cryogel, and v is the volume of the cryogel (ml).

Time-resolved adsorption was performed on different cryogels with a haemin solution (0.2 mg/ml). The cryogel was left in contact with the solution for 1, 2, 5, 10, 20, 30, 40, 50, 60, 120, 180, 240, 300, 360, 960, 1,020, 1,080, 1,140, 1,200, 1,260, 1,320, 1,380 and 1,440 min (24 h) before the haemin concentration in solution was measured using the above molar adsorption coefficient. One cryogel (0.25 ml) was added to the haemin solution in a separate tube for each data point.

Binding site

The following procedure was used to determine the number of binding sites of the crosslinked proteins in single- and double-layer cryogels. The gels were frozen at −20°C overnight, and then thin film layers (<< 1 mm thickness, approximately 5–9 mg dried weight) were manually cut with a sharp surgical blade. The film was held between two plastic parts with a hole (Figure 1) and inserted diagonally (45°) into a 10-mm quartz cuvette. The plastic holder was custom-designed, and 3D-printed in-house on a Prusa MK3 fused filament printer (Prague, Czech Republic) with polylactic acid. The fluorescence was excited at 295 nm, and the emission spectrum was recorded between 300 and 500 nm. Cryogel fluorescence emissions with and without haemin were measured using Cary Eclipse Spectrofluorometer, Agilent Technologies, Frankfurt, Germany. For the inner filter effect corrections, the cryogel films were placed inside the same holders and read by a UV-Vis spectrophotometer. However, due to the thickness of the film, no data could be extracted.

Each thin film of cryogels was placed in separate haemin solutions (2 ml) with different concentrations (1.2, 2.4, 3.5, 4.7, 5.8, 6.9, 8.02 and 9.08 μM) and gently shaken on a rocking table overnight at room temperature. Then, the films were mounted in the plastic holder to measure their fluorescence emission spectrum. The estimation of the number of binding sites was done by fitting the following equation:

$$\log\frac{F_0 - F}{F} = \log K_a + n\log[Q] \tag{5}$$

where K_a is the binding constant, n denotes the number of binding sites and [Q] is the final concentration of the quencher (haemin).

Results and discussion

Albumin-based cryogel's characterisation

BSA (molecular mass of approximately 66.4 kDa) carries 583 amino acid residues, including 35 cysteines, 99 residues of aspartic and glutamic acids (in total), and 60 lysine units (Peters, 1995). The presence of β- and γ-carboxyl groups and ε-amino groups in the protein makes it possible to crosslink them in solution by applying coupling agents, such as carbodiimide, where inter and intrachain peptide bond formation is responsible for the gel matrices (Topală et al., 2014).

Different carboxyl and amino groups in BSA have different steric accessibilities for inter (intra) molecular crosslinking. Thus, to improve cryogel mechanical properties, various concentrations of BSA and the coupling agent were selected to conclude which concentration would give the most suitable gel

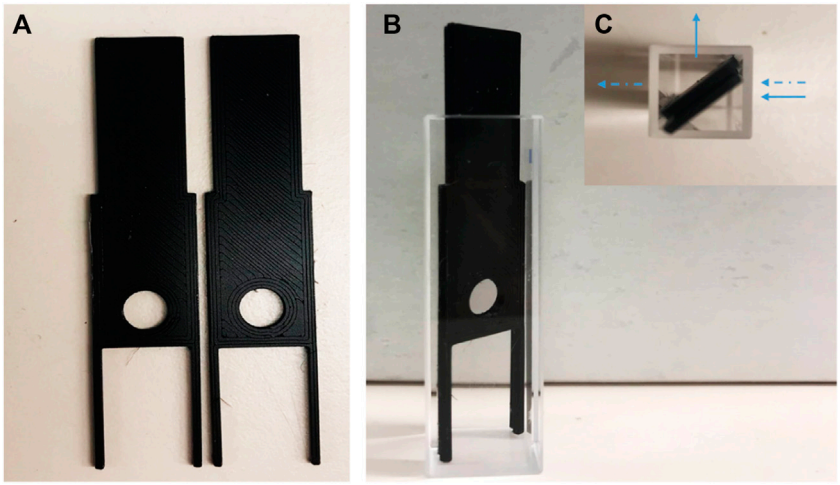

FIGURE 1
Digital image of **(A)** plastic holders; **(B)** plastic holder inside cuvette with 45° (side view); **(C)** the holders in the cuvette (top view). The arrows show the direction of fluorescent light (←) and UV-Visible light (←).

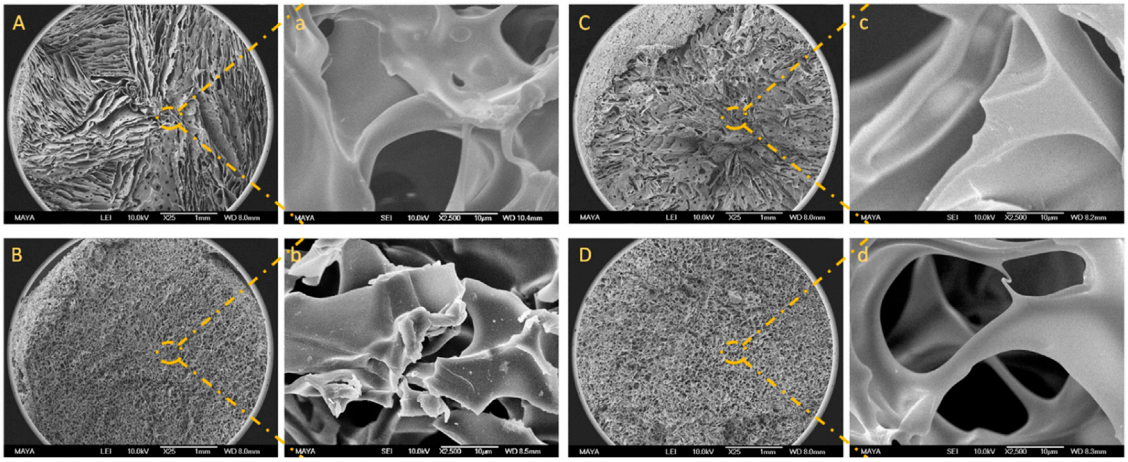

FIGURE 2
SEM images of BSA-CG with BSA (50 mg/ml) and EDC: **(A)** 37 mg/ml; **(B)** 46 mg/ml; **(C)** 56 mg/ml, and **(D)** 62 mg/ml. Images a, b, c and d are the high magnification of images A, B, C and D, respectively. The scale bars are 1 mm and 10 μm for low- and high-magnification images, respectively.

network with the right physical properties for this work (Table 1). Lozinsky and his team explained the mechanism of the crosslinking agent and the BSA elsewhere. They estimated the molar ratio between the carboxyl group, coupling agent and the amine group (COOH: EDC: NH_4) to be from 1:0.8:0.6 to 1:5.5: 0.6 range (Rodionov et al., 2016).

The macroporous structure of BSA-CG was assessed by scanning electron microscopy (Figure 2; Supplementary Figure S1). From Figure 2A, the gel cross-section seems to have divided sections, and in each section, the direction of the wall (pores) was more aligned, while in Figures 2B,D, the formation of the pores seemed to be more random. The differences in alignment and configuration of the cryogel's structure depend on the freezing conditions, such as the rate of freezing, presence of impurity (in this case, protein and the coupling agent concentrations), temperature, and formation of ice crystals' nuclei (Kirsebom et al., 2010). Based on the SEM images (Supplementary Figure S1) and the ImageJ (1.53 C version), the average pore size for the three cryogels (A, B and C) with different protein concentrations is 30, 44 and 37 μm, respectively. The difference originated from

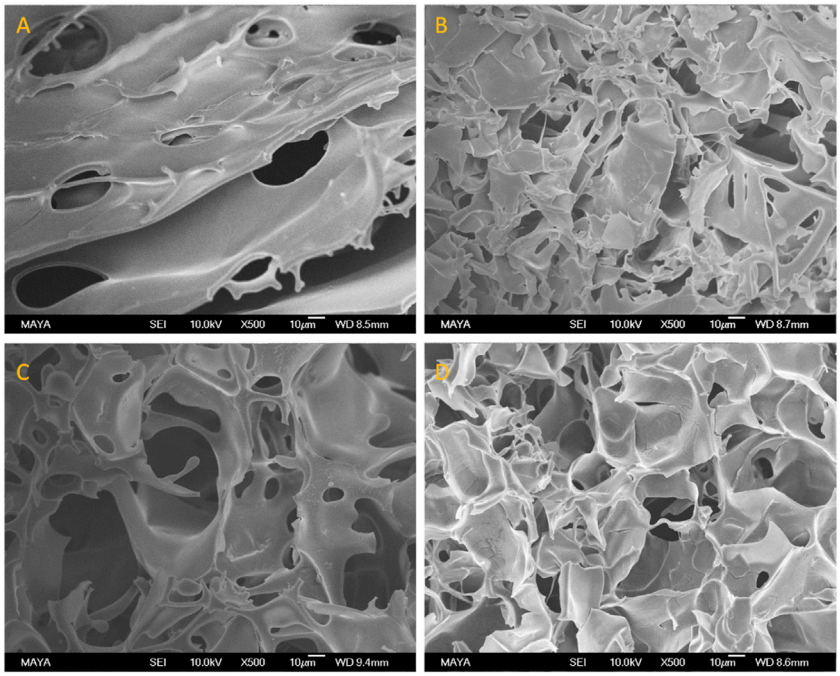

FIGURE 3
SEM images of **(A)** HEMA-CG, **(B)** HEMA-BSA-CG, **(C)** Am-CG, and **(D)** Am-BSA-CG. The scale bar is 10 μm.

the freezing procedure and the formation of ice crystals in the material (Plieva et al., 2004). The pore size distribution inside a dry cryogel was studied and reported using mercury porosimetry analysis (Hajizadeh et al., 2010).

Based on the polymerisation yield, swelling ratio and mechanical strength of the BSA-CGs, the most suitable gel formation condition was selected for further study. BSA (30 mg/ml) stands in a group with a high polymerisation yield and average swelling ratio. However, the gel was very soft and fragile as it collapsed under compression. Compared to the other cryogels, 40 mg/ml BSA had the highest swelling ratio but the lowest mechanical strength. The BSA-CG formed with 50 mg/ml BSA and 56 mg/ml EDC displayed the highest mechanical strength among the other cryogels. The result of the higher mechanical strength was explained by increasing the number of covalent bonds between the crosslinker and the protein during polymerisation. The polymerisation yield and the swelling ratio were in the average range compared to the other cryogels in Table 1. However, the repeatability of the experiment was low and resulted in a significant difference between the mechanical strength of the cryogels (Table 1; Supplementary Figure S2). Thus, 50 mg/ml and 46 mg/ml were selected as reference concentrations for BSA and EDC, respectively, for the rest of this work. The same biomolecule concentrations and the coupling agent was used for OVA-CG, Am-BSA-CG and HEMA-BSA-CG.

One of the disadvantages of biomacromolecule-based cryogels is that the resulting gels are often soft and require less energy to break than synthetic equivalents (Panahi and Baghban-Salehi, 2019). Different strategies may be applied to improve this physical shortcoming, such as forming composite cryogels by adding additional monomers during polymerisation to strengthen the final material (Gonzalez and Alvarez, 2014; de Lima et al., 2018) or cryogelation inside an external carrier. For the latter, plastic holders (Le Noir et al., 2009; Önnby et al., 2010) or a premade cryogel (Sedlačík et al., 2020). In this study, the robustness of the albumin-based cryogel was improved by forming a cryogel inside a primary cryogel. Acrylamide and HEMA monomers were selected as the building blocks for the first cryogel layer. Polyacrylamide and pHEMA cryogels are well studied and have shown great potential in different applications (Carvalho et al., 2014; Ali et al., 2018). However, their application in the biomedical field is limited due to the risk of toxicity of free Am monomers (Zamani et al., 2017; Cantrell and McDougal, 2021). Thus, a poly (HEMA) cryogel was designed as an alternative. HEMA is compliant with medical applications (Zare et al., 2021).

Figure 3 shows the Am-CG and HEMA-CG structures before and after introducing the albumin-based second crosslinked network. The images display the macroporous structure of the cryogel after the second cryogelation process. The average pore size measured by ImageJ based on the SEM image (Figures 3B,D)

TABLE 2 The mechanical properties of the cryogels.

	BSA-CG	OVA-CG	Am-BSA-CG	HEMA-BSA-CG	Autoclaved BSA-CG
E (kPa)	1.93 ± 0.08	1.02 ± 0.17	5.01 ± 0.82	6.82 ± 3.03	11.51 ± 2.64
Hardness (N)	0.47 ± 0.15	0.27 ± 0.19	0.42 ± 0.14	0.45 ± 0.38	0.12 ± 0.02
Compressibility (N.mm)	0.54 ± 0.13	0.41 ± 0.12	1.23 ± 0.45	1.27 ± 0.76	0.35 ± 0.08

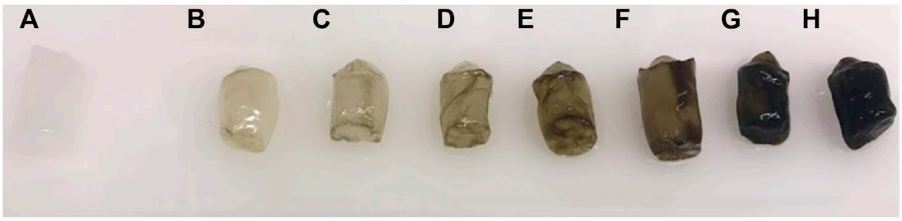

FIGURE 4
Digital image of BSA-CG before and after interaction with different concentrations of haemin solutions: **(A)** 0; **(B)** 0.004; **(C)** 0.008; **(D)** 0.016; **(E)** 0.032; **(F)** 0.065; **(G)** 0.13 and **(H)** 0.26 mg/ml haemin in 0.1 M phosphate buffer pH 7.4.

was 42 and 37 μm for Am-BSA-CG and HEMA-BSA-CG, respectively.

The ultimate goal of this study is to design materials for biomedical applications, so being able to sterilise them and retain their initial properties is crucial. BSA-CG was autoclaved, and its physical and chemical properties were compared with those before autoclaving. Other methods for sterilisation, e.g., ionising radiation and liquid chemical sterilisation (e.g. ethylene oxide), can be applied and may not dramatically affect soft materials (Berovic, 2005). However, this work did not prioritise evaluating different sterilisation methods on the designed materials. After autoclaving, the size of the cryogel was slightly shrunk (~1 mm in diameter), and its colour changed to beige-yellow due to protein oxidation (Supplementary Figure S3). The SEM images of the albumin-based cryogel before and after autoclaving illustrate that the macroporous network was undamaged during the post-treatment. The results indicated that the covalent bonds between the biomolecules and the crosslinker are stable at the macro scale (Supplementary Figure S4). However, at higher magnification, the initially smooth surface of the albumin-based cryogels showed wrinkles after autoclaving compared to the control cryogel, Am-CG (Supplementary Figure S4B,D). Under such extreme operating conditions, dehydration was expected for the two types of cryogel (protein and synthetic based). However, denaturation of the biomolecules under high temperature and pressure seemed to have more impact on the surface morphology.

The mechanical properties of the cryogels are summarised in Table 2; Supplementary Figure S5. The linear range between 5 and 30% of strain was considered the elastic region for calculating the elasticity by using Young's modulus (E) and comparing the data for all the different cryogels. The double-layer cryogels had a higher modulus than the single albumin-based cryogels, explained by the presence of the second polymeric layer, providing a denser gel with more crosslinks. The gain in mechanical strength allowed better handling of the cryogel.

Batch binding adsorption

Figure 4 displays a digital image of BSA-CG before and after contact with different concentrations of haemin solution. The dark green colour of the cryogel in the image indicates a high accumulation of the porphyrin molecule as a result of both specific and nonspecific interactions (Makarska-Bialokoz, 2018). The green colour stemmed from the oxe-bridge Fe-O-Fe dimer of haemin in solution (Brown et al., 1969).

Figure 5 shows the binding adsorption of haemin on different types of cryogels. The number of tryptophan residues plays an essential role in the interaction and adsorption of the porphyrin molecule (Yadav et al., 2012; Makarska-Bialokoz, 2018). OVA and BSA have 3 and 2 tryptophan residues, respectively (Ishimaru et al., 2010; Raut et al., 2014). However, only one residue is available on the surface of these proteins, which can interact with the target (Makarska-Bialokoz, 2018) for the free proteins in the solution. Crosslinked proteins in a network may have different conformations (secondary and tertiary structures)

10.3389/fbioe.2022.1072153

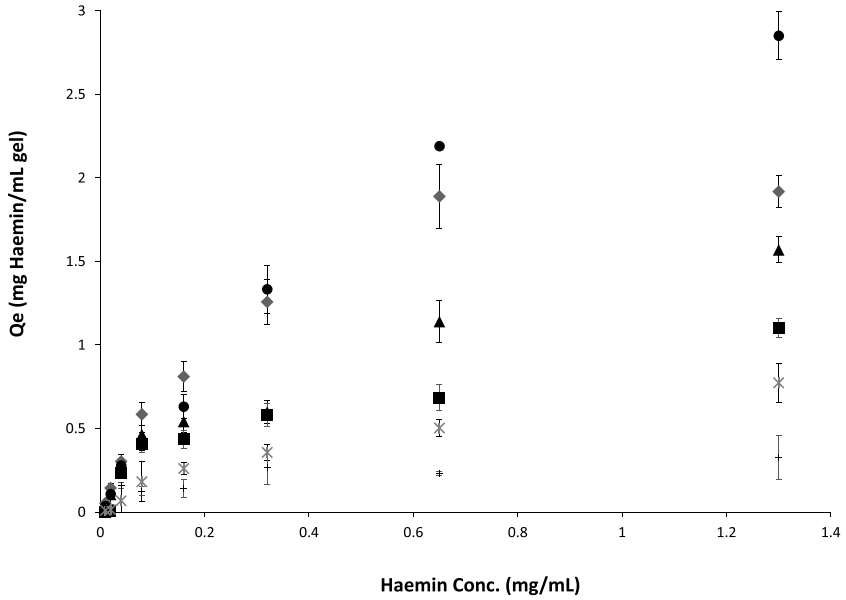

FIGURE 5
Haemin adsorption isotherms on different cryogels at room temperature for 24 h. ●: OVA-CG; ◆: BSA-CG; ▲: Am-BSA-CG; ■: HEMA-BSA-CG; *: autoclaved BSA-CG and +: Am-CG.

TABLE 3 The Freundlich adsorption isotherm for haemin adsorption on different types of protein cryogels.

	BSA-CG	OVA-CG	Am-BSA-CG	HEMA-BSA-CG	Am-CG	HEMA-CG
K_F ($mg^{1-1/n}mL^{1/n}/mL$)	2.27 ± 0.73	4.05 ± 0.51	1.39 ± 0.3	1.06 ± 0.43	4.85 ± 0.31	4.74 ± 0.11
1/n	0.24 ± 0.1	0.63 ± 0.05	0.31 ± 0.01	0.27 ± 0.07	0.29 ± 0.09	0.31 ± 0.07
R^2	0.98	0.89	0.94	0.94	0.85	0.87

and surface accessibility. For example, the crosslinking-induced protein opening could expose the inner tryptophan residues. In addition, the nonspecific binding of the porphyrin molecule with the polymeric network is another factor to consider in batch adsorption. For the single-layer cryogel, the nonspecific adsorption can be related to the accumulation of the target molecules inside the micro and macro pores or their physical interaction with each other, which can be calculated from the washing step using carbonate buffer. However, in the double-layer cryogel, the premade cryogel can interact physically with the porphyrin molecules in addition to the other nonspecific interactions. Therefore, a control experiment was conducted to study the batch-binding adsorption of haemin on Am and HEMA-CGs. The data revealed that both synthetic cryogels have low-affinity interaction with the target molecules (Figure 5, data related to HEMA-CG is not shown). The results showed that OVA-CG has a slightly higher binding capacity towards haemin than the other cryogels (Figure 5).

We fitted and compared the adsorption isotherm using Langmuir, Freundlich and Temkin models. A F-test ($p < 0.05$) comparison of the models suggested that the Freundlich model was best suited for all cryogels except for BSA-CG autoclaved (Supplementary Figure S6; Table 3).

In the Freundlich model, surface adsorption is assumed heterogeneous. As the concentration of the adsorbate increases, its amount rises on the adsorbent surface. The Freundlich equation and its linearisation are as follows:

$$q_e = K_F C_e^{1/n} \quad (6)$$

$$\ln q_e = \ln K_F + 1/n \ln C_e \quad (6a)$$

where KF is the Freundlich constant related to adsorption capacity, and n is the constant related to adsorption intensity. K_F is defined as the adsorption or distribution coefficient and represents the amount of adsorbate onto the adsorbent surface for a unit equilibrium concentration. The slope of $1/n$ ranging between 0 and 1 is a measure of adsorption intensity or surface

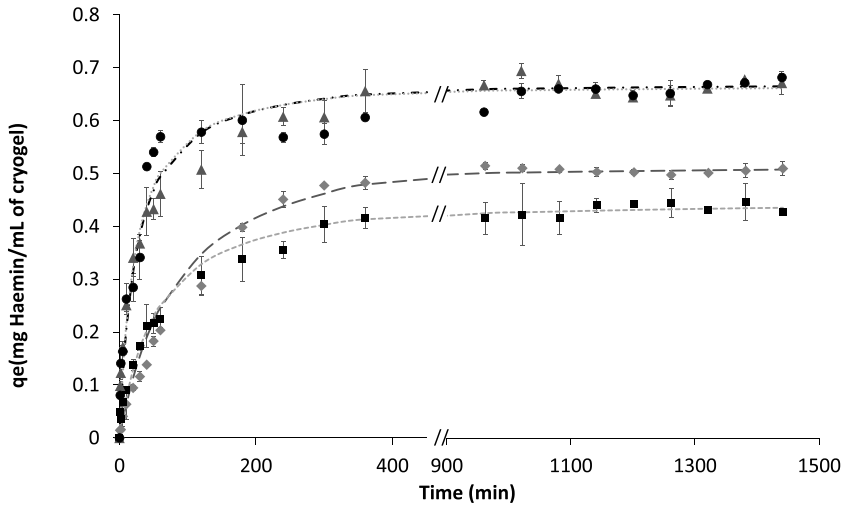

FIGURE 6
Fitting experimental data of haemin adsorption with initial concentrations of 0.2 mg/ml in 0.1 M phosphate buffer pH 7.4 for different cryogels. ▲ BSA-CG; ● OVA-CG; ◆ Am-BSA-CG and ■ HEMA-BSA-CG. Pseudo-second-order equation fitting with data: -- HEMA-BSA-CG; -.- BSA-CG; . . .. OVA-CG; _ _ _ Am-BSA-CG; No data available between 400 and 900 min.

TABLE 4 Pseudo-second-order parameters for the adsorption of haemin on albumin-based cryogels.

	BSA-CG	OVA-CG	Am-BSA-CG	HEMA-BSA-CG	Autoclaved BSA-CG
qe (mg/mL of gel)	0.69 ± 0.07	0.68 ± 0.03	0.59 ± 0.06	0.47 ± 0.03	0.43 ± 0.08
K2 (ml/mg h)	0.059 ± 0.003	0.064 ± 0.001	0.020 ± 0.007	0.039 ± 0.004	0.056 ± 0.01
R2	0.98	0.99	0.99	0.99	0.98

heterogeneity. If the value approaches zero, the surface adsorption is more heterogeneous (Sathasivam and Mas Haris, 2010). The complex cryogelation process (e.g., dissolving the protein in water and not buffer, freezing at low temperature, crosslinking biomolecules) was expected to impact the protein structure and cause heterogeneous binding on the adsorption surface. Among the studied cryogels in this work, OVA-CG displays less heterogeneous surface adsorption when in contact with haemin based on the 1/n value. However, the goodness of fit was the lowest (Table 3). Autoclaved BSA-CG batch adsorption experimental data with haemin did not fit any of the well-known models, which may be explained by the oxidation of the protein molecules and densification of the cryogel during the treatment.

Kinetics isotherm

The time-resolved binding studies were further performed to understand the interaction of haemin with the different cryogels. Different models were considered to fit the adsorption kinetic isotherm, e.g., the pseudo-first-order model, pseudo-second-order model, Elovich's equations and intraparticle diffusion model (Weber and Morris, 1962) (Supplementary Figure S7). Based on a visual inspection of experimental data and confirmed by a model comparison using an F-test ($p < 0.05$), we concluded that the pseudo-second-order model is the better fit for different cryogels (Figure 6; Table 4).

Figure 6; Supplementary Figure S8 show the kinetics studies for all the cryogels where the graphs showed two stages before reaching equilibrium; 1) a rapid increase based on the amount of haemin adsorbed as a function of time up to 60 min, and 2) the curve continues to increase with a much slower pace until reaching equilibrium for the initial haemin concentration (0.2 mg/ml in 0.1 M phosphate buffer pH 7.4). The two-step saturation curve may be explained by the free tryptophan residues available on the surface of the cryogel and those located inside the walls. In the latter case, diffusion of haemin through the walls is the limiting factor, while on the surface of the cryogel, the mass transfer is high between the available amino acid and free haemin (Supplementary Figure S8).

TABLE 5 Number of binding sites on albumin-based cryogels and biomolecule solutions.

	BSA-CG	OVA-CG	Am-BSA-CG	HEMA-BSA-CG	BSA solution	OVA solution
n	1.1 ± 0.3	1.65 ± 0.15	1.37 ± 0.5	1.45 ± 0.3	0.95 Makarska-Bialokoz, (2018)	~1 Wang et al. (2013)

The time-resolved trace from the autoclaved BSA-CG (Supplementary Figure S9) was best fitted using the pseudo-second-order model. However, we observed a large discrepancy in the early stage of the binding. Visually, the non-autoclaved cryogel has a higher affinity (stronger colour) toward the porphyrin molecule (Supplementary Figure S10 digital image comparison of the autoclaved and non-autoclaved BSA-CGs in contact with haemin). The naked eye can detect the green colour changes in the non-autoclaved BSA-CG immediately after 1 min. In contrast, for the autoclaved cryogel, changes can be seen after a much longer time (Supplementary Figure S10).

As haemin can only be dissolved in a highly alkaline solution and some organic solvents, such as DMSO, removing the porphyrin molecule from cryogels is difficult. The strong binding of haemin to protein is used in affinity chromatography to separate and purify proteins. In those studies, to regenerate the column, one uses a high concentration of NaOH (1 M) and sodium dodecyl sulphate (SDS) solution (5%) (Tsutsui and Mueller, 1982; Jiang et al., 2017). This approach is incompatible with albumin-based cryogels and will destroy the structure of the gels, and the polymeric network will disintegrate during the process (Supplementary Figure S11). Additionally, in medical applications, one-time-use materials are preferred to minimise the risk of cross-contamination. Thus, regeneration and recycling of the designed material were not pursued further.

Binding sites

There are reports in the literature investigating the mechanism of binding dye molecules to proteins using fluorescence quenching measurements (Barbero et al., 2009; Yadav et al., 2012). The interaction of haemin with BSA and the number of their binding sites was studied in detail elsewhere in an aqueous solution (Makarska-Bialokoz, 2018). However, none of these studies dealt with semi-solid materials. In this work, the protein is not a free molecule in a solution and, due to the crosslinking procedure, may even have a different structure inside the cryogel. FTIR spectra of the protein-based cryogels and pure BSA powder are plotted in Supplementary Figure S12. The results indicate that the secondary structure of the protein (amide I and II peaks at 1,650 and 1,540 cm^{-1}, respectively) has changed after crosslinking compared to the free protein. The alteration was more noticeable in the double-layer cryostructured. Thus, different levels of accessibility of the haemin molecule to tryptophan can be expected. We studied the binding by fluorescence quenching of the tryptophan signal by haemin. First, the Stern–Volmer equation validity was confirmed for semi-solid gels. Before measuring the fluorescence emission, each film was incubated in its corresponding solution for 24 h on a rocking table to account for mass transfer limitation in the quenching process. As expected, the linearity was for F0/F vs. haemin concentration (Supplementary Figure S13). The linearity of the double-layer cryogels was lower than the single-protein cryogels, which was tentatively attributed to an inner filter effect. In addition, Am and HEMA polymers are hydrophilic (Domingues et al., 2013; Kordjazi et al., 2020). Thus, before cryogelation polymerisation, BSA can physically bind to the surface and within the premade cryogels, which could affect the protein positioning in the unfrozen region during cryogelation and, thus, accessibility of EDC to carboxylic and primary amine groups. In addition, even though Am and HEMA cryogels do not have any fluorescent properties (Supplementary Figure S14), their presence as an extra layer may not be neglected in collecting data from the fluorimeter.

The number of binding sites was determined by fitting the Stern–Volmer Eq. 5. Table 5 summarises the results.

Free BSA in solution showed one single primary binding site during interaction with haemin in a solution (Makarska-Bialokoz, 2018). Wang and his team have shown that the binding site for OVA protein is one by studying the interaction of OVA with three purine alkaloids (caffeine, theophylline and diprophylline) (Wang et al., 2013). The deviation in the number of binding sites in this work with the reported number stemmed from the different operational conditions and the fact that protein molecules are crosslinked together and present a new binding interface inside the cryogel. Thus, comparing semi-solid cryogels with free protein solutions may be inaccurate.

Conclusion

We designed and optimised albumin-based cryogels by crosslinking polymerisation at subzero temperatures. To increase the mechanical stability and improve the handling of the gel, BSA-CG was prepared inside a premade cryogel. Single-layer cryogels (OVA-CG and BSA-CG) demonstrated a higher affinity towards haemin (0.68 mg/ml of cryogel) than double-layer cryogels. In contrast, the double-layer cryogels have revealed superior mechanical stability with less adsorption capacity (0.47 and 0.59 mg/ml of cryogel for HEMA-BSA-CG and Am-BSA-CG, respectively). The number of binding sites of

albumin-based cryogels with haemin was calculated to be between 1.1 and 1.65 for different cryogels.

The cryogelation technique is relatively straightforward and economical compared to other methods, such as membrane, yet practical for the mentioned goal. The possibility of autoclaving the network without destroying the macroporous configuration is another highlight of this material. However, increasing the mechanical strength and scaling up are common criticisms of cryogelation products. In this study, we tried to address the mechanical stabilities using a double-layer approach. Taking advantage of the interconnected channels of the cryogel to separate haemin from a particulate-containing fluid, e.g., blood and non-clarified crude, or using a different kind of crosslinking agent, are parts of ongoing research and will be addressed in future studies.

Data availability statement

The original contributions presented in the study are included in the article/Supplementary Material, further inquiries can be directed to the corresponding author.

Author contributions

SH designed and performed the experiments and drafted the manuscript. CD conducted the FTIR analysis and contributed to a fruitful data discussion and analysis. All authors revised the manuscript, and they approved the final version.

Funding

This research was funded by Swedish Research Council for Environment Agricultural Sciences and Spatial Planning, grant number 2020-0185, and The Swedish Research Council, grant number 2019-03996.

Conflict of interest

The authors declare that the research was conducted in the absence of any commercial or financial relationships that could be construed as a potential conflict of interest.

Publisher's note

All claims expressed in this article are solely those of the authors and do not necessarily represent those of their affiliated organizations, or those of the publisher, the editors and the reviewers. Any product that may be evaluated in this article, or claim that may be made by its manufacturer, is not guaranteed or endorsed by the publisher.

Supplementary material

The Supplementary Material for this article can be found online at: https://www.frontiersin.org/articles/10.3389/fbioe.2022.1072153/full#supplementary-material

References

Agarwal, G., Kumar, N., and Srivastava, A. (2021). Highly elastic, electroconductive, immunomodulatory graphene crosslinked collagen cryogel for spinal cord regeneration. *Mater. Sci. Eng. C* 118, 111518. doi:10.1016/j.msec.2020.111518

Ahmed, M. H., Ghatge, M. S., and Safo, M. K. (2020). Hemoglobin: Structure, function and allostery. *Subcell. Biochem.* 94, 345–382. doi:10.1007/978-3-030-41769-7_14

Aich, A., Freundlich, M., and Vekilov, P. G. (2015). The free heme concentration in healthy human erythrocytes. *Blood Cells Mol. Dis.* 55, 402–409. doi:10.1016/j.bcmd.2015.09.003

Ali, S., Shehzad, F. K., Maitlo, I., Valiev, S., Muhyodin, G., and Nie, J. (2018). Binary phase solid-state photopolymerization behavior of acrylate cryogels under different light sources. *J. Appl. Polym. Sci.* 135, 46686. doi:10.1002/app.46686

Aragão Börner, R., Zaushitsyna, O., Berillo, D., Scaccia, N., Mattiasson, B., and Kirsebom, H. (2014). Immobilization of Clostridium acetobutylicum DSM 792 as macroporous aggregates through cryogelation for butanol production. *Process Biochem.* 49, 10–18. doi:10.1016/j.procbio.2013.09.027

Barbero, N., Barni, E., Barolo, C., Quagliotto, P., Viscardi, G., Napione, L., et al. (2009). A study of the interaction between fluorescein sodium salt and bovine serum albumin by steady-state fluorescence. *Dyes Pigments* 80, 307–313. doi:10.1016/j.dyepig.2008.08.006

Berillo, D., Al-Jwaid, A., and Caplin, J. (2021). Polymeric materials used for immobilisation of bacteria for the bioremediation of contaminants in water. *Polymers* 13, 1073. doi:10.3390/polym13071073

Berovic, M. (2005). "Sterilisation in biotechnology," in *Biotechnology annual review* (Amsterdam, Netherlands: Elsevier), 257–279.

Bialas, C., Moser, C., and Sims, C. A. (2019). Artificial oxygen carriers and red blood cell substitutes: A historic overview and recent developments toward military and clinical relevance. *J. Trauma Acute Care Surg.* 87, S48–S58. doi:10.1097/ta.0000000000002250

Brown, S. B., Jones, P., and Lantzke, I. R. (1969). Infrared evidence for an oxo-bridged (Fe-O-Fe) haemin dimer. *Nature* 223, 960–961. doi:10.1038/223960a0

Cantrell, M. S., and Mcdougal, O. M. (2021). Biomedical rationale for acrylamide regulation and methods of detection. *Compr. Rev. Food Sci. Food Saf.* 20, 2176–2205. doi:10.1111/1541-4337.12696

Carvalho, B. M. A., Da Silva, S. L., Da Silva, L. H. M., Minim, V. P. R., Da Silva, M. C. H., Carvalho, L. M., et al. (2014). Cryogel poly(acrylamide): Synthesis, structure and applications. *Sep. Purif. Rev.* 43, 241–262. doi:10.1080/15422119.2013.795902

Coronel, F., Herrero, J. A., Montenegro, J., Fernandez, C., Gandara, A., Conesa, J., et al. (2003). Erythropoietin requirements: A comparative multicenter study between peritoneal dialysis and hemodialysis. *J. Nephrol.* 16, 697–702.

De Lima, G. G., Traon, F., Moal, E., Canillas, M., Rodriguez, M. A., Mccarthy, H. O., et al. (2018). Composite cryogels for dual drug delivery and enhanced mechanical properties. *Polym. Compos.* 39, E210–E220. doi:10.1002/pc.24450

Domingues, J. a. L., Bonelli, N., Giorgi, R., Fratini, E., Gorel, F., and Baglioni, P. (2013). Innovative hydrogels based on semi-interpenetrating p(HEMA)/PVP networks for the cleaning of water-sensitive cultural heritage artifacts. *Langmuir* 29, 2746–2755. doi:10.1021/la3048664

Fontanellas, A., Coronel, F., Santos, J. L., Herrero, J. A., Moran, M. J., Guerra, P., et al. (1994). Heme biosynthesis in uremic patients on CAPD or hemodialysis. *Kidney Int.* 45, 220–223. doi:10.1038/ki.1994.26

Gonzalez, J. S., and Alvarez, V. A. (2014). Mechanical properties of polyvinylalcohol/hydroxyapatite cryogel as potential artificial cartilage. *J. Mech. Behav. Biomed. Mater.* 34, 47–56. doi:10.1016/j.jmbbm.2014.01.019

Graça-Souza, A. V., Maya-Monteiro, C., Paiva-Silva, G. O., Braz, G. R. C., Paes, M. C., Sorgine, M. H. F., et al. (2006). Adaptations against heme toxicity in blood-feeding arthropods. *Insect Biochem. Mol. Biol.* 36, 322–335. doi:10.1016/j.ibmb.2006.01.009

Hajizadeh, S. (2012). *Composite cryogels : Stationary phase for separation of complex media*. Lund: Department of Biotechnology, Lund University.

Hajizadeh, S., Kettisen, K., Bülow, L., and Ye, L. (2021). Rapid separation of human hemoglobin on a large scale from non-clarified bacterial cell homogenates using molecularly imprinted composite cryogels. *Front. Bioeng. Biotechnol.* 9, 671229. doi:10.3389/fbioe.2021.671229

Hajizadeh, S., Kirsebom, H., Leistner, A., and Mattiasson, B. (2012). Composite cryogel with immobilized concanavalin A for affinity chromatography of glycoproteins. *J. Sep. Sci.* 35, 2978–2985. doi:10.1002/jssc.201200433

Hajizadeh, S., Kirsebom, H., and Mattiasson, B. (2010). Characterization of macroporous carbon-cryostructured particle gel, an adsorbent for small organic molecules. *Soft Matter* 6, 5562–5569. doi:10.1039/c0sm00311e

Hargrove, M. S., Whitaker, T., Olson, J. S., Vali, R. J., and Mathews, A. J. (1997). Quaternary structure regulates hemin dissociation from human hemoglobin. *J. Biol. Chem.* 272, 17385–17389. doi:10.1016/s0021-9258(19)65896-5

Hebbel, R. P., Morgan, W. T., Eaton, J. W., and Hedlund, B. E. (1988). Accelerated autoxidation and heme loss due to instability of sickle hemoglobin. *Proc. Natl. Acad. Sci. U. S. A.* 85, 237–241. doi:10.1073/pnas.85.1.237

Henderson, T. M. A., Ladewig, K., Haylock, D. N., Mclean, K. M., and O'connor, A. J. (2013). Cryogels for biomedical applications. *J. Mat. Chem. B* 1, 2682–2695. doi:10.1039/c3tb20280a

Ishimaru, T., Ito, K., Tanaka, M., and Matsudomi, N. (2010). Thermostabilization of ovalbumin by alkaline treatment: Examination of the possible roles of D-serine residues. *Protein Sci.* 19, 1205–1212. doi:10.1002/pro.398

Jain, E., and Kumar, A. (2013). Disposable polymeric cryogel bioreactor matrix for therapeutic protein production. *Nat. Protoc.* 8, 821–835. doi:10.1038/nprot.2013.027

Jiang, X., Zhang, D., Li, X., Wang, X., Bai, L., Liu, H., et al. (2017). Fabrication of a novel hemin-based monolithic column and its application in separation of protein from complex bio-matrix. *J. Pharm. Biomed. Analysis* 138, 14–21. doi:10.1016/j.jpba.2017.01.035

Jones, D. S., Woolfson, A. D., and Brown, A. F. (1997). Textural analysis and flow rheometry of novel, bioadhesive antimicrobial oral gels. *Pharm. Res.* 14, 450–457. doi:10.1023/a:1012091231023

Jones, L. O., Williams, L., Boam, T., Kalmet, M., Oguike, C., and Hatton, F. L. (2021). Cryogels: Recent applications in 3D-bioprinting, injectable cryogels, drug delivery, and wound healing. *Beilstein J. Org. Chem.* 17, 2553–2569. doi:10.3762/bjoc.17.171

Kirsebom, H., Elowsson, L., Berillo, D., Cozzi, S., Inci, I., Piskin, E., et al. (2013). Enzyme-catalyzed crosslinking in a partly frozen state: A new way to produce supermacroporous protein structures. *Macromol. Biosci.* 13, 67–76. doi:10.1002/mabi.201200343

Kirsebom, H., Topgaard, D., Galaev, I. Y., and Mattiasson, B. (2010). Modulating the porosity of cryogels by influencing the nonfrozen liquid phase through the addition of inert solutes. *Langmuir* 26, 16129–16133. doi:10.1021/la102917c

Kordjazi, S., Kamyab, K., and Hemmatinejad, N. (2020). Super-hydrophilic/oleophobic chitosan/acrylamide hydrogel: An efficient water/oil separation filter. *Adv. Compos. Hybrid. Mat.* 3, 167–176. doi:10.1007/s42114-020-00150-8

Le Noir, M., Plieva, F. M., and Mattiasson, B. (2009). Removal of endocrine-disrupting compounds from water using macroporous molecularly imprinted cryogels in a moving-bed reactor. *J. Sep. Sci.* 32, 1471–1479. doi:10.1002/jssc.200800670

Makarska-Bialokoz, M. (2018). Interactions of hemin with bovine serum albumin and human hemoglobin: A fluorescence quenching study. *Spectrochimica Acta Part A Mol. Biomol. Spectrosc.* 193, 23–32. doi:10.1016/j.saa.2017.11.063

Morgan, W. T., Heng Liem, H., Sutor, R. P., and Muller-Eberhard, U. (1976). Transfer of heme from heme-albumin to hemopexin. *Biochimica Biophysica Acta (BBA) - General Subj.* 444, 435–445. doi:10.1016/0304-4165(76)90387-1

Önnby, L., Giorgi, C., Plieva, F. M., and Mattiasson, B. (2010). Removal of heavy metals from water effluents using supermacroporous metal chelating cryogels. *Biotechnol. Prog.* 26, 1295–1302. doi:10.1002/btpr.422

Panahi, R., and Baghban-Salehi, M. (2019). "Protein-based hydrogels," in *Cellulose-based superabsorbent hydrogels*. Editor M. I. H. Mondal (Cham: Springer International Publishing), 1561–1600.

Peters, T. (1995). *All about albumin: Biochemistry, genetics and medical applications*. Amsterdam, Netherlands: Elsevier Science.

Plieva, F. M., Andersson, J., Galaev, I. Y., and Mattiasson, B. (2004). Characterization of polyacrylamide based monolithic columns. *J. Sep. Sci.* 27, 828–836. doi:10.1002/jssc.200401836

Raut, S., Chib, R., Butler, S., Borejdo, J., Gryczynski, Z., and Gryczynski, I. (2014). Evidence of energy transfer from tryptophan to BSA/HSA protected gold nanoclusters. *Methods Appl. Fluoresc.* 2, 035004. doi:10.1088/2050-6120/2/3/035004

Rodionov, I. A., Grinberg, N. V., Burova, T. V., Grinberg, V. Y., and Lozinsky, V. I. (2016). Study of cryostructuring of polymer systems. 42. Physicochemical properties and microstructure of wide-porous covalently cross-linked albumin cryogels. *Colloid J.* 78, 492–504. doi:10.1134/s1061933x1603011x

Sathasivam, K., and Mas Haris, M. R. H. (2010). Adsorption kinetics and capacity of fatty acid-modified banana trunk fibers for oil in water. *Water Air Soil Pollut.* 213, 413–423. doi:10.1007/s11270-010-0395-z

Sedlačík, T., Nonoyama, T., Guo, H., Kiyama, R., Nakajima, T., Takeda, Y., et al. (2020). Preparation of tough double- and triple-network supermacroporous hydrogels through repeated cryogelation. *Chem. Mat.* 32, 8576–8586. doi:10.1021/acs.chemmater.0c02911

Topală, T., Bodoki, A., Oprean, L., and Oprean, R. (2014). Bovine serum albumin interactions with metal complexes. *Med. Pharm. Rep.* 87, 215–219. doi:10.15386/cjmed-357

Tsutsui, K., and Mueller, G. C. (1982). Affinity chromatography of heme-binding proteins: An improved method for the synthesis of hemin-agarose. *Anal. Biochem.* 121, 244–250. doi:10.1016/0003-2697(82)90475-4

Vijayan, V., Greite, R., Schott, S., Doricic, J., Madyaningrana, K., Pradhan, P., et al. (2022). Determination of free heme in stored red blood cells with an apo-horseradish peroxidase-based assay. *Biol. Chem.* 403, 1091–1098. doi:10.1515/hsz-2022-0184

Wagener, F. a. D. T. G., Abraham, N. G., Van Kooyk, Y., De Witte, T., and Figdor, C. G. (2001). Heme-induced cell adhesion in the pathogenesis of sickle-cell disease and inflammation. *Trends Pharmacol. Sci.* 22, 52–54. doi:10.1016/s0165-6147(00)01609-6

Wang, R.-Q., Yin, Y.-J., Li, H., Wang, Y., Pu, J.-J., Wang, R., et al. (2013). Comparative study of the interactions between ovalbumin and three alkaloids by spectrofluorimetry. *Mol. Biol. Rep.* 40, 3409–3418. doi:10.1007/s11033-012-2418-x

Weber, W. J., and Morris, J. C. (1962). "Advances in water pollution research: Removal of biologically resistant pollutant from waste water by adsorption," in *Proc. Int. Conf. Water pollution symposium* (Oxford, UK: Pergamon Press).

Yadav, R., Das, S., and Sen, P. (2012). Static and dynamic aspects of supramolecular interactions of coumarin 153 and fluorescein with bovine serum albumin. *Aust. J. Chem.* 65, 1305–1313. doi:10.1071/ch12034

Zamani, E., Shokrzadeh, M., Fallah, M., and Shaki, F. (2017). A review of acrylamide toxicity and its mechanism. *Mazums-pbr.* 3, 1–7. doi:10.18869/acadpub.pbr.3.1.1

Zare, M., Bigham, A., Zare, M., Luo, H., Rezvani Ghomi, E., and Ramakrishna, S. (2021). pHEMA: An overview for biomedical applications. *Int. J. Mol. Sci.* 22, 6376. doi:10.3390/ijms22126376

frontiers | Frontiers in Bioengineering and Biotechnology

TYPE Original Research
PUBLISHED 30 November 2022
DOI 10.3389/fbioe.2022.1056419

OPEN ACCESS

EDITED BY
Yong Liu,
University of Chinese Academy of Sciences, China

REVIEWED BY
Hsiu-Wen Chien,
National Kaohsiung University of Science and Technology, Taiwan
Paolo Catalano,
CONICET Institute of Nanoscience and Nanotechnology (CNEA), Argentina

*CORRESPONDENCE
Hua Qiu,
qiuhua1990@foxmail.com
Jialong Chen,
jialong_dt@126.com
Xiangyang Li,
hlxiangyang@163.com

†These authors have contributed equally to this work

SPECIALTY SECTION
This article was submitted to Biomaterials, a section of the journal Frontiers in Bioengineering and Biotechnology

RECEIVED 28 September 2022
ACCEPTED 16 November 2022
PUBLISHED 30 November 2022

CITATION
Wei Z, Li K, Wang S, Wen L, Xu L, Wang Y, Chen Z, Li W, Qiu H, Li X and Chen J (2022), Controllable AgNPs encapsulation to construct biocompatible and antibacterial titanium implant.
Front. Bioeng. Biotechnol. 10:1056419.
doi: 10.3389/fbioe.2022.1056419

Controllable AgNPs encapsulation to construct biocompatible and antibacterial titanium implant

Zhangao Wei[1†], Kexin Li[1†], Shuang Wang[1†], Lan Wen[2], Linghan Xu[1], Yankai Wang[1], Zirui Chen[1], Wei Li[1], Hua Qiu[1*], Xiangyang Li[1*] and Jialong Chen[1*]

[1]Key Laboratory of Oral Diseases Research of Anhui Province, Stomatologic Hospital and College, Anhui Medical University, Hefei, China, [2]Department of Neurosurgery, West China Hospital, Sichuan University, Chengdu, China

Silver nanoparticles (AgNPs) are progressively becoming an in-demand material for both medical and life use due to their effective antimicrobial properties. The high surface area-to-volume ratio endows AgNPs with enhanced antibacterial capacity accompanied by inevitable cytotoxicity. Surface coating technique could precisely regulate the particle shape, aggregation, and Ag^+ release pattern of AgNPs, by which the cytotoxicity could be significantly reduced. Various coating methods have been explored to shell AgNPs, but it remains a great challenge to precisely control the aggregation state of AgNPs and their shell thickness. Herein, we proposed a simple method to prepare a tunable polydopamine (pDA) coating shell on AgNPs just by tuning the reaction pH and temperature, yet we obtained high antibacterial property and excellent biocompatibility. SEM and TEM revealed that pDA coated AgNPs can form core-shell structures with different aggregation states and shell thickness. Both *in vitro* and *in vivo* antibacterial tests show that acid condition and heat-treatment lead to appropriate AgNPs cores and pDA shell structures, which endow Ti with sustained antibacterial properties and preferable cell compatibility. One month of implantation in an infected animal model demonstrated that the obtained surface could promote osteogenesis and inhibit inflammation due to its strong antibacterial properties. Therefore, this study provides a promising approach to fabricate biocompatible antibacterial surface.

KEYWORDS

AgNPs, pDA shell, one-pot method, biocompatible, anti-bacterial

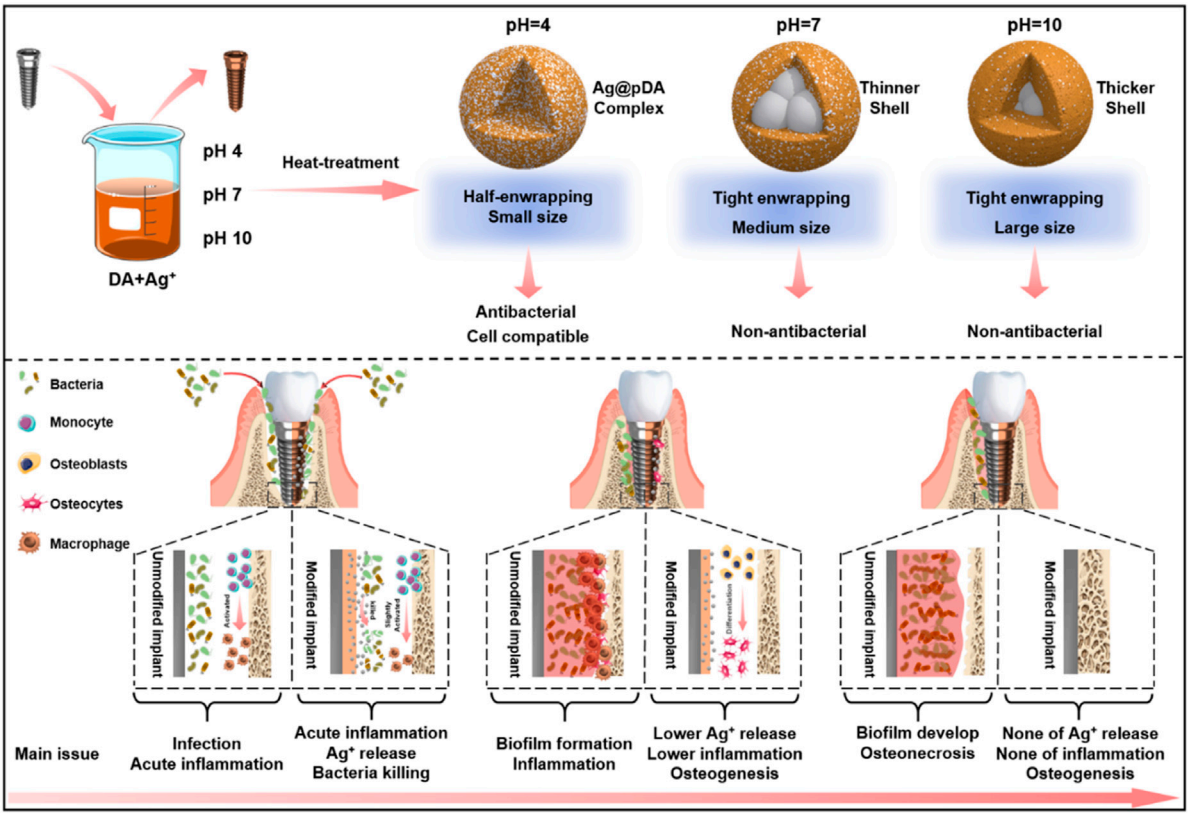

GRAPHICAL ABSTRACT

Introduction

The number of orthopedic/dental implant failures increases year by year, primarily due to bacterial infection; accordingly, antibacterial materials that prevent bacterial infections have attracted increasing attention (Wang et al., 2021a). Various strategies for fabricating antibacterial surfaces on titanium have been developed (Elliott et al., 2021; Ghilini et al., 2021). However, such surfaces are used as bone-related antibacterial materials, the long-term stability and biosafety are considered the two most important properties in this field. Surface modification to endow titanium with the aforementioned properties is the main method to constructing ideal orthopedic/dental implants (Yang et al., 2017; Kitagawa et al., 2021). To date, various antibacterial agents have been developed for the surface modification of implants, including antibiotics (Hasan et al., 2021), antimicrobial peptides (Wu et al., 2021), and antibacterial metallic elements (Zhang et al., 2016). Among these agents, silver is an enduring research hotspot for antibacterial surface preparation due to its broad-spectrum effectiveness, low resistance and high efficiency (Prencipe et al., 2021). However, considering the cytotoxicity of silver, ideal silver-modified surfaces must be able to balance antibacterial behavior and osteogenic response in accordance with the dose and loading behavior (Pryshchepa et al., 2020).

The cytotoxicity and antibacterial ability of silver nanoparticles (AgNPs) are both strongly dependent on the amount, size, shape, loading behavior and other physiological characteristics. AgNPs showed a clear effect on lactate dehydrogenase activity, reactive oxygen species (ROS) generation and DNA damage in a size-dependent manner (Akter et al., 2018; Yaqoob et al., 2020). Wang et al. reported that AgNPs with a size of 20 nm showed more cytotoxicity than 110 nm AgNPs, and further investigation indicated that smaller AgNPs cause acute neutrophilic inflammation in mouse lung (Wang et al., 2014). The influence of particle size may be ascribed to the uptake mechanism of Ag, which will ultimately affect its cytotoxicity. Coating is a conventional strategy to modulate the release of Ag^+ and produce electrostatic repulsion, thus helping stabilize the particles (Guo et al., 2016; Fahmy et al., 2019). Uncoated AgNPs kill cells in a size- and dose-dependent manner, while coating can affect the shape, aggregation, and surface electrical behavior of AgNPs, which prevents direct toxicity. Various coatings, including organic agents (polyvinylpyrrolidone (Kyrychenko et al., 2015), citrates (Gutierrez et al., 2015), proteins (Chakraborty et al., 2018)

and inorganic agents (sulfide, chloride and carbonate), have been developed to modify AgNPs. As reported, citrate- and polyvinylpyrrolidone-coated AgNPs showed increased stability and reduced cytotoxicity compared with bare AgNPs (Nguyen et al., 2013). However, both organic and inorganic coatings are characterized by the disadvantages of complex processes, high cost and poor controllability.

Mussel-inspired surface modification has attracted extensive attention since it was reported by Haeshin Lee et al. (2007). Dopamine, a mussel-inspired molecule, was reported to form a material-independent coating based on covalent bonding and π–π stacking through oxidative polymerization and noncovalent bonds (Saiz-Poseu et al., 2019). Subsequently, they proposed that catechol/o-quinone can trigger strong coordination with metals and reduce noble metal ions to form metal NPs on diverse surfaces (Hong et al., 2011). Thus, mussel-inspired chemistry started a new chapter in the field of AgNPs, and various studies on polydopamine (pDA)-mediated AgNPs have been carried out (Jo et al., 2014; Islam et al., 2018). First, researchers mainly focused on the formation of AgNPs with strong antibacterial properties, but with the deepening of research, more attention is being given to the balance of biosafety and biofunction (Alarcon et al., 2012; Yang et al., 2020). Changsheng Zhao et al. fabricated AgNP-loaded carbon nanotubes by means of dopamine-mediated chemistry, and both gram-negative and gram-positive bacteria were effectively killed. However, significant negative effects were observed in *in vitro* cell culture due to the cytotoxicity of Ag. To improve compatibility, they used heparin and chitosan to reduce the amount of Ag and adjust its loading behavior which ultimately resulted in an antibacterial material with good cell compatibility (Nie et al., 2016). While these previous researchers favored the use of additives to control the shape and release mechanism of AgNPs, they overlooked the fact that dopamine is a first-class coating material that can be successfully wrapped around the target under proper reaction conditions. Jiuju et al. used a similar one-step method to prepare AgNPs@PDA composites in the field of photocatalysis. The particles had core-shell structure, which gave us great encouragement, that is, the simple preparation method could make dopamine wrapped silver particles (Feng et al., 2012). Using polydopamine as an adhesive, reducing agent, diffusion barrier and inducer, Yan Cheng et al. constructed nanocomposite Ag/Cap coatings on titanium dioxide nanotubes under proper reaction conditions, which enabled TiO2 surface to have osteointegration-promoting and antibacterial properties without requiring complex equipment and reaction steps (Li et al., 2015).

Generally, pDA coatings are prepared in alkaline environments because alkaline conditions benefit the oxidative polymerization of catecholamines, which promotes pDA coating formation (Bernsmann et al., 2011). However, many researchers overlooked the fact that in acidic environments, the stability of the transient oxidation intermediates of catechol will increase, resulting in a decreased self-polymerization rate (Zheng et al., 2015), which may favor the enwrapping of AgNPs. Moreover, metal ions with strong oxidizability can accelerate oxidative polymerization even under acidic conditions (pH = 4). David Ruch et al. proposed that oxidative metal ions can receive the electrons produced in the oxidation of dopamine, which will promote polymerization (Ball et al., 2013). Furthermore, ion-dopamine coordination may enable linking between the intermediate state of pDA produced in solution and surfaces and hence promote the formation of stable coatings (Ejima et al., 2017; Wang et al., 2020). Therefore, different pH values will cause different polymerization forms of pDA, hence leading to different degrees of reduction and enwrapping of AgNPs, which will open the door for fabricating controllable antibacterial pDA@AgNP surfaces.

Herein, we developed a novel one-pot method to construct dopamine/silver composite antibacterial surfaces. pH and temperature are two variables in the reaction system. Different pH values were set to adjust the oxidation degree of dopamine; variations in pH will also influence the participation degree of Ag^+ in the redox/coordination reaction between Ag^+ and dopamine, which will ultimately determine the enwrapping degree of the resultant pDA@AgNP surface. Heat treatment after simple cleaning was performed as a crucial procedure that will recapture residual dopamine and initiate further oxidation crosslinking (Luo et al., 2013), thus forming a stable coating surrounding the AgNPs to slow Ag release and reduce cytotoxicity. The results indicate that the dopamine/Ag composite surface prepared under acidic conditions had the best antibacterial properties. Heat treatment increased the durability of the surface antibacterial ability and reduced cytotoxicity, which has applicable value for preventing implant infection complications.

Materials and methods

Materials

Commercially pure titanium was purchased from Baoji Nonferrous Metal Co., Ltd. Dopamine-HCl, silver nitrate, rhodamine 123 and MTT were purchased from Sigma-Aldrich. Nitric acid, hydrochloric acid, dimethyl sulfoxide and glutaraldehyde were purchased from Acros Organics. Fetal bovine serum, α-minimum Eagle's medium, and trypsin-EDTA solution were purchased from Gibco. Other reagents were purchased from Sinopharm Chemical Reagent Co., Ltd.

Preparation of Ag/dopamine coating

After being mechanically polished to 2000 grit, the titanium discs were ultrasonically cleaned successively with acetone,

ethanol and deionized water and denoted Ti. Then, Ti was immersed in a 2.5 M NaOH solution at 60°C for 24 h and was ultrasonically cleaned in deionized water at 100°C for 2 h, allowing it to acquire the micro/nanoporous structure, which was denoted as pTi. After that, the sample was immersed in a mixed solution of dopamine (2 mg/mL) and silver nitrate (0.02 mg/mL) at three pH values (4, 7, and 10). After reaction for 24 h at 37°C in a light-free environment, all the samples were removed, and each group was then divided into two identical groups. Half of the samples in each group were cleaned by ultrasound in deionized water for 3 min and were denoted as pH 4, pH 7 and pH 10. The other half were transferred to the oven for 2 h at 150°C, cleaned by ultrasound in deionized water for 3 min, and denoted as pH 4-H, pH 7-H and pH 10-H.

Surface characterization

The surface morphology and structure of the samples were investigated using scanning electron microscopy (SEM) with an accelerating voltage of 3 kV, and the distribution of silver on the surfaces and solutions was investigated using detectors for backscatter electron images (BSE) with an accelerating voltage of 10 kV and transmission electron microscope (Hitachi, Tokyo, Japan), respectively. X-ray photoelectron spectroscopy (XPS) with an Al Ka X-ray source (1,486.6 eV photons) was applied to analyze the surface chemical composition. A survey scan was performed between 0 and 1,100 eV electron binding energies at a pass energy of 100 eV, and a high-resolution spectral scan was performed at 30 eV to obtain detailed information. Due to the 45° take-off angle in XPS, the maximum detection depth did not exceed 10 nm. To investigate the total amount of silver loaded on the coating, the samples were immersed in 2 mL aqua regia for 2 h and were then diluted with deionized water to 10 mL to measure the silver concentration by inductively coupled plasma-mass spectrometry (ICP-MS). To study the release behavior of silver in coatings, the samples were immersed in 10 mL physiological saline at 37°C. At a scheduled time (1, 3, 5, 7, 14 days), the entire volume was collected, and fresh physiological saline was added. The silver concentration in the collection solution was measured by ICP-MS.

In Vitro antibacterial test experiments

During implantation, bacteria in the mouth can attach to implant surfaces or invade implant sites through the crevice between implants and surrounding tissues, leading to infection or inflammation (peri-implant inflammation and peri-implant mucositis). Therefore, antibacterial implants should inhibit bacterial adhesion and biofilm formation on the implant surface and inhibit the bacteria in surrounding tissues to avoid infection-associated inflammation. Thus, the evaluation of antibacterial ability of materials involves two parts. One is to evaluate the inhibitory ability of samples to bacteria in the surrounding environment by the turbidimetric method, inhibition ring method and serial dilution method, and the other is to evaluate the ability of sample surface to inhibit bacterial adhesion and biofilm formation by live/dead bacteria staining and the spread plate method. Here, *Staphylococcus aureus* (*S. aureus*) was incubated aerobically in brain heart infusion (BHI) broth supplemented with 2% sucrose. *Actinobacillus actinomycetemcomitans (Aa)* was incubated anaerobically (85% N_2, 10% H_2, 5% CO_2) on horse blood agar. Then, a colony was removed and added to Luria–Bertani (LB) broth and diluted to 10^5 CFU/mL to obtain the test strain solution for the following antibacterial evaluation. 1) Turbidimetric method: 60 μl aliquots of test strain solution were distributed onto the sample surfaces in a 24-well plate, and after incubation for 4 h at 37°C, 2 mL of LB broth was added to each well and cultured at 37°C. After incubation for 24 h with *S. aureus* and 48 h with *Aa*, 100 μl of LB broth was removed, and the optical density was measured at 660 nm (OD660) using a microplate reader. 2) Inhibition ring method: 100 μl of *S. aureus* or *Aa* test strain solution was spread evenly onto a solid LB agar or a horse blood agar plate surface, and then the samples were lightly placed face down on the solid agar. After an incubation of 24 h for *S. aureus* and 48 h for *Aa* at 37°C, the transparent inhibition zone around the sample was photographed. 3) Serial dilution method: test strain solutions of *S. aureus* with different dilutions were incubated with samples for 1, 3, and 5 days, and the turbidity of the solution was photographed. 4) Live/Dead bacteria staining and spread plate method: 60 μl aliquots of the test strain solution were distributed onto the sample surfaces in a 24-well plate, and after incubation for 4 h at 37°C, 2 mL of LB broth was added to each well and cultured at 37°C. After incubation for 24 h with *S. aureus* and 48 h with *Aa*, the samples were removed, rinsed with physiological saline and stained using a LIVE/DEAD Bac Light Bacterial Viability Kit. In addition, the samples were put into a sterilized centrifuge tube with 2 mL of physiological saline. After ultrasonic treatment for 2 min and vortexing for 5 min and 1000-fold dilution, 100 μl aliquots with *S. aureus* or *Aa* were removed and spread evenly onto a solid LB agar or horse blood agar plate surface, respectively. After an incubation of 24 h for *S. aureus* and 48 h for *Aa*, the CFUs on the plates were observed.

To evaluate the stability of the antibacterial ability of the samples, multiple inoculations with different dilutions of *S. aureus* were used to simulate the continuous invasion of bacteria in the implant site, and the samples were immersed in physiological saline for 7 days. Then, the samples were evaluated for antibacterial performance by the turbidimetric method and spread plate method with S. aureus at 10^5 CFU/mL.

Cytocompatibility evaluation

The mouse osteoblastic cell line (MC3T3-E1) and the mouse fibroblastic cell line (NIH-3T3) were employed to assess the cytotoxicity. Cells were cultured in α-MEM containing 15% fetal bovine serum in a humidified atmosphere of 5% CO_2 at 37°C.

After UV sterilization, the samples were placed in a 24-well plate. A 1 mL cell suspension with a density of 5×10^4 cells/mL was added to each well, and the medium was refreshed every 2 days. After incubation for 1, 3, and 5 days, the samples were rinsed with sterile physiological saline, and some samples were transferred to 2.5% glutaraldehyde and underwent a 4 h for fixation. Then, the samples were stained with YF555-phalloidin for F-actin and DAPI for nuclei, and the other samples were used for MTT tests. In addition, to assess the toxicity of the material to the surrounding tissue, a 1 day extraction of the samples were collected to assess their toxicity by crystal violet staining and MTT tests. The percent inhibition was calculated by the following formula:

$$\text{relative growth rate (RGR) (\%)} = (\text{OD490 nm value of sample well} - \text{OD490 nm value of blank well}) / (\text{OD490 nm value of control well} - \text{OD490 nm value of blank well}) \times 100$$

Competitive bacterial-cell adhesion

First, 60 μl of LB broth containing *S. aureus* or *Aa* at a density of 10^5 CFU/mL was distributed onto sample surfaces and incubated for 4 h at 37°C. Then, 1 mL of cell suspension (MC3T3-E1 or NIH-3T3) with a density of 5×10^4 cells/mL was inoculated onto the samples. After incubation for 1 and 3 days at 37°C and 5% CO_2, the samples were rinsed with physiological saline. Then, both the live and dead bacteria/cells on the samples were stained using the LIVE/DEAD Bac Light Bacterial Viability Kit to assess competitive bacterial-cell adhesion to the different materials.

In Vivo experiments

After anaesthetization by intraperitoneal injection of 1% pentobarbital, both hind legs of SD rats were shaved, depilated, and disinfected with iodine. Then, the femoral condyles of both hind legs were exposed by skin incision, and a Kirschner wire was employed to drill a hole through the cortical and cancellous bones. At the same time, a 10 mm longitudinal skin area was cut to expose the superficial layer of the deep fascia to form a pocket. Sterile titanium rods (2 mm in diameter and 8 mm in length) or titanium discs (1 cm in diameter and 1 mm in thickness) with different surface modifications were immersed into the *S. aureus* suspensions at a concentration of 10^5 CFU/mL for 1 h, and then the samples were inserted in the legs or pockets in the skin. After implantation, the hole was blocked by bone wax, and the wound in the leg and skin was closed with a suture. After 1 and 7 days, some of the samples were explanted, rolled on solid LB agar plates and recultured for 1 days. In addition, other samples were immersed in 1 mL of physiological saline with ultrasonic and vortex treatment, and then 100 μl aliquots were removed and spread evenly onto solid LB agar plates. The samples were recultured for 1 days, and the CFUs on the plates were observed. After 1 month, the animals were euthanized, and the titanium rods and discs with the surrounding tissues were harvested for further micro-CT analysis and histological analysis, respectively.

Statistics

All experiments were performed at least three independent times. All quantitative data are presented as the means ± standard deviations and were compared with one-way ANOVA tests to evaluate statistical significance using SPSS software. After ANOVA, Tukey's multiple comparisons test was performed to find significant differences between pairs.

Results and discussion

Surface morphology of AgNPs-loaded coatings

As the scanning electron microscopy (SEM) images in Figure 1A showed, after alkali-heat treatment, the Ti surface presented a uniform micro/nanoporous morphology with increased specific surface area. After immersion in the dopamine/silver solution, a large number of AgNPs were coupled with the porous surfaces. In addition, with increasing pH, the number of AgNPs increased, and their size decreased; as a result, the pH 10 surface was completely covered by AgNPs (Fernando and Zhou, 2019). Compared with the unheated surfaces, the number of AgNPs significantly increased on the heated surfaces, and the AgNPs tended to merge together with the aid of residual dopamine which more closely resembled a pDA@NPs complex than two separate parts. To further study the loading behavior of AgNPs in the pDA@NPs complex, backscattered electron (BSE) imaging was performed. Backscattered electrons are high-energy electrons that can be used to obtain high-resolution images of the distribution of elements in a sample (Maitland and Sitzman, 2007). As displayed in Figure 1B, the complexes at pH 7 and pH 10 showed an obvious change in which the highlighted core was covered by a translucent shell, which may indicate that Ag was warpped by pDA. Of particular interest was the enwrapping manner of Ag in pDA@NP complexes prepared at different pH values. Under neutral and alkaline conditions (pH = 10), Ag cores were separately coated by shells, while in acidic conditions (pH = 4), many Ag cores were assembled first and then coated with pDA. Since alkaline conditions can accelerate the oxidative polymerization of dopamine (Saiz-Poseu et al., 2019), we speculate that increased dopamine cross-linking led

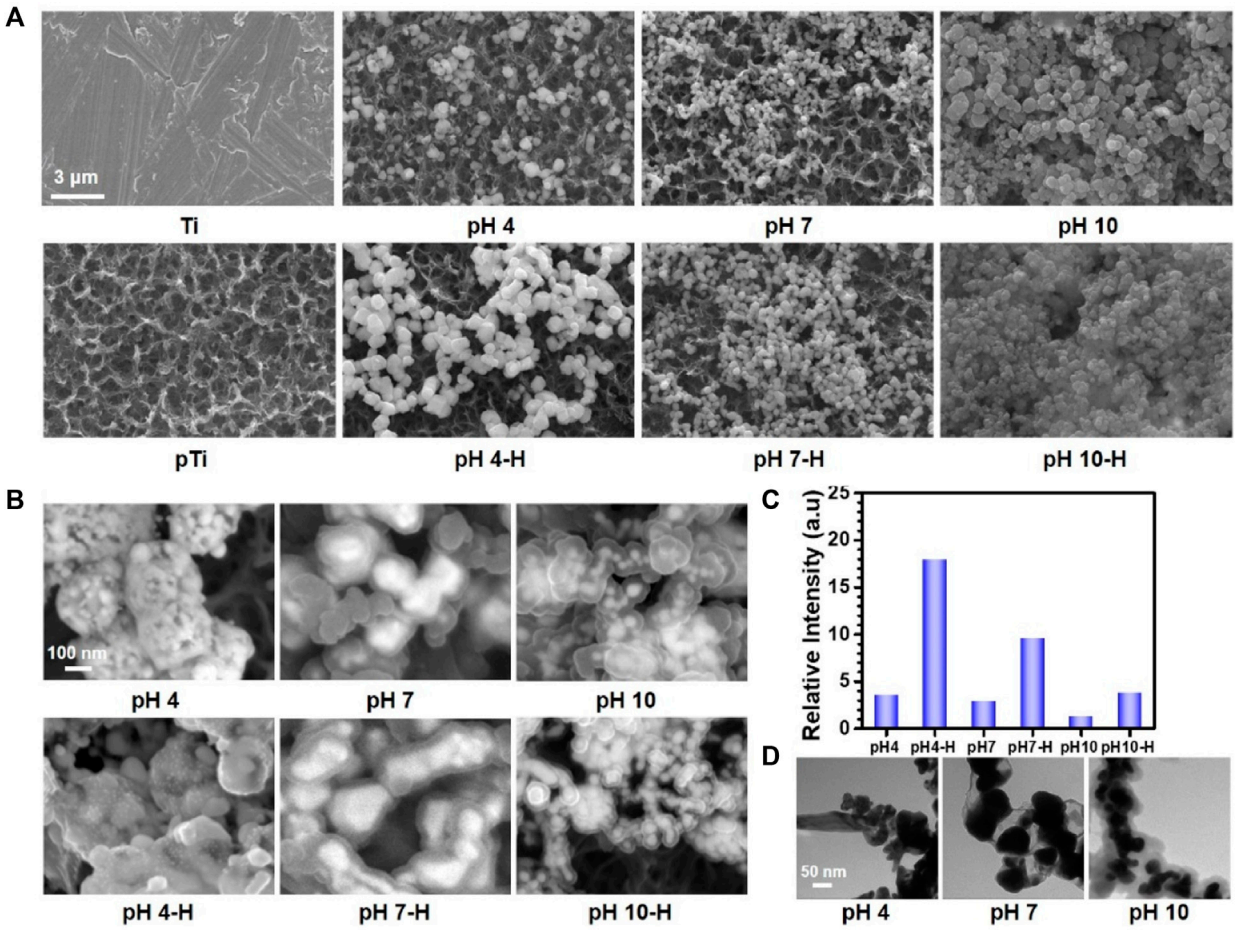

FIGURE 1
The surface morphology of different samples: **(A)** scanning electron microscopy (SEM) images of different samples; **(B)** Backscattered electron (BSE) images of different samples; **(C)** relative intensive of Ag by X-ray photoelectron spectroscopy (XPS); **(D)** Transmission electron microscope (TEM) analysis of AgNPs in solutions at pH 4, pH7, pH10.

to high shell shrinkage and the accelerated oxidative polymerization of dopamine favored the enwrapping of silver particles. However, under acidic conditions, the driving force of dopamine oxidative polymerization was mainly provided by Ag^{+}, so the polymerization was slower. In addition, pH value also affected the size of Ag core, which gradually decreases with the increase of pH value, which provides favorable conditions for dopamine encapsulation (Fernando and Zhou, 2019; Marciniak et al., 2020). And the two processes of Ag core formation and enwrapping proceeded together, which may led to this specific coating.

In contrast to the thickly wrapped samples, AgNPs at pH 4 showed tight but not very thick enwrapping, which was also demonstrated in the X-ray photoelectron spectroscopy (XPS) results. As Figure 1C shows, after heat treatment, the amount of Ag increased significantly, and this effect was most pronounced at pH 4. Since the detection depth of XPS is approximately 10 nm, atoms deeper than 10 nm cannot be effectively detected (Guy and Walker, 2016). Therefore, even the pDA@NP complex displayed in Figure 1A did not show much of a difference between pH 4-H, pH 7-H and pH 10-H, but the atomic percent of Ag exhibited a downward trend with increasing pH (Figure 1C). To further explore the Ag distribution at different pH values, transmission electron microscope (TEM) analysis was carried out (Padhi and Behera, 2022). As the results in Figure 1D showed, high-density and low-density substances were observed, which correspond to Ag and pDA, respectively. At pH 4, AgNPs were closely wrapped by pDA, and some AgNPs were exposed in the solution, which may benefit the release and function of Ag. In contrast, in the particles prepared at pH 7 and 10, Ag was coated by a greater thickness of pDA than that at pH 4, which is consistent with the results of BSE and XPS analysis. In conclusion, pH 7 and more alkaline conditions will accelerate

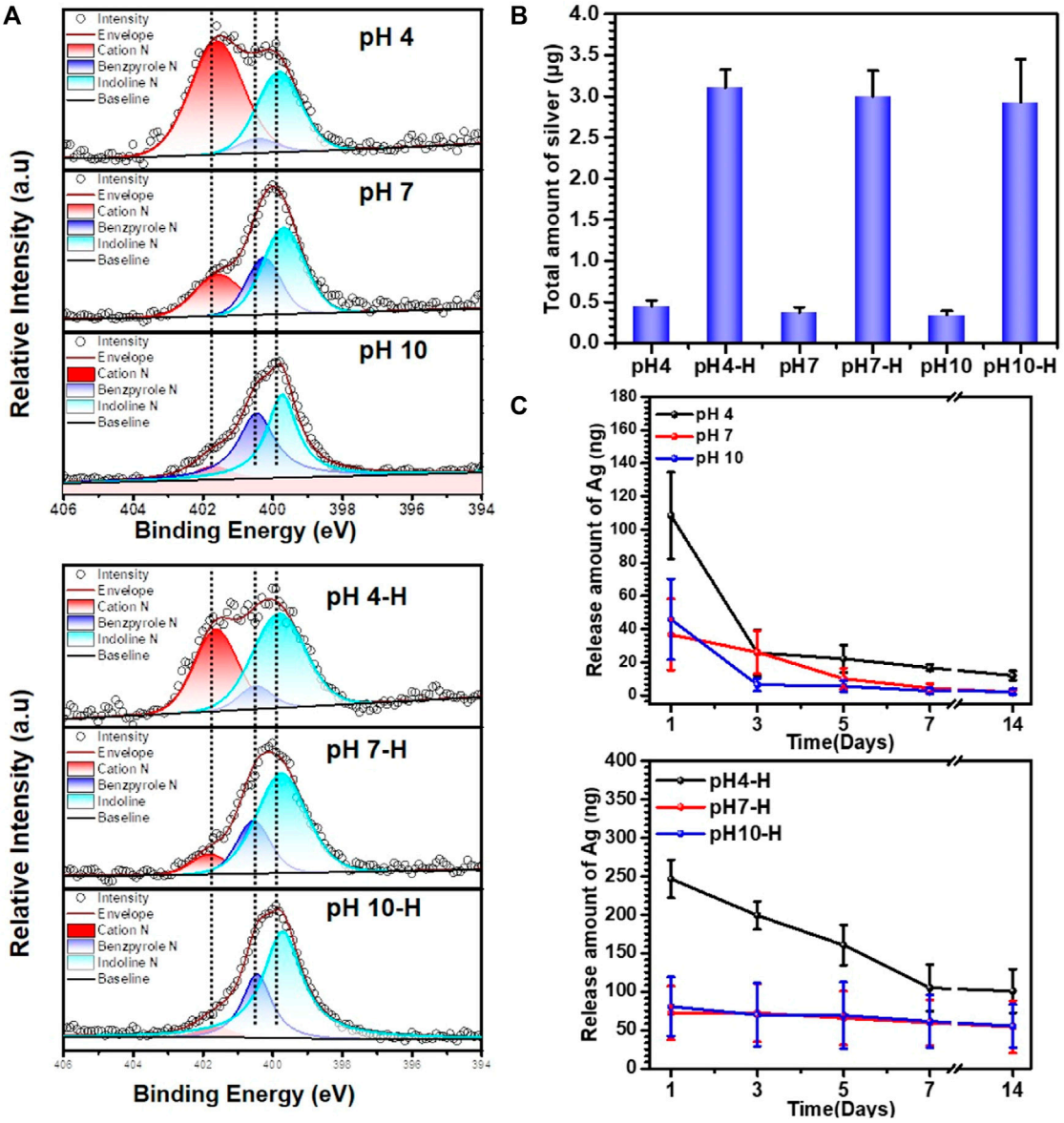

FIGURE 2
Characterization of different samples: **(A)** XPS high-resolution N analyses of pH4-H, pH7-H and pH10-H; **(B)** total amount of Ag in different samples investigated by Inductively Coupled Plasma Mass Spectrometry (ICP-MS); **(C)** the release amount with time of different samples detected by ICP-MS.

the polymerization of dopamine and consequently form a thicker coating outside the AgNPs, which may influence the release mechanism and function of AgNPs.

Characterization of the pDA@NPs complex

To further analyze the chemical composition and structure of the pDA@NPs complex, XPS full-spectrum and high-resolution N analyses were carried out. As the results in Supplementary Figure S4 show, with the formation of the pDA@NPs complex, the N1s peak increased, and the Ag3d peak appeared. Since the detection depth of XPS was limited, the Ti2p peaks significantly decreased after samples were coated by the pDA@NP complex (Guy and Walker, 2016). As the pH value of the mixed solution increased, the intensity of the Ag3d and Ti2p peaks decreased regardless of the use of heating, demonstrating that more AgNPs were formed in acidic conditions, which was consistent with the BSE results. Moreover, the intensity of the Ag3d peaks on the

heated surfaces was significantly higher than that on the unheated surfaces because there must be Ag^+ and dopamine in the residual solution, and heat treatment will trigger further crosslinking of dopamine and Ag^+, which ultimately cause the relocation of the pDA@NPs complex (Zhang et al., 2016). Moreover, heating made the coating more stable, so more particles were retained after ultrasonic cleaning, which was in agreement with the results of the surface morphology tests. To extensively analyze the status of the pDA@NPs complex, high-resolution N spectra were collected. As displayed in Figure 2A, the dopamine molecule can be oxidized in the presence of oxygen in solution, followed by the formation of an indoline moiety through Michael addition (Saiz-Poseu et al., 2019). Then, the molecule undergoes further oxidation and is rearranged to a benzopyrrole-type molecule, a more stable form of oxidized dopamine. During this process, two kinds of nitrogen, indoline N and benzopyrrole N, formed (Liebscher et al., 2013). Ammonium ion (cation N) also existed in the pDA coating due to the protonation of N-containing groups. Based on the understanding of the resulting structure of oxidized dopamine, the peaks at 399.8, 400.4, and 401.6 eV can be assigned to indoline N, benzopyrrole N and cation N according to the charge of N atom.

At lower pH, the ionization of phenol is inhibited, while the ionization of amino groups is enhanced, which leads to a reduced polymerization rate of dopamine and the formation of many cation N groups in the pDA coating (Liu et al., 2014). The oxidation degree of dopamine will increase in alkaline solution, while the content of cation N will decrease significantly through a possible deprotonation process. Moreover, indoline N and benzopyrrole N also tended to increase. These results indicated that, consistent with previous reports, a higher pH contributes to the deep oxidation of dopamine (Vatrál et al., 2015; Wang et al., 2019).

The intragroup variation in N contents in the high-temperature-treatment group under different pH values was similar to that in the room-temperature-treatment group. According to intergroup comparison, the high-temperature treatment led to a dramatic decrease in cation N at a certain pH. However, the changes in the contents of indoline N and benzopyrrole N were different. It is generally believed that oxidation will lead to more benzopyrrole N under high-temperature treatment, but the data show that the benzopyrrole N content decreased instead (Lee et al., 2007). One possible interpretation is that indoles are reduced to an indoline structure by silver at high temperature.

As demonstrated above, pH and heat treatment play vital role in the pDA@NP complex formation, which may influence the Ag^+ release mechanism (Zheng et al., 2015). To quantify the total amount of Ag and detect the Ag release mechanism, Inductively Coupled Plasma Mass Spectrometry (ICP-MS) was used. As shown in Figure 2B, pH did not influence the volume loading of Ag, but heat treatment significantly improved it. After simple cleaning, a certain amount of Ag and dopamine was retained. During heat treatment in air, the oxidative polymerization triggered by both oxygen and Ag^+ increase tremendously, which results in a higher loading capacity of Ag and a specific coating manner (Proks et al., 2013). Accordingly, the release behavior was correlated with the loading method to a certain degree. As shown in Figure 2C, different pH values did not substantially influence the release of Ag when temperature was not considered. However, in the heat-treatment groups, the release amount of Ag increased with an elevated loading amount, among which the initial release of pH 4-H reached 250 ng on the first day, and a release plateau of 100 ng was maintained at a prolonged detection time of 7–14 days.

In conclusion, the fine spectra of N1s (Figure 2A) showed that the degree of dopamine oxidative polymerization was enhanced with increasing pH, SEM results showed that the coating thickness on titanium sheet gradually increased with the increase of pH (Figure 1A). ICP-MS showed that there was no evident distinction in the total amount of silver in each group (Figure 2B). It indicated that the amount of substance increased in the coating was mainly formed by oxidative polymerization of dopamine into a polymer and then precipitation at high pH. For silver, silver nitrate would form sediment under both acidic and alkaline conditions, so pH had little effect on the amount of silver deposited, as shown by ICP-MS. In addition, the higher the pH was, the faster the oxidative polymerization reaction of dopamine. When silver had not formed a large core, it was wrapped to isolate its reaction. Moreover, the higher the pH was, the faster the oxidative polymerization reaction would be and the deeper the degree would be, so the thicker the dopamine shell would be. As shown in the results of BSE (Figure 1B) and TEM (Figure 1D), the higher the pH was, the thicker the dopamine shell and the smaller the silver core. Therefore, even if the amount of substance in the coating increased under high pH conditions, the increased component was dopamine, and the proportion of silver in the coating decreased and could not be released by wrapping. Therefore, the relative strength results of surface elements in XPS showed that the strength of silver gradually decreased because the measured depth and surface area were constant (Figure 1C, Supplementary Figure S4). In addition, when the pH was lower, silver would also precipitate and polymerize, but at this time, the degree of oxidative polymerization of dopamine was low and mainly depended on the reaction and cross-linking polymerization with silver. Therefore, at pH4, the thickness of the coating was significantly reduced, and the main component of the coating was silver. Because dopamine was polymerized mainly by cross-linking with silver, the particles formed by the reaction looked like complex particles rather than inclusions. By heating the sample, the loading of the coating was mainly improved, and the reaction of dopamine and silver was not significantly affected. In summary, the innovative AgNPs preparation system reused residual dopamine and Ag^+ and significantly increased the

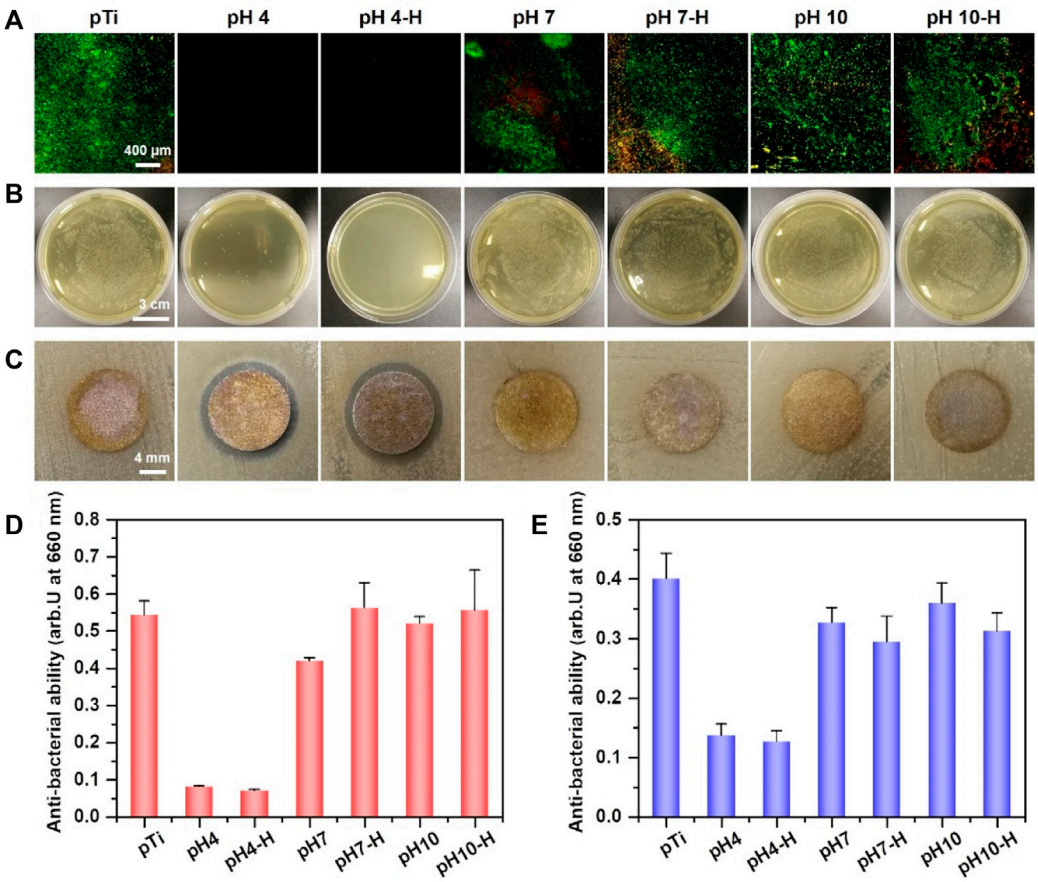

FIGURE 3
Assessment of antibacterial activity of different samples: **(A)** Live/Dead bacteria staining of S. aureus on different samples; **(B)** antibacterial property (S. aureus) of various sample surfaces determined by spread plate method; **(C)** the diameter of inhibition zone around various samples for S. aureus; **(D)** bacterial amount in the inoculum after incubation of various samples with S. aureus for 24 h by turbidimetric method; **(E)** bacterial amount in the inoculum of various samples after incubation with Aa for 24 h by turbidimetric method.

loading of Ag; heat treatment improved the oxidative crosslinking of dopamine, which enhanced the stability of the pDA@Ag complex; and pH played a key role in determining the Ag enwrapping method, which ultimately led to sustained and smooth release.

In Vitro antibacterial properties

Antibacterial surface modification endows implants with appropriate antibacterial properties to inhibit bacterial adhesion and biofilm formation after implantation. Fürst et al. (2007) reported that bacterial colonization occurred within 30 min after implantation, among which *S. aureus* and *Aa* were the main species that contributed to local implant infection, even in the oral cavity. Here, live/dead bacteria staining and the spread plate method were used to evaluate the ability of the prepared surface to inhibit bacterial adhesion or kill adhered bacteria. First, *in situ* evaluation of adhered *S. aureus* and *Aa* was performed by fluorescent staining of live/dead bacteria. As shown in Figure 3A and Supplementary Figure S1A, many bacteria adhered rapidly to the surface of pTi, and most of the adhered bacterial cells were alive (stained green). Among the pDA@NP-modified surfaces, only the pH 4 and pH 4-H surfaces completely inhibited bacterial adhesion. Moreover, the spread plate method was used to observe the number of live *S. aureus* and *Aa* adhered to the surface. As shown in Figure 3B and Supplementary Figure S1B, there was almost nothing on the surface of pH 4-H, and sporadic live bacteria were observed on pH4. In contrast, many live bacteria adhered to the dopamine/Ag-modified surfaces prepared in neutral and alkaline conditions, which was attributed to the distribution of silver on the surface: the dopamine shell made it difficult for silver to directly contact bacteria and exert antibacterial effects. These results show that the surfaces of pH 4 and pH 4-H samples possess the

best antibacterial ability, which is consistent with the ICP-MS and XPS results that acid conditions led to the formation of more pDA@NP complexes and a better Ag release process.

To further evaluate the antibacterial properties of the surroundings of these samples, the inhibition zone method (Figure 3C and Supplementary Figure S1C), turbidimetric method (Figure 3D) and serial dilution method (Supplementary Figures S2A–C) were carried out. After incubation with bacterial suspensions (*S. aureus* and *Aa*) for 24 h, the optical density at 660 nm (OD 660) was measured to evaluate the indirect antibacterial ability of different samples. As shown in Figure 3D (*S. aureus)* and Figure 3E *(Aa*), only pH 4 and pH 4-H exhibited better antibacterial activity. The results of the zone of inhibition were the same as those of the turbidimetric method (Figure 3C and Supplementary Figure S1C): the only clear inhibition zone was observed around the pH 4 and pH 4-H samples. In addition to the direct and indirect antibacterial properties for the short term, the sustained antibacterial ability is also important for orthopedic/dental implants (Guo et al., 2021). To assess the sustained antibacterial ability, the antibacterial properties of pDA@NP-modified samples was tested for 1, 3, and 5 days by serial dilution method as shown in Supplementary Figures S2A–C. The results demonstrate that with the increases of bacterial inoculation amount and culture time, the pH 4 samples gradually lost the ability to inhibit surrounding bacteria, and only the pH 4-H samples still inhibited bacterial proliferation and maintained a clear inoculum on the day 5. To test the stability of these pDA@NP-modified samples, samples from the same batch as above were immersed in physiological saline for 7 days, and then the spread plate method (Supplementary Figure S1D) and the turbidimetric method were used to evaluate their antibacterial ability (Supplementary Figure S3) (Assenza et al., 2012). The results demonstrate that only pH 4-H samples could inhibit bacterial proliferation while others did not show obvious antibacterial activity. To test the continued antibacterial property of samples of pH 4-H, they were inoculated with *S.aureus* for fifth times, and as the results in Supplementary Figure S2D show, they could keep combatting bacteria. All these results indicated that the pH 4 and pH 4-H samples had a good ability to inhibit the proliferation of gram-positive and gram-negative bacteria around them in the short term, but the pH 4-H sample had a stronger and more durable bacterial inhibition ability due to the release of a larger amount of silver (Figures 2B,C). The pH 7-H and pH 10-H surfaces released large amounts of silver but showed no antibacterial activity, which may indicate that silver was released by particle stripping and that pDA will function as a shell even when particles stripped from the surface as a whole.

In Vivo antibacterial properties

More than 700 bacterial species inhabit the oral cavity, so the influence of bacteria cannot be avoided (Chattopadhyay et al., 2019). Bacterial infection will continue to develop if invasion happens, so the *in vivo* antibacterial ability needs to be evaluated. Herein, a rat model was developed to investigate the antibacterial ability of these AgNP-loaded coatings. Since implants will contact both bone and soft tissue, titanium rods and titanium discs dipped in bacteria solution were implanted into the femoral medullary cavity and a subcutaneous location of a rat model, respectively (Shimazaki et al., 2010; Masamoto et al., 2021). Samples of the pH 4 and pH 4-H treatments were chosen for further evaluation because only the samples prepared in acid conditions presented good antibacterial ability in the *in vitro* experiment. After 1 and 7 days of implantation, the samples were removed and rolled on agar to be recultured for 24 h. As shown in Figure 4A, after 1 day of implantation, a large number of bacteria adhered to the pure titanium rod surface, and the number of bacteria that adhered to the pH 4 and pH 4-H surfaces was significantly lower than that of the pure titanium rod surface. In addition, the bacteria adhered to the samples were detached by ultrasound for the spread plate test. The results showed that the number of bacterial colonies on pTi, pH 4 and pH 4-H decreased successively, and only sporadic colonies were found on the surfaces of pH 4 and pH 4-H, which was consistent with the results of the rolling culture. After 7 days of implantation, the results of the rolling culture and spread plate method showed that the number of adherent bacteria on the surface of pTi and pH 4 increased significantly compared with that of 1 day culture, and the number of bacteria on the pH 4 surface was still much lower than that on the pTi surface. These results indicated that the pH 4-H surface exhibited better *in vivo* antibacterial properties. Titanium discs inoculated with bacteria were subcutaneously implanted into rats. After 1 and 7 days of culture, the samples were removed and pressed on an agar culture plate; at the same time, bacteria were detached by ultrasound for the spread plate test. As shown in Figure 4B, the number of bacteria adhered to the surface of pTi increased with the extension of implantation time, showing no antibacterial ability. The pH 4 surface showed antibacterial ability at the initial stage of implantation, but with prolonged time, the number of bacteria on the surface increased, indicating that the pH 4 sample could only delay bacterial proliferation. In contrast, pH 4-H showed stronger antibacterial ability with the extension of implantation time, and no living bacteria were found on the surface of the implant after 7 days due to the high silver loading and the relatively abundant Ag release, which formed an antibacterial area around the implant. These results indicated that the pH 4-H surface possessed better *in vivo* antibacterial properties at the gap between samples with bone or soft tissue.

Biocompatibility of AgNPs loaded coatings

Surface antibacterial modification is considered to be a short-term method because the antibacterial substance on the surface is gradually embedded or released, leading to a decline in

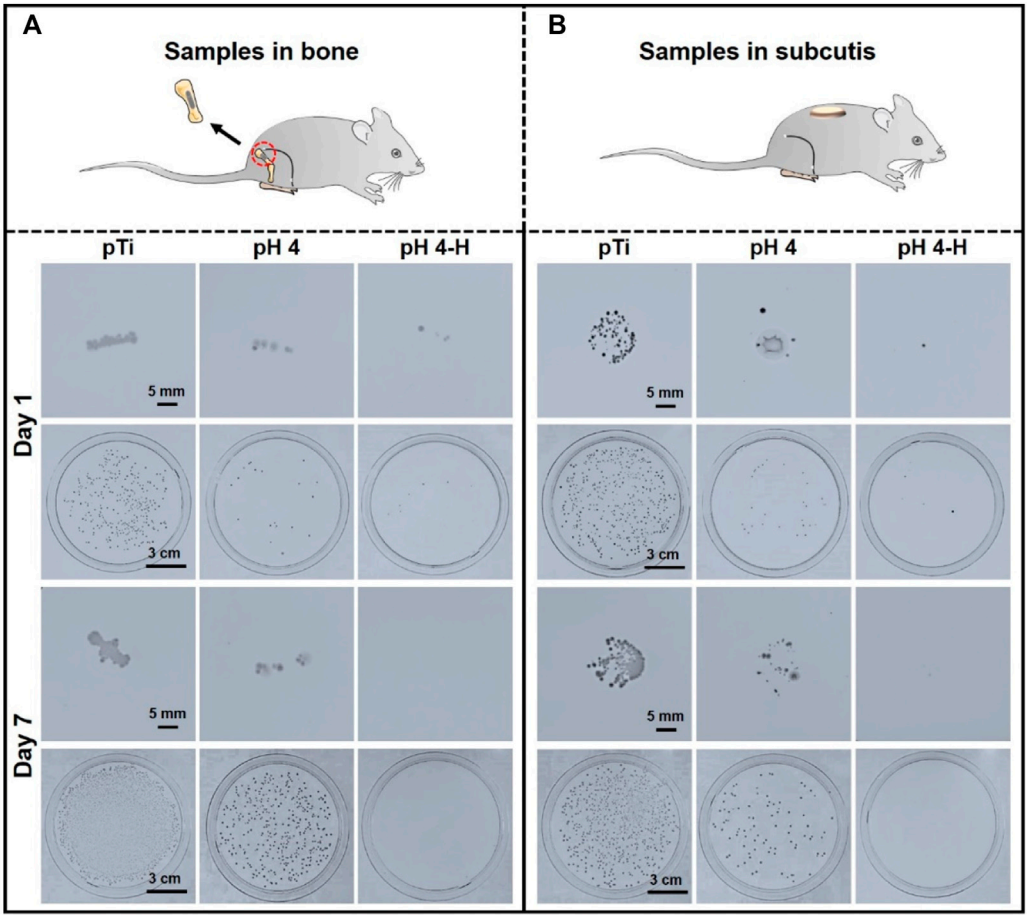

FIGURE 4
In-vivo antibacterial assay of the pH 4 and pH 4-H treatments:**(A)** Titanium rods dipped in bacteria solution were implanted into the femoral medullary cavity of rat models for one and 7 days; **(B)** titanium discs dipped in bacteria solution were implanted into the subcutaneous location of rat models for one and 7 days.

antibacterial ability. To ensure a long-term therapeutic effect, it is very important to achieve rapid osseointegration with alveolar bone at the bone-implant interface and soft tissue integration at the trans-mucosal region to seal the crevice between the implant and surrounding tissues to prevent bacterial invasion (Guo et al., 2021). Therefore, cell fluorescence staining and MTT assays were used to evaluate the biocompatibility of the samples with the mouse osteoblastic cell line (MC3T3-E1) (Figure 5) and the mouse fibroblastic cell line (NIH-3T3) (Figure 6). As shown in Figure 5A and Figure 6A, the results of fluorescence staining showed that the number of osteoblasts and fibroblasts attached to pH 4 and pH 4-H was similar to that of the pTi. After 5 days of culture, all surfaces were completely covered by osteoblasts and fibroblasts. In addition, to assess the toxicity to the surrounding tissue, a 1-day extraction of the samples were collected to assess their toxicity by crystal violet staining and MTT tests. As the results of Supplementary Figure S5 show, there was also no obvious difference in the number of osteoblasts and fibroblasts among the leach liquor of various samples. These results suggest that samples of pH 4-H did not show significant cytotoxicity. The MTT assay (Figure 5B and Figure 6B) showed that the activity of osteoblasts and fibroblasts on the surface or in the leach liquor of pTi, pH 4 and pH 4-H samples decreased successively. Compared to that of pTi, the relative growth rate (RGR) of pH 4-H after 5 days was 89.5% for osteoblasts and 92.4% for fibroblasts, and in the leach liquor, the it was 85.6% for osteoblasts and 93.4% for fibroblasts, indicating that the pH 4-H sample had low cytotoxicity and was slightly more toxic to osteoblasts than to fibroblasts. In our previous study, silver-loaded composite coatings were prepared by depositing dopamine and then silver nitrate in an alkaline environment. When the concentration of silver nitrate was 10 mg/mL (Chen et al., 2016) and 0.1 mg/mL (Wang et al., 2021b), the RGRs of osteoblasts on these surfaces at 5 days was 36.7% and 79.2%, respectively. In this study, the pH 4 and pH 4-H surfaces demonstrated remarkable superiority, suggesting that the

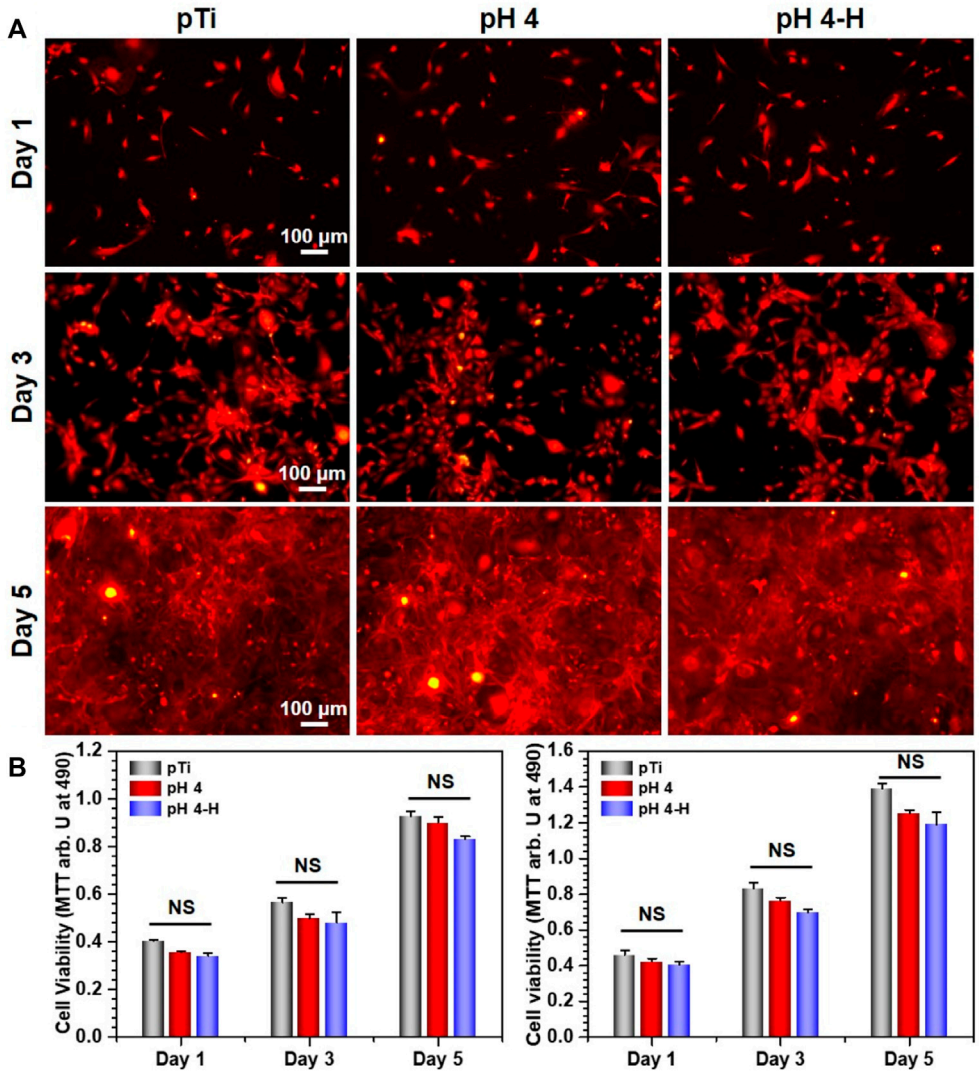

FIGURE 5
Biocompatibility evaluation of samples in group pH 4 and pH 4-H:**(A)** YF555-phalloidin (for F-actin) and DAPI (for nuclei) staining of MC3T3-E1 on various samples; **(B)** Left: MTT tests for MC3T3-E1of various samples. Right: MTT tests for MC3T3-E1 of leach liquor of various samples. NS: no significance.

silver in the previous study was completely exposed on the surface, but here it was deposited in the manner of pDA@NP complex, and the pDA coating outside the complex reduced the exposure of silver on the surface and the amount of silver released, thus reducing the direct cytotoxicity of AgNPs.

Since the oral cavity is rich in bacteria, dental implants operate where host cells and bacteria co-exist and the competition is intense (Fernández et al., 2011). Here, the coculture of bacteria with cells was performed to evaluate the biological effect of antibacterial implants in a complex environment (Wang et al., 2016). Specifically, osteoblasts (Figure 7) and fibroblasts (Supplementary Figure S6) were seeded on samples inoculated with *S. aureus* and cultured for 1 and 3 days. After 1 day of culture, many osteoblasts were observed on both the pTi surface and the modified surface, while there were a few bacteria on pTi and pH4. After 3 days of culture, many live bacteria and sporadic apoptotic cells were observed on the pTi surface, and many adherent bacteria covered the pH 4 surface, while there were a large number of healthy osteoblasts and fibroblasts on the pH 4-H surface. The results were consistent with the antibacterial evaluation (Figure 3 and Supplementary Figure S1D, Supplementary Figures S2, S3), which showed that the pH-4 sample possessed limited antibacterial ability and could only delay bacterial proliferation, while the pH 4-H sample had sufficient capacity to inhibit the proliferation of bacteria. Thus, we speculated that if

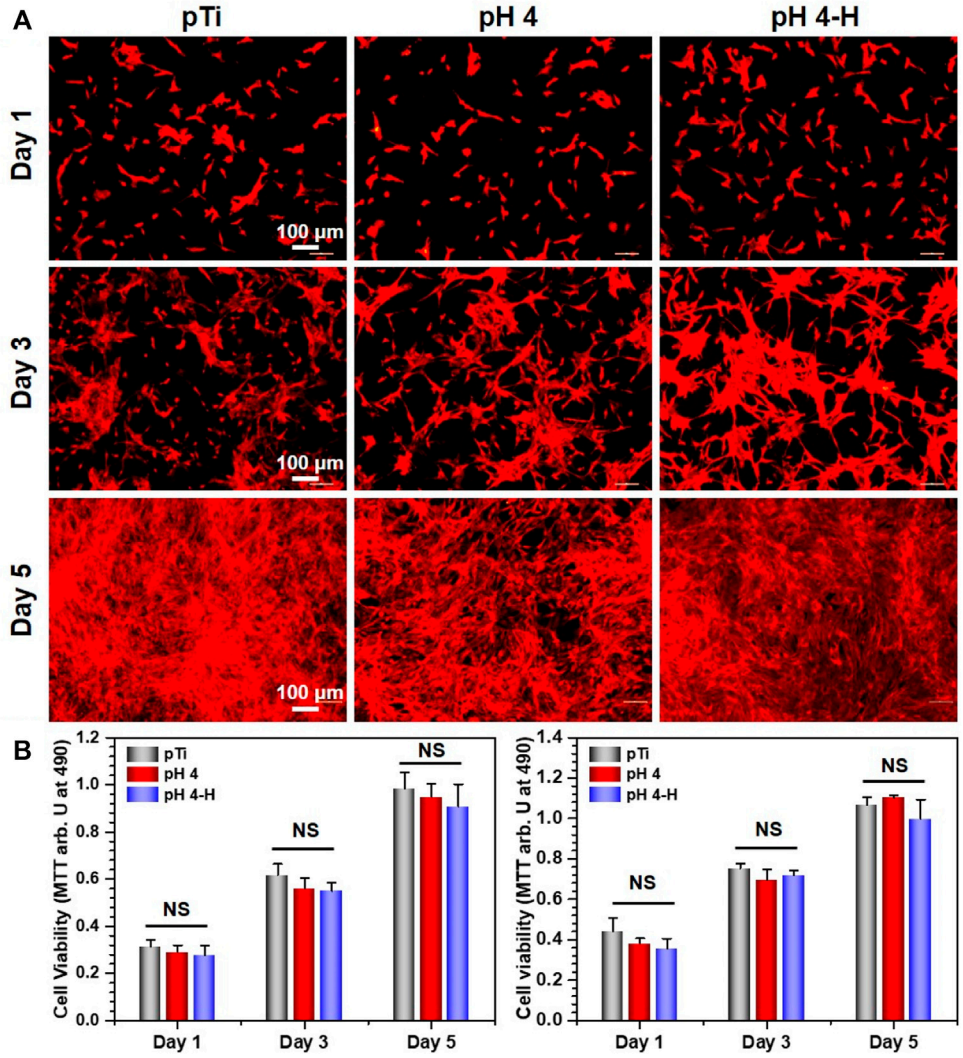

FIGURE 6
Biocompatibility of the pH 4 and pH 4-H treatments: **(A)** YF555-phalloidin (for F-actin) and DAPI (for nuclei) staining of NIH-3T3 on various samples; **(B)** Left: MTT tests for NIH-3T3 of various samples. Right: MTT tests for NIH-3T3 of leach liquor of various samples. NS: no significance.

the surface cannot completely inhibit or kill bacteria, bacteria can ultimately thrive in the gap between implant and tissue, which will also lead to implant failure, so the pDA@NP complex prepared in acidic conditions that possess strong antibacterial ability are indispensable. Clinically, the service sites of orthopedic and dental implants are not only bone but also soft tissue, and soft tissue is more easily infected by bacteria and causes postoperative failure [11]. Therefore, specimens pretreated with bacteria were implanted into the subcutis to evaluate the subcutaneous antibacterial properties. After 1 month of implantation, the tissue around the materials was harvested, and H&E staining for histological examination was carried out, the results of which are shown in Figure 7B. As a representation of soft tissue inflammation, the fibrous capsule thickness around pTi, pH 4 and pH 4-H was 80–90, 60–70, and 30–40 μm, respectively, indicating that the pH 4-H surface had a stronger inhibitory effect to microorganisms, which reduced microbe-related inflammation, thus preventing capsule formation. Implantation-induced fibrotic capsules are considered to be caused by a tissue response, so the results also demonstrate that these Ag-loaded surfaces would not cause inflammation. Instead, the surfaces with durable antibacterial properties could inhibit the tissue response caused by bacteria, which makes them promising candidates for orthopedic and dental implants.

Recent studies have demonstrated the excellent reproducibility and accuracy of micro-CT measurements of bone morphology (Bouxsein et al., 2010; Liu et al., 2021).

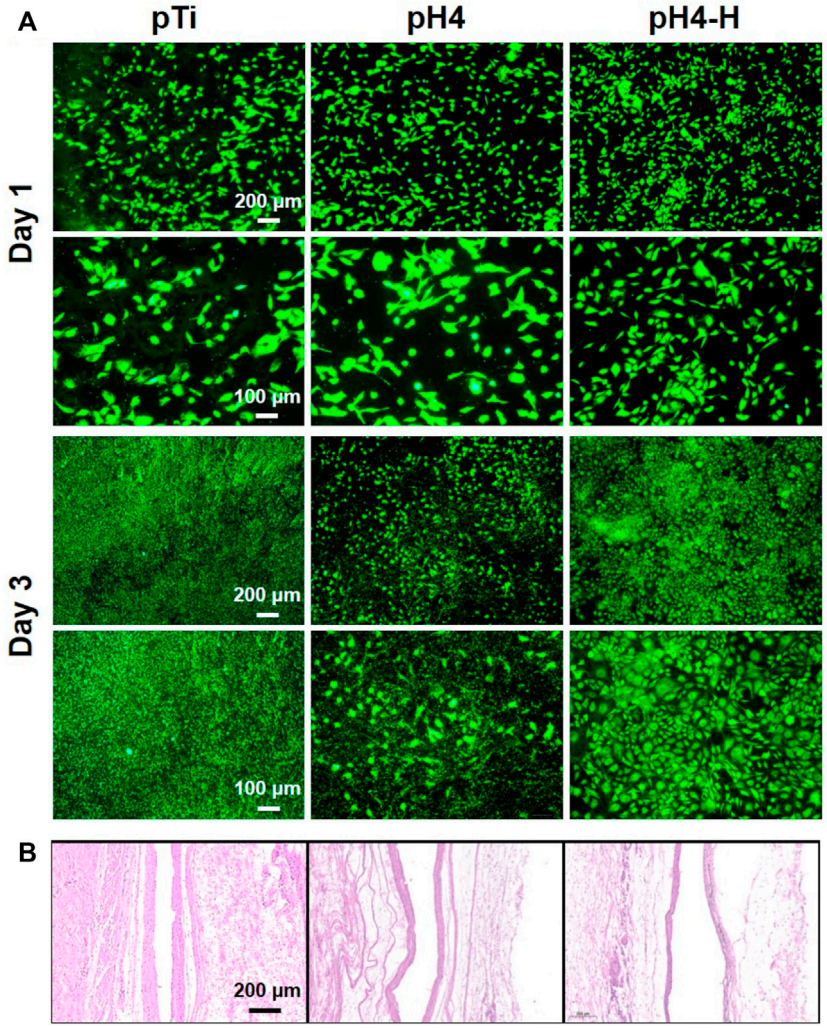

FIGURE 7
Co-culture of bacterial and cell or tissue: **(A)** Osteoblasts (MC3T3-E1) were seeded on different samples inoculated with S. aureus and cultured for 1 and 3 days; **(B)** HE staining about local tissue (pretreated with S.aureus) of various samples after 1 month of subcutaneous implantation.

Therefore, 3D micro-CT analysis was performed to investigate bone regeneration under bacterial infection conditions (Figure 8D). Prior to implantation, *S. aureus* inoculum was added, and then Ti rods were implanted into the infected marrow cavity (Ribeiro et al., 2012). According to the results of Figures 8A–C), the Ti rod with pH 4 heat treatment-modified AgNPs presented the highest percentage of bone volume to tissue volume (BV/TV), which may be due to the strongest antibacterial properties of this sample. Moreover, consistent with the BV/TV results, the increased trabecular number (Tb. N) and lower trabecular separation (Tb. SP) also indicate that pH 4 heat treatment-modified AgNPs expressed exceptional osteogenesis capacity. In contrast, severe bone loss occurred around the pTi, pH 4-modified Ti rods due to their insufficient antibacterial properties. Bone regeneration is a complex process (Figure 8E), during which tissue cells, immune cells, microbes and implants interact with each other (Trindade et al., 2016). Apart from host cells, microbes and implants are two main types of foreign matter. Pathogenic bacteria will compete with local tissue cells and their secretion will inevitably influence the normal physiological behavior of the host cells. Furthermore, once bacteria-triggered dysbacteriosis occurs, immune cells are activated and a series of inflammatory reactions, such as inflammatory factors (IL-6, IL-8, TNF-α, etc.) secretion, tissue fluid exudation, vascular permeability increase and blood cell exudation, are initiated, which ultimately prolong the tissue repair (Sherwood and Toliver-Kinsky, 2004). Therefore, implants with strong antibacterial ability will reduce the incidence rate of microbe-related inflammation thus promoting bone regeneration, so, pH 4-H exhibits better

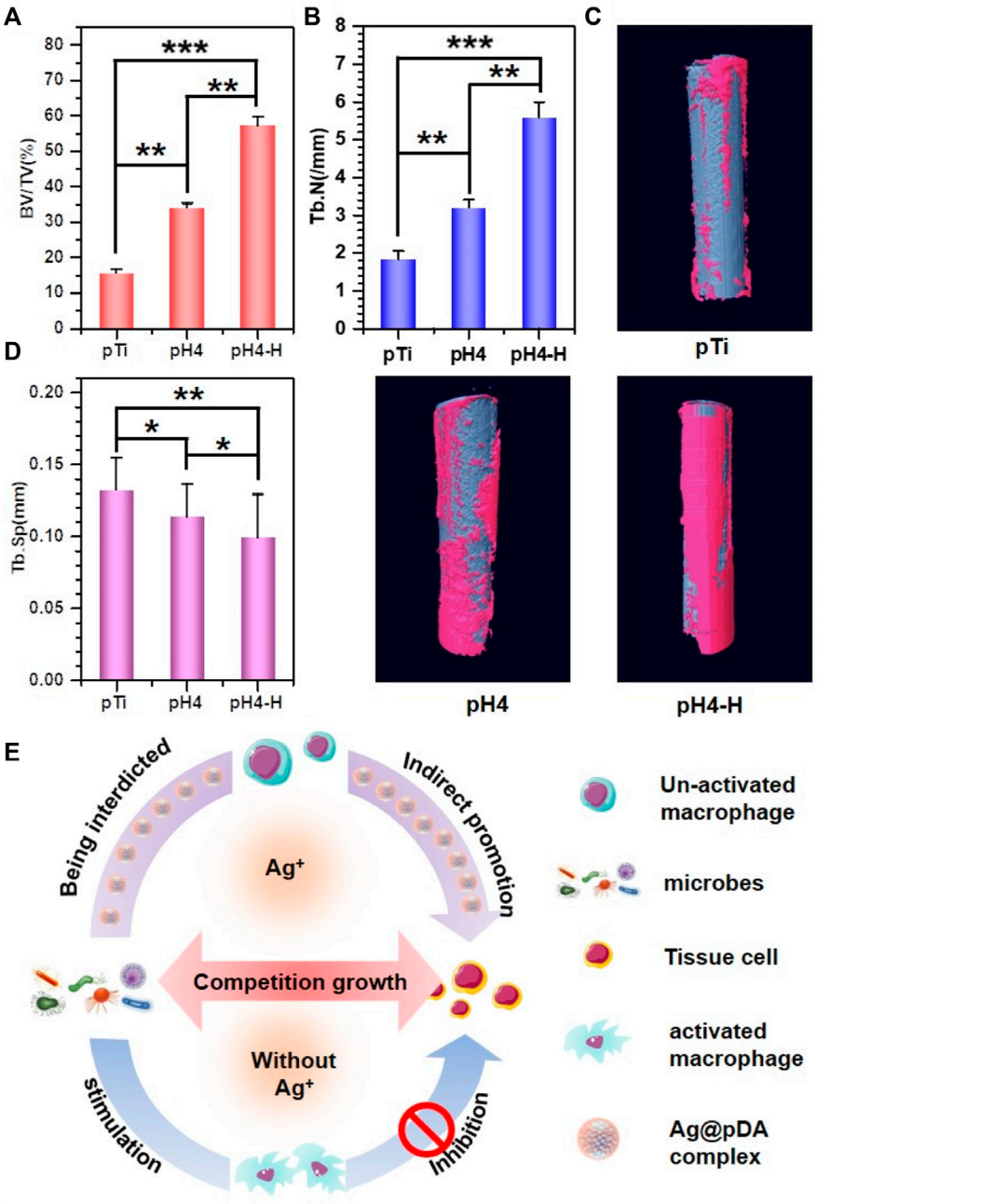

FIGURE 8
3D micro-CT modeling of various samples: **(A–C)** Quantitative evaluation of new bone surrounding the implants on the basis of the percentage of bone volume to tissue volume (BV/TV) **(A)**, Tb.N **(B)** and Tb.SP **(C)** value. **(D)** 3D micro-CT reconstructed images; **(E)** schematic illustration of induced-osteogenesis hypothesis. Data were expressed as the mean ± SD, $n = 3$. Statistically significant differences are indicated by $^{*}p < 0.05$, $^{**}p < 0.01$ or $^{***}p < 0.001$.

osteogenic capability due to the excellent release manner, the high antibacterial ability and appropriate cytocompatibility. The heat treatment improved the oxidative crosslinking of dopamine, thus enhancing the stability of the pDA@NP complex. The residual dopamine and Ag^{+} after simple washing could maintain the pDA@NP content at a high level, and pH plays a key role in determining the Ag enwrapping manner, which ultimately realize the balance of antibacterial and cytotoxicity.

Conclusion

A pDA@NP complex was successfully prepared on porous Ti by a redox reaction of silver with dopamine under acidic conditions. Acidic conditions and heat treatment are two key factors to ensure enough Ag content and proper release manner which endow the surface with antibacterial properties and excellent cell compatibility. Surface morphology, XPS and ICP-MS synthetically proved that pDA coatings were formed around AgNPs and different enwrapping behavior was exhibited. Two kinds of bacteria: *S. aureus* and *Aa* were used to detect the bacterial properties, and two kinds of cell, MC 3T3-E1 and MC 3T3 fibroblasts, were chosen to investigate their cell compatibility. Both the *in vitro* and *in vivo* experiments demonstrate that the pDA@Ag complex formed at pH 4 and 150°C showed the strongest antibacterial property and appropriate cytotoxicity. Microbe-related infection models were build and the tissue response in bacterial-exposed environment proved that pH4-H could prevent the microbe-related inflammation, thus promoting the tissue repair indirectly.

Data availability statement

The original contributions presented in the study are included in the article/Supplementary Material, further inquiries can be directed to the corresponding authors.

Ethics statement

The animal study was reviewed and approved by Animal Center of Anhui Medical University. Written informed consent was obtained from the owners for the participation of their animals in this study.

Author contributions

ZW, KL, and SW contributed equally to this work. Conceptualization: ZW. Methodology: ZW and SW. Experimentation: ZW, KL, and SW. Writing—Original Draft: ZW. Writing—Review and Editing: ZW, KL, SW, LW, LX, YW, ZC, and WL. Supervision Resources: JC, XL, and HQ. Project Administration: JC and XL. Funding Acquisition: JC, XL, SW, and WL.

Funding

This work was supported by the National Natural Science Foundation of China (No 32000932 and 31670967), the Key Research and Development Projects in Anhui Province (No. 202104j07020039), and research improvement program in Stomatologic Hospital and College of Anhui Medical University (No 2020kqkyT01 and 2020kqsy09). 2021 Disciplinary Construction Project in School of Dentistry, Anhui Medical University (No. 2021kqxkFY13). Key Project of Natural Science Research of the Anhui Provincial Department of Education (No. KJ 2021A0270). The authors thank the Center for Scientific Research of Anhui Medical University for valuable help in our experiment.

Conflict of interest

The authors declare that the research was conducted in the absence of any commercial or financial relationships that could be construed as a potential conflict of interest.

Publisher's note

Supplementary material

The Supplementary Material for this article can be found online at: https://www.frontiersin.org/articles/10.3389/fbioe.2022.1056419/full#supplementary-material

References

Akter, M., Sikder, M. T., Rahman, M. M., Ullah, A. A., Hossain, K. F. B., Banik, S., et al. (2018). A systematic review on silver nanoparticles-induced cytotoxicity: Physicochemical properties and perspectives. *J. Adv. Res.* 9, 1–16. doi:10.1016/j.jare.2017.10.008

Alarcon, E. I., Udekwu, K., Skog, M., Pacioni, N. L., Stamplecoskie, K. G., González-Béjar, M., et al. (2012). The biocompatibility and antibacterial properties of collagen-stabilized, photochemically prepared silver nanoparticles. *Biomaterials* 33, 4947–4956. doi:10.1016/j.biomaterials.2012.03.033

Assenza, B., Tripodi, D., Scarano, A., Perrotti, V., Piattelli, A., Iezzi, G., et al. (2012). Bacterial leakage in implants with different implant–abutment connections: An *in vitro* study. *J. Periodontol.* 83, 491–497. doi:10.1902/jop.2011.110320

Ball, V., Gracio, J., Vila, M., Singh, M. K., Metz-Boutigue, M. H. L. N., Michel, M., et al. (2013). Comparison of synthetic dopamine–eumelanin formed in the presence of oxygen and Cu2+ cations as oxidants. *Langmuir* 29, 12754–12761. doi:10.1021/la4029782

Bernsmann, F., Ball, V., Addiego, F., Ponche, A., Michel, M., Gracio, J. J. D. A., et al. (2011). Dopamine– melanin film deposition depends on the used oxidant and buffer solution. *Langmuir* 27, 2819–2825. doi:10.1021/la104981s

Bouxsein, M. L., Boyd, S. K., Christiansen, B. A., Guldberg, R. E., Jepsen, K. J., and Müller, R. (2010). Guidelines for assessment of bone microstructure in rodents using micro–computed tomography. *J. Bone Min. Res.* 25, 1468–1486. doi:10.1002/jbmr.141

Chakraborty, I., Feliu, N., Roy, S., Dawson, K., and Parak, W. J. (2018). Protein-mediated shape control of silver nanoparticles. *Bioconjugate Chem.* 29, 1261–1265. doi:10.1021/acs.bioconjchem.8b00034

Chattopadhyay, I., Verma, M., and Panda, M. (2019). Role of oral microbiome signatures in diagnosis and prognosis of oral cancer. *Technol. Cancer Res. Treat.* 18, 153303381986735. doi:10.1177/1533033819867354

Chen, J., Mei, M. L., Li, Q. L., and Chu, C. H. (2016). Mussel-inspired silver-nanoparticle coating on porous titanium surfaces to promote mineralization. *RSC Adv.* 6, 104025–104035. doi:10.1039/c6ra20673e

Ejima, H., Richardson, J. J., and Caruso, F. (2017). Metal-phenolic networks as a versatile platform to engineer nanomaterials and biointerfaces. *Nano Today* 12, 136–148. doi:10.1016/j.nantod.2016.12.012

Elliott, D. T., Wiggins, R. J., and Dua, R. (2021). Bioinspired antibacterial surface for orthopedic and dental implants. *J. Biomed. Mat. Res.* 109, 973–981. doi:10.1002/jbm.b.34762

Fahmy, H. M., Mosleh, A. M., Abd Elghany, A., Shams-Eldin, E., Serea, E. S. A., Ali, S. A., et al. (2019). Coated silver nanoparticles: Synthesis, cytotoxicity, and optical properties. *RSC Adv.* 9, 20118–20136. doi:10.1039/c9ra02907a

Feng, J. J., Zhang, P. P., Wang, A. J., Liao, Q. C., Xi, J. L., and Chen, J. R. (2012). One-step synthesis of monodisperse polydopamine-coated silver core–shell nanostructures for enhanced photocatalysis. *New J. Chem.* 36, 148–154. doi:10.1039/c1nj20850k

Fernández, I. C. S., Busscher, H. J., Metzger, S. W., Grainger, D. W., and Van Der Mei, H. C. (2011). Competitive time-and density-dependent adhesion of staphylococci and osteoblasts on crosslinked poly (ethylene glycol)-based polymer coatings in co-culture flow chambers. *Biomaterials* 32, 979–984. doi:10.1016/j.biomaterials.2010.10.011

Fernando, I., and Zhou, Y. (2019). Impact of pH on the stability, dissolution and aggregation kinetics of silver nanoparticles. *Chemosphere* 216, 297–305. doi:10.1016/j.chemosphere.2018.10.122

Fürst, M. M., Salvi, G. E., Lang, N. P., and Persson, G. R. (2007). Bacterial colonization immediately after installation on oral titanium implants. *Clin. Oral Implants Res.* 18, 501–508. doi:10.1111/j.1600-0501.2007.01381.x

Ghilini, F., Fagali, N., Pissinis, D. E., Benítez, G., and Schilardi, P. L. (2021). Multifunctional titanium surfaces for orthopedic implants: Antimicrobial activity and enhanced osseointegration. *ACS Appl. Bio Mat.* 4, 6451–6461. doi:10.1021/acsabm.1c00613

Guo, T., Gulati, K., Arora, H., Han, P., Fournier, B., and Ivanovski, S. (2021). Orchestrating soft tissue integration at the transmucosal region of titanium implants. *Acta Biomater.* 124, 33–49. doi:10.1016/j.actbio.2021.01.001

Guo, X., Li, Y., Yan, J., Ingle, T., Jones, M. Y., Mei, N., et al. (2016). Size-and coating-dependent cytotoxicity and genotoxicity of silver nanoparticles evaluated using *in vitro* standard assays. *Nanotoxicology* 10, 1373–1384. doi:10.1080/17435390.2016.1214764

Gutierrez, L., Aubry, C., Cornejo, M., and Croue, J. P. (2015). Citrate-coated silver nanoparticles interactions with effluent organic matter: Influence of capping agent and solution conditions. *Langmuir* 31, 8865–8872. doi:10.1021/acs.langmuir.5b02067

Guy, O. J., and Walker, K. A. D. (2016). Graphene functionalization for biosensor applications. *Silicon Carbide Biotechnology (Second Edition)*, 85–141. doi:10.1016/b978-0-12-802993-0.00004-6

Hasan, R., Schaner, K., Mulinti, P., and Brooks, A. (2021). A bioglass-based antibiotic (vancomycin) releasing bone void filling putty to treat osteomyelitis and aid bone healing. *Int. J. Mol. Sci.* 22, 7736. doi:10.3390/ijms22147736

Hong, S., Lee, J. S., Ryu, J., Lee, S. H., Lee, D. Y., Kim, D. P., et al. (2011). Bio-inspired strategy for on-surface synthesis of silver nanoparticles for metal/organic hybrid nanomaterials and LDI-MS substrates. *Nanotechnology* 22, 494020. doi:10.1088/0957-4484/22/49/494020

Islam, M. S., Akter, N., Rahman, M. M., Shi, C., Islam, M. T., Zeng, H., et al. (2018). Mussel-inspired immobilization of silver nanoparticles toward antimicrobial cellulose paper. *ACS Sustain. Chem. Eng.* 6, 9178–9188. doi:10.1021/acssuschemeng.8b01523

Jo, Y. K., Seo, J. H., Choi, B-H., Kim, B. J., Shin, H. H., Hwang, B. H., et al. (2014). Surface-independent antibacterial coating using silver nanoparticle-generating engineered mussel glue. *ACS Appl. Mat. Interfaces* 6, 20242–20253. doi:10.1021/am505784k

Kitagawa, I. L., Miyazaki, C. M., Pitol-Palin, L., Okamoto, R., De Vasconcellos, L. M., Constantino, C. J., et al. (2021). Titanium-based alloy surface modification with TiO2 and poly (sodium 4-styrenesulfonate) multilayers for dental implants. *ACS Appl. Bio Mat.* 4, 3055–3066. doi:10.1021/acsabm.0c01348

Kyrychenko, A., Korsun, O. M., Gubin, I. I., Kovalenko, S. M., and Kalugin, O. N. (2015). Atomistic simulations of coating of silver nanoparticles with poly (vinylpyrrolidone) oligomers: Effect of oligomer chain length. *J. Phys. Chem. C* 119, 7888–7899. doi:10.1021/jp510369a

Lee, H., Dellatore, S. M., Miller, W. M., and Messersmith, P. B. (2007). Mussel-inspired surface chemistry for multifunctional coatings. *Science* 318, 426–430. doi:10.1126/science.1147241

Li, M., Liu, Q., Jia, Z., Xu, X., Shi, Y., Cheng, Y., et al. (2015). Polydopamine-induced nanocomposite Ag/CaP coatings on the surface of titania nanotubes for antibacterial and osteointegration functions. *J. Mat. Chem. B* 3, 8796–8805. doi:10.1039/c5tb01597a

Liebscher, J. R., MróWczyńSki, R., Scheidt, H. A., Filip, C., HăDade, N. D., Turcu, R., et al. (2013). Structure of polydopamine: A never-ending story? *Langmuir* 29, 10539–10548. doi:10.1021/la4020288

Liu, Y., Ai, K., and Lu, L. (2014). Polydopamine and its derivative materials: Synthesis and promising applications in energy, environmental, and biomedical fields. *Chem. Rev.* 114, 5057–5115. doi:10.1021/cr400407a

Liu, Y., Xie, D., Zhou, R., and Zhang, Y. (2021). 3D X-ray micro-computed tomography imaging for the microarchitecture evaluation of porous metallic implants and scaffolds. *Micron* 142, 102994. doi:10.1016/j.micron.2020.102994

Luo, R., Tang, L., Zhong, S., Yang, Z., Wang, J., Weng, Y., et al. (2013). *In vitro* investigation of enhanced hemocompatibility and endothelial cell proliferation associated with quinone-rich polydopamine coating. *ACS Appl. Mat. Interfaces* 5, 1704–1714. doi:10.1021/am3027635

Maitland, T., and Sitzman, S. (2007). "Electron backscatter diffraction (EBSD) technique and materials characterization examples," in *Scanning microscopy for nanotechnology: Techniques and applications* (New York, NY: Springer Science & Business Media, LLC), 41–75.

Marciniak, L., Nowak, M., Trojanowska, A., Tylkowski, B., and Jastrzab, R. (2020). The effect of pH on the size of silver nanoparticles obtained in the reduction reaction with citric and malic acids. *Materials* 13, 5444. doi:10.3390/ma13235444

Masamoto, K., Fujibayashi, S., Yamaguchi, S., Otsuki, B., Okuzu, Y., Kawata, T., et al. (2021). Bioactivity and antibacterial activity of strontium and silver ion releasing titanium. *J. Biomed. Mat. Res.* 109, 238–245. doi:10.1002/jbm.b.34695

Nguyen, K. C., Seligy, V. L., Massarsky, A., Moon, T. W., Rippstein, P., Tan, J., et al. (2013). Comparison of toxicity of uncoated and coated silver nanoparticles. *J. Phys. Conf. Ser.* 429, 012025. doi:10.1088/1742-6596/429/1/012025

Nie, C., Cheng, C., Peng, Z., Ma, L., He, C., Xia, Y., et al. (2016). Mussel-inspired coatings on Ag nanoparticle-conjugated carbon nanotubes: Bactericidal activity and mammal cell toxicity. *J. Mat. Chem. B* 4, 2749–2756. doi:10.1039/c6tb00470a

Padhi, S., and Behera, A. (2022). *Agri-waste and microbes for production of sustainable nanomaterials*. Amsterdam: Elsevier, 397–440.

Prencipe, F., Zanfardino, A., Di Napoli, M., Rossi, F., D'errico, S., Piccialli, G., et al. (2021). Silver (I) n-heterocyclic carbene complexes: A winning and broad spectrum of antimicrobial properties. *Int. J. Mol. Sci.* 22, 2497. doi:10.3390/ijms22052497

Proks, V., Brus, J., Pop-Georgievski, O., Večerníková, E., Wisniewski, W., Kotek, J., et al. (2013). Thermal-induced transformation of polydopamine structures: An efficient route for the stabilization of the polydopamine surfaces. *Macromol. Chem. Phys.* 214, 499–507. doi:10.1002/macp.201200505

Pryshchepa, O., Pomastowski, P., and Buszewski, B. (2020). Silver nanoparticles: Synthesis, investigation techniques, and properties. *Adv. Colloid Interface Sci.* 284, 102246. doi:10.1016/j.cis.2020.102246

Ribeiro, M., Monteiro, F. J., and Ferraz, M. P. (2012). Infection of orthopedic implants with emphasis on bacterial adhesion process and techniques used in studying bacterial-material interactions. *Biomatter* 2, 176–194. doi:10.4161/biom.22905

Saiz-Poseu, J., Mancebo-Aracil, J., Nador, F., Busqué, F., and Ruiz-Molina, D. (2019). The chemistry behind catechol-based adhesion. *Angew. Chem. Int. Ed.* 58, 696–714. doi:10.1002/anie.201801063

Sherwood, E. R., and Toliver-Kinsky, T. (2004). Mechanisms of the inflammatory response. *Best Pract. Res. Clin. Anaesthesiol.* 18, 385–405. doi:10.1016/j.bpa.2003.12.002

Shimazaki, T., Miyamoto, H., Ando, Y., Noda, I., Yonekura, Y., Kawano, S., et al. (2010). *In vivo* antibacterial and silver-releasing properties of novel thermal sprayed silver-containing hydroxyapatite coating. *J. Biomed. Mat. Res. B Appl. Biomater.* 92, 386–389. doi:10.1002/jbm.b.31526

Trindade, R., Albrektsson, T., Tengvall, P., and Wennerberg, A. (2016). Foreign body reaction to biomaterials: On mechanisms for buildup and breakdown of osseointegration. *Clin. Implant Dent. Relat. Res.* 18, 192–203. doi:10.1111/cid.12274

Vatrál, J., Boča, R., and Linert, W. (2015). Oxidation properties of dopamine at and near physiological conditions. *Monatsh. Chem.* 146, 1799–1805. doi:10.1007/s00706-015-1560-2

Wang, J., Li, J., Guo, G., Wang, Q., Tang, J., Zhao, Y., et al. (2016). Silver-nanoparticles-modified biomaterial surface resistant to staphylococcus: New insight into the antimicrobial action of silver. *Sci. Rep.* 6, 32699–32716. doi:10.1038/srep32699

Wang, X., Ji, Z., Chang, C. H., Zhang, H., Wang, M., Liao, Y. P., et al. (2014). Use of coated silver nanoparticles to understand the relationship of particle dissolution and bioavailability to cell and lung toxicological potential. *Small* 10, 385–398. doi:10.1002/smll.201301597

Wang, X., Ning, B., and Pei, X. (2021a). Tantalum and its derivatives in orthopedic and dental implants: Osteogenesis and antibacterial properties. *Colloids Surfaces B Biointerfaces* 208, 112055. doi:10.1016/j.colsurfb.2021.112055

Wang, X., Xu, K., Cui, W., Yang, X., Maitz, M. F., Li, W., et al. (2021b). Controlled synthesis of mussel-inspired Ag nanoparticle coatings with demonstrated *in vitro* and *in vivo* antibacterial properties. *Mater. Des.* 208, 109944. doi:10.1016/j.matdes.2021.109944

Wang, Z., Yang, H-C., He, F., Peng, S., Li, Y., Shao, L., et al. (2019). Mussel-inspired surface engineering for water-remediation materials. *Matter* 1, 115–155. doi:10.1016/j.matt.2019.05.002

Wang, Z., Zou, Y., Li, Y., and Cheng, Y. (2020). Polydopamine nanomaterials: Metal-containing polydopamine nanomaterials: Catalysis, energy, and theranostics (small 18/2020). *Small* 16, 2070102. doi:10.1002/smll.202070102

Wu, P., Chen, D., Yang, H., Lai, C., Xuan, C., Chen, Y., et al. (2021). Antibacterial peptide-modified collagen nanosheet for infected wound repair. *Smart Mater. Med.* 2, 172–181. doi:10.1016/j.smaim.2021.06.002

Yang, D. H., Moon, S. W., and Lee, D. W. (2017). Surface modification of titanium with BMP-2/GDF-5 by a heparin linker and its efficacy as a dental implant. *Int. J. Mol. Sci.* 18, 229. doi:10.3390/ijms18010229

Yang, J., Chen, Y., Zhao, L., Feng, Z., Peng, K., Wei, A., et al. (2020). Preparation of a chitosan/carboxymethyl chitosan/AgNPs polyelectrolyte composite physical hydrogel with self-healing ability, antibacterial properties, and good biosafety simultaneously, and its application as a wound dressing. *Compos. Part B Eng.* 197, 108139. doi:10.1016/j.compositesb.2020.108139

Yaqoob, A. A., Umar, K., and Ibrahim, M. N. M. (2020). Silver nanoparticles: Various methods of synthesis, size affecting factors and their potential applications–a review. *Appl. Nanosci.* 10, 1369–1378. doi:10.1007/s13204-020-01318-w

Zhang, H., Xie, L., Deng, J., Zhuang, W., Luo, R., Wang, J., et al. (2016a). Stability research on polydopamine and immobilized albumin on 316L stainless steel. *Regen. Biomater.* 3, 277–284. doi:10.1093/rb/rbw030

Zhang, X. F., Liu, Z. G., Shen, W., and Gurunathan, S. (2016b). Silver nanoparticles: Synthesis, characterization, properties, applications, and therapeutic approaches. *Int. J. Mol. Sci.* 17, 1534. doi:10.3390/ijms17091534

Zheng, W., Fan, H., Wang, L., and Jin, Z. (2015). Oxidative self-polymerization of dopamine in an acidic environment. *Langmuir* 31, 11671–11677. doi:10.1021/acs.langmuir.5b02757

frontiers | Frontiers in Bioengineering and Biotechnology

TYPE Original Research
PUBLISHED 05 December 2022
DOI 10.3389/fbioe.2022.1052535

OPEN ACCESS

EDITED BY
Qihui Zhou,
Qingdao University, China

REVIEWED BY
Anamika Prasad,
Florida International University,
United States

*CORRESPONDENCE
Quan Zhu,
zhuquan@njmu.edu.cn

†These authors have contributed equally to this work and share first authorship

SPECIALTY SECTION
This article was submitted to Biomaterials,
a section of the journal
Frontiers in Bioengineering and Biotechnology

RECEIVED 24 September 2022
ACCEPTED 22 November 2022
PUBLISHED 05 December 2022

CITATION
Yang H, Dong Z, Wang H, Liu Z, Sun W, Wang K, Xu X, Wen W, Wang J, Chen L and Zhu Q (2022), Efficacy of oxidized regenerated cellulose combined with fibrin glue in reducing pulmonary air leakage after segmentectomy in a porcine lung model.
Front. Bioeng. Biotechnol. 10:1052535.
doi: 10.3389/fbioe.2022.1052535

Efficacy of oxidized regenerated cellulose combined with fibrin glue in reducing pulmonary air leakage after segmentectomy in a porcine lung model

He Yang[1†], Zhiqiang Dong[2†], Hongya Wang[1†], Zicheng Liu[3], Wenbo Sun[1], Kun Wang[1], Xinfeng Xu[1], Wei Wen[1], Jun Wang[1], Liang Chen[1] and Quan Zhu[1*]

[1]Department of Thoracic Surgery, The First Affiliated Hospital of Nanjing Medical University, Nanjing, China, [2]Department of Cardiovascular Surgery, The First Affiliated Hospital of Nanjing Medical University, Nanjing, China, [3]Department of Thoracic Surgery, Nanjing Chest Hospital, Nanjing, China

Objectives: Pulmonary air leakage is a common complication following lung resection. We have designed a new method combining oxidized regenerated cellulose and fibrin glue to cover the intersegmental plane in clinical lung segmentectomy to prevent postoperative air leakage. In this study, an excised porcine lung segmentectomy model was created to validate its adhesive strength and effect on reducing air leakage.

Methods: In the pre-experiment, six different larger lung segments were separated using electrocautery on the fresh isolated porcine lungs (n = 5 in each group). The air leakage degree and operation time of the lung segments were comprehensively evaluated to select the most suitable target segment for establishing the *ex vivo* porcine lung segmentectomy models. In the experiment, according to the different materials covered on the intersegmental plane, these models were randomly divided into four groups: group A used fibrin glue and oxidized regenerated cellulose (ORC) mesh (n = 20); group B used fibrin glue and polyglycolic acid (PGA) sheet (n = 20); group C used fibrin glue (n = 20); group D was the blank control group (n = 20). The minimum air leakage pressure (MALP) of the selected target segment in each group was measured using a stepwise increase of airway pressure, and histological assessment was performed on the sealed area samples from the four groups.

Results: The operation time of the a segment of the right cranial lobe (R1a) was shorter than that of other segments ($p < 0.05$), and there was no significant difference in the air leakage pressures between the six isolated segments (p = 0.76); thus, R1a was chosen for segmentectomy. In addition, the MALP was

Abbreviations: Polyglycolic acid, (PGA); oxidized regenerated cellulose, (ORC); minimum air leakage pressure, (MALP); a and b segments of the right cranial lobe, (R1a, R1b); a and b segments of the left cranial lobe, (L1a, L1b); a and b segments of the left caudal lobe, (L2a, L2b).

significantly higher in group A (41.8 ± 4.5 cmH_2O) than in groups C (28.1 ± 2.3 cmH_2O) and D (17.3 ± 1.2 cmH_2O) (both $p < 0.001$). The MALP of group B (69.5 ± 5.2 cmH_2O) was significantly higher than that of group A ($p < 0.001$), whereas that of group C was significantly higher than that of group D ($p < 0.001$). Histological examination confirmed that the combined use of fibrin glue and ORC or PGA patch adhered more firmly to the intersegmental plane than that of fibrin glue alone, although some gaps could be seen between the fibrin glue and the surface of the lung segments in group C.

Conclusion: The application of ORC combined with fibrin glue on the intersegmental plane has a good sealing performance in the *ex vivo* porcine lung segmentectomy model, suggesting that ORC may be an effective alternative material to replace PGA sheet to combine with fibrin glue for preventing air leakage after segmentectomy.

KEYWORDS

segmentectomy, pulmonary air leakage, oxidized regenerated cellulose, fibrin glue, polyglycilic acid sheet

Introduction

Recently, precise anatomical segmentectomy is increasingly being used as an important option for treating early non-small cell lung cancer to preserve more effective lung tissue without compromising oncologic outcomes (Leshnower et al., 2010). However, the incidence of pulmonary air leakage after segmentectomy is higher than that for lobectomy (Suzuki et al., 2019) because air leakage occurs easily when using electrocautery, ultrasonic scalpel, or stapler to cut the intersegmental plane (Yazawa et al., 2021; Saito et al., 2017).

Studies have shown that polyglycolic acid (PGA) mesh and fibrin glue can be used to cover the pleura defect, which can effectively reduce postoperative pulmonary air leakage (Gika et al., 2007; Ueda et al., 2007; Kawai et al., 2012; Matoba et al., 2018; Tanaka et al., 2018). However, most animal experiments have only focused on the peripheral pleural defects caused by artificial damage, such as needle puncture (Matoba et al., 2018; Gika et al., 2007). Furthermore, this method may be applicable to wedge resection and lobectomy even though the intersegmental plane has not been well studied, thus suggesting an inconsistency with clinical segmentectomy. However, the high cost of PGA patches in lung surgery may increase hospital costs (Budak et al., 2020). In addition, several studies have shown that PGA degradation can cause inflammation (Ceonzo et al., 2006; Yang et al., 2005), and severe thoracic adhesion can be caused by the PGA felt (Nakamura et al., 2010; Saito et al., 2017). Therefore, we tried to find a substitute for the PGA mesh and design a new experimental method to investigate the adhesion properties of various materials in segmentectomy.

Oxidized regenerated cellulose (ORC) is a bio-absorbable material obtained by controlled chemical oxidation of cellulose. It is often used in surgical operation because of its low price, strong hemostatic properties, and good biocompatibility (Lewis et al., 2013; Martyn et al., 2015; Khoshmohabat et al., 2019). Moreover, the application of the ORC mesh to the staple line effectively reduces the postoperative recurrence rate after bullectomy (Lee et al., 2006; Cho et al., 2008; Lee et al., 2014). We pioneered the combined use of ORC and fibrin glue in segmentectomy performed at our center, and we observed that the incidence of postoperative pulmonary air leakage was low; however, whether ORC could enhance the adhesive strength of fibrin glue has not been confirmed.

In this study, a porcine lung model was created to test the adhesive quality of the combined application of fibrin glue and ORC in the intersegmental plane. Histological examination was also performed to confirm the adhesive strength and explore whether ORC can replace PGA mesh in segmentectomy.

Materials and methods

Porcine lungs

Isolated bilateral porcine lungs (purchased from Jiangsu Jurong Kangrong Poultry Industry Co., Ltd.) were obtained from healthy domestic 6-month-old pigs weighing (100 ± 25) kg, which were slaughtered on the same day. The lungs were excluded from the experiment when there were bullae, severe congestion, infection, damage, anatomical variation, or other factors that might influence the experimental results. To maintain the physiological state of the lungs and avoid the loss of pulmonary surfactant as much as possible, all experiments were completed within 4 h after the lung was isolated.

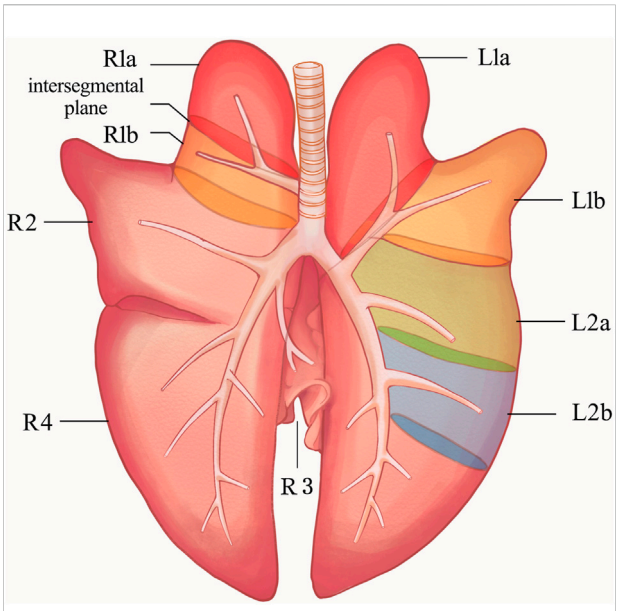

FIGURE 1
Anatomical diagram of porcine lung. L1, left cranial lobe; L2, left caudal lobe; R1, right cranial lobe; R2, right middle lobe; R3, right accessory lobe; R4, right caudal lobe. The ventilation of each lung segment is controlled by its corresponding bronchus. The bronchus of R1 opens directly to the main trachea. The R1a, R1b, L1a, L1b, L2a, and L2b segments were used in the pre-experiments, and finally R1a was selected for the segmentectomy, the intersegmental plane was the location of the sealant application in the experiments. R1a, R1b (a and b segments of the right cranial lobe); L1a, L1b (a and b segments of the left cranial lobe); L2a, L2b (a and b segments of the left caudal lobe).

Tissue sealants

Fibrin glue (Beixiu®, Porcine Fibrin Sealant Kit, Guangzhou, China) is a synthetic absorbable biomaterial comprising main glue and catalyst. The main glue contains fibrinogen and coagulation factor XIII. The catalyst is a solution containing thrombin and $CaCl_2$. When the two solutions are mixed, simulating the last stage of the blood coagulation process, a stable fibrin polymer is formed, which presents a cross-multi-layered and homogeneous mesh structure that can trap erythrocytes and the active ingredients in plasma and provide biological scaffolds for the growth of fibroblasts and capillaries to seal and repair the pleura. Moreover, as a flexible mechanical leakage barrier, it is durable for 14 days, making the tissue of the treatment site expand completely and promoting wound healing. Once the fibrin glue is applied, it will be degraded by hydrolysis, releasing biocompatible ingredients which are metabolized or removed by the kidneys.

ORC (Ethicon Surgicel® absorbable hemostat mesh, Johnson & Johnson, NJ, United States), which can be trimmed to any shape, makes full contact with human tissue easily because of its fabric-like property. Furthermore, being a cellulose derivative, it has good biocompatibility, biodegradability, and low toxicity. Its hemostatic function involves coagulating the wound's blood on mesh gauze through physical action, promoting platelet rupture, producing many platelet coagulation factors, and converting fibrinogen to fibrin to form a thrombus. At the same time, the hydroxyl group in cellulose forms acid-hematin with Fe^{2+} in plasma, a black gel-like substance that aids hemostasis (Wu et al., 2012). Moreover, Surgicel® is almost completely absorbed by the human body in 7 days, without causing adverse reactions to the surrounding tissues.

Absorbable PGA patch (Neville®, Gunze Ltd., Kyoto, Japan) is made of a loose and highly elastic PGA sheet with a fiber diameter of 16.1 nm, an average distance of 27.4 nm between fibers, and an average thickness of 0.15 mm. Neville® has two variants—the tubular type and the flake type. The flake type was used in this study. The human body completely absorbs the sheet in approximately 15 weeks.

Surgical procedure

To determine the suitable lung segment for this experiment, we performed a pre-experiment on six large porcine lung segments to compare the surgical separation time, and the respective air leakage pressures were evaluated. As shown in Figure 1, the ventilation of each lung segment is controlled by its corresponding bronchus. Therefore, the a and b segments of the right cranial lobe (R1a, R1b), the a and b segments of the left cranial lobe (L1a, L1b), and the a and b segments of the left caudal lobe (L2a, L2b) were used in the pre-experiments.

After sputum aspiration in the bronchus, a 12-Fr cuffed endotracheal tube attached to the mechanical ventilator (Aestiva/5 7,100, Datex-Ohmeda, Madison, WI, United States) was inserted into the six segmental bronchi sequentially and the cuff was inflated to ensure air tightness. Subsequently, the lungs were sunk into a tank of saline solution kept at a temperature of 37°C, and the target segment was slowly inflated in water by the ventilator. A micromanometer (BENETECH, Jumaoyuan Technology Co., Ltd., Shenzhen, China, GM520, ±35 kPa, ±0.3%) was used to measure the air leak pressure (Figure 2). To avoid alveolar structural damage caused by overinflation, the inflation pressure was controlled to less than 20 cmH_2O. The lung was abandoned if the target lung was difficult to expand or leak. Using this stepwise increase of airway pressure method, we observed that the target lung was obviously expanded, with a stable intersegmental interface between it and the uninflated lung tissue of the adjacent segment, and the boundary line was marked (Figures 3A,B).

When separating the intersegmental interface, an electric cautery was used as the energy device in the coagulation mode at a power of 40 W (POWER-420B, Changzhou Yanling Electronic equipment Co., Ltd., Changzhou, China) (Figure 3C). During the separation process, the intersegmental interface was carefully identified to avoid misoperation, and the lung was discarded in case of wrong segmentation. Then, sharp instruments such as

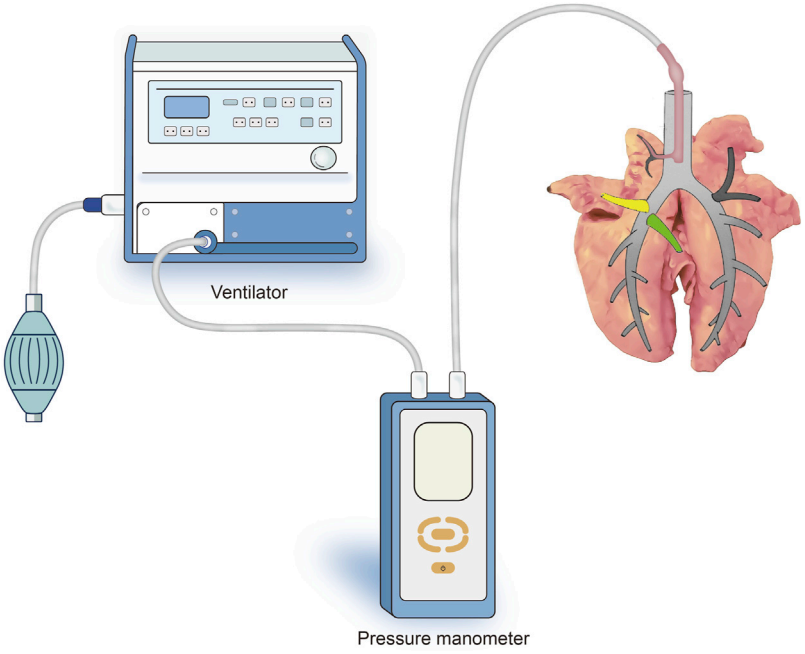

FIGURE 2
Schematic representation of the experimental setup for ventilating the target segment and measuring the pressure in the airway. The 12-Fr cuffed endotracheal tube attached to the mechanical ventilator was inserted into the six segmental bronchi sequentially to ventilate the target segment and the cuff was inflated to ensure air tightness (At this point, the endotracheal tube was inserted into the R1a bronchus).

scalpel were used to cut off the hilar connective tissue and blood vessels, and the target bronchus was finally cut off to complete the segmentectomy. The operation time for the surgical separation of the six lung segments was recorded.

Measurement of the pulmonary air leak pressure

The micromanometer and ventilator were connected to the target lung segments by the soft catheter. Then the segments were immersed in a physiologic saline tank maintained at 37°C and airway pressure of 10 cmH_2O. The ventilation started with 10 cmH_2O, and stepwise increments of 5 cmH_2O per minute were applied up to 70 cmH_2O, which is the maximum pressure of the ventilator. The ventilator settings were as follows: pressure control ventilation, (respiratory frequency 12; inspiration-to-expiration ratio = 1:2; positive end-expiratory pressure 0). The intratracheal pressure was measured using a manometer attached to the ventilator through a tracheal tube. The minimum air leakage pressure (MALP) was defined as the pressure at the emersion of the bubble flow from the intersegmental plane under water. If the sealants persisted to the maximum pressure setting of the ventilator, an additional pressure of 70 cmH_2O was applied manually using a ventilation bag at the speed of 2 cmH_2O/min until air leakage occurred. Two experimenters independently observed and recorded the MALP. The values were retested and read if the date deviation was more than 1 cmH_2O. However, the lung segment was abandoned if the deviation was more than 1 cmH_2O again. The average values of the dates recorded by the two experimenters were taken as the final results.

The operation time and MALP of the six lung segments were comprehensively evaluated to select the most suitable target segment for establishing the *ex vivo* porcine lung segmentectomy model.

Randomized grouping

To avoid selection bias, porcine segmentectomy models were randomly divided into four groups. Group A: 0.25 ml of the liquid main glue was sprayed at the intersegmental plane, then the ORC sheet (5.1 × 10.2 cm^2, thickness of 2 mm) was placed over the interface after cutting off the extra parts of the periphery, and 0.25 ml of the liquid catalyst solution was sprayed on the sheet, followed by 0.25 ml of the liquid main glue and 0.25 ml of the liquid catalyst (n = 20) (Figure 3D). Group B: 0.25 ml of the liquid main glue was sprayed at the intersegmental plane, and then the PGA sheet (100 × 50, 0.15 mm in thickness) was covered on the interface. The peripheral excess was cut off, and 0.25 ml of

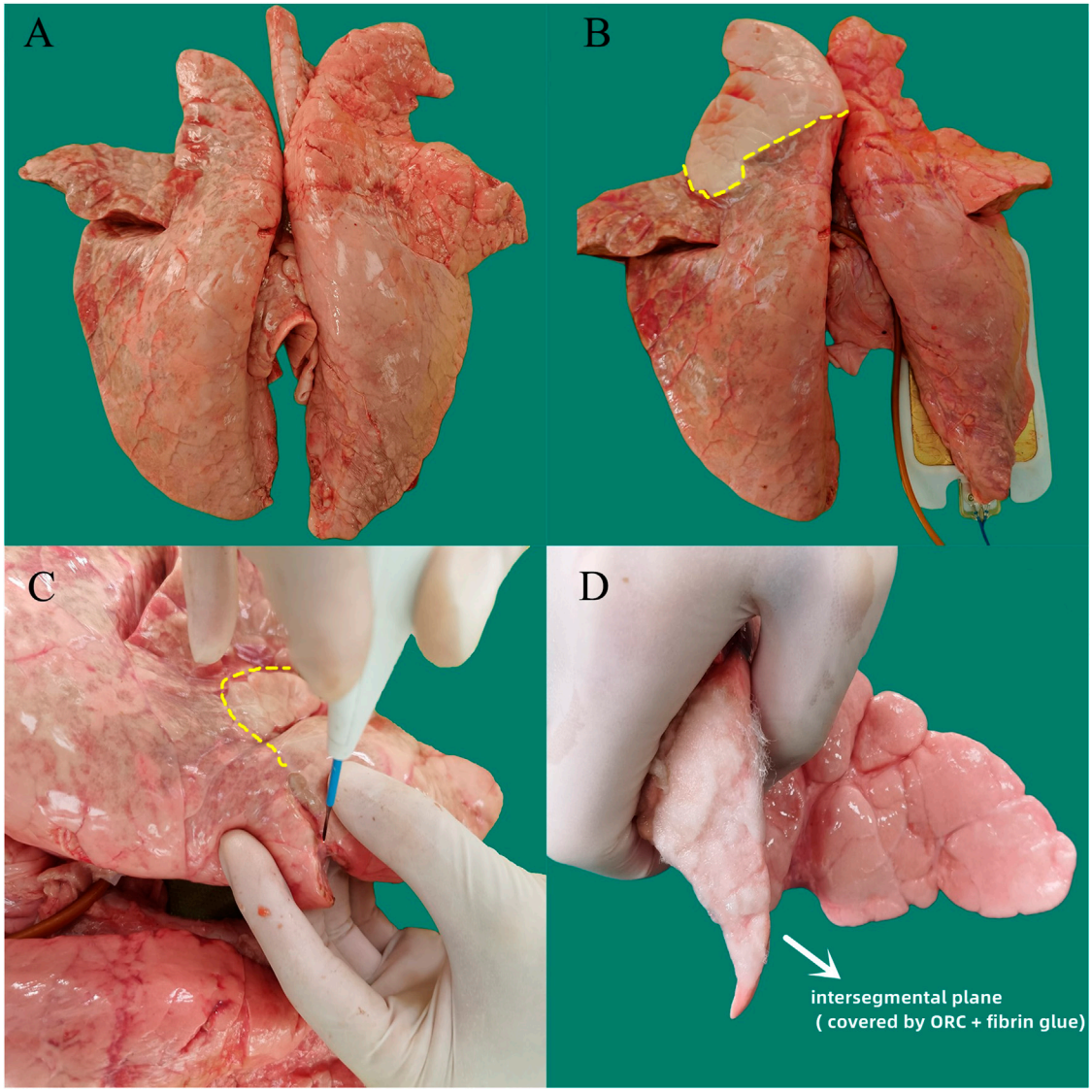

FIGURE 3
Experimental procedure for separating the target segment and covering the intersegmental plane with sealing materials in the *ex vivo* porcine lung segmentectomy model. **(A)** Normal isolated bilateral porcine lungs. **(B)** The target segment was obviously inflated by the ventilation, with a stable intersegmental interface (yellow dotted line) between it and the surrounding uninflated lung tissue of the adjacent lung segfment. **(C)** An electric cautery was used as the energy device to separate the intersegmental plane (yellow dotted line), and scalpel was used to cut off the hilar connective tissue and blood vessels. **(D)** ORC sheet and fibrin glue were conbined using the method of group A (ORC + fibrin glue) to seal the intersegmental plane. ORC (oxidized regenerated cellulose).

the liquid catalyst solution was sprayed on the sheet, followed by 0.25 ml of liquid main glue and 0.25 ml of the liquid catalyst (n = 20). Group C: 0.5 ml of the liquid main glue was sprayed on the intersegmental interface, followed by 0.5 ml of the liquid catalyst (n = 20). Group D did not receive any intervention at the intersegmental plane (n = 20). The pack method we used to apply the sealing materials in groups A and B was shown in Figure 4. The lung segmentectomy models in each group were allowed to stand for 5 min to fix the sealing materials, and their MALPs were measured using the method mentioned above, similar to the measurement of the pulmonary air leak pressure.

Histological assessment

The pulmonary segmentectomy models of groups A, B, C, and D were obtained in the same preparation manner as that for the pressure resistance test, then the lung tissue in the center of

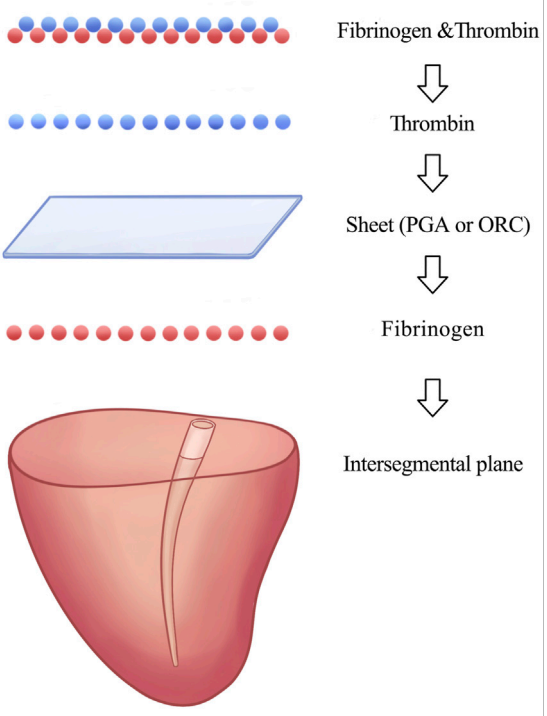

FIGURE 4
Sealing material application procedures of pack method in experimental groups **(A)** and **(B)**.

the intersegmental plane covered with the sealing materials was resected for histologic assessment (1 × 1 cm). The specimens were fixed in 10% formalin, embedded in paraffin, and sectioned for hematoxylin-eosin staining. We examined at least five different sites in each specimen.

Statistical analysis

SPSS version 24.0 (SPSS Inc., Chicago, IL, United States) software package was used for all statistical analyses. All data are expressed as the mean ± standard deviation. One-way analysis of variance and Tukey's test were used to compare the data among the groups. Statistical significance was set at $p < 0.05$.

Results

Operation time and pressure resistance in the pre-experiment

The average operation times of the different segmentectomy models were as follows: R1a (880 ± 83) s; R1b (1531 ± 79) s; L1a (1384 ± 75) s; L1b (1207 ± 56) s; L2a (1273 ± 94) s; L2b (1179 ± 108) s. The operation time of R1a was shorter than that of other groups (F = 27.26, $p < 0.05$) (Figure 5A), this may be because the bronchus of R1 opens directly to the main trachea. However, the difference in the MALP between the six models was not statistically significant (F = 0.52, $p = 0.76$) (Figure 5B). The MALPs measured in the lung segment models were as follows: R1a (17.1 ± 1.1) cmH_2O; R1b (17.4 ± 0.7) cmH_2O; L1a (17.0 ± 1.1) cmH_2O; L1b (16.6 ± 1.0) cmH_2O, L2a (17.6 ± 0.7) cmH_2O, and L2b (17.0 ± 0.9) cmH_2O. Due to the short operation time, R1a was chosen for segmentectomy.

Pressure resistance of the porcine lung segmentectomy models

The MALPs of the intersegmental plane in each experimental group were as follows: group A (n = 20): ORC + fibrin glue, 41.8 ± 4.5 cmH_2O; group B (n = 20): PGA + fibrin glue, 69.5 ± 5.2 cmH_2O; group C (n = 20): fibrin glue, 28.1 ± 2.3 cmH_2O; group D (n = 20): control group, 17.3 ± 1.2 cmH_2O (Figure 6). Furthermore, eight cases in group B showed no air leakage with maximum setting ventilator pressure (70.0 cm H_2O). Therefore, additional pressure was manually applied in these cases.

One-way analysis of variance indicated a significant difference in the MALP of the four groups (F = 761.97, $p < 0.001$). Tukey's test showed that the MALP was significantly higher in group A than in groups C and D (both $p < 0.001$), with a significant difference between groups C and D ($p < 0.001$), whereas a significantly higher MALP was obtained for group B compared to the other three groups (both $p < 0.001$).

In the intersegmental plane, the combined application of fibrin glue and the PGA patch had the strongest ability to prevent air leakage, followed by the combination of ORC and fibrin glue group. Fibrin glue could effectively improve the air leakage prevention ability of segmentectomy models, whereas the ORC or PGA sheet could significantly enhance the sealing capacity of fibrin glue.

Histopathological findings of the porcine lung segmentectomy models

In order to verify the adhesion strength microscopically, we performed histological examination on each group of experimental specimens. In the histological specimens of the porcine lung, hematoxylin-eosin staining revealed that the ORC and fibrin glue layer adhered tightly to the surface of the intersegmental plane in group A, while at the junction, cellulose was completely encapsulated by fibrin glue and some gel-like black substance could be seen near the pleural, which were formed by the reaction of the Fe^{2+} group in the hemoglobin with the carboxyl groups in the ORC to produce an acid-hematin complex. This black gel was

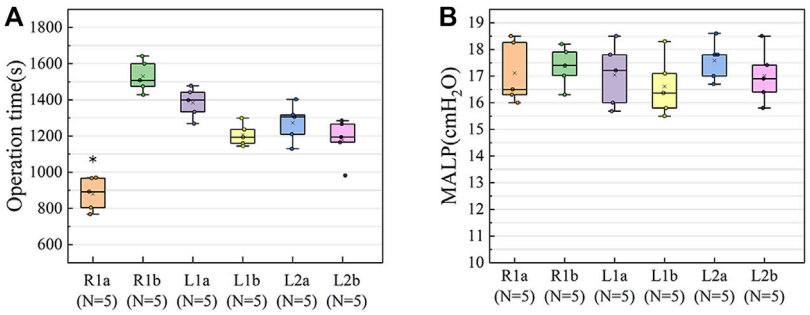

FIGURE 5
Results of the pre-experiments. **(A)** The operation time of R1a was shorter than in the other groups ($F = 27.26$, $p < 0.05$). **(B)** The difference in the MALP between the six groups of models was not statistically significant ($F = 0.519$, $p = 0.76$). The upper and lower borders of the box represent, the upper and lower quartiles. The middle horizontal line represents the median. The cross represents the mean. The whiskers show the minimum and maximum values excluding the outliers. *$p < 0.05$, the operation time of R1a *versus* the other lung segments. R1a, R1b (a and b segments of the right cranial lobe); L1a, L1b (a and b segments of the left cranial lobe); L2a, L2b (a and b segments of the left caudal lobe); MALP (minimum air leakage pressure).

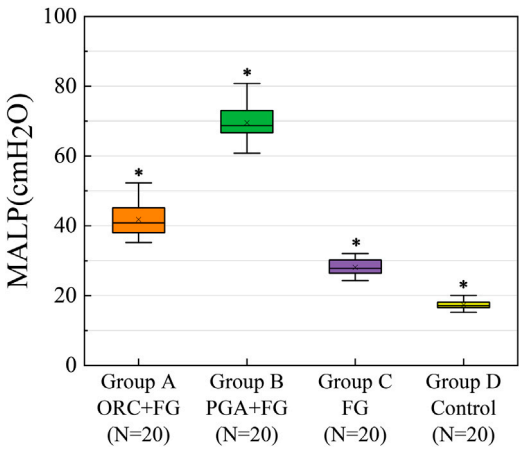

FIGURE 6
The MALP of the intersegmental plane in each experimental group. MALP was significantly higher in the group A, as compared with the group C and group D (both $p < 0.001$) with a significant difference between the latter two groups ($p < 0.001$). A significantly greater MALP was obtained for group B than the other groups (both $p < 0.001$). The upper and lower borders of the box represent, the upper and lower quartiles. The middle horizontal line represents the median. The cross represents the mean. The whiskers show the minimum and maximum values excluding the outliers. *$p < 0.05$, group A *versus* group B *versus* group C *versus* group D. MALP (minimum air leakage pressure), ORC (oxidized regenerated cellulose), PGA (polyglycolic acid), FG (fibrin glue).

tightly embedded in the sealing layer composed of ORC and fibrin glue and accumulated in large amounts in the pleural defect (Figure 7A).

The layer of PGA patch and fibrin glue in group B also adhered firmly to the interface of the lung segment (Figure 7B). However, there were some gaps between the fibrin glue and the surface of the lung segment in group C. The sealing layer did not fit evenly with the surface of the lung tissue, and the thickness of it was not as uniform as that in groups A and B. (Figure 7C). Conversely, in groups A and B specimens, no interspace was found between the lung tissue and the sealant layer. Figure 7D shows the normal intersegmental interface separated by electrocauterization. However, the pleural defect was severe due to the cauterization of the electric cautery.

Discussion

According to the Japanese JCOG0802/WJOG4607L trial project results, segmentectomy provides a significantly better overall survival than lobectomy for patients with stage IA non-small cell lung cancer, suggesting that segmentectomy will become the standard treatment for early lung cancer in the future (Saji et al., 2022). However, air leakage was detected more in the segmentectomy arm than in the lobectomy arm (3.8% vs. 6.5%, $p = 0.04$), especially in patients undergoing complex segmentectomy or long-term smokers (Suzuki et al., 2019). Thus, how to reduce the incidence of air leakage after segmentectomy is an urgent clinical problem to be solved.

Clinically, sutures, staplers, and ligation are often used to close pulmonary air leaks; however, these methods may further reduce lung volume or cause further trauma to lung tissues (Saito et al., 2017) and have an indefinite effect in patients with fragile lung quality such as emphysema (Gika et al., 2007). Previous studies have shown that the combination of PGA and fibrin glue for covering the surgical area in pulmonary surgery can significantly decrease the occurrence of postoperative air leakage (Gika et al., 2007; Ueda et al., 2007; Kawai et al., 2012; Matoba et al., 2018; Tanaka et al., 2018); however, PGA

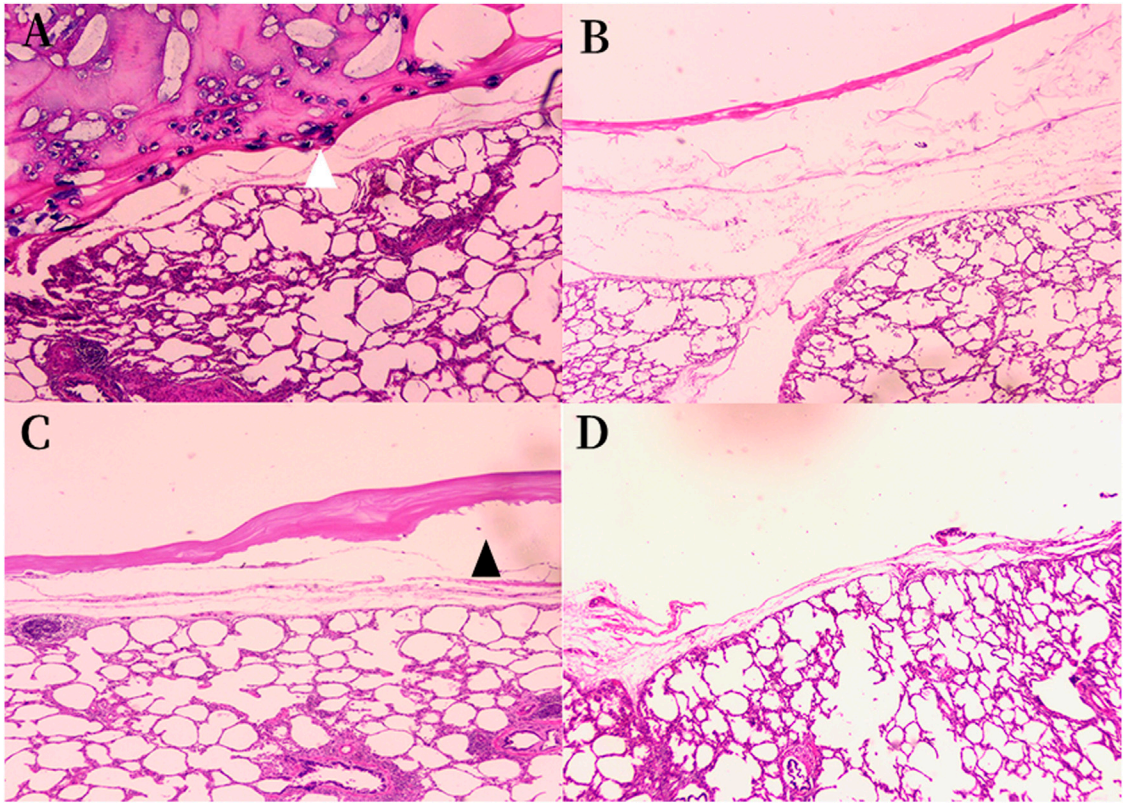

FIGURE 7
Histologic findings of the sealing materials on the intersegmental plane of the lung (original magnification ×40). **(A)** Group A ORC + fibrin glue, hematoxylin-eosin staining; **(B)** Group B PGA + fibrin glue, hematoxylin-eosin staining; **(C)** Group C fibrin glue, hematoxylin-eosin staining; **(D)** Group D control group, hematoxylin-eosin staining. **(A)** The sealing layer of ORC and fibrin glue adhered tightly to the intersegmental plane, some black gel blocked the pleural defect (white arrowhead). **(B)** The sealing layer of PGA and fibrin glue adhered firmly to the intersegmental plane. **(C)** A gap was observed between the sealing layer and the intersegmental plane (black arrowhead) in the group C. The sealing layer did not fit evenly with the surface of the lung tissue, and the thickness of it was not as uniform as that in groups A and B. **(D)** The normal intersegmental interface separated by electrocauterization. The pleural defect was severe due to the cauterization of the electric cautery. ORC (oxidized regenerated cellulose), PGA (polyglycolic acid).

sheet is expensive (Budak et al., 2020), and the method of covering the surgical wound with multi-layer PGA patch combined with fibrin glue proposed by Nomori et al. is difficult to popularize in clinical operations (Nomori et al., 2014). Furthermore, although PGA can be degraded completely, its degradation product, glycolide, can activate the classical complement pathway *in vivo*. Moreover, an inflammatory response to already weakened and stressed cells may result in significant cellular death and the failure of the implant of artificial materials (Ceonzo et al., 2006). Meanwhile, with the gradual replacement of lobectomy by segmentectomy, the number of patients undergoing secondary surgery due to ipsilateral recurrence or new-onset malignant tumors will increase, and the use of PGA sheets will be limited due to their tendency to cause thoracic adhesions (Nakamura et al., 2010; Saito et al., 2017). Therefore, identifying a substitute for PGA is critical.

Surgicel® is a widely used hemostatic material, and ORC is widely recognized as an effective agent of postoperative adhesion-prevention (Ten Broek et al., 2014). Several studies confirmed in animal model (beagle dogs) that ORC mesh is the preferred material for inducing increased thickening of the visceral pleura without inducing severe visceral-to-parietal pleural adhesions (Kurihara et al., 2016; Kanai et al., 2020; Yamanaka et al., 2019). Ebana et al. (2018) also confirmed this conclusion in clinical trials based on the detailed histopathological analyses of the resected lung specimens from five patients with recurrent pneumothorax after pleural covering with ORC mesh, and they found that 3 months after covering, the thickened pleura showed inflammatory cell infiltration, but those findings virtually disappeared after 1 year. Furthermore, we observed that postoperative air leakage in patients who underwent segmentectomy was reduced after the combined use of ORC and fibrin glue at the intersegmental plane in our

center, implying that this method is a good choice for reducing postoperative air leakage. However, to our knowledge, few studies have been conducted on the use of ORC and fibrin glue for preventing pulmonary air leakage, and there is no recognized pleural covering technique to prevent air leakage after segmentectomy. Therefore, we designed a model of isolated porcine segmentectomy to test this conjecture.

To explore the effect of sealants in segmentectomy more realistically, we designed an *ex vivo* porcine segmentectomy model because of the similarity between the porcine lungs and human lungs (Judge et al., 2014). We observed that the MALP of the control group was (17.3 ± 1.2) cmH_2O. After sealing the intersegmental plane with fibrin glue, the MALP reached (28.1 ± 2.3) cmH_2O, which was significantly higher than that of group D, thus confirming the ability of the fibrin glue to prevent postoperative air leakage, in accordance with previous studies (Araki et al., 2007; Moser et al., 2008). However, this method is insufficient to meet the clinical need of segmentectomy. The ideal lung tissue sealant should be strong enough to withstand the expected lung expansion to 30–40 cmH_2O pressure (Araki et al., 2007). Matoba et al., 2018 suggested that the sealant should provide 35 cmH_2O strength to prevent air leakage under mechanical ventilation, and the pressure in the airway should be increased without causing air leakage when the patient has an irritative cough postoperatively. The MALP was 41.8 ± 4.5 cmH_2O after combining ORC and fibrin glue in the intersegmental plane and 69.5 ± 5.2 cmH_2O after combining PGA and fibrin glue, both of which were significantly higher than that of group C with fibrin glue alone. Thus, we can preliminarily conclude that the combination of ORC or PGA sheet with fibrin glue can effectively resist the increased airway pressure caused by cough, airway sputum blockage, or bronchospasm without causing postoperative air leakage. Therefore, this novel method of combining ORC with fibrin glue on intersegmental plane during operation can meet the demand for early airway pressure tolerance after segmentectomy.

In order to verify the adhesion strength microscopically, we performed a histological examination to verify the adhesion of different sealing materials. As shown in Figure 7, we observed that in group A, the sealing layer formed by ORC and fibrin glue adhered closely to the lung segment, while at the interface, we observed some black gel-like materials formed by the reaction of Fe^{2+} in the blood hemoglobin with the carboxyl groups in the cellulose to form acid-hematin (Wu et al., 2012). Therefore, we hypothesized that this black gel could help close the ruptured alveolar wall at the pleural defect. Furthermore, the sealing layer formed by the PGA patch and fibrin glue in group B also adhered tightly to the interface of the lung segment. In contrast, there were some gaps between the fibrin glue and the surface of the lung segment in group C, which did not exist in the sealing layer of groups A and B. The thickness of sealing layer in group C was not as uniform as that in groups A and B. Figure 7D shows the normal intersegmental interface separated by electrocauterization, the pleural defect was severe due to the cauterization of the electric cautery. Histological examination confirmed that both ORC and PGA could be combined with fibrin glue to enhance the sealing properties of fibrin glue.

Compared with the PGA sheet, the sealing effect of ORC is slightly weaker to combine with fibrin glue; however, the advantages of ORC are diverse, which include cheaper price and superior hemostatic properties. ORC also has the advantages of better extensibility and faster hydrolytic degradation in meeting certain tensile strengths. An elastic sealing layer material was used in group A with a uniform surface load that did not fall off with the expansion of target lung tissue. ORC is absorbed faster by the human body than PGA (7–14 days vs. 15 weeks) (Lewis et al., 2013; Kanai et al., 2020), and the degradation products are less toxic and are mostly oligosaccharides, which trigger minimal adverse reactions in the human body and have better biocompatibility (Dimitrijevich et al., 1990; Lewis et al., 2013). PGA is hydrolyzed to glycolic acid, then dimerized into glycolide, which is incorporated into the tricarboxylic acid cycle and eventually excreted by the kidneyd (Yang et al., 2005). Moreover, PGA and its degradation product, glycolide, can activate the classical complement pathway and cause inflammation *in vivo* (Ceonzo et al., 2006).

We used the classical pack method proposed by Gika et al. to apply the sealing materials in groups A and B (Gika et al., 2007). Previous studies have shown that the pack method has significantly higher seal-breaking pressure and better fibrin clot penetration into the tissue than other methods (Gika et al., 2007; Itano, 2008), possibly because the fibrinogen solution was 34.8 times more viscous and had 3.5 times higher osmolality than the thrombin solution (Itano, 2008). Thus, thrombin can easily penetrate the sheet, unlike fibrinogen.

In our study, the thrombin solution saturated the ORC sheet and then reacted with fibrinogen to form a stable fibrin clot in the tissue of the defect and adjacent intersegmental planes, which acted as a foothold that fixes the sealing material to the lung tissue. Furthermore, the fibrinogen solution can be absorbed by the sheet through capillary phenomena (Itano, 2008) to interact with the thrombin in the sheet fibers forming fibrin clots that fill the air spaces in the ORC sheet. In addition, the black gel mentioned above may help seal the pleural defect. Eventually, the sealing layer was integrated into a whole by adding the remaining fibrinogen and thrombin solutions on the felt, thereby contributing to excellent adhesion strength—histological findings of lung tissues in group A support this mechanism.

One limitation of this study is that these experiments were carried out using excised healthy pig lungs; thus, the MALP results cannot be applied directly to *in vivo* conditions or emphysematous lungs. In addition, a long-term study regarding the repair of pleural defects by ORC and PGA has not been performed.

In conclusion, we believe that ORC is a safe and low-cost material that can replace Neville® to combine with fibrin glue in the prevention and treatment of air leakage after segmentectomy. Our novel method has a strong sealing effect and good biocompatibility, prospects for use in clinical segmentectomy.

Data availability statement

The raw data supporting the conclusion of this article will be made available by the authors, without undue reservation.

Ethics statement

The animal study was reviewed and approved by Animal Ethical and Welfare Committee of Nanjing Medical University.

Author contributions

HY and ZD wrote the manuscript. ZL and WS participated in the experimental operation. HW and KW contributed to the date analysis and creation of figures; JW and WW performed data proofreading; LC and XX were involved in material and technical support; QZ designed the outline and revised the manuscript. All authors have read and approved the final version of this manuscript.

Funding

This work was supported by the Natural Science Foundation of Jiangsu Province (BE2016790).

Conflict of interest

The authors declare that the research was conducted in the absence of any commercial or financial relationships that could be construed as a potential conflict of interest.

Publisher's note

All claims expressed in this article are solely those of the authors and do not necessarily represent those of their affiliated organizations, or those of the publisher, the editors and the reviewers. Any product that may be evaluated in this article, or claim that may be made by its manufacturer, is not guaranteed or endorsed by the publisher.

References

Araki, M., Tao, H., Nakajima, N., Sugai, H., Sato, T., Hyon, S. H., et al. (2007). Development of new biodegradable hydrogel glue for preventing alveolar air leakage. *J. Thorac. Cardiovasc. Surg.* 134, 1241–1248. doi:10.1016/j.jtcvs.2007.07.020

Budak, K., Sogut, O., and Sezer, U. A. (2020). A review on synthesis and biomedical applications of polyglycolic acid. *J. Polym. Res.* 27, 208. doi:10.1007/s10965-020-02187-1

Ceonzo, K., Gaynor, A., Shaffer, L., Kojima, K., Vacanti, C. A., and Stahl, G. L. (2006). Polyglycolic acid-induced inflammation: Role of hydrolysis and resulting complement activation. *Tissue Eng.* 12, 301–308. doi:10.1089/ten.2006.12.301

Cho, S., Huh, D. M., Kim, B. H., Lee, S., Kwon, O. C., Ahn, W. S., et al. (2008). Staple line covering procedure after thoracoscopic bullectomy for the management of primary spontaneous pneumothorax. *Thorac. Cardiovasc. Surg.* 56, 217–220. doi:10.1055/s-2007-989366

Dimitrijevich, S. D., Tatarko, M., Gracy, R. W., Wise, G. E., Oakford, L. X., Linsky, C. B., et al. (1990). *In vivo* degradation of oxidized, regenerated cellulose. *Carbohydr. Res.* 198, 331–341. doi:10.1016/0008-6215(90)84303-c

Ebana, H., Hayashi, T., Mitani, K., Kobayashi, E., Kumasaka, T., Mizobuchi, T., et al. (2018). Oxidized regenerated cellulose induces pleural thickening in patients with pneumothorax: Possible involvement of the mesothelial-mesenchymal transition. *Surg. Today* 48, 462–472. doi:10.1007/s00595-017-1597-4

Gika, M., Kawamura, M., Izumi, Y., and Kobayashi, K. (2007). The short-term efficacy of fibrin glue combined with absorptive sheet material in visceral pleural defect repair. *Interact. Cardiovasc. Thorac. Surg.* 6, 12–15. doi:10.1510/icvts.2006.139436

Itano, H. (2008). The optimal technique for combined application of fibrin sealant and bioabsorbable felt against alveolar air leakage. *Eur. J. Cardio-Thoracic Surg.* 33, 457–460. doi:10.1016/j.ejcts.2007.12.036

Judge, E. P., Hughes, J. M., Egan, J. J., Maguire, M., Molloy, E. L., and O'Dea, S. (2014). Anatomy and bronchoscopy of the porcine lung. A model for translational respiratory medicine. *Am. J. Respir. Cell Mol. Biol.* 51, 334–343. doi:10.1165/rcmb.2013-0453tr

Kanai, E., Matsutani, N., Aso, T., Yamamoto, Y., and Sakai, T. (2020). Long-term effects of pleural defect repair using sheet materials in a canine model. *Gen. Thorac. Cardiovasc. Surg.* 68, 615–622. doi:10.1007/s11748-019-01270-9

Kawai, H., Harada, K., Ohta, H., Tokushima, T., and Oka, S. (2012). Prevention of alveolar air leakage after video-assisted thoracic surgery: Comparison of the efficacy of methods involving the use of fibrin glue. *Thorac. Cardiovasc. Surg.* 60, 351–355. doi:10.1055/s-0031-1293599

Khoshmohabat, H., Paydar, S., Karami, M. Y., Makarem, A., Dastgheib, S. N., Pourdavood, A., et al. (2019). SURGICEL compared with simple gauze packing in grade IV liver injury: An experimental study. *Comp. Clin. Pathol.* 28, 467–471. doi:10.1007/s00580-018-2880-5

Kurihara, M., Mizobuchi, T., Kataoka, H., Sato, T., Kumasaka, T., Ebana, H., et al. (2016). A total pleural covering for lymphangioleiomyomatosis prevents pneumothorax recurrence. *PLoS One* 11, e0163637. doi:10.1371/journal.pone.0163637

Lee, J. M., Pan, J. D., Lin, W. C., and Lee, Y. C. (2006). Using Surgicel to buttress the staple line in lung volume reduction surgery for chronic obstructive pulmonary disease. *J. Thorac. Cardiovasc. Surg.* 131, 495–496. doi:10.1016/j.jtcvs.2005.09.039

Lee, S., Kim, H. R., Cho, S., Huh, D. M., Lee, E. B., Ryu, K. M., et al. (2014). Staple line coverage after bullectomy for primary spontaneous pneumothorax: A randomized trial. *Ann. Thorac. Surg.* 98, 2005–2011. doi:10.1016/j.athoracsur.2014.06.047

Leshnower, B. G., Miller, D. L., Fernandez, F. G., Pickens, A., and Force, S. D. (2010). Video-assisted thoracoscopic surgery segmentectomy: A safe and effective procedure. *Ann. Thorac. Surg.* 89, 1571–1576. doi:10.1016/j.athoracsur.2010.01.061

Lewis, K. M., Spazierer, D., Urban, M. D., Lin, L., Redl, H., and Goppelt, A. (2013). Comparison of regenerated and non-regenerated oxidized cellulose hemostatic agents. *Eur. Surg.* 45, 213–220. doi:10.1007/s10353-013-0222-z

Martyn, D., Meckley, L. M., Miyasato, G., Lim, S., Riebman, J. B., Kocharian, R., et al. (2015). Variation in hospital resource use and cost among surgical procedures using topical absorbable hemostats. *Clin. Outcomes Res.* 7, 567–574. doi:10.2147/ceor.s88698

Matoba, M., Takagi, T., Tsujimoto, H., Ozamoto, Y., Ueda, J., and Hagiwara, A. (2018). Reduction of pulmonary air leaks with a combination of polyglycolic acid sheet and alginate gel in rats. *Biomed. Res. Int.* 2018, 3808675. doi:10.1155/2018/3808675

Moser, C., Opitz, I., Zhai, W., Rousson, V., Russi, E. W., Weder, W., et al. (2008). Autologous fibrin sealant reduces the incidence of prolonged air leak and duration of chest tube drainage after lung volume reduction surgery: A prospective randomized blinded study. *J. Thorac. Cardiovasc. Surg.* 136, 843–849. doi:10.1016/j.jtcvs.2008.02.079

Nakamura, T., Suzuki, K., Mochizuki, T., Ohde, Y., Kobayashi, H., and Toyoda, F. (2010). An evaluation of the surgical morbidity of polyglycolic acid felt in pulmonary resections. *Surg. Today* 40, 734–737. doi:10.1007/s00595-009-4131-5

Nomori, H., Abe, M., Sugimura, H., Takegawa, Y., Oka, S., and Takeshi, A. (2014). Triple-layer sealing with absorptive mesh and fibrin glue is effective in preventing air leakage after segmentectomy: Results from experiments and clinical study. *Eur. J. Cardio-Thoracic Surg.* 45, 910–913. doi:10.1093/ejcts/ezt502

Saito, H., Konno, H., Atari, M., Kurihara, N., Fujishima, S., Sato, Y., et al. (2017). Management of intersegmental plane on pulmonary segmentectomy concerning postoperative complications. *Ann. Thorac. Surg.* 103, 1773–1780. doi:10.1016/j.athoracsur.2017.01.014

Saji, H., Okada, M., Tsuboi, M., Nakajima, R., Suzuki, K., Aokage, K., et al. (2022). Segmentectomy versus lobectomy in small-sized peripheral non-small-cell lung cancer (JCOG0802/WJOG4607L): A multicentre, open-label, phase 3, randomised, controlled, non-inferiority trial. *Lancet* 399, 1607–1617. doi:10.1016/s0140-6736(21)02333-3

Suzuki, K., Saji, H., Aokage, K., Watanabe, S. I., Okada, M., Mizusawa, J., et al. (2019). Comparison of pulmonary segmentectomy and lobectomy: Safety results of a randomized trial. *J. Thorac. Cardiovasc. Surg.* 158, 895–907. doi:10.1016/j.jtcvs.2019.03.090

Tanaka, T., Ueda, K., Murakami, J., and Hamano, K. (2018). Use of stitching and bioabsorbable mesh and glue to combat prolonged air leaks. *Ann. Thorac. Surg.* 106, e215–e218. doi:10.1016/j.athoracsur.2018.04.046

Ten Broek, R. P. G., Stommel, M. W. J., Strik, C., Van Laarhoven, C., Keus, F., and Van Goor, H. (2014). Benefits and harms of adhesion barriers for abdominal surgery: A systematic review and meta-analysis. *Lancet* 383, 48–59. doi:10.1016/s0140-6736(13)61687-6

Ueda, K., Tanaka, T., Jinbo, M., Yagi, T., Li, T. S., and Hamano, K. (2007). Sutureless pneumostasis using polyglycolic acid mesh as artificial pleura during video-assisted major pulmonary resection. *Ann. Thorac. Surg.* 84, 1858–1861. doi:10.1016/j.athoracsur.2007.06.080

Wu, Y., He, J., Cheng, W., Gu, H., Guo, Z., Gao, S., et al. (2012). Oxidized regenerated cellulose-based hemostat with microscopically gradient structure. *Carbohydr. Polym.* 88, 1023–1032. doi:10.1016/j.carbpol.2012.01.058

Yamanaka, S., Kurihara, M., and Watanabe, K. (2019). A novel dual-covering method in video-assisted thoracic surgery for pediatric primary spontaneous pneumothorax. *Surg. Today* 49, 587–592. doi:10.1007/s00595-019-01785-x

Yang, J., Yamato, M., Kohno, C., Nishimoto, A., Sekine, H., Fukai, F., et al. (2005). Cell sheet engineering: Recreating tissues without biodegradable scaffolds. *Biomaterials* 26, 6415–6422. doi:10.1016/j.biomaterials.2005.04.061

Yazawa, T., Igai, H., Numajiri, K., Ohsawa, F., Matsuura, N., and Kamiyoshihara, M. (2021). Comparison of stapler and electrocautery for division of the intersegmental plane in lung segmentectomy. *J. Thorac. Dis.* 13, 6331–6342. doi:10.21037/jtd-21-1397

frontiers | Frontiers in Bioengineering and Biotechnology

TYPE Original Research
PUBLISHED 09 January 2023
DOI 10.3389/fbioe.2022.1083763

OPEN ACCESS

EDITED BY
Shige Wang,
University of Shanghai for Science and Technology, China

REVIEWED BY
Chunyan Cui,
Tianjin University, China
Yunlong Yu,
Army Medical University, China
Carlos Guimarães,
University of Minho, Portugal

*CORRESPONDENCE
Changqing Yuan,
yuancq@qdu.edu.cn
Qihui Zhou,
qihuizhou@qdu.edu.cn

SPECIALTY SECTION
This article was submitted to Biomaterials, a section of the journal Frontiers in Bioengineering and Biotechnology

RECEIVED 29 October 2022
ACCEPTED 24 November 2022
PUBLISHED 09 January 2023

CITATION
Deng X, Wang D, Zhang D, Sun M, Zhou L, Wang Y, Kong X, Yuan C and Zhou Q (2023), Antibacterial quaternary ammonium chitosan/carboxymethyl starch/alginate sponges with enhanced hemostatic property for the prevention of dry socket.
Front. Bioeng. Biotechnol. 10:1083763.
doi: 10.3389/fbioe.2022.1083763

Antibacterial quaternary ammonium chitosan/ carboxymethyl starch/alginate sponges with enhanced hemostatic property for the prevention of dry socket

Xuyang Deng[1,2], Danyang Wang[1,2,3], Dongjie Zhang[4], Ming Sun[1], Liying Zhou[3], Yuxi Wang[3], Xiaowen Kong[1,2], Changqing Yuan[1,2,3,5]* and Qihui Zhou[1,2,3,6,7]*

[1]Department of Stomatology, The Affiliated Hospital of Qingdao University, Qingdao University, Qingdao, China, [2]School of Stomatology, Qingdao University, Qingdao, China, [3]Institute for Translational Medicine, The Affiliated Hospital of Qingdao University, Qingdao University, Qingdao, China, [4]Department of Gastroenterology, The Affiliated Hospital of Qingdao University, Qingdao, China, [5]Dental Biomaterials Technology Innovation Center of Qingdao, Qingdao, Shandong, China, [6]School of Rehabilitation Sciences and Engineering, University of Health and Rehabilitation Sciences, Qingdao, China, [7]Zhejiang Engineering Research Center for Tissue Repair Materials, Wenzhou Institute, University of Chinese Academy of Sciences, Wenzhou, China

Tooth extraction commonly leads to postoperative wound bleeding, bacterial infection, and even the occurrence of dry socket. Therefore, developing a biomedical material with favorable antibacterial and excellent hemostatic properties to prevent the post-extraction dry socket is necessary. Herein, quaternary ammonium chitosan/ carboxymethyl starch/alginate (ACQ) sponges are developed *via* Ca^{2+} cross-linking, electrostatic interaction, and lyophilization methods. The results show that the bio-multifunctional sponges exhibit interconnected porous structures with significant fluid absorption rates and suitable water vapor transmission rates. *In vitro* cellular and hemolysis experiments indicate that the developed sponges have acceptable biocompatibility. Notably, the constructed sponges effectively inhibit the growth of *E. coli*, *S. aureus,* and *C. albicans*, as well as achieve rapid hemostasis in the mouse liver injury and mini-pig tooth extraction models by absorbing blood and promoting red blood cell adhesion. Thus, the created bio-multifunctional sponges show tremendous promise as a hemostatic material for wound management after tooth extraction.

KEYWORDS

marine polysaccharide, bio-multifunctional sponge, antibacteria, rapid hemostasis, tooth extraction, dry socket

1 Introduction

In oral surgery, tooth extraction is a general treatment that frequently results in severe trauma. The elderly, especially patients on anticoagulants, have difficulty forming blood clots and often experience uncontrollable bleeding after dental extraction (Inokoshi et al., 2021). And dry socket would occur when the blood clot is removed or dissolved too early to

expose the alveolar bone (Catanzano et al., 2018). Dry socket can cause sharp pain that affects the patient's chewing and swallowing, making oral hygiene difficult to maintain (Yan et al., 2022). Absorbable gelatin sponges (AGS) with hemostatic properties have been employed to avoid dry socket in tooth extraction treatment (Wang et al., 2023). However, AGS lacks antimicrobial components and may cause an allergic reaction in the body, leading to inflammation at the wound site and increasing the rate of infection (Wei et al., 2020). Additionally, some biomaterials, such as platelet-rich fibrin (PRF) have also been used in clinical treatment. However, PRF is difficult and expensive to prepare and has insufficient hemostatic capacity, which limits its application to tooth post-extraction treatment (Otake et al., 2021). Therefore, it is highly desirable to develop a hemostatic material with good biocompatibility, low cost, and antibacterial properties for managing socket wounds and preventing dry socket following tooth extraction.

Sponge materials that present 3D network structures have developed rapidly in recent years (Jesionowski et al., 2018; Yuan et al., 2022; Wang et al., 2023). The porous network with high absorptive properties could serve as a physical barrier at the injured site to absorb exudate, maintain a moist microenvironment and promote wound healing (Wan et al., 2020; Yang E. et al., 2022). Meanwhile, this effective and rapidly absorbed effect may also lead to an enrichment of endogenous blood coagulation factors at the site of injury, thus promoting thrombosis and ultimately hemostasis (Ghobril and Grinstaff, 2015). Natural sodium alginate (AG) with good biocompatibility and biodegradability is commonly used as a matrix material for sponges (Hao et al., 2021; Xie et al., 2022b). AG could absorb water several times its weight and also promotes adhesion between the composite and the wound, making it a desirable material for hemostasis (Wang Y. et al., 2021; Lv et al., 2021; Xie et al., 2022a). Starch-based hemostatic agents belong to the class of passive hemostatic agents and exhibit good biodegradability and biocompatibility (Panwar et al., 2019). Starch granules could increase the concentration of platelets and endogenous clotting factors at the bleeding site by absorbing fluid from the blood, thus producing an effective hemostasis effect (Antisdel et al., 2009). Carboxymethyl starch (CMS) is an anionic polysaccharide that is soluble in water at room temperature, and as a derivative of starch, it has been widely used in wound healing and regenerative medicine (Chen et al., 2018). Carboxymethylation of starch increases the hydrophilicity, thereby increasing the fluid absorption of starch and further improving hemostatic efficiency (Massicotte et al., 2008). Therefore, CMS is often used with other hemostatic materials to enhance the hemostatic effect.

As the only naturally derived alkaline polysaccharide with a positive charge, CS has numerous beneficial characteristics, including satisfied biodegradability, biocompatibility, hemostatic capabilities, and antibacterial properties, as well as the promotion of wound healing (Yu et al., 2019; Wang Z. et al., 2021; Hao et al., 2022b; Xu N. et al., 2022). However, the application of CS is limited by poor water solubility (Zhao et al., 2017). It was found that the modification of CS with quaternary ammonium salts can significantly improve water solubility while enhancing antimicrobial properties (Zhao et al., 2018; Liang et al., 2020; Zong et al., 2022). Moreover, the enhanced positive charge of quaternary ammonium chitosan (Qch) is thought to improve the hemostatic ability of CS, which attracts and interacts with large numbers of red blood cells through electrostatic action (Huang et al., 2017). A positive charge-based procoagulant effect like this has also accelerated the development of new hemostatic materials with cationic properties (Behrens et al., 2014). Inspired by the observations above, AG/CMS/Qch (ACQ) composite sponge would be an excellent candidate as a bio-multifunctional socket dressing, which has not been reported.

In the present study, a series of composite sponges based on AG were prepared through electrostatic interaction, Ca^{2+} crosslinking, and lyophilization methods. The physicochemical features of the composite sponges were measured by fourier transform-infrared (FTIR) spectra, scanning electron microscopy (SEM), pore size, porosity, fluid absorption, and water vapor transmission rate (WVTR). The interaction between materials and cells was also detected *in vitro* to evaluate the biocompatibility of sponges. The antibacterial performances, as well as the *in vitro* and *vivo* hemostatic properties of the sponges, were systematically characterized. Our results indicate that the use of bio-multifunctional ACQ compound sponges after tooth extraction holds out a lot of potential for hemostasis and the avoidance of dry socket.

2 Materials and methods

2.1 Synthesis of Qch

The CS powder (Mw = 300 kDa, Golden-Shell, China) was dissolved in an amalgamated solution made up of KOH, LiOH-H_2O, urea (Sinopharm, China), and double distilled water (DDW) with a weight ratio of 7:8:8:77. To create a clear solution, the mixture was frozen at -20°C for an entire night before being thawed and mixed at 5°C. 3-Chloro-2-hydroxypropyl trimethyl ammonium chloride (Sinopharm, China) was then added dropwise to the CS solution. After adjusting the pH with sufficient HCl solution (Sinopharm, China), the mixture was dialyzed with DDW for a week. The solution was freeze-dried using a lyophilizer (Christ, Germany) to get pure Qch powder.

2.2 Synthesis of ACQ composite sponges

Briefly, the AG (M/G = 1.2, Mw = 600 Kg/mol, the viscosity is 700 mPa s, Qingdao Bright Moon Seaweed Group Co., Ltd, China) was dissolved in DDW (2 wt%), stirred at room temperature for 4 h, and filtered 3 times with a pressure pump. The AG solution was then poured into 24-well plates and lyophilized to form AG sponges. The freeze-dried sponges were cross-linked with a mixture of glycerol, $CaCl_2$, and anhydrous ethanol in the ratio of 3:7:90 by weight for 6 h, rinsed with excess DDW, and lyophilized again to fabricate the final AG sponges (Hao et al., 2020). The rest of the sponges were synthesized in a similar way to AG sponges. AC sponges were made by dissolving 1 g AG and 1 g CMS in 66.66 mL DDW. For ACQ-1 sponges, 1 g AG, 1 g CMS and .4 g Qch were dissolved in 70.66 mL DDW. ACQ-2 sponges were obtained by dissolving 1 g each of AG, CMS, and Qch in 76.66 mL of DDW. These sponges also need to be cross-linked and lyophilized to obtain the final sponges.

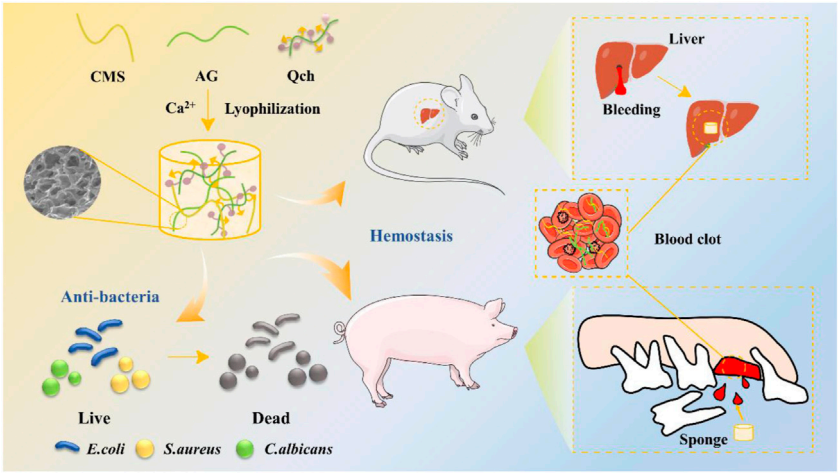

FIGURE 1
Schematic diagram of the synthesis of ACQ sponges and their application in antibacteria and hemostasis.

2.3 Physicochemical characterizations

2.3.1 FTIR spectroscopy

The FTIR spectrometer (Thermo Fisher Scientific, Waltham, MA, United States) was used to measure the infrared spectra of sponges in the wavelength range of 500–3,500 cm^{-1}.

2.3.2 SEM

By using SEM (VEGA3, TESAGN, Czech Republic) with an acceleration voltage of 10 kV, the porous morphology of the sponges was examined. To calculate the pore size, Image J software was used to analyze the SEM images. The pore size was calculated from measurements of more than 30 pores taken from different SEM images.

2.3.3 Porosity test

The volume (V) was obtained by measuring the diameter and height of the sponge, and then the pre-weighed sponge (m_0) was entirely submerged in anhydrous ethanol and the weight was recorded as m_1 after removing the excess ethanol on the surface. The porosity was calculated by the following formula:

$$Porsity = \frac{m_1 - m_0}{\rho V}$$

where ρ is the density of anhydrous ethanol.

2.3.4 Fluid absorption rate measurement

The pre-weighed sponge (m_0) was placed on the slides and phosphate buffer solution (PBS) was added drop by drop to the sponge until the sponge reached equilibrium. Excess liquid was removed from the sponge surface with filter paper and the weight of the wet sponge was recorded as m_1. The fluid absorption ratio was calculated as below:

$$\text{Fluid absorption rate} = \frac{m_1 - m_0}{m_0} \times 100\%$$

2.3.5 WVTR

Dried sponges of equal size were placed on the mouth of a cylindrical bottle containing 10 mL of DDW and tightly covered with plastic wrap to prevent additional evaporation of water. The weight of water absorbed by the sponge after 24 h was measured and the WVTR was calculated as follows:

$$WVTR = \frac{W_i - W_t}{S} \text{g} \Big/ \text{m}^2 \Big/ \text{day}$$

where W_i, W_t, and S are the weight of the bottle containing, the weight of the bottle containing water after 24 h, and the area of the mouth of cylindrical bottles, respectively.

2.4 *In vitro* cytocompatibility assay

The Cell Culture Centre of Shanghai Institutes for Biological Science Chinese Academy of Sciences (Shanghai, China) contributed the mouse fibroblast cells (L929). L929 cells were incubated at 37°C in 5% CO_2 and the medium was changed every 2 days.

The cell live/dead assay kit (Meilunbio, China) and CCK-8 assay kit (MedChem Express Co., Ltd., China) were used to assess the sponge's cytotoxicity. For live/dead staining, L929 cells were grown in 24-well plates at a density of 1×10^4/well. 12 h later, equal amounts of sterile sponges were added to each well separately. After co-culture with L929 cells overnight, the sponges were removed. Cells were then washed with PBS and incubated for 30 min at 37°C with the addition of 2.5 μm calcein-AM and 2.5 μm ethidium homodimer protected from light. After rinsing again with PBS, images of the cells were acquired by fluorescence microscopy (Nikon A1 MP, Japan), and the proportion of living cells was calculated. As for the CCK-8 assay, L929 cells were planted on 24-well plates at a density of 2×10^3/well. 12 h later, the cells were treated with different sponges. The sponges were co-cultured with the cells for 1–5 days, respectively. The sponges were removed, and the cells were rinsed with PBS. Cells were then cultured in a

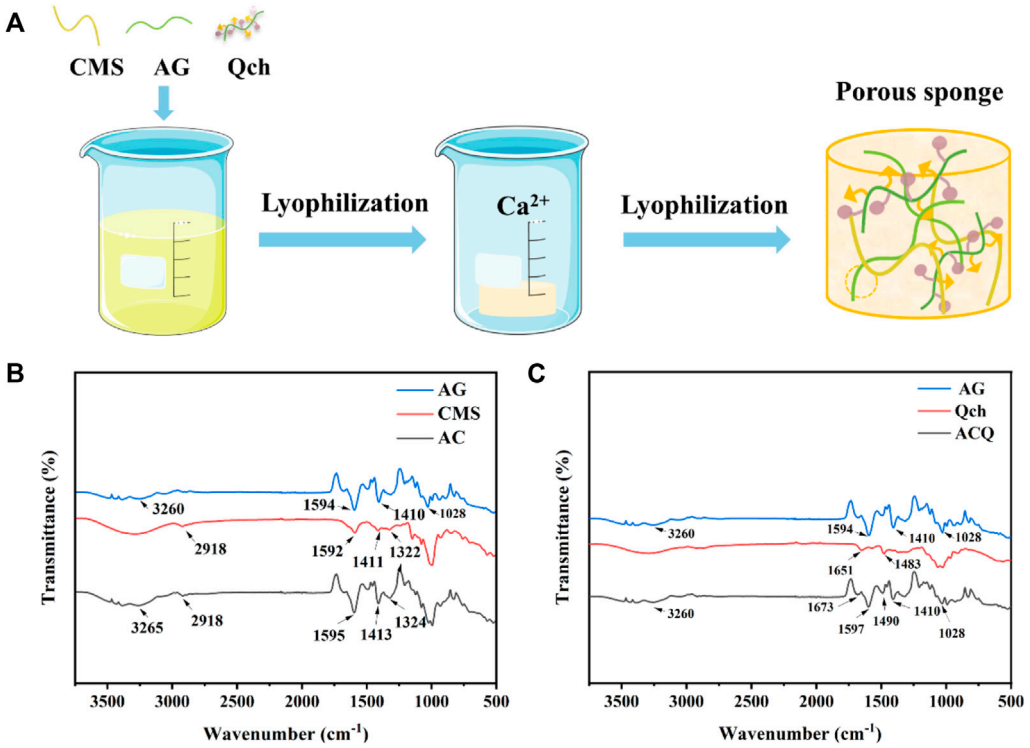

FIGURE 2
(A) Schematic diagram of the synthesis of ACQ sponges. **(B)** FTIR spectra of AG, CMS, and AC. **(C)** FTIR spectra of AG, Qch, and ACQ.

medium supplemented with 10% CCK-8 solution and the optical density (OD) value was measured at 450 nm by a microplate reader (Bio-Tek, United States).

2.5 *In vitro* antibacterial activity test

Escherichia coli (*E. coli*, Gram-negative), *Staphylococcus aureus* (*S. aureus*, Gram-positive), and *Candida albicans* (*C. albicans*) were cultured with LB Broth (Solarbio, China), Tryptic Soy Broth (Solarbio, China), and Brian Heart Infusion (Solarbio, China), respectively. Equal masses of sponges were co-incubated with 4 mL 10^6 CFU/mL bacterial suspension for 12 h. The control group was the normal bacterial solution without the addition of samples. The co-cultured bacterial solution was diluted and 20 µL suspension was evenly spread on agar plates. After incubation at 37°C for 18 h, the microbial colonies formed on the agar plates were counted.

2.6 Blood coagulation test

Different composite sponges and AGS (Xiangen Medicine, China) were prepared to the same size and placed on Petri dishes. The AGS was used as a positive control (+) and fresh blood was used as a negative control (−). Next, the sponge was then loaded with 200 µl of whole blood and incubated at 37°C for 5 min. And 5 mL DDW was added carefully to the Petri dish to remove the unclotted blood. Coagulation of the blood on the sponge was observed. Subsequently, the OD value of the solution containing hemoglobin was measured at 540 nm with a microplate reader to assess the coagulation capacity of the sponge.

2.7 Hemolysis assay

The whole blood was donated by healthy volunteers according to the relevant guidelines and used after dilution five times. 10 mg of the sponge was added to 1 mL of PBS, followed by 50 µl of diluted blood. DDW and PBS solution was used as the positive control (+) and negative control (−), respectively. After thorough mixing, the samples were incubated in a 5% CO_2 incubator at 37°C for 1 h and then centrifuged at 1,500 rpm for 5 min. The absorbance of the supernatant at 540 nm was recorded using a microplate reader. The hemolysis ratio was calculated with the formula below:

$$Hemolysis\,\% = \frac{OD_{sponge} - OD_{(-)}}{OD_{(+)} - OD_{(-)}} \times 100\%$$

2.8 Red blood cell (RBC) adhesion

Petri dishes were used to place AGS and composite sponges. 200 µl of whole blood containing 10% sodium citrate was added dropwise to the sponges and incubated at 37°C for 30 min. All samples were carefully rinsed with PBS solution to remove the unadhered RBC. Sponges with agglutinated RBC on the surface were fixed by 2.5% glutaraldehyde for 2 h. The samples were then dehydrated with different concentrations of alcohol solutions and further observed by SEM.

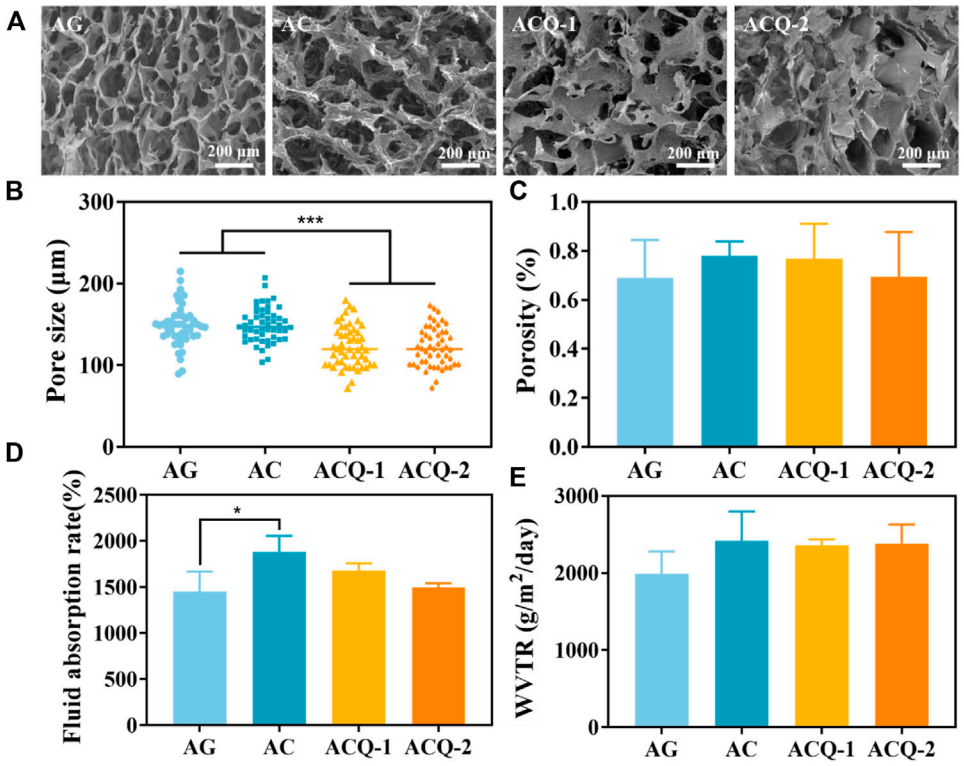

FIGURE 3
(A) SEM images of AG, AC, ACQ-1, and ACQ-2 sponges at ×100 magnifications, respectively. **(B)** Pore size, **(C)** porosity, **(D)** fluid absorption rate, and **(E)** WVTR of various sponges. Data are mean ± SD (n = 3) (*$p < 0.05$, ***$p < 0.001$).

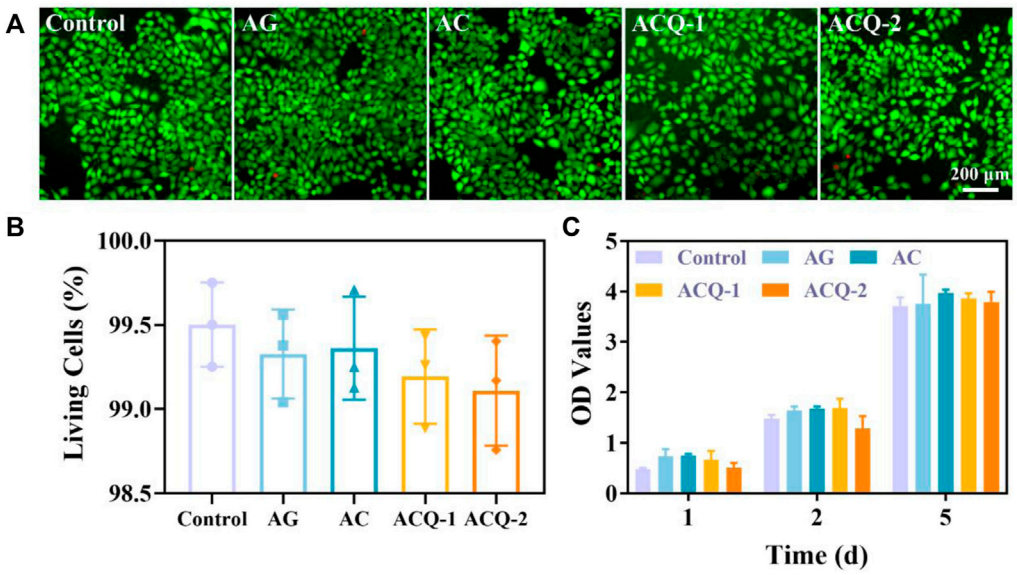

FIGURE 4
(A) Fluorescent images of cell live/dead staining of fibroblasts, and **(B)** the rate of living cells after co-cultivation with various sponges for 24 h, respectively. **(C)** The cytotoxicity of sponges after incubation with L929 cells for 1–5 days. Data are mean ± SD (n = 3).

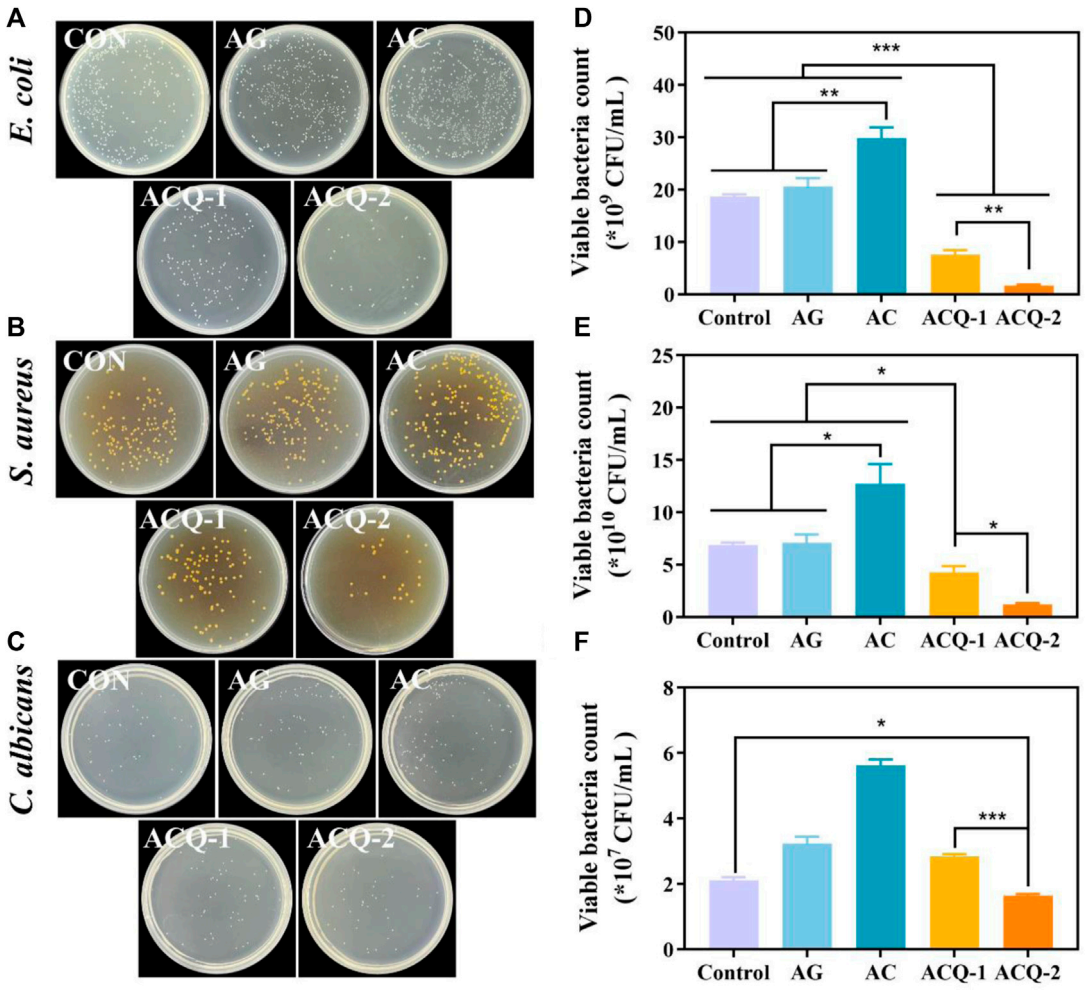

FIGURE 5
(A–C) Bacterial and fungus colonies, and **(D–F)** quantitative analysis of viable bacteria of *E. coli*, *S. aureus*, and *C. albicans* on agar plates after being co-cultured with the sponges, respectively. Data are mean ± SD (n = 3) (*$p < 0.05$, **$p < 0.01$, ***$p < 0.001$).

2.9 *In vivo* hemostatic assessment

2.9.1 Hepatic trauma model of mouse

A mouse model of liver injury was used to perform *in vivo* hemostasis studies. 8-week male mice were selected for the surgery. The mouse was anesthetized with sodium pentobarbital and fixed on a wooden board. A linear wound with a depth of 1 mm and length of 5 mm was created in the liver and the lost blood was collected with a pre-weighed filter paper located below the liver. The composite sponges and AGS (14 mm × 14 mm × 5 mm) were quickly placed on the wound site. The untreated liver wound was used as a negative control. The hemostasis of the liver was photographed and recorded at specific time points, and the filter paper was weighed to calculate the amount of blood loss.

2.9.2 Tooth extraction model of pig

The tooth extraction model was used to evaluate the hemostasis effect of the composite sponges on post-extraction bleeding. 6-week male mini pigs were selected for the surgery. After anesthesia, the mini pig was secured to the operating table and the mouth was pulled apart to expose the maxillary second primary molar. The gingiva was carefully separated with a dental probe. After extraction, the socket was filled with the ACQ-2 sponge or AGS to stop the bleeding. Sterile gauze was used to absorb the spilled blood. The time of hemostasis and the amount of blood loss were recorded as described in 2.9.1. All the experiments were approved by the Ethics Committee of the Affiliated Hospital of Qingdao University (approval number: QYFY WZLL 27368).

2.10 Statistical analysis

All data were presented as mean ± standard deviation. GraphPad Prism eight software was used for statistical evaluation. To determine differences between groups, one-way analysis of variance (ANOVA) was used to determine statistical significance, and a value of $p < .05$ was considered to be statistically significant.

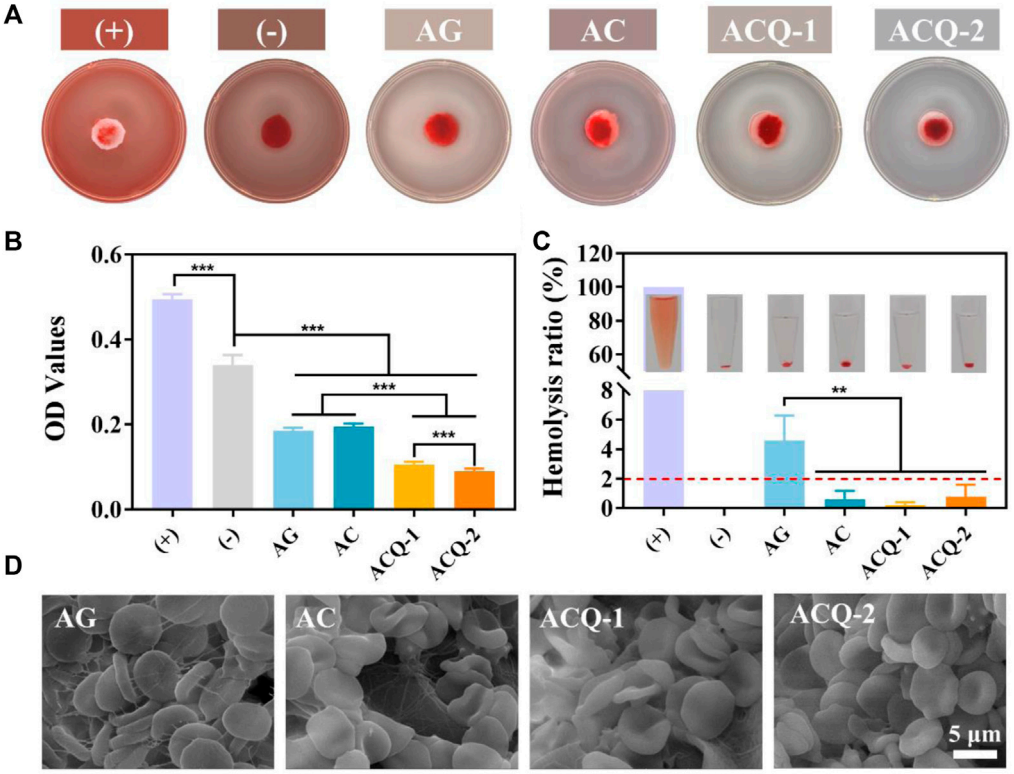

FIGURE 6
(A) Pictures and **(B)** quantitative results of blood coagulation experiments. **(C)** Photographs and quantification of hemolysis test. **(D)** SEM images of RBC adhering to sponges. Data are mean ± SD (n = 3) (**$p < 0.01$, ***$p < 0.001$).

3 Results and discussion

3.1 Preparation and characterization of composite sponges

The strategy to develop ACQ composite sponges with enhanced hemostatic and antibacterial performances is outlined in Figure 1. The porous ACQ sponges were fabricated *via* Ca^{2+} crosslinking, electrostatic interaction, and lyophilization, which possess great promise to be a hemostatic material for avoiding dry socket following tooth extraction.

ACQ composite sponges were developed as a hemostatic material *via* Ca^{2+} crosslinking, electrostatic interaction, and lyophilization procedures for wound management after tooth extraction as shown in Figure 2A–C show the FTIR spectra of AG, CMS, Qch, and various sponges. The prominent peaks at 3,260, 1,594, 1,410, and 1,028 cm^{-1} in the AG were generated by the stretching vibration of -OH, symmetric and asymmetric stretching vibrations of the carboxylate groups, and the vibration of the COC group, respectively (Zhao et al., 2016). For the CMS, there were obvious absorption peaks at 2,918 and 1,592 cm^{-1}, which were assigned to the tensile vibration of C-H bonds in methylene and modification of starch by carbonyl functional groups, respectively. The transmittance bands at 1,411 and 1,322 cm^{-1} belong to -CH_2 stretching vibration and -OH bending vibration, respectively (You et al., 2016). The spectra of AC revealed the characteristic bands of both AG and CMS. Qch showed two characteristic absorption peaks of 1,651 and 1,483 cm^{-1}, which correspond to the vibration of amide I and the introduction of quaternary ammonium groups on the chitosan, respectively (Li et al., 2010). ACQ preserved these feature peaks, illustrating the successful preparation of the composite sponge.

The internal microstructure of the sponges was observed by SEM (Figure 3A). Each group of sponges exhibited an interconnected porous structure with an irregular arrangement. As shown in Figure 3B, the pore size of ACQ-1 and ACQ-2 sponges was significantly smaller than that of AG and AC sponges due to the addition of Qch. However, there was no significant difference in porosity among the various sponges (Figure 3C). The high specific surface area and hierarchically porous structure of composite sponges could vastly improve the contact area with blood, accelerate hemostasis and absorb wound exudate, as well as promote trauma healing (Yan et al., 2022). High liquid absorption capacity can effectively absorb tissue exudate and achieve rapid hemostasis (Shen et al., 2022). As depicted in Figure 3D, the fluid absorption rate of the AC sponge was higher than that of the AG sponge, but not significantly different from that of the ACQ-1 and ACQ-2 sponges. The high fluid absorption rate could enhance the sponge's ability to absorb blood, which is closely related to the pore size and specific surface area (Bian et al., 2022). Meanwhile, the polysaccharide chain of CMS contains a large number of hydrophilic groups, and the O-H and -COOH groups could enhance the attraction to water molecules (Yusof et al., 2018). Proper infiltration of water and gas could accelerate wound healing while promoting blood absorption in the

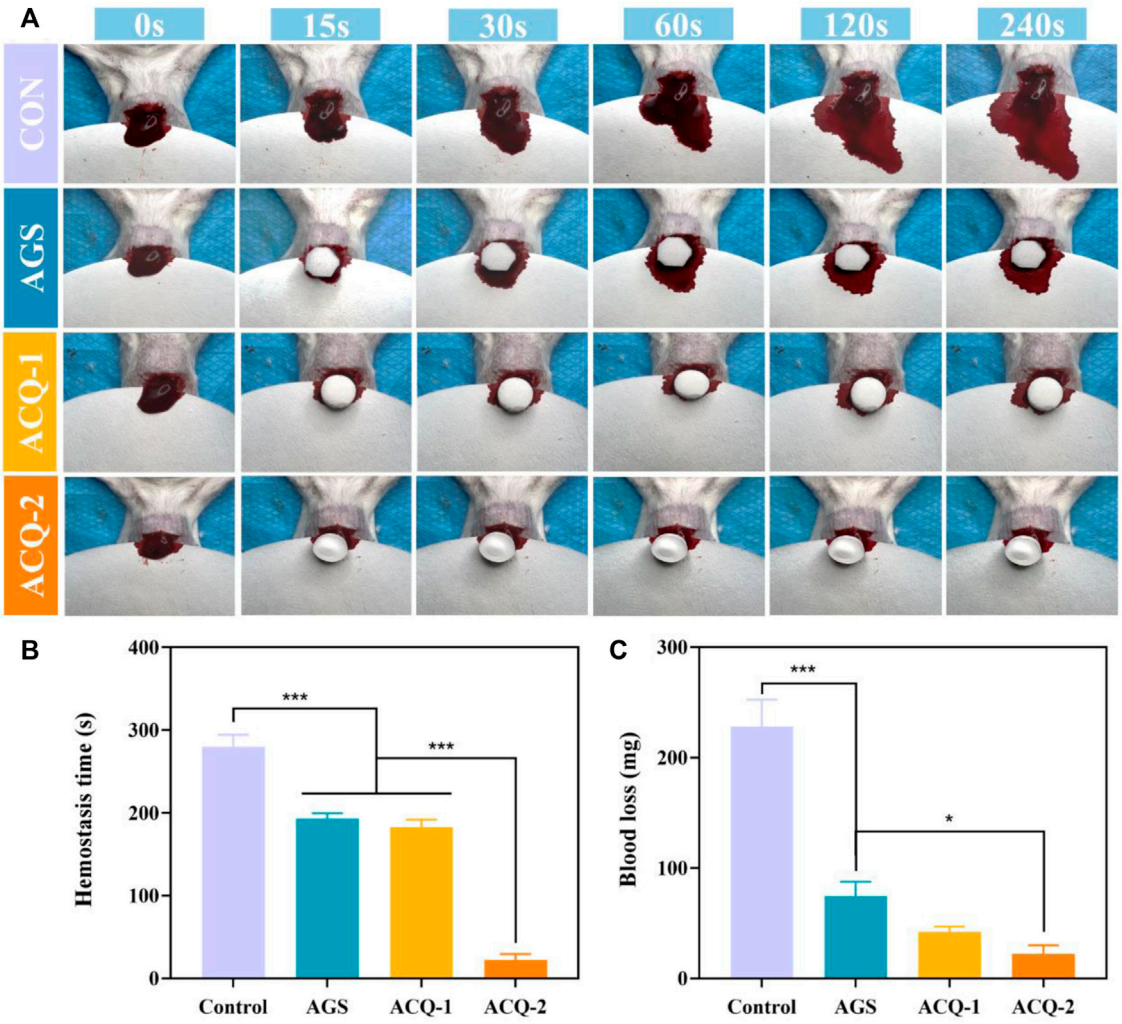

FIGURE 7
(A) Photographs of blood flow taken at specific times during liver hemostasis experiments. **(B)** Blood loss and **(C)** hemostasis time in liver hemostasis experiments. Data are mean ± SD (n = 3) (*$p < 0.05$, ***$p < 0.001$).

wound dressing (Yang Y. et al., 2022). There was no significant difference in WVTR among various sponges as WVTR is mainly related to porosity (Figure 3E).

3.2 Cytocompatibility evaluation of composite sponges

The hemostatic material should possess good biocompatibility to avoid delaying wound healing. Various sponges were co-cultured with L929 cells to assess their cytocompatibility using cell live/dead staining and CCK-8 assay, as fibroblasts are vital for wound healing (He et al., 2021; Mei et al., 2021; Hao et al., 2022a). The live/dead staining displayed in Figure 4A demonstrated that there were no significant differences in cell number and cell viability among sponges, and the cell viability was all higher than 98.5% (Figure 4B). As detailed in Figure 4C, the number of cells increased steadily from 1–5 days, indicating that the composite sponge promoted the cell proliferation which could contribute to the wound healing. This may be due to the fact that AG, CMS, and Qch have been proven to possess desirable biocompatibility and are widely used in biomaterials and tissue engineering (Jin et al., 2018; Yusof et al., 2018).

3.3 Antibacterial ability of the composite sponges

The effect of composite sponges against *E. coli*, *S. aureus*, and *C. albicans* was tested by CFU count test. As illustrated by Figure 5A,B, the colonies in ACQ-1 and ACQ-2 sponge groups were significantly reduced due to the incorporation of Qch. Moreover, the effect of inhibiting bacteria was significantly enhanced with the increase of Qch content (Figure 5D,E). This may be due to the fact that quaternary ammonium salts could alter the permeability of the bacterial cell wall and reduce the exchange of bacterial nutrients, leading to protein denaturation and ultimately cell death (Cheah et al., 2019). As for *C.*

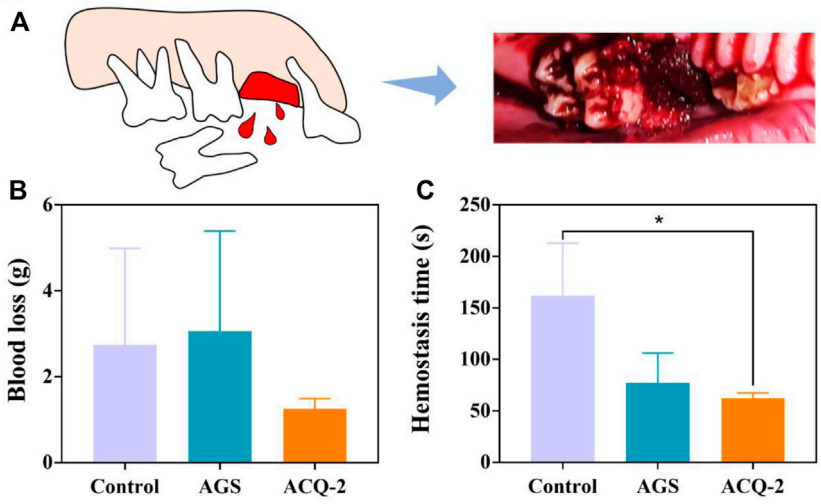

FIGURE 8
(A) Schematic diagram of pig tooth extraction. **(B)** Blood loss and **(C)** hemostasis time in tooth extraction hemostasis experiments. Data are mean ± SD (n = 3) (*$p < .05$).

albicans, only the ACQ-2 sponge effectively inhibited the growth of the fungus (Figure 5C,F). The interaction of CS cationic chains with negatively charged macromolecular residues on the fungal cell membrane, which results in death by allowing internal electrolytes and other components to leak out, may be the cause of the antifungal effects of Qch (Lee et al., 2018). Quantitative results showed that the AG, AC, and ACQ-2 groups could not inhibit the growth of bacteria and fungi. This may be because fungi are eukaryotes and are more difficult to eliminate than bacteria (Campoy and Adrio, 2017). Thus, only ACQ-2 with the highest Qch content had a slight antifungal effect.

3.4 Blood coagulation and hemocompatibility tests of composite sponges

An excellent hemostatic material should be able to promote blood clotting. The hemostatic effect of sponges was verified by detecting the formation of blood clots. As displayed in Figure 6A, after rinsing with DDW, the AGS and (-) control groups showed a red color due to the uncoagulated blood, while the developed sponge groups were significantly lighter in color. Meanwhile, the area of blood stains on the sponges of the AC, ACQ-1, and ACQ-2 groups was smaller than that of the AG group, which also indicates that the designed sponges possessed the ability of fast hemostasis. Figure 6B exhibits the quantitative results of blood coagulation experiments. Interestingly, the coagulation-promoting effect of AGS appeared to be very limited, and its OD value was even higher than that of the (-) control group. It can be observed that both AG and AC sponges effectively promoted the formation of blood clots, which is related to the fact that AG and CMS could promote fibrinogen adsorption and platelet aggregation (Chen et al., 2018; Shen et al., 2022). The ability of the sponge loaded with Qch to promote clotting was further enhanced. The positive charge on the sponge surface could adhere to more RBCs due to electrostatic interactions as shown in Figure 6D (Xu G. et al., 2022; Wei et al., 2022). Moreover, an excellent hemostatic material should be hemocompatible while promoting clotting. The hemolysis experiments revealed that the hemolysis rate of all groups of sponges was less than 2% (Figure 6C), and the RBC adhering to the sponges all showed a typical biconcave disc shape (Figure 6D). These results indicate that the synthetic composite sponges are highly desirable materials for trauma treatment after tooth extraction and the prevention of dry socket.

3.5 *In vivo* hemostatic activity of sponges

The formation of blood clots rich in growth factors can protect the tooth extraction wound to prevent the occurrence of dry socket, and also plays an important role in mediating the early inflammatory response, leading to the acceleration of tissue repair and regeneration (Wu et al., 2022). The hemostatic effect of composite sponges *in vivo* was further evaluated by a mouse liver injury model. Figure 7A depicts the coagulation process in the injured liver. It was found that blood loss has been increasing rapidly in the untreated control group. As shown in Figure 7B, blood loss was significantly reduced with AGS and composite sponges, and the hemostatic effect of composite sponges was more pronounced. In terms of hemostasis time, ACQ-2 achieves effective hemostasis in a very short period (Figure 7C).

Based on the above experimental results, the ACQ-2 sponge was used to perform hemostasis experiments for tooth extraction in mini pigs. Due to individual differences in the pigs and the effect of the extraction operation on blood loss, there was no statistical difference in blood loss among the control, AGS, and ACQ-2 groups. However, the ACQ-2 sponge group had the least mean blood loss. Moreover, the hemostasis time of ACQ-2 was almost halved relative to the control group, indicating that it accelerated the formation of blood clots in the extraction sockets. As mentioned above, this may be due to the fact that the positive charge on Qch could attract the negative charge on

the erythrocyte surface through electrostatic interaction, thus promoting the aggregation of RBC. Meanwhile, the Ca^{2+} contained in the cross-linker can activate endogenous and exogenous coagulation pathways, enriching more RBC and promoting blood coagulation Figure 8.

4 Conclusion

In summary, bio-multifunctional AG/CMS/Qch sponges with excellent antibacterial and rapid hemostatic properties were successfully fabricated by Ca^{2+} cross-linking, electrostatic interaction, and lyophilization methods for hemostasis of tooth extraction wound and prevention of postoperative dry socket. It was found that the developed sponges with porous structures possess a high fluid absorption rate and suitable WVTR to speed up the hemostasis process. Furthermore, biological experiments suggest that the fabricated sponges exhibited satisfactory biocompatibility and a distinctly antibacterial effect. Additionally, sponges could absorb blood and promote the aggregation of RBC to achieve rapid hemostasis. Therefore, the bio-multifunctional sponges with satisfactory antibacterial properties and significant rapid hemostatic effect can be performed as a potential novel type of clinical hemostatic products for trauma treatment after tooth extraction and prevention of dry socket.

Data availability statement

The original contributions presented in the study are included in the article/supplementary material, further inquiries can be directed to the corresponding authors.

Ethics statement

The animal study was reviewed and approved by the Ethics Committee of the Affiliated Hospital of Qingdao University.

Author contributions

QZ and CY contributed to the conception and design of the study. XD, DW, and DZ, and MS performed the experiments. XD, LZ, and YW prepared the figures. XD, DW, and XK wrote the first draft of the manuscript. QZ and CY revised the draft of the manuscript. QZ provided the funding. All authors contributed to the manuscript revision, read, and approved the submitted version.

Funding

The authors are very thankful for financial support by the National Natural Science Foundation of China (Grant No. 31900957), Shandong Provincial Natural Science Foundation (Grant No. ZR2019QC007), Innovation and technology program for the excellent youth scholars of higher education of Shandong province (Grant No. 2019KJE015), Traditional Chinese Medicine Science and Technology Project of Shandong province (Grant No. 2021Q069), Open Fund of Tianjin Enterprise Key Laboratory for Application Research of Hyaluronic Acid (Grant No. KTRDHA-Y201902), and Zhejiang Engineering Research Center for Tissue Repair Materials (Grant No. WIUCASZZXF21004).

Conflict of interest

The authors declare that the research was conducted in the absence of any commercial or financial relationships that could be construed as a potential conflict of interest.

Publisher's note

All claims expressed in this article are solely those of the authors and do not necessarily represent those of their affiliated organizations, or those of the publisher, the editors and the reviewers. Any product that may be evaluated in this article, or claim that may be made by its manufacturer, is not guaranteed or endorsed by the publisher.

References

Antisdel, J. L., West-Denning, J. L., and Sindwani, R. (2009). Effect of microporous polysaccharide hemospheres (MPH) on bleeding after endoscopic sinus surgery: Randomized controlled study. *Otolaryngol. - Head. Neck Surg.* 141, 353–357. doi:10.1016/j.otohns.2009.06.078

Behrens, A. M., Sikorski, M. J., Li, T., Wu, Z. J., Griffith, B. P., and Kofinas, P. (2014). Blood-aggregating hydrogel particles for use as a hemostatic agent. *Acta Biomater.* 10, 701–708. doi:10.1016/j.actbio.2013.10.029

Bian, J., Bao, L., Gao, X., Wen, X., Zhang, Q., Huang, J., et al. (2022). Bacteria-engineered porous sponge for hemostasis and vascularization. *J. Nanobiotechnology* 20, 47–20. doi:10.1186/s12951-022-01254-7

Campoy, S., and Adrio, J. L. (2017). Antifung. *Biochem. Pharmacol.* 133, 86–96. doi:10.1016/j.bcp.2016.11.019

Catanzano, O., D'Esposito, V., Formisano, P., Boateng, J. S., and Quaglia, F. (2018). Composite alginate-hyaluronan sponges for the delivery of tranexamic acid in postextractive alveolar wounds. *J. Pharm. Sci.* 107, 654–661. doi:10.1016/j.xphs.2017.09.026

Cheah, W. Y., Show, P. L., Ng, I. S., Lin, G. Y., Chiu, C. Y., and Chang, Y. K. (2019). Antibacterial activity of quaternized chitosan modified nanofiber membrane. *Int. J. Biol. Macromol.* 126, 569–577. doi:10.1016/j.ijbiomac.2018.12.193

Chen, X., Yan, Y., Li, H., Wang, X., Tang, S., Li, Q., et al. (2018). Evaluation of absorbable hemostatic agents of polyelectrolyte complexes using carboxymethyl starch and chitosan oligosaccharide both: *In vitro* and *in vivo*. *Biomater. Sci.* 6, 3332–3344. doi:10.1039/c8bm00628h

Ghobril, C., and Grinstaff, M. W. (2015). The chemistry and engineering of polymeric hydrogel adhesives for wound closure: A tutorial. *Chem. Soc. Rev.* 44, 1820–1835. doi:10.1039/c4cs00332b

Hao, Y., Yuan, C., Deng, J., Zheng, W., Ji, Y., and Zhou, Q. (2022a). Injectable self-healing first-aid tissue adhesives with outstanding hemostatic and antibacterial performances for trauma emergency care. *ACS Appl. Mat. Interfaces* 14, 16006–16017. doi:10.1021/acsami.2c00877

Hao, Y., Zhao, W., Zhang, H., Zheng, W., and Zhou, Q. (2022b). Carboxymethyl chitosan-based hydrogels containing fibroblast growth factors for triggering diabetic wound healing. *Carbohydr. Polym.* 287, 119336. doi:10.1016/j.carbpol.2022.119336

Hao, Y., Zhao, W., Zhang, L., Zeng, X., Sun, Z., Zhang, D., et al. (2020). Bio-multifunctional alginate/chitosan/fucoidan sponges with enhanced angiogenesis and hair follicle regeneration for promoting full-thickness wound healing. *Mat. Des.* 193, 108863. doi:10.1016/j.matdes.2020.108863

Hao, Y., Zheng, W., Sun, Z., Zhang, D., Sui, K., Shen, P., et al. (2021). Marine polysaccharide-based composite hydrogels containing fucoidan: Preparation, physicochemical characterization, and biocompatible evaluation. *Int. J. Biol. Macromol.* 183, 1978–1986. doi:10.1016/j.ijbiomac.2021.05.190

He, Y., Zhao, W., Dong, Z., Ji, Y., Li, M., Hao, Y., et al. (2021). A biodegradable antibacterial alginate/carboxymethyl chitosan/Kangfuxin sponges for promoting blood coagulation and full-thickness wound healing. *Int. J. Biol. Macromol.* 167, 182–192. doi:10.1016/j.ijbiomac.2020.11.168

Huang, Y., Feng, L., Zhang, Y., He, L., Wang, C., Xu, J., et al. (2017). Hemostasis mechanism and applications of N-alkylated chitosan sponge. *Polym. Adv. Technol.* 28, 1107–1114. doi:10.1002/pat.4003

Inokoshi, M., Kubota, K., Yamaga, E., Ueda, K., and Minakuchi, S. (2021). Postoperative bleeding after dental extraction among elderly patients under anticoagulant therapy. *Clin. Oral Investig.* 25, 2363–2371. doi:10.1007/s00784-020-03559-z

Jesionowski, T., Norman, M., Zółtowska-Aksamitowska, S., Petrenko, I., Joseph, Y., and Ehrlich, H. (2018). Marine spongin: Naturally prefabricated 3D scaffold-based biomaterial. *Mar. Drugs* 16, 88–23. doi:10.3390/md16030088

Jin, J., Ji, Z., Xu, M., Liu, C., Ye, X., Zhang, W., et al. (2018). Microspheres of carboxymethyl chitosan, sodium alginate, and collagen as a hemostatic agent *in vivo*. *ACS Biomater. Sci. Eng.* 4, 2541–2551. doi:10.1021/acsbiomaterials.8b00453

Lee, H., Wang, R., Hsu, Y., Chuang, C., Chan, H., Chiu, H., et al. (2018). Antifungal effect of tissue conditioners containing poly(acryloyloxyethyltrimethyl ammonium chloride)-grafted chitosan on Candida albicans growth *in vitro*. *J. Dent. Sci.* 13, 160–166. doi:10.1016/j.jds.2017.06.004

Li, S. D., Zhang, C. H., Dong, J. J., Ou, C. Y., Quan, W. Y., Yang, L., et al. (2010). Effect of cupric ion on thermal degradation of quaternized chitosan. *Carbohydr. Polym.* 81, 182–187. doi:10.1016/j.carbpol.2010.02.049

Liang, Y., Chen, B., Li, M., He, J., Yin, Z., and Guo, B. (2020). Injectable antimicrobial conductive hydrogels for wound disinfection and infectious wound healing. *Biomacromolecules* 21, 1841–1852. doi:10.1021/acs.biomac.9b01732

Lv, C., Li, L., Jiao, Z., Yan, H., Wang, Z., Wu, Z., et al. (2021). Improved hemostatic effects by Fe3+ modified biomimetic PLLA cotton-like mat via sodium alginate grafted with dopamine. *Bioact. Mat.* 6, 2346–2359. doi:10.1016/j.bioactmat.2021.01.002

Massicotte, L. P., Baille, W. E., and Mateescu, M. A. (2008). Carboxylated high amylose starch as pharmaceutical excipients. *Int. J. Pharm.* 356, 212–223. doi:10.1016/j.ijpharm.2008.01.039

Mei, L., Zhang, D., Shao, H., Hao, Y., Zhang, T., Zheng, W., et al. (2021). Injectable and self-healing probiotics-loaded hydrogel for promoting superbacteria-infected wound healing. *ACS Appl. Mat. Interfaces* 14, 20538–20550. doi:10.1021/acsami.1c23713

Otake, H., Sato, Y., Nakatani, E., Hawke, P., Takei, S., Ogino, A., et al. (2021). Oxytetracycline-hydrocortisone ointment reduces the occurrence of both dry socket and post-extraction pain after third molar extraction: An observational study. *PLoS One* 16, 0254221. doi:10.1371/journal.pone.0254221

Panwar, V., Sharma, A., Thomas, J., Chopra, V., Kaushik, S., Kumar, A., et al. (2019). *In-vitro* and *in-vivo* evaluation of biocompatible and biodegradable calcium-modified carboxymethyl starch as a topical hemostat. *Materialia* 7, 100373. doi:10.1016/j.mtla.2019.100373

Shen, Y., Wang, X., Li, B., Guo, Y., and Dong, K. (2022). Development of silk fibroin-sodium alginate scaffold loaded silk fibroin nanoparticles for hemostasis and cell adhesion. *Int. J. Biol. Macromol.* 211, 514–523. doi:10.1016/j.ijbiomac.2022.05.064

Wan, Y., Han, J., Cheng, F., Wang, X., Wang, H., Song, Q., et al. (2020). Green preparation of hierarchically structured hemostatic epoxy-amine sponge. *Chem. Eng. J.* 397, 125445. doi:10.1016/j.cej.2020.125445

Wang, D., Sun, Y., Zhang, D., Kong, X., Wang, S., Lu, J., et al. (2023). Root-shaped antibacterial alginate sponges with enhanced hemostasis and osteogenesis for the prevention of dry socket. *Carbohydr. Polym.* 299, 120184. doi:10.1016/j.carbpol.2022.120184

Wang, Y., Wang, P., Ji, H., Ji, G., Wang, M., and Wang, X. (2021). Analysis of safety and effectiveness of sodium alginate/poly(γ-glutamic acid) microspheres for rapid hemostasis. *ACS Appl. Bio Mat.* 4, 6539–6548. doi:10.1021/acsabm.1c00671

Wang, Z., Wang, X., Wang, Y., Zhu, Y., Liu, X., and Zhou, Q. (2021). NanoZnO-modified titanium implants for enhanced anti-bacterial activity, osteogenesis and corrosion resistance. *J. Nanobiotechnology* 19, 353–423. doi:10.1186/s12951-021-01099-6

Wei, W., Liu, J., Peng, Z. B., Liang, M., Wang, Y. S., and Wang, X. Q. (2020). Gellable silk fibroin-polyethylene sponge for hemostasis. *Artif. Cells, Nanomedicine, Biotechnol.* 48, 28–36. doi:10.1080/21691401.2019.1699805

Wei, X., Cai, J., Wang, C., Yang, K., Ding, S., Tian, F., et al. (2022). Quaternized chitosan/cellulose composites as enhanced hemostatic and antibacterial sponges for wound healing. *Int. J. Biol. Macromol.* 210, 271–281. doi:10.1016/j.ijbiomac.2022.05.007

Wu, S., Shan, Z., Xie, L., Su, M., Zeng, P., Huang, P., et al. (2022). Mesopore controls the responses of blood clot-immune complex via modulating fibrin network. *Adv. Sci.* 9, 2103608–2103616. doi:10.1002/advs.202103608

Xie, M., Liu, X., and Wang, S. (2022a). Degradation of methylene blue through Fenton-like reaction catalyzed by MoS2-doped sodium alginate/Fe hydrogel. *Colloids Surfaces B Biointerfaces* 214, 112443. doi:10.1016/j.colsurfb.2022.112443

Xie, M., Zeng, Y., Wu, H., Wang, S., and Zhao, J. (2022b). Multifunctional carboxymethyl chitosan/oxidized dextran/sodium alginate hydrogels as dressing for hemostasis and closure of infected wounds. *Int. J. Biol. Macromol.* 219, 1337–1350. doi:10.1016/j.ijbiomac.2022.08.166

Xu, G., Xu, N., Ren, T., Chen, C., Li, J., Ding, L., et al. (2022). Multifunctional chitosan/silver/tannic acid cryogels for hemostasis and wound healing. *Int. J. Biol. Macromol.* 208, 760–771. doi:10.1016/j.ijbiomac.2022.03.174

Xu, N., Yuan, Y., Ding, L., Li, J., Jia, J., Li, Z., et al. (2022). Multifunctional chitosan/gelatin@tannic acid cryogels decorated with *in situ* reduced silver nanoparticles for wound healing. *Burn. Trauma* 10, tkac019–15. doi:10.1093/burnst/tkac019

Yan, M., Pan, Y., Lu, S., Li, X., Wang, D., Shao, T., et al. (2022). Chitosan-CaP microflowers and metronidazole loaded calcium alginate sponges with enhanced antibacterial, hemostatic and osteogenic properties for the prevention of dry socket after tooth removal. *Int. J. Biol. Macromol.* 212, 134–145. doi:10.1016/j.ijbiomac.2022.05.094

Yang, E., Hou, W., Liu, K., Yang, H., Wei, W., Kang, H., et al. (2022). A multifunctional chitosan hydrogel dressing for liver hemostasis and infected wound healing. *Carbohydr. Polym.* 291, 119631. doi:10.1016/j.carbpol.2022.119631

Yang, Y., Zhang, H., Zeng, F., Jia, Q., Zhang, L., Yu, A., et al. (2022). A quaternized chitin derivatives , egg white protein and montmorillonite composite sponge with antibacterial and hemostatic effect for promoting wound healing. *Compos. Part B* 234, 109661. doi:10.1016/j.compositesb.2022.109661

You, J., Xie, S., Cao, J., Ge, H., Xu, M., Zhang, L., et al. (2016). Quaternized chitosan/poly(acrylic acid) polyelectrolyte complex hydrogels with tough, self-recovery, and tunable mechanical properties. *Macromolecules* 49, 1049–1059. doi:10.1021/acs.macromol.5b02231

Yu, Y., Li, P., Zhu, C., Ning, N., Zhang, S., and Vancso, G. J. (2019). Multifunctional and recyclable photothermally responsive cryogels as efficient platforms for wound healing. *Adv. Funct. Mat.* 29, 1904402–1904411. doi:10.1002/adfm.201904402

Yuan, Y., Ding, L., Chen, Y., Chen, G., Zhao, T., and Yu, Y. (2022). Nano-silver functionalized polysaccharides as a platform for wound dressings: A review. *Int. J. Biol. Macromol.* 194, 644–653. doi:10.1016/j.ijbiomac.2021.11.108

Yusof, M. R., Shamsudin, R., Abdullah, Y., Yalcinkaya, F., and Yaacob, N. (2018). Electrospinning of carboxymethyl starch/poly(L-lactide acid) composite nanofiber. *Polym. Adv. Technol.* 29, 1843–1851. doi:10.1002/pat.4292

Zhao, X., Guo, B., Wu, H., Liang, Y., and Ma, P. X. (2018). Injectable antibacterial conductive nanocomposite cryogels with rapid shape recovery for noncompressible hemorrhage and wound healing. *Nat. Commun.* 9, 2784. doi:10.1038/s41467-018-04998-9

Zhao, X., Wang, T., Qian, S., Liu, X., Sun, J., and Li, B. (2016). Silicon-doped titanium dioxide nanotubes promoted bone formation on titanium implants. *Int. J. Mol. Sci.* 17, 292. doi:10.3390/ijms17030292

Zhao, X., Wu, H., Guo, B., Dong, R., Qiu, Y., and Ma, P. X. (2017). Antibacterial anti-oxidant electroactive injectable hydrogel as self-healing wound dressing with hemostasis and adhesiveness for cutaneous wound healing. *Biomaterials* 122, 34–47. doi:10.1016/j.biomaterials.2017.01.011

Zong, B., Li, X., Xu, Q., Wang, D., Gao, P., and Zhou, Q. (2022). Enhanced eradication of *Enterococcus faecalis* biofilms by quaternized chitosan-coated upconversion nanoparticles for photodynamic therapy in persistent endodontic infections. *Front. Microbiol.* 13, 909492–909514. doi:10.3389/fmicb.2022.909492

frontiers | Frontiers in Bioengineering and Biotechnology

TYPE Original Research
PUBLISHED 26 January 2023
DOI 10.3389/fbioe.2023.1130315

OPEN ACCESS

EDITED BY
Yong Liu,
University of Chinese Academy of Sciences, China

REVIEWED BY
Miao Zhang,
Qingdao University, China
Jue Ling,
Nantong University, China

*CORRESPONDENCE
Yanzhong Zhang,
yzzhang@dhu.edu.cn

SPECIALTY SECTION
This article was submitted to Biomaterials, a section of the journal Frontiers in Bioengineering and Biotechnology

RECEIVED 23 December 2022
ACCEPTED 12 January 2023
PUBLISHED 26 January 2023

CITATION
Wang X, Zhang Z, Qin C, Guo X and Zhang Y (2023), Shape-memory responses compared between random and aligned electrospun fibrous mats.
Front. Bioeng. Biotechnol. 11:1130315.
doi: 10.3389/fbioe.2023.1130315

Shape-memory responses compared between random and aligned electrospun fibrous mats

Xianliu Wang[1], Zhaowenbin Zhang[1], Chunping Qin[1], Xuran Guo[1] and Yanzhong Zhang[1,2,3]*

[1]College of Biological Science and Medical Engineering, Donghua University, Shanghai, China, [2]Shanghai Engineering Research Centre of Nano-Biomaterials and Regenerative Medicine, Donghua University, Shanghai, China, [3]China Orthopaedic Regenerative Medicine Group (CORMed), Hangzhou, China

Significant progress has been made in the design of smart fibers toward achieving improved efficacy in tissue regeneration. While electrospun fibers can be engineered with shape memory capability, both the fiber structure and applied shape-programming parameters are the determinants of final performance in applications. Herein, we report a comparison study on the shape memory responses compared between electrospun random and aligned fibers by varying the programming temperature T_{prog} and the deforming strain ε_{deform}. A PLLA–PHBV (6:4 mass ratio) polymer blend was first electrospun into random and aligned fibrous mat forms; thereafter, the effects of applying specific T_{prog} (37°C and 46°C) and ε_{deform} (30%, 50%, and 100%) on the morphological change, shape recovery efficiency, and switching temperature T_{sw} of the two types of fibrous structures were examined under stress-free condition, while the maximum recovery stress σ_{max} was determined under constrained recovery condition. It was identified that the applied T_{prog} had less impact on fiber morphology, but increasing ε_{deform} gave rise to attenuation in fiber diameters and bettering in fiber orientation, especially for random fibers. The efficiency of shape recovery was found to correlate with both the applied T_{prog} and ε_{deform}, with the aligned fibers exhibiting relatively higher recovery ability than the random counterpart. Moreover, T_{sw} was found to be close to T_{prog}, thereby revealing a temperature memory effect in the PLLA–PHBV fibers, with the aligned fibers showing more proximity, while the σ_{max} generated was ε_{deform}-dependent and 2.1–3.4 folds stronger for the aligned one in comparison with the random counterpart. Overall, the aligned fibers generally demonstrated better shape memory properties, which can be attributed to the macroscopic structural orderliness and increased molecular orientation and crystallinity imparted during the shape-programming process. Finally, the feasibility of using the shape memory effect to enable a mechanoactive fibrous substrate for regulating osteogenic differentiation of stem cells was demonstrated with the use of aligned fibers.

KEYWORDS

shape-memory polymers, electrospinning, temperature memory effect, osteogenic differentiation, mechanoactive scaffold

1 Introduction

Shape-memory polymers (SMPs) are highly morphologically responsive active materials (Huang et al., 2012), which are typically characterized by the shape recovery capability if having the polymers prior shape-programmed to any possible temporary shapes and later on stimulated to revert by applying certain environmental stimuli [e.g., heat (Lendlein and Kelch, 2002), light (Xie et al., 2018), and ultrasound (Bao et al., 2013)]. When the SMPs

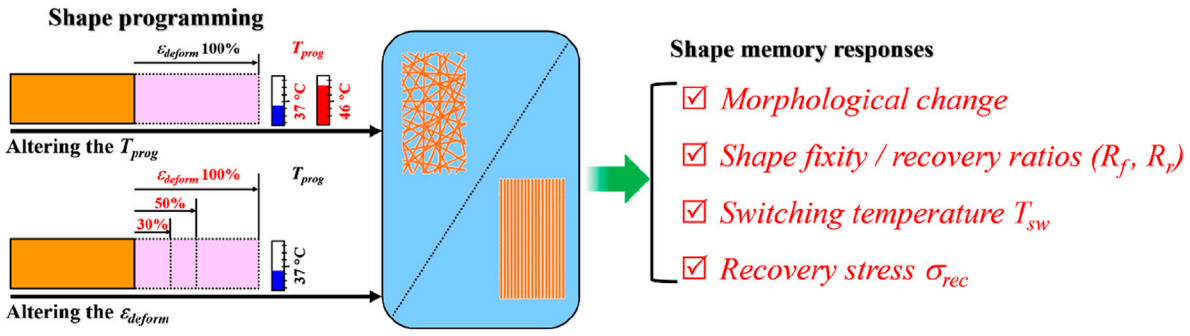

GRAPHICAL ABSTRACT

are produced in fibrous form and endowed with shape memory functionality by shape-programming, they give rise to a new type of functional fiber—shape-memory polymer fibers (SMPfs). Due to the intrinsic advantages in fibrous materials, such as high specific surface area, adjustable porosity, excellent mechanical properties, and structural designability, SMPfs have found a plethora of applications in textiles (Hu et al., 2012; Leist et al., 2017; Veloso-Fernandez et al., 2021), electronics (Dubal et al., 2018), aeronautics (Ahmed et al., 2021), and biomedical engineering, aimed for attaining enhanced functionalities (Lendlein et al., 2010; Zhao et al., 2019). Given that the shape memory performance of SMPs is closely correlated with their shape-memory creation procedure (SMCP) or shape-programming, an in-depth understanding on the influences of shape-programming parameters, in particular, the programming temperature T_{prog} and deforming (or programming) strain ε_{deform}, on shape memory responses in SMPfs is essential.

Electrospinning has been widely recognized as one of the most efficient enabling nanotechnologies to produce ultrafine fibers at micro/nanoscale fineness. In the past decade, SMPfs from electrospinning have drawn a great deal of attention toward multifunctional applications, particularly in the fields of tissue engineering and regenerative medicine (Bao et al., 2014; Bao et al., 2016; Guo et al., 2022; L.-F. Tseng et al., 2013; Wang et al., 2020; Zhang et al., 2017). Just like routine SMPs, the performance of electrospun SMPfs is mainly defined by a few key shape-memory-responsive parameters, such as the shape fixity ratio (R_f, the capability to fix the deformed shape) and shape recovery ratio (R_r, the capability to recover the original shape), the switching temperature (T_{sw}, the temperature above which the action of shape recovery takes place instantly), and the shape recovery stress (σ_{rec}, the mechanical stress generated while the shape recovery action is activated under constrained recovery condition). Since electrospun fibers can be typically produced into random and aligned fibrous mat forms, a comparative study with respect to the shape-memory responses between the two types of fibrous structure is necessary, from which targeted applications with such SMPfs can be rationally designed.

Previously, we have demonstrated that incorporation of a small amount of poly(3-hydroxybutyrate-*co*-3-hydroxyvalerate) (PHBV) into poly($_L$-lactic acid) (PLLA) fibers resulted in significant improvement on the shape memory performance of PLLA (Wang et al., 2021). Here, using the electrospun PLLA–PHBV hybrid system as a model fibrous material, we performed a comparative study on the shape-memory responses compared between the random and aligned fibrous mats while having them shape-programmed using two sets of programming schemes (i.e., varying T_{prog} or ε_{deform}, Figure 1). Finally, the aligned fibrous mat of PLLA–PHBV was chosen to demonstrate the feasibility of using the integrated shape-memory effect (SME) to direct osteogenic differentiation of bone mesenchymal stem cells (BMSCs) *in vitro*.

2 Materials and methods

2.1 Electrospinning of random and aligned fibrous mats

The polymer blend of PLLA (M_v = 100,000 Da, DaiGang Biomaterial, Jinan, China) and PHBV (M_w = 520, 000 Da TianAn Biologic, Ningbo, China) at a mass ratio of 6:4 was electrospun into random fibrous mats (named random) and aligned fibrous mats (named aligned) by conventional electrospinning and stable jet electrospinning (SJES) methods (Yuan et al., 2012), respectively. In brief, 0.2 g of PHBV was added to 4.5 mL of trichloromethane (purity ≥99.0%, Changshu Yang-Park Chemicals, Changshu, China). The PHBV solution was subsequently heated to 65°C under stirring for 5 min, followed by adding 0.3 g of PLLA to obtain a homogeneous PLLA–PHBV solution. Last, a volume of 0.5 mL of N,N-dimethylformamide (purity ≥99.0%, Changshu Yang-Park Chemicals, Changshu, China) was introduced into the PLLA–PHBV solution to formulate the final polymer concentration of 10% w/v. Afterward, electrospinning was conducted as per the variables listed in Table 1. All the obtained fibrous mats were dried in vacuum at room temperature (23 ± 2°C).

2.2 Characterization of the as-electrospun random and aligned fibrous mats

2.2.1 Scanning electron microscopy

Surface morphology of the fibrous mats was observed by SEM (scanning electron microscopy) (FEI Quanta 250, Czech) at an accelerating voltage of 10 kV. Prior to imaging, the samples were subjected to sputter coating with a thin layer of gold for better conductivity. Upon acquiring the SEM images, fiber diameters were measured directly from the images using the ImageJ software, and 2D fast Fourier transform (FFT) was used to analyze the images and quantify the degree of fiber orientation through an oval profile plug-in (Ayres et al., 2008).

TABLE 1 Parameters used for electrospinning aligned and random fibrous mats.

	Applied voltage (kV)	Solution feed rate (mL/h)	Collecting distance (cm)	Drum rotating speed (rpm)	Ambient temperature (°C)/ humidity (%)
Aligned	7–9	0.5	3–6	1,000	20–30/40–50
Random	14–16	1	15–20	—	20–30/40–50

2.2.2 Polarized Fourier transform infrared spectroscopy

The molecular orientation of the two types of fibrous mats was assessed by P-FTIR (polarized Fourier transform infrared spectroscopy) (Nicolet NEXUS 670 FTIR spectrometer, Thermo Fisher Scientific) (Wang et al., 2006), in which a PerkinElmer polarized wire grid over the range of 800–2,000 cm^{-1} at a scanning resolution of 2 cm^{-1} was used. Dichroic ratio (D_r) for the specific absorption bands of the molecular chains within the PLLA–PHBV constituents can be calculated by Formula 1:

$$D_r = \frac{A_{//}}{A_{\perp}}, \quad (1)$$

where $A_{//}$ and $A_{\perp}$ represent the peak absorption of infrared radiation polarized parallel and perpendicular to the fiber direction, respectively.

2.2.3 X-ray diffraction

The crystalline structure of the two types of fibrous mats was examined by an X-ray diffractometer (Rigaku, Japan) using Cu–Kα radiation. Crystallinity was calculated from the ratio of the integrated area of all crystalline peaks to the total integrated area under the XRD (X-ray diffraction) peaks after background subtraction.

2.2.4 Tensile test

The tensile properties of the two types of fibrous mats were assessed using a universal material testing machine (H5K-S, Hounsfield, United Kingdom) equipped with a 50-N load cell. A constant strain rate of 50%/min was used to stretch the samples at room temperature (n = 5). Ultimate tensile strength, Young's modulus, and fracture strain were determined from the generated stress–strain curves.

2.2.5 Dynamic mechanical analysis

Phase transition temperatures of the two types of fibrous mats were detected by DMA (dynamic mechanical analysis) (Q800, TA Instruments) in the multi-frequency strain mode. Briefly, rectangular fibrous mat samples (dimension: 10 × 5 × 0.06 mm) were stretched in the temperature sweep mode (applied oscillation frequency: 10 Hz) from −50 to 120°C with a constant heating rate of 1°C min^{-1}. Phase transition temperatures can be scrutinized and accordingly determined at the peak maximum of the tan δ *vs*. temperature curves.

2.3 Examination of the SME-resultant morphological changes and mechanostructural properties

Rectangular fibrous samples (named Original dimension: 20 × 10 × 0.06 mm) were divided into different groups and deformed by stretching in warm water (37°C and 46°C) to the predesignated strain (ε_{deform} = 30%, 50%, and 100%), followed by shape-fixing without releasing the applied stress in a 4°C refrigerator (thus, deformed samples were named deformed). The so-programmed fibrous samples can be actuated to recover in warm water (37°C and 46°C); thus, recovered samples were named recovered. Fiber morphology, structural analysis, and tensile properties of the original, deformed, and recovered samples were examined as follows.

2.3.1 Morphological observation

Morphological features including mainly fiber diameter and fiber orientation (defined as the degree to which fibers deviated from the tensile-loading direction) of the original, deformed, and recovered samples were similarly examined through SEM imaging as performed in 2.2.1 and quantitatively analyzed by the ImageJ software.

2.3.2 Structural analysis

To examine the effect of shape-programming on the crystalline structure within the polymer fibers, the diffraction peaks and crystallinity of the original and deformed (ε_{deform} = 30%, 50%, and 100%) samples were similarly examined through XRD as performed in 2.2.3.

2.3.3 Tensile test

The original and deformed (ε_{deform} = 30%, 50%, and 100%) samples were stretched at a strain rate of 50%/min by the aforementioned testing machine equipped with a 50-N load cell at room temperature. Young's modulus can be computed accordingly from the generated stress–strain curves.

2.4 Determination of shape recovery ability by DMA

Shape recovery ability under the variation of pre-designated programming parameters (i.e., T_{prog} and ε_{deform} shown in Figure 1) was assessed by DMA. In general, each test cycle was consisted of three steps in sequence: stretching to deform into a temporary shape at the deforming temperature, having the deformed shape fixed at low temperature, and applying thermal stimulus to trigger the shape recovery. Specific procedures for performing the shape memory tests regulated by T_{prog} and ε_{deform} are depicted as follows.

Shape memory tests regulated by T_{prog}: 1) At a high temperature T_{high} of 60°C, the fibrous mat sample was stretched using a strain ramp rate of 2%/min to 10% strain (ε_{begin}); 2) the temperature was cooled down from T_{high} to T_{prog} (i.e., 37°C or 46°C) at 3°C/min; 3) at T_{prog}, the sample was stretched to 100% strain (ε_{deform}) at a ramp rate of 4%/min; 4) at the 100% strain, the temperature was

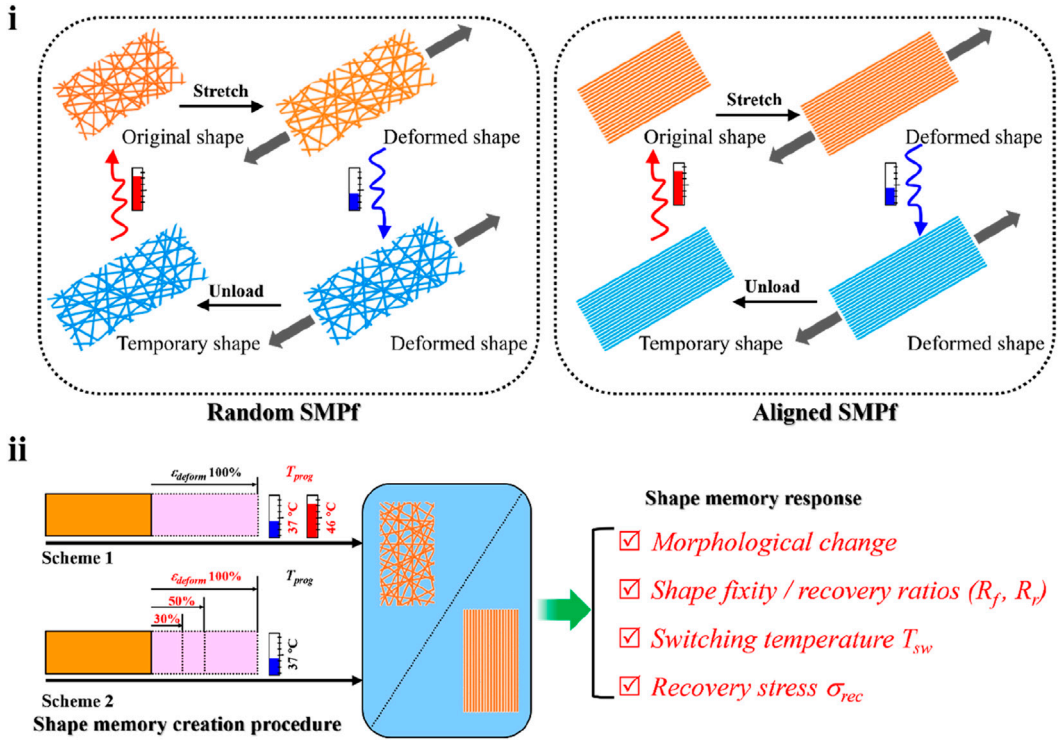

FIGURE 1
Study design overview. (i) Typical shape memory cycles including the SMCP and thermal-triggered shape recovery for the random (left) and aligned (right) fibrous mats. (ii) Comparative study on shape-memory responses including morphology change, shape fixity, recovery ratios (i.e., R_f and R_r), switching temperature T_{sw}, and recovery stress σ_{rec} regulated by two sets of programming schemes, namely, 1) altering the programming temperature T_{prog} (i.e., 37°C and 46°C) at the stretch deforming strain ε_{deform} of 100% and 2) altering ε_{deform} (i.e., 30%, 50%, and 100%) at T_{prog} of 37°C.

decreased to a low temperature T_{low} of 0°C at 3°C/min for vitrification; 5) at 0°C, the applied stress was released to 0, from which the fixed strain (ε_{fix}) can be obtained; and 6) the recovered strain (ε_{final}) was determined by reheating the temperature to the T_{high} of 60°C for activating shape recovery. Based on the generated strain–temperature curves, a particular T_{sw} can be determined by finding the inflection point (corresponding to the maximum recovery speed) through differentiation, and R_f and R_r were calculated according to Formulas 2, 3, respectively:

$$R_f(\%) = \frac{\varepsilon_{fix} - \varepsilon_{begin}}{\varepsilon_{deform} - \varepsilon_{begin}} \times 100\%; \quad (2)$$

$$R_r(\%) = \frac{\varepsilon_{deform} - \varepsilon_{final}}{\varepsilon_{deform} - \varepsilon_{begin}} \times 100\%. \quad (3)$$

Shape memory tests regulated by ε_{deform}: 1) At T_{high} of 60 °C, the fibrous mat sample was stretched at 2%/min to 10% strain (ε_{begin}); 2) the temperature was cooled down from T_{high} to T_{prog} of 37°C at 3°C/min; 3) at 37°C, the sample was stretched using a strain ramp rate of 4%/min to ε_{deform} of 30%, 50%, or 100%; 4) at the same designated strain, the temperature was decreased to the T_{low} of 0°C at 3°C/min for vitrification; 5) at 0°C, the stress was released to 0, from which the fixed strain ε_{fix} was obtained; and 6) the sample was reheated to T_{prog} of 37°C and then maintained for *ca.* 3 h, during which a plot depicting the kinetics of deformed strain versus time can be generated. Normalization to 100% strain percentage was performed for the cases where ε_{deform}=30%, 50%, and 100%.

2.5 Determination of the shape recovery stress

Similar to the procedure described in **2.3**, the fibrous mat samples deformed to the predesignated strain (ε_{deform} = 10–100% at a 10% interval) were prepared in 37°C warm water, followed by shape-fixing in a 4°C refrigerator. Thereafter, upon being triggered to recover in 37°C warm water, the maximal recovery stress σ_{max} of the deformed samples with their two ends fixed by clamps can be measured using a 5-N force gauge.

2.6 Proof-of-concept biological test

2.6.1 Cell culture

Primary rat BMSCs were isolated from the bone marrow of 4-week-old male SD rats with the approval of the Animal Ethics Committee of Donghua University (No. 20140022). The obtained BMSCs were cultured in α-MEM supplemented with 10% (v/v) fetal bovine serum (FBS) and 1% (v/v) penicillin–streptomycin solution. The culture medium was refreshed every 2 days.

2.6.2 Cell culture involving the *in situ* applied SME

BMSC-laden aligned fibrous scaffolds, prior sterilized by ethanol for 2 h and medium soaking overnight, were placed in a 6-well plate with 2 mL medium per well for 1 day of cultivation and then subjected

TABLE 2 Primer sequences used for qRT-PCR gene expression analysis.

Gene	Forward primer sequence (5′-3′)	Reverse primer sequence (5′-3′)
Runx2	TCCGCCACCACTCACTA	GGACGCTGACGAAGTACC
Alp	CCGCAGGATGTGAACTACT	GGTACTGACGGAAGAAGGG
Ocn	ACCGAGACACCATGAGAGC	GCTGCACCTTTGCTGGA
GAPDH	TGGAATTGTGAGGGAGATG	GCCCAGCAAGGATACTGA

to shape-programming in a Bose ElectroForce BioDynamic 5200 multi-chamber bioreactor. In brief, the cell-seeded fibrous scaffold was stretched in 37°C culture medium to 10% strain for 30 min (named Aligned 10%), followed by shape-fixing in 25°C culture medium for 1 h. Then, the temperature was increased to 37°C to trigger constrained shape recovery (Cui et al., 2011; Guo et al., 2022) in the scaffold for 4 h. Afterward, the cell–scaffold construct was moved to a 6-well plate for continuous culturing under stress-free condition. The previously described process was repeated at 3, 5, and 7 days. For comparison, the aligned fibrous scaffold seeded with BMSCs for cultivation but without undergoing the previously mentioned shape-programming process was used as a control and named Aligned 0%.

2.6.3 Cell morphology

BMSCs were seeded onto the fibrous scaffolds at a density of 1×10^5 cells/well in a 6-well plate. After 4 and 8 days of culture, the cell–scaffold constructs were washed three times with PBS and fixed in 2.5% glutaraldehyde at 4°C overnight. After being washed three times in distilled water, the constructs were dehydrated with gradient alcohol concentrations (25%, 50%, 75%, 85%, 95%, and 100% for 15 min each), followed by immersion in tertiary butanol for 10 min. Afterward, the constructs were freeze-dried and coated with gold for morphological observation by SEM.

2.6.4 Cell proliferation

BMSCs were seeded onto the fibrous scaffolds at a density of 1×10^5 cells/well in a 6-well plate. Cell proliferation was monitored by performing MTT (3-(4,5-dimethylthiazol-2-y1)-2,5-diphenyltetrazolium bromide) assay after 1, 4, 8, and 12 days of cultivation. Briefly, the medium was removed to have the constructs washed with PBS three times, and then 1 mL of medium and 100 μL of MTT (5 mg/mL) were added to each well. The plate was then incubated for 4 h, followed by removing the mixed solution of medium and MTT, adding 1 mL of dimethyl sulfoxide to each well, and pipetting up and down to dissolve crystals in dark. Finally, the solutions were transferred to a microplate reader (MK3, Thermo Fisher Scientific, USA) for absorbance measurements at 570 nm.

2.6.5 Alkaline phosphatase activity

BMSCs were seeded onto the fibrous scaffolds at a density of 1×10^5 cells/well in a 6-well plate. At days 8 and 21, the constructs were trypsin-treated to detach the cells for seeding into 24-well plates for ALP (alkaline phosphatase) staining. Briefly, after being fixed in 2.5% glutaraldehyde for 10 min on ice, the cells were incubated in a mixture of nitroblue tetrazolium and 5-bromo-4-chloro-3-indolylphosphate working solution (Alkaline Phosphatase Staining Kit, Beyotime, Shanghai, China) for 20 min. The reaction was stopped by removing the working solution and rinsing with PBS. Stained cells were visualized using an inverted optical microscope (ECLIPSE Ti-S, Nikon, Japan).

2.6.6 Quantification of calcium deposits

BMSCs were seeded onto the fibrous scaffolds at a density of 1×10^5 cells/well in a 6-well plate. The Calcium (CPC) LiquiColor Test (StanBio, USA) was used to quantify the calcium deposition of cells cultured for 8, 14, and 21 days according to the manufacturer's instructions. In brief, the constructs were washed with PBS (free of calcium and magnesium ions) and treated with 0.5 N hydrochloric acid, and then cells were scraped and collected into an appropriate centrifuge tube. After shaking for 3 h with an orbital shaker, the cells were centrifuged, and the supernatant was transferred into a new centrifuge tube followed by adding ortho-cresolphthalein complexone (OCPC). The optical absorbance was then measured using a microplate reader (BioTek, USA) at a wavelength of 550 nm.

2.6.7 Gene expression analysis

BMSCs at a density of 1×10^5 cells/well in a 6-well plate were seeded onto the fibrous scaffolds for 1, 8, and 21 days of culture. After total RNA extraction using TRIzol reagent (Invitrogen, USA), amplifications were performed with different primers (Table 2). The quality and quantity of the obtained RNA were subjected to spectrophotometric analysis using a bio-photometer (Thermo Scientific, NanoDrop 2000). The RNA was then reverse-transcribed onto complementary DNA (cDNA) using a reverse transcription kit (Takara, Japan). Quantitative real-time polymerase chain reaction (qPCR) was performed with the SYBR Green PCR reagent kit (Roche, Germany) on an ABI Prism 7500 (Applied Biosystems, USA). The comparative expression level (fold change) was obtained by transforming the logarithmic values into absolute values using the $2^{-\triangle\triangle Ct}$ method (Livak and Schmittgen, 2001).

2.7 Statistical analysis

Quantitative data are generally presented as mean ± standard deviation and checked by normality tests. Statistical analysis was performed using the Origin software (OriginLab, Northampton, MA, USA). One-way ANOVA with *post hoc* Tukey's HSD test was used to make pairwise comparisons between groups. $^*p < 0.05$, $^{**}p < 0.01$, or $^{***}p < 0.001$ is considered to be statistically significant.

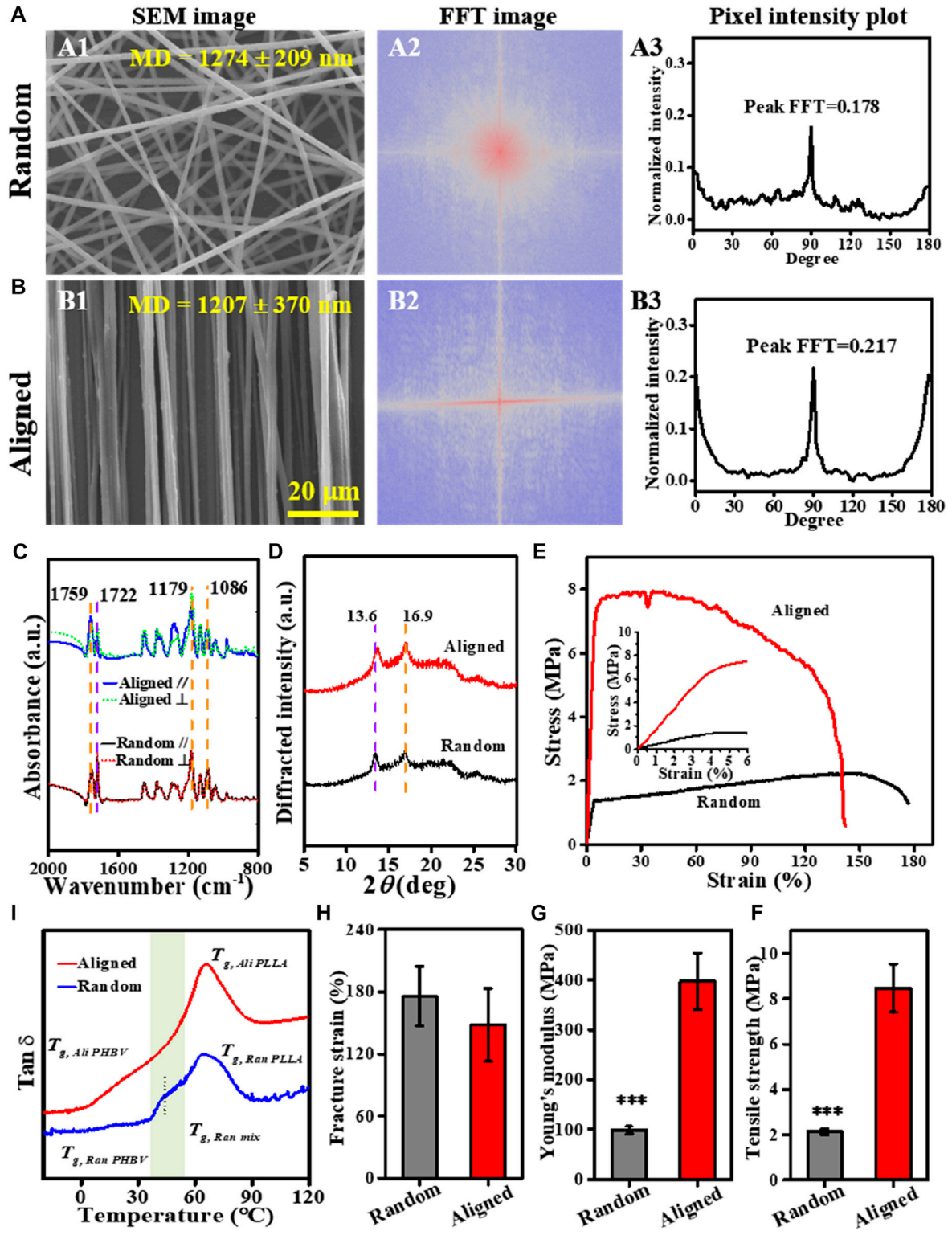

FIGURE 2
Characterization of the PLLA–PHBV based on random and aligned fibrous mats. **(A, B)** Alignment analysis of the electrospun fibers: SEM images (A1 and B1), FFT output images (A2 and B2), and pixel intensity plots (A3 and B3). **(C)** Polarized FTIR spectra [The black and blue lines are obtained with the beam polarized parallel to the fiber axis ($A_{//}$), whereas the dotted red and green lines are obtained with the beam polarized perpendicular to the fiber axis ($A_{\perp}$)]. **(D)** XRD patterns. **(E–H)** Tensile tests showing typical stress–strain curves, tensile strength, Young's modulus, and fracture strain, respectively. **(I)** Tan δ–temperature curves *via* DMA.

3 Results and discussion

3.1 Characterization of the as-electrospun fibrous mats

Both random and aligned fibers of the PLLA–PHBV blend with comparable diameters (1,274 ± 209 nm *vs.* 1,207 ± 370 nm) could be readily produced using the conventional electrospinning and SJES methods, respectively (Figures 2A1, B1). The FFT output images (graphical depiction of FFT frequency, Figures 2A2, B2) and the derived pixel intensity plots (Figures 2A3, B3) indicate that, compared to the random group, a distinctly higher degree of fiber anisotropy is noted in the aligned group by showing concentrated pixels mainly in a cross-like style and a sharp peak (Ayres et al., 2006; Ayres et al., 2007). At the molecular level, the P-FTIR results (Figure 2C) show strong molecular orientation of the polymer chains within the aligned fibers, as there were pronounced differences in absorbance intensity in the directions parallel and perpendicular to the fiber alignment. This is true either for the characteristic C-O-C symmetric stretch at 1,086 cm^{-1}, OC-O asymmetric stretch at 1,179 cm^{-1}, and C=O vibration at 1,759 cm^{-1} in PLLA (Zhang et al., 2010) or the C=O stretch at 1,722 cm^{-1} ascribed to PHBV (Furukawa et al., 2005). However, the polarized measurements in the ⊥ and // directions were almost identical in the case of random fibers. The quantitative dichroic ratios (D_r) with respect to the aligned group, showing values of higher deviation from the data of 1.00 (Supplementary Table S1), support the observed enhancement of molecular orientation in the aligned fibers (Chan et al., 2009; Wang et al., 2006). Such an enhancement in molecular orientation can be attributed to the SJES technique itself (Yuan et al., 2012; Zhang & Zhang, 2016) and the strong stretching exerted by the high-speed rotating drum. A higher extent of molecular orientation benefits the formation of more crystalline structures (Figure 2D). This was also evidenced by the appearance of reflection peaks at 2θ = 16.9 and 2θ = 13.6, corresponding to the (110) and (020) crystal planes of PLLA (Sun, Yu, Zhuang, Chen, & Jing, 2011; Zembouai et al., 2013) and PHBV (Zembouai et al., 2013; Montanheiro et al., 2019), respectively. Obviously, the characteristic peak intensities in the XRD pattern of the aligned group are higher than those in the random group. As anticipated, due to the macroscopic and molecular orientation, aligned fibers exhibited superior mechanical properties (Figures 2E–H) than the random counterpart. Despite a slightly lower fracture strain, the aligned fibers are about 4-fold stronger in tensile strength (i.e., 8.5 ± 1.1 *vs.* 2.1 ± 0.1 MPa, $p < 0.001$) and Young's modulus (i.e., 397.4 ± 56.3 *vs.* 98.8 ± 7.6 MPa, $p < 0.001$) than the random fibers.

Thermal-responsive SMPs usually rely on the thermal transition (e.g., glass transition temperature T_g) to determine the temperature window for shape-programming. Figure 2I shows the tan δ–temperature curves of the random and aligned fibers non-isothermally scanned *via* DMA. Clearly, either the random or the aligned fibers exhibited a pretty broad thermal transition region with the maximum peak at *ca.* 65°C, which can be ascribed to T_g of the dominant constituent PLLA ($T_{g,\ PLLA}$) within the PLLA–PHBV blend (Nanda et al., 2011; Jaszkiewicz et al., 2013; Li et al., 2015). A further subtle scrutinization below $T_{g,\ PLLA}$ revealed the presence of an indistinct peak around 18°C attributed to T_g of PHBV ($T_{g,\ PHBV}$) (Nanda et al., 2011; Jaszkiewicz et al., 2013) and a relaxation process with the peak maximum at 43.7°C in the range from 36°C to 54°C, indicative of T_g of the mixed phase ($T_{g,\ mix}$) (Nanda et al., 2011), especially in the case of random. Although the much higher $T_{g,\ PLLA}$ does not allow adaptation of T_{sw} for shape recovery up to the physiologically relevant temperature, choosing T_{prog} in the vicinity of $T_{g,\ mix}$ of PLLA–PHBV would afford an alternative strategy to easily adjust T_{sw} due to the well-documented temperature-memory effect (TME) (Miaudet et al., 2007; Kratz et al., 2011; Kratz et al., 2012). In this sense, 37°C and 46°C (slightly above body temperature) in the range of $\Delta T_{g,\ mix}$ for the mixed phase (i.e., 36–54°C) can be chosen as T_{prog} for our subsequent shape-memory response studies.

TABLE 3 Crystallinity of Deformed and Original measured by XRD for random and aligned.

Sample		$X_{c\ PLLA}$ (%)	$X_{c\ PHBV}$ (%)	$X_{c\ Overall}$ (%)
Random	Original	1.3	3.4	4.8
	30% deform	1.7	3.4	5.1
	50% deform	2.0	3.3	5.3
	100% deform	2.0	3.8	5.9
Aligned	Original	3.7	6.4	10.1
	30% deform	6.2	6.1	12.3
	50% deform	7.8	6.2	14.0
	100% deform	14.5	6.8	21.3

3.2 Effects of shape-programming parameters on fiber morphology

For shape-memory polymer fibers, stretching deformation to generate a temporary shape usually results in a reduction in fiber fineness together with improved fiber orientation along the loading direction; and upon being triggered for shape recovery, the morphological features of the original fibrous structure can be generally recovered (Figures 3A, B). This was verified in our current study by varying T_{prog} and ε_{deform}. As shown in Figures 3C, D summarized from the SEM quantification data (Supplementary Figures S1A–F), under the deforming conditions of stretching in warm water (37°C and 46°C), for instance, 100% of ε_{deform}, it gave rise to fiber diameter attenuation by 16–21% in random, slightly larger than that of aligned (15–18%). Also, a higher magnitude of improvement in fiber orientation was observed in the random group (16–18%) than in the aligned group (<1%). In terms of shape recovery, while the fiber thickness and orientation features of the aligned fibers could be largely reverted, small differences in morphological restoration can be noted in the random fibers.

Mechanistically, apart from the macroscopic differences in their fibrous architectures (Figures 2A, B), the initial status of molecular orientation (Figure 2C) and the stretching deformation resultant enhancement in crystallization may also be responsible for the different responses in the previously noted morphological changes. Taking the stretching deformation for shape-programming at 37°C for illustration (Figures 3E, F), due to the strain-induced crystallization effect (Tabatabaei et al., 2009; Tcharkhtchi et al., 2014; Nissenbaum et al., 2020), the increments of polymer crystallites formed in overall

10.3389/fbioe.2023.1130315

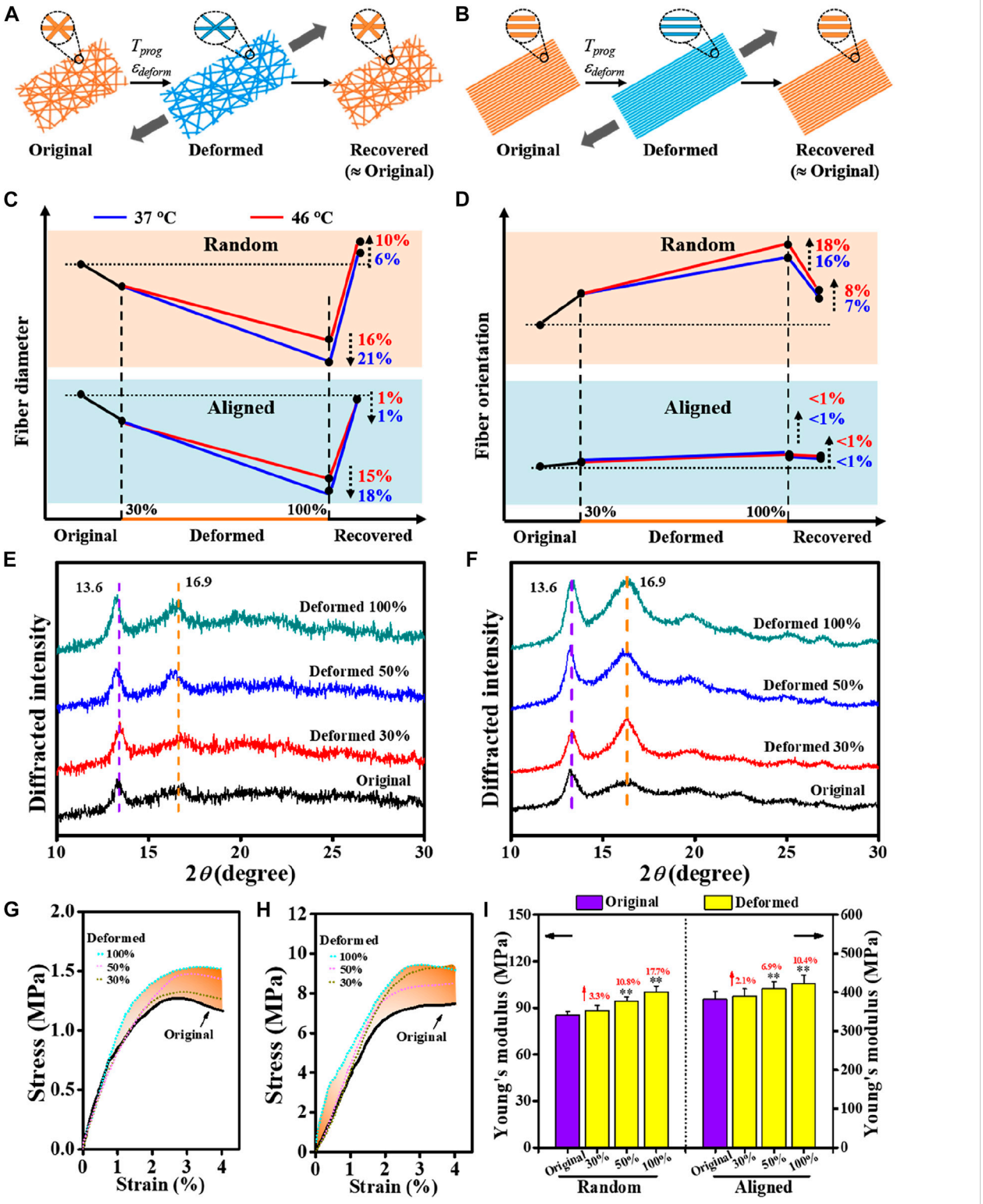

FIGURE 3
Comparative study on morphology changes regulated by shape-programming parameters between random and aligned fibers. **(A, B)** Schematics of morphology changes in a complete shape memory cycle. **(C, D)** Dynamic changes in fiber diameter and fiber orientation regulated by shape-programming. **(E, F)** XRD patterns due to applying ε_{deform} varied in 30%, 50%, and 100% at T_{prog} of 37°C **(E)** for random and **(F)** for aligned). **(G, H)** Representative tensile stress–strain curves of original and deformed (G for random and H for aligned). **(I)** Young's moduli derived from **(G)** and **(H)**.

TABLE 4 Shape-memory properties of random and aligned determined in cyclic shape memory tests by DMA.

	T_{prog} (°C)	ε_{begin} (%)	ε_{deform} (%)	ε_{fix} (%)	ε_{final} (%)	R_f (%)	R_r (%)	T_{sw} (°C)	T_{sw}/T_{prog}
Random	37	10	100	96.8	32.1	96.4	75.4	39.4	1.06
	46	10	100	98.1	36.0	97.9	71.1	47.7	1.04
Aligned	37	10	100	96.0	32.1	95.6	75.4	38.2	1.03
	46	10	100	97.2	36.4	96.9	70.7	47.0	1.02

crystallinity at 100% of ε_{deform} could be increased by 22.9% and 110.9% (both mainly contributed by the PLLA crystalline phase, Table 3) for the random and aligned fibers, respectively. As a result, it also gave rise to the progressively strengthened elastic modulus and stiffness (Figures 3G–I; Supplementary Figure S2) if increasing ε_{deform} of both the random and aligned fibers during the stage of shape-programming. Collectively, these results demonstrated that the morphological changes were not dramatically influenced by T_{prog} but responded more to changes in ε_{deform}. The stretching deformation and recovery process could, therefore, be applied to control the diameter and orientation of the shape-memory-capable electrospun fibrous structures, which may provide a dynamic topography for modulating the cellular behavior (Ahn et al., 2014; Madl et al., 2021; Song et al., 2013).

3.3 Effects of shape-programming parameters on T_{sw}, R_f, and R_r

TME is the capability of a shape-memory polymer to memorize its thermomechanical history, in particular the T_{prog} at which it was deformed before, by reversing the deformation at a characteristic T_{sw} roughly identical to the previously applied T_{prog}. While the TME concept has been previously demonstrated in different material systems (Cui et al., 2011; Kratz et al., 2011; Miaudet et al., 2007; Xie et al., 2011), how well T_{sw} coordinates with T_{prog} in SMPfs remains to be understood. It has been known that temperature memory polymers usually exhibit a broad thermal transition temperature region ΔT_{trans} within which the T_{prog} applied for deformation can be memorized (Cui et al., 2010; Cui et al., 2011) during a specific SMCP. Based on the identified $\Delta T_{g,\,mix}$ for the mixed phase (Figure 2I), the effects of applying T_{prog} with physiological relevance (37°C and 46°C) at 100% of ε_{deform} on T_{sw}, R_f, and R_r were first examined (Figure 4A). A quantitative summary on the comparison of shape-memory properties between random and aligned (Table 4) indicates an impressive fixation of the deformation with $R_f > 95.0$, while $R_r > 70\%$ could be obtained. It is to be noted that the characteristic T_{sw}, defined by the temperature with the maximum recovery speed under stress-free conditions, was always slightly higher than T_{prog} (Figures 4B, C). As a proximity indicator, the much lower T_{sw}/T_{prog} ratios of 1.02–1.06 compared to other forms of SMPs (e.g., films) with $T_{sw}/T_{prog} \approx 1.3$ at 37°C reported in the literature (Cui et al., 2010) suggest superior thermal sensitivity of the fibrous structures due to their intrinsic attribute of high specific surface area (Lu et al., 2017). When making a comparison between random and aligned, the characteristic T_{sw} is closer to the applied T_{prog} in aligned. This can be ascribed to the better thermal conductivity in aligned fibers with structural features that include not only the high degree of macroscopic fiber alignment (Figures 2A, B) but also the increased molecular orientation and crystallinity (Figures 3E, F) (Shen et al., 2010; Lu et al., 2017; Bai et al., 2018). These results confirmed that the characteristic T_{sw} of TME can be more accurately correlated with T_{prog} for shape-memory polymer fibers, which could therefore permit a facile adjustment of T_{sw} according to specific biological application requirements (Kratz et al., 2012).

To examine whether varying ε_{deform} (30%, 50%, and 100%) would regulate the recovery ability of the two types of fibrous structures at body temperature, a further comparison between random and aligned fibers was then performed (Figure 4D). As shown in Figures 4E, F, depicting the recovery kinetics for random and aligned which were prior-deformed at different ε_{deform}, and upon being triggered at T_{prog} of 37°C, the shape recovery events can be activated for both. Notably, occurrences of the maximum recovery rates determined by differentiation to the normalized ε_{deform} curves in aligned fibers were shorter than those in random ones (aligned 8.5–10.7 min *vs.* random 9–11 min), and the recovered strain of aligned fibers during the testing time frame was always higher than that of random counterparts at the same ε_{deform}. Again, the observed better shape recovery performance in aligned fibers can be attributed to its high thermal conductivity and the underlying conducive molecular structures in connection. Consistent with previous investigations (Wong and Venkatraman, 2010; Wu et al., 2018; Zhao et al., 2017), in both cases, fibrous structures with increased ε_{deform} during the SMCP gave rise to decreased shape recovery efficiency.

3.4 Effect of deforming strain on recovery stress

The shape recovery process upon being triggered is usually accompanied by the release of the strain energy stored during deformation, which accordingly enables the generation of recovery stress (σ_{rec}) and other shape-memory responses. To compare the impact of varying ε_{deform} on the generated σ_{rec} between random and aligned, a pair of custom-made grips was used to fasten the fibrous mat sample for σ_{rec} measurement under constrained recovery condition (Figure 5A). This allowed producing a stress versus time curve showing a maximum stress point (σ_{max}) (Figure 5B). The presence of such a peak recovery stress under constrained recovery condition has also been observed previously for other SMPs (Cui et al., 2010; Kratz et al., 2011; Kratz et al., 2012). By plotting the σ_{max} versus ε_{deform} graphs (Figures 5C, D), it was revealed that σ_{max} could be systematically adjusted by variation of ε_{deform}, and the σ_{max} versus ε_{deform} correlations for random and

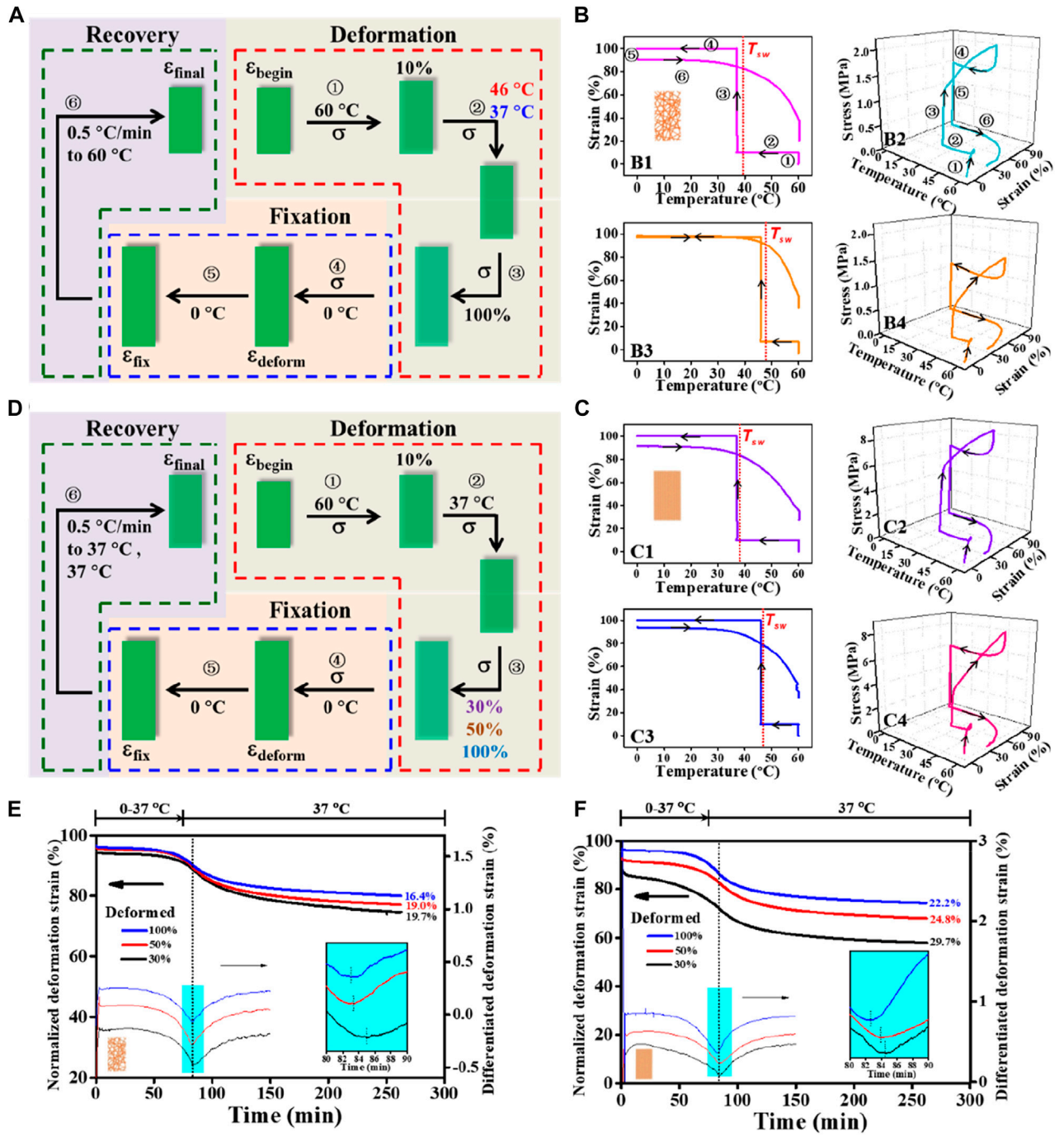

FIGURE 4
Comparative study on shape fixity, recovery ratios (i.e., R_f and R_r), and switching temperature T_{sw} regulated by T_{prog} and ε_{deform} between random and aligned fibers. **(A)** Schematic representation of a cyclic shape memory test protocol consisted of stretching deformation (T_{prog} varied at 37°C and 46°C; ε_{deform} = 100%), fixation, and recovery stages under stress-free condition. **(B, C)** Two-dimensional illustrations of strain–temperature and three-dimensional diagrams of stress–strain–temperature for random **(B)** and aligned **(C)** tested using the protocol depicted in **(A)**; T_{prog} used for B1, B2, C1, and C2 is 37°C and for B3, B4, C3, and C4 is 46°C. **(D)** Schematic representation of a cyclic shape memory test protocol consisted of stretching deformation (ε_{deform} varied at 30%, 50%, and 100%; T_{prog} = 37°C), fixation, and recovery stages under the stress-free condition. **(E, F)** Kinetics of the recovery process for random **(E)** and aligned **(F)** tested using the protocol depicted in **(D)**.

aligned could be mathematically well-fitted in polynomial and linear regressions, respectively. As the stress generated by shape recovery is a growing function of the strain energy stored during deformation at a high temperature (Miaudet et al., 2007), it is reasonable to observe continuous increases in σ_{max} with increasing ε_{deform}. In comparison, σ_{max} generated by aligned is significantly

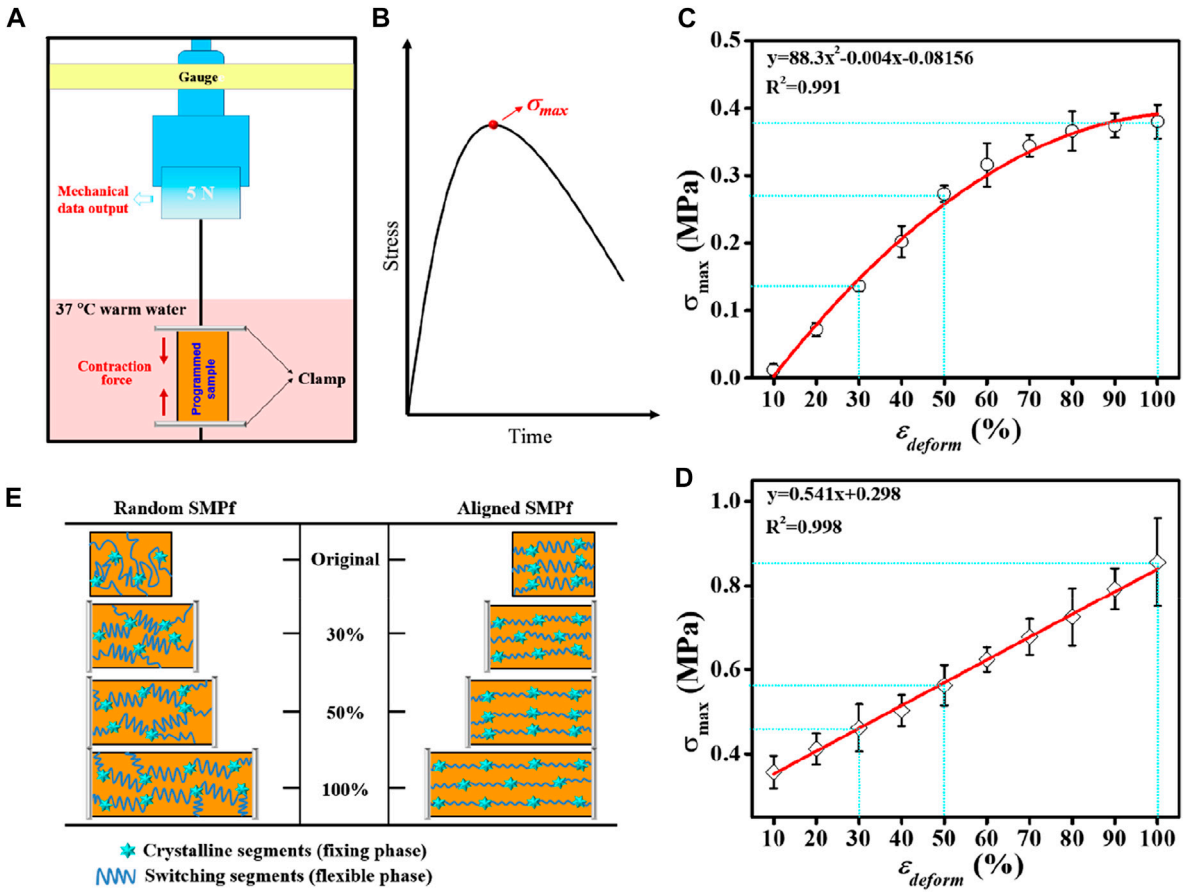

FIGURE 5
Comparative study on the shape recovery stress σ_{rec} regulated by the deforming strain ε_{deform} between random fibers and aligned fibers. **(A)** Schematic representation of the test device for σ_{rec} measurements. **(B)** Schematic representation of the stress–time curve from the constrained recovery test in **(A)**, with the peak stress indicating σ_{max}. **(C, D)** Relationships of the maximum recovery stress (σ_{max}) versus ε_{deform} determined from **(A)** for random **(C)** and aligned **(D)**, respectively. **(E)** Proposed mechanism of PLLA–PHBV shape-memory fibers using a stretch deforming process with the varied ε_{deform} (30%, 50%, and 100%).

higher than that generated by the random counterpart. Specifically, when the two types of fibrous mats with 30%, 50%, and 100% ε_{deform} were recovered in 37°C warm water, the σ_{max} generated from aligned was correspondingly 3.4-fold, 2.1-fold, and 2.3-fold stronger than that generated by random.

For the thermal-responsive SMP systems on the molecular level, it is the netpoints (e.g., crystallites, rigid segments, or chemical crosslinks that determine the permanent shape) and the switching segments (e.g., amorphous fractions in a polymer acting as a reversible phase) within the SMPs that constitute the two structural elements responsible for the SME (Salaris et al., 2022). Also, applying a stretch deforming strain ε_{deform} at a high temperature (i.e., T_{prog}) and then cooling down cause the polymer chains to become oriented and trapped in the temporarily fixed shape, thus storing strain energy. When being reheated in the vicinity of T_{trans} (e.g., T_g) associated with the switching domains, the polymer chains become mobile enough to move back to their random coil-like conformation, thus leading to recovery of the original shape. Since the σ_{max} generated during the shape recovery process is associated with the netpoint/switching segment density or hard segment weight content (Cui et al., 2010; Kratz et al., 2012) and considering the fact that increasing ε_{deform} by stretching gave rise to the polymer chains highly oriented (Yano et al., 2012; Youm et al., 2016) accompanying with the formation of more crystallites (Figure 3F), the observed higher recovery stress in aligned than in random can be reasonably explicated as illustrated in Figure 5E.

3.5 SME regulated osteogenic differentiation

The previously presented results suggest that the TME allows us to judiciously choose T_{prog} from ΔT_{trans} for shape-programming and triggering shape recovery at T_{sw} with physiological relevance (e.g., 37°C) and that the shape recovery stress generated under constrained recovery condition may be utilized to endow the fibrous scaffolds with mechanoactivity for *in situ* modulating cellular behavior (e.g., osteogenic differentiation of stem cells). To prove this concept, an aligned fibrous mat was chosen for stretch deforming the aligned fibers to 10% of ε_{deform} (without affecting cell survival (Altman et al., 2001)) at T_{prog} of 37°C, from which a mechanically dynamic culture system based on the SME-

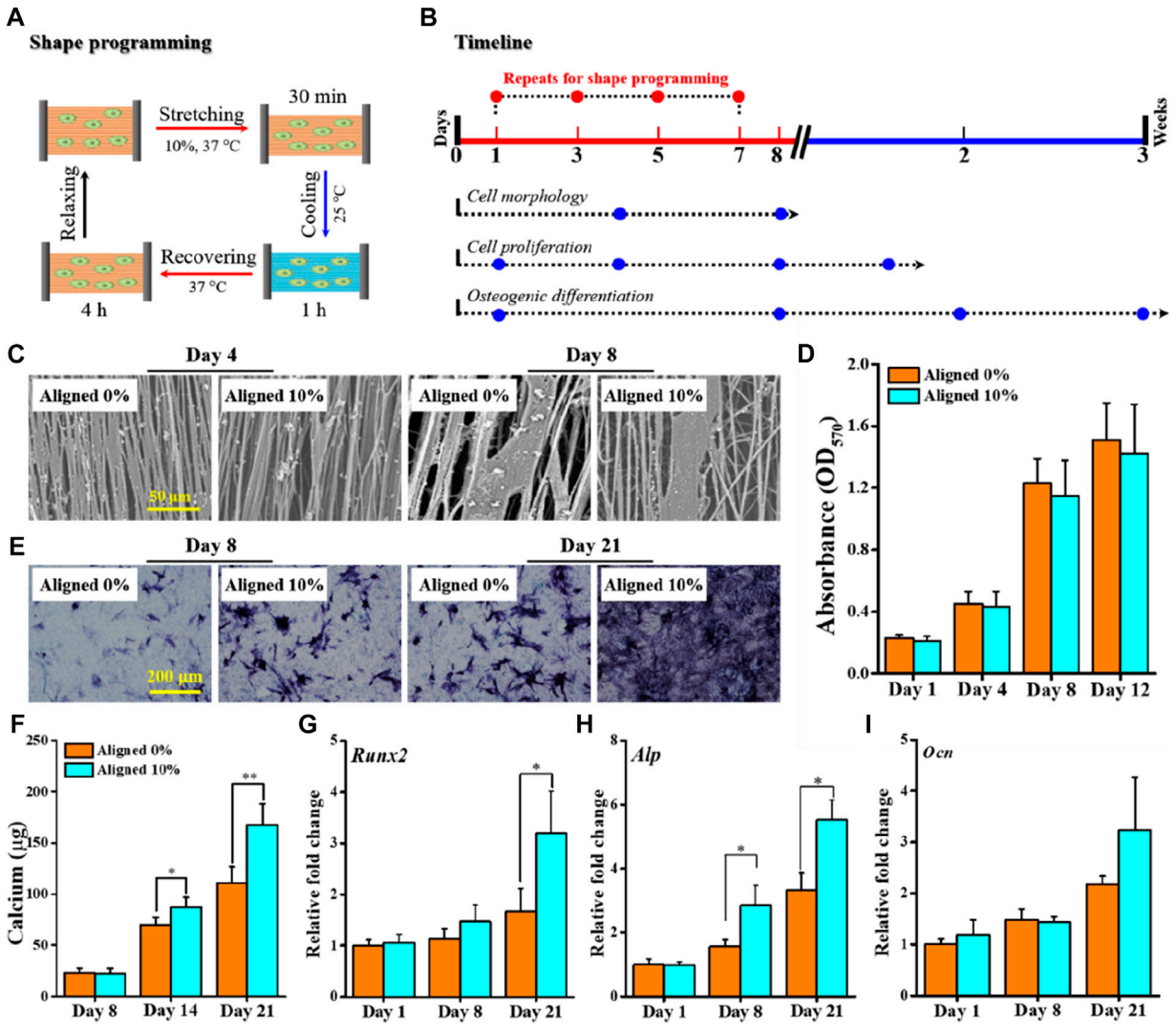

FIGURE 6
Proof-of-concept test of applying aligned fibrous substrate-based SME for regulating osteogenic differentiation. **(A)** Schematic representation of a complete cycle of shape-programming and recovery processes applied for *in vitro* cell culture with BMSCs. **(B)** Timeline depicting the process of cell culture and the designated biological assays to be performed at the specified time points. **(C)** SEM images of BMSCs cultured for 4–8 days; scale bar is 50 μm. **(D)** Histogram of BMSC proliferation by the MTT assay. **(E, F)** Osteogenic differentiation evaluated by ALP staining **(E)** and quantification of calcium deposits **(F)**. **(G–I)** Gene expression levels of representative osteogenic markers *Runx2* **(G)**, *Alp* **(H)**, and *Ocn* **(I)** at 1, 8, and 21 days.

enabled mechanoactive fibrous scaffold can be constructed to direct the fate of BMSCs (Figure 6A). Cytocompatibility assessments based on the planned experimental scheme (Figure 6B) indicated that both the plain aligned 0% and the mechanoactive aligned 10% could support BMSCs to attach and grow along the fiber direction (Figure 6C), and the cell proliferation capacities of both were comparable during the 12 days of observation (Figure 6D). These results suggest that the integrated dynamic shape-programming and recovery processes during cell culture had no detrimental effect on cell growth, which is in good accordance with previous observations (Guo et al., 2022; Tseng et al., 2016; Xing et al., 2016).

Both the ALP staining and calcium quantification assay were performed to evaluate the efficacy of using the mechanoactive scaffold for promoting osteogenic commitment of BMSCs in the absence of any osteogenic induction factors. Obviously, the cells on the mechanoactive aligned 10% stained positively for endogenous ALP activity, whereas the expression of ALP in cells cultured on the aligned 0% was comparably quite low during the 21 days of culture (Figure 6E). The quantified content of calcium deposits, as another key indicator of osteogenic differentiation of BMSCs, similarly revealed statistically significant higher levels of calcium production in the aligned 10% group than in the aligned 0% group after 14 and 21 days of culture (Figure 6F). At the gene level, expressions of representative osteogenic markers including *Runx2*, *Ocn*, and *Alp* were also detected (Figures 6G–I). The mRNA expression patterns generally show that while the early time of expression (e.g., at days 1 and 8) is comparable, higher levels of markers at day 21 can be detected. These

results consistently corroborated that applying *in situ* mechanical cues provided by the SME-enabled mechanoactive scaffold *per se* indeed resulted in achieving enhanced efficiency in directing osteogenic differentiation of stem cells.

In bone tissue engineering, applying appropriate means to efficiently drive osteodifferentiation of mesenchymal stem cells (MSCs) is crucial to osteogenesis. While utilization of various potent osteogenic factors (e.g., bone morphogenetic protein, dexamethasone, and transforming growth factor) has been demonstrated to be effective, given the mechanosensitive nature of bone, an attractive strategy for regulating osteogenic differentiation of MSCs has been the use of mechanical stimuli. Amongst, substrate stiffness has been identified to play a key role in directing stem cell osteodifferentiation (Gazquez et al., 2016; Lee et al., 2018; Song et al., 2021). In our current study, since shape recovery under constrained recovery condition can generate a stress-stiffening effect in the fibrous substrate (Guo et al., 2022), directing stem cell differentiation into an osteogenic lineage based on the SME-enabled mechanoactive scaffold itself, rather than using external bioreactors for exerting mechanical stimulus, was proved to be successful. The feasibility demonstrated here provided a fresh paradigm for developing mechanically active scaffolds for regulation of osteogenic differentiation in MSCs without using any biological supplements and/or bioreactors to provide osteogenic induction cues.

4 Conclusion

In summary, a systematic comparison of shape-memory responses between random and aligned electrospun fibrous mats was successfully performed by varying T_{prog} (37°C and 46°C) and ε_{deform} (30%, 50%, and 100%) applied during the SMCP. Compared to the applied T_{prog}, increasing the ε_{deform} was found to have a more pronounced influence on the fiber diameters and fiber orientation, especially for the random one. The efficiency of shape recovery was T_{prog}- and ε_{deform}-dependent, with the aligned fibers exhibiting better recovery capability than random fibers. The $\sigma_{\max}$ generated in aligned was 2.1–3.4 folds stronger than that generated in random. The fibrous PLLA–PHBV was observed to possess a temperature memory effect as the determined characteristic T_{sw} was found to be close to the applied T_{prog}. This distinctive temperature memory feature provides a possibility to select a physiologically relevant temperature for applications in the tissue engineering setting. The demonstrated feasibility of the shape memory fibrous substrate for osteogenic differentiation exploited the shape recovery stress controlled at a physiologically relevant temperature as an *in situ* exerted mechanical stimulus for modulation of stem cell fate, without using any biological or other mechanical induction cues. This proof-of-concept study may, therefore, provide a new paradigm in engineering mechanoactive scaffolds for promoting cellular functions to achieve desired outcomes in tissue regeneration.

Data availability statement

The original contributions presented in the study are included in the article/Supplementary Material; further inquiries can be directed to the corresponding author.

Ethics statement

The studies involving animals were reviewed and approved by the Animal Ethical Committee of Donghua University.

Author contributions

XW and YZ designed the study. XW and ZZ performed fiber fabrication, characterization, and *in vitro* experiment. XW, XG, and CQ analyzed the data. XW and YZ wrote the manuscript. All authors read and approved the final manuscript.

Acknowledgments

The authors acknowledge the partial financial support provided by the National Natural Science Foundation of China (31771050, 32071345, and 31570969), the Key Basic Research Foundation of the Shanghai Committee of Science and Technology (14JC1490100), the Science and Technology Commission of Shanghai Municipality (20DZ2254900), and the Fundamental Research Funds for the Central Universities (CUSF-DH-D-2017049) by the Ministry of Education of China.

Conflict of interest

The authors declare that the research was conducted in the absence of any commercial or financial relationships that could be construed as a potential conflict of interest.

Publisher's note

Supplementary material

The Supplementary Material for this article can be found online at: https://www.frontiersin.org/articles/10.3389/fbioe.2023.1130315/full#supplementary-material

References

Ahmed, N., Dilbraiz, M. A., Niaz, B., Ahmed, N., Farooq, U., and Ahmed, S. (2021). A facile approach towards fabrication of multi-walled nanotubes embedded polyurethane high performance nanocomposite with efficient shape recovery. *J. Polym. Res.* 28 (9), 336. doi:10.1007/s10965-021-02631-w

Ahn, E. H., Kim, Y., Kshitiz, An, S. S., Afzal, J., Lee, S., et al. (2014). Spatial control of adult stem cell fate using nanotopographic cues. *Biomaterials* 35 (8), 2401–2410. doi:10.1016/j.biomaterials.2013.11.037

Altman, G. H., Horan, R. L., Martin, I., Farhadi, J., Stark, P. R. H., Volloch, V., et al. (2001). Cell differentiation by mechanical stress. *Faseb J.* 15 (14), 270–272. doi:10.1096/fj.01-0656fje

Ayres, C. E., Bowlin, G. L., Henderson, S. C., Taylor, L., Shultz, J., Alexander, J., et al. (2006). Modulation of anisotropy in electrospun tissue-engineering scaffolds: Analysis of fiber alignment by the Fast fourier Transform. *Biomaterials* 27 (32), 5524–5534. doi:10.1016/j.biomaterials.2006.06.014

Ayres, C. E., Bowlin, G. L., Pizinger, R., Taylor, L. T., Keen, C. A., and Simpson, D. G. (2007). Incremental changes in anisotropy induce incremental changes in the material properties of electrospun scaffolds. *Acta Biomater.* 3 (5), 651–661. doi:10.1016/j.actbio.2007.02.010

Ayres, C. E., Jha, B. S., Meredith, H., Bowman, J. R., Bowlin, G. L., Henderson, S. C., et al. (2008). Measuring fiber alignment in electrospun scaffolds: A user's guide to the 2D Fast fourier Transform approach. *J. Biomat. Sci.-Polym. E.* 19 (5), 603–621. doi:10.1163/156856208784089643

Bai, L., Zhao, X., Bao, R.-Y., Liu, Z.-Y., Yang, M.-B., and Yang, W. (2018). Effect of temperature, crystallinity and molecular chain orientation on the thermal conductivity of polymers: A case study of PLLA. *J. Mat. Sci.* 53 (14), 10543–10553. doi:10.1007/s10853-018-2306-4

Bao, M., Lou, X., Zhou, Q., Dong, W., Yuan, H., and Zhang, Y. (2014). Electrospun biomimetic fibrous scaffold from shape memory polymer of PDLLA-co-TMC for bone tissue engineering. *ACS Appl. Mat. Interfaces* 6 (4), 2611–2621. doi:10.1021/am405101k

Bao, M., Wang, X., Yuan, H., Lou, X., Zhao, Q., and Zhang, Y. (2016). HAp incorporated ultrafine polymeric fibers with shape memory effect for potential use in bone screw hole healing. *J. Mat. Chem. B* 4 (31), 5308–5320. doi:10.1039/c6tb01305h

Bao, M., Zhou, Q., Dong, W., Lou, X., and Zhang, Y. (2013). Ultrasound-modulated shape memory and payload release effects in a biodegradable cylindrical rod made of chitosan-functionalized PLGA microspheres. *Biomacromolecules* 14 (6), 1971–1979. doi:10.1021/bm4003464

Chan, K. H. K., Wong, S. Y., Li, X., Zhang, Y. Z., Lim, P. C., Lim, C. T., et al. (2009). Effect of molecular orientation on mechanical property of single electrospun fiber of poly (R)-3-hydroxybutyrate-co-(R)-3-hydroxyvalerate. *J. Phys. Chem. B* 113 (40), 13179–13185. doi:10.1021/jp905820h

Cui, J., Kratz, K., Heuchel, M., Hiebl, B., and Lendlein, A. (2011). Mechanically active scaffolds from radio-opaque shape-memory polymer-based composites. *Polym. Advan. Technol.* 22 (1), 180–189. doi:10.1002/pat.1733

Cui, J., Kratz, K., and Lendlein, A. (2010). Adjusting shape-memory properties of amorphous polyether urethanes and radio-opaque composites thereof by variation of physical parameters during programming. *Smart Mat. Struct.* 19 (6), 065019. doi:10.1088/0964-1726/19/6/065019

Dubal, D. P., Chodankar, N. R., Kim, D.-H., and Gomez-Romero, P. (2018). Towards flexible solid-state supercapacitors for smart and wearable electronics. *Chem. Soc. Rev.* 47 (6), 2065–2129. doi:10.1039/c7cs00505a

Furukawa, T., Sato, H., Murakami, R., Zhang, J. M., Duan, Y. X., Noda, I., et al. (2005). Structure, dispersibility, and crystallinity of poly(hydroxybutyrate)/poly(L-lactic acid) blends studied by FT-IR microspectroscopy and differential scanning calorimetry. *Macromolecules* 38 (15), 6445–6454. doi:10.1021/ma0504668

Gazquez, G. C., Chen, H., Veldhuis, S. A., Solmaz, A., Mota, C., Boukamp, B. A., et al. (2016). Flexible yttrium-stabilized zirconia nanofibers offer bioactive cues for osteogenic differentiation of human mesenchymal stromal cells. *ACS Nano* 10 (6), 5789–5799. doi:10.1021/acsnano.5b08005

Guo, X., Wang, X., Tang, H., Ren, Y., Li, D., Yi, B., et al. (2022). Engineering a mechanoactive fibrous substrate with enhanced efficiency in regulating stem cell tenodifferentiation. *ACS Appl. Mat. Interfaces* 14 (20), 23219–23231. doi:10.1021/acsami.2c04294

Hu, J., Meng, H., Li, G., and Ibekwe, S. I. (2012). A review of stimuli-responsive polymers for smart textile applications. *Smart Mat. Struct.* 21 (5), 053001. doi:10.1088/0964-1726/21/5/053001

Huang, W. M., Zhao, Y., Wang, C. C., Ding, Z., Purnawali, H., Tang, C., et al. (2012). Thermo/chemo-responsive shape memory effect in polymers: A sketch of working mechanisms, fundamentals and optimization. *J. Polym. Res.* 19 (9), 9952. doi:10.1007/s10965-012-9952-z

Jaszkiewicz, A., Bledzki, A. K., and Meljon, A. (2013). Dynamic mechanical thermal analysis of biocomposites based on PLA and PHBV-A comparative study to PP counterparts. *J. Appl. Polym. Sci.* 130 (5), 3175–3183. doi:10.1002/app.39562

Kratz, K., Madbouly, S. A., Wagermaier, W., and Lendlein, A. (2011). Temperature-memory polymer networks with crystallizable controlling units. *Adv. Mat.* 23 (35), 4058–4062. doi:10.1002/adma.201102225

Kratz, K., Voigt, U., and Lendlein, A. (2012). Temperature-memory effect of copolyesterurethanes and their application potential in minimally invasive medical technologies. *Adv. Funct. Mat.* 22 (14), 3057–3065. doi:10.1002/adfm.201200211

Lee, H.-B., Kang, J.-I., Chung, W. J., Lee, D. H., Lee, B. Y., Lee, S.-W., et al. (2018). Engineered phage matrix stiffness-modulating osteogenic differentiation. *ACS Appl. Mat. Interfaces* 10 (5), 4349–4358. doi:10.1021/acsami.7b17871

Leist, S. K., Gao, D., Chiou, R., and Zhou, J. (2017). Investigating the shape memory properties of 4D printed polylactic acid (PLA) and the concept of 4D printing onto nylon fabrics for the creation of smart textiles. *Virtual Phys. prototy.* 12 (4), 290–300. doi:10.1080/17452759.2017.1341815

Lendlein, A., Behl, M., Hiebl, B., and Wischke, C. (2010). Shape-memory polymers as a technology platform for biomedical applications. *Expert Rev. Med. devic.* 7 (3), 357–379. doi:10.1586/erd.10.8

Lendlein, A., and Kelch, S. (2002). Shape-memory polymers. *Angew. Chem. Int. Ed.* 41 (12), 2034–2057. doi:10.1002/1521-3773(20020617)41:12<2034::aid-anie2034>3.0.co;2-m

Li, L., Huang, W., Wang, B., Wei, W., Gu, Q., and Chen, P. (2015). Properties and structure of polylactide/poly (3-hydroxybutyrate-co-3-hydroxyvalerate) (PLA/PHBV) blend fibers. *Polymer* 68, 183–194. doi:10.1016/j.polymer.2015.05.024

Livak, K. J., and Schmittgen, T. D. (2001). Analysis of relative gene expression data using real-time quantitative PCR and the $2^{-\Delta\Delta CT}$ method. *Methods* 25 (4), 402–408. doi:10.1006/meth.2001.1262

Lu, C., Chiang, S. W., Du, H., Li, J., Gan, L., Zhang, X., et al. (2017). Thermal conductivity of electrospinning chain-aligned polyethylene oxide (PEO). *Polymer* 115, 52–59. doi:10.1016/j.polymer.2017.02.024

Madl, C. M., Flaig, I. A., Holbrook, C. A., Wang, Y. X., and Blau, H. M. (2021). Biophysical matrix cues from the regenerating niche direct muscle stem cell fate in engineered microenvironments. *Biomaterials* 275, 120973. doi:10.1016/j.biomaterials.2021.120973

Miaudet, P., Derre, A., Maugey, M., Zakri, C., Piccione, P. M., Inoubli, R., et al. (2007). Shape and temperature memory of nanocomposites with broadened glass transition. *Science* 318 (5854), 1294–1296. doi:10.1126/science.1145593

Montanheiro, T. L. A., Campos, T. M. B., Montagna, L. S., da Silva, A. P., Ribas, R. G., de Menezes, B. R. C., et al. (2019). Influence of CNT pre-dispersion into PHBV/CNT nanocomposites and evaluation of morphological, mechanical and crystallographic features. *Mat. Res. Express* 6, 105375. doi:10.1088/2053-1591/ab42ed

Nanda, M. R., Misra, M., and Mohanty, A. K. (2011). The effects of process engineering on the performance of PLA and PHBV blends. *Macromol. Mat. Eng.* 296 (8), 719–728. doi:10.1002/mame.201000417

Nissenbaum, A., Greenfeld, I., and Wagner, H. D. (2020). Shape memory polyurethane - amorphous molecular mechanism during fixation and recovery. *Polymer* 190, 122226. doi:10.1016/j.polymer.2020.122226

Salaris, V., Leones, A., Lopez, D., Kenny, J. M., and Peponi, L. (2022). Shape-memory materials via electrospinning: A review. *Polymers* 14 (5), 995. doi:10.3390/polym14050995

Shen, S., Henry, A., Tong, J., Zheng, R., and Chen, G. (2010). Polyethylene nanofibres with very high thermal conductivities. *Nat. Nanotechnol.* 5 (4), 251–255. doi:10.1038/nnano.2010.27

Song, M. J., Dean, D., and Tate, M. L. K. (2013). Mechanical modulation of nascent stem cell lineage commitment in tissue engineering scaffolds. *Biomaterials* 34 (23), 5766–5775. doi:10.1016/j.biomaterials.2013.04.023

Song, Y., Long, J., Dunkers, J. P., Woodcock, J. W., Lin, H., Fox, D. M., et al. (2021). Micromechanical compatibility between cells and scaffolds directs the phenotypic transition of stem cells. *ACS Appl. Mat. Interfaces* 13 (48), 58152–58161. doi:10.1021/acsami.1c17504

Sun, J., Yu, H., Zhuang, X., Chen, X., and Jing, X. (2011). Crystallization behavior of asymmetric PLLA/PDLA blends. *J. Phys. Chem. B* 115 (12), 2864–2869. doi:10.1021/jp111894m

Tabatabaei, S. H., Carreau, P. J., and Ajji, A. (2009). Effect of processing on the crystalline orientation, morphology, and mechanical properties of polypropylene cast films and microporous membrane formation. *Polymer* 50 (17), 4228–4240. doi:10.1016/j.polymer.2009.06.071

Tcharkhtchi, A., Abdallah-Elhirtsi, S., Ebrahimi, K., Fitoussi, J., Shirinbayan, M., and Farzaneh, S. (2014). Some new concepts of shape memory effect of polymers. *Polymers* 6 (4), 1144–1163. doi:10.3390/polym6041144

Tseng, L.-F., Mather, P. T., and Henderson, J. H. (2013). Shape-memory-actuated change in scaffold fiber alignment directs stem cell morphology. *Acta Biomater.* 9 (11), 8790–8801. doi:10.1016/j.actbio.2013.06.043

Tseng, L. F., Wang, J., Baker, R. M., Wang, G. R., Mather, P. T., and Henderson, J. H. (2016). Osteogenic capacity of human adipose-derived stem cells is preserved following triggering of shape memory scaffolds. *Tissue Eng. A* 22 (15-16), 1026–1035. doi:10.1089/ten.tea.2016.0095

Veloso-Fernandez, A., Manuel Laza, J., and Luis Vilas-Vilela, J. (2021). Controlling tackiness of shape memory polyurethanes for textile applications. *J. Polym. Res.* 28 (8), 315. doi:10.1007/s10965-021-02687-8

Wang, J., Xiong, H., Zhu, T., Liu, Y., Pan, H., Fan, C., et al. (2020). Bioinspired multichannel nerve guidance conduit based on shape memory nanofibers for potential application in peripheral nerve repair. *ACS Nano* 14 (10), 12579–12595. doi:10.1021/acsnano.0c03570

Wang, M., Yu, J. H., Kaplan, D. L., and Rutledge, G. C. (2006). Production of submicron diameter silk fibers under benign processing conditions by two-fluid electrospinning. *Macromolecules* 39 (3), 1102–1107. doi:10.1021/ma0517749

Wang, X., Yan, H., Shen, Y., Tang, H., Yi, B., Qin, C., et al. (2021). Shape memory and osteogenesis capabilities of the electrospun poly(3-hydroxybutyrate-co-3-hydroxyvalerate) modified poly(l-lactide) fibrous mats. *Tissue Eng. A* 27 (1-2), 142–152. doi:10.1089/ten.tea.2020.0086

Wong, Y. S., and Venkatraman, S. S. (2010). Recovery as a measure of oriented crystalline structure in poly(L-lactide) used as shape memory polymer. *Acta Mater* 58 (1), 49–58. doi:10.1016/j.actamat.2009.08.075

Wu, R., Lai, J., Pan, Y., Zheng, Z., and Ding, X. (2018). High-strain slide-ring shape-memory polycaprolactone-based polyurethane. *Soft Matter* 14 (22), 4558–4568. doi:10.1039/c8sm00570b

Xie, H., Shao, J., Ma, Y., Wang, J., Huang, H., Yang, N., et al. (2018). Biodegradable near-infrared-photoresponsive shape memory implants based on black phosphorus nanofillers. *Biomaterials* 164, 11–21. doi:10.1016/j.biomaterials.2018.02.040

Xie, T., Page, K. A., and Eastman, S. A. (2011). Strain-based temperature memory effect for nafion and its molecular origins. *Adv. Funct. Mat.* 21 (11), 2057–2066. doi:10.1002/adfm.201002579

Xing, J., Ma, Y., Lin, M., Wang, Y., Pan, H., Ruan, C., et al. (2016). Stretching-induced nanostructures on shape memory polyurethane films and their regulation to osteoblasts morphology. *Colloid. Surf. B* 146, 431–441. doi:10.1016/j.colsurfb.2016.06.044

Yano, T., Higaki, Y., Tao, D., Murakami, D., Kobayashi, M., Ohta, N., et al. (2012). Orientation of poly(vinyl alcohol) nanofiber and crystallites in non-woven electrospun nanofiber mats under uniaxial stretching. *Polymer* 53 (21), 4702–4708. doi:10.1016/j.polymer.2012.07.067

Youm, J. S., Kim, J. H., Kim, C. H., Kim, J. C., Kim, Y. A., and Yang, K. S. (2016). Densifying and strengthening of electrospun polyacrylonitrile-based nanofibers by uniaxial two-step stretching. *J. Appl. Polym. Sci.* 133 (37)–43945. doi:10.1002/app.43945

Yuan, H., Zhao, S., Tu, H., Li, B., Li, Q., Feng, B., et al. (2012). Stable jet electrospinning for easy fabrication of aligned ultrafine fibers. *J. Mat. Chem.* 22 (37), 19634–19638. doi:10.1039/c2jm33728b

Zembouai, I., Kaci, M., Bruzaud, S., Benhamida, A., Corre, Y.-M., and Grohens, Y. (2013). A study of morphological, thermal, rheological and barrier properties of Poly(3-hydroxybutyrate-co-3-Hydroxyvalerate)/polylactide blends prepared by melt mixing. *Polym. Test.* 32 (5), 842–851. doi:10.1016/j.polymertesting.2013.04.004

Zhang, B., Filion, T. M., Kutikov, A. B., and Song, J. (2017). Facile stem cell delivery to bone grafts enabled by smart shape recovery and stiffening of degradable synthetic periosteal membranes. *Adv. Funct. Mat.* 27, 1604784. doi:10.1002/adfm.201604784

Zhang, K., Wang, X., Yang, Y., Wang, L., Zhu, M., Hsiao, B. S., et al. (2010). Aligned and molecularly oriented semihollow ultrafine polymer fiber yarns by a facile method. *J. Polym. Sci. Pol. Phys.* 48 (10), 1118–1125. doi:10.1002/polb.22003

Zhang, X., and Zhang, Y. (2016). Reinforcement effect of poly(butylene succinate) (PBS)-Grafted cellulose nanocrystal on toughened PBS/polylactic acid blends. *Carbohydr. Polym.* 140, 374–382. doi:10.1016/j.carbpol.2015.12.073

Zhao, W., Liu, L. W., Zhang, F. H., Leng, J. S., and Liu, Y. J. (2019). Shape memory polymers and their composites in biomedical applications. *Mat. Sci. Eng. C-Mater.* 97, 864–883. doi:10.1016/j.msec.2018.12.054

Zhao, Z., Zhang, K., Liu, Y., Zhou, J., and Liu, M. (2017). Highly stretchable, shape memory organohydrogels using phase-transition microinclusions. *Adv. Mat.* 29 (33), 1701695. doi:10.1002/adma.201701695

frontiers | Frontiers in Bioengineering and Biotechnology

TYPE Original Research
PUBLISHED 04 May 2023
DOI 10.3389/fbioe.2023.1168136

OPEN ACCESS

EDITED BY
Yong Liu,
University of Chinese Academy of Sciences, China

REVIEWED BY
Xuan Mei,
Harvard Medical School, United States
Jiansu Chen,
Aier Eye Institute, China

*CORRESPONDENCE
Zeng-Ming Li,
lizhengming@163.com

†These authors have contributed equally to this work

RECEIVED 17 February 2023
ACCEPTED 24 April 2023
PUBLISHED 04 May 2023

CITATION
Zhu Y, Wang T, Bao M-J, Qu X-H and Li Z-M (2023), Effect of stem cell conditional medium-loading adhesive hydrogel on TGF-β1-induced endometrial stromal cell fibrosis. *Front. Bioeng. Biotechnol.* 11:1168136. doi: 10.3389/fbioe.2023.1168136

Effect of stem cell conditional medium-loading adhesive hydrogel on TGF-β1-induced endometrial stromal cell fibrosis

Yuan Zhu[1,2†], Ting Wang[2†], Ming-Jie Bao[2], Xiao-Hui Qu[3] and Zeng-Ming Li[1*]

[1]JXHC Key Laboratory of Fertility Preservation, Jiangxi Provincial Maternal and Child Health Hospital, Nanchang, Jiangxi, China, [2]Department of Reproductive Health, Jiangxi Provincial Maternal and Child Health Hospital, Nanchang, Jiangxi, China, [3]Pathology Department, Jiangxi Provincial Maternal and Child Health Hospital, Nanchang, Jiangxi, China

Introduction: Uterine adhesion (IUA) is a severe complication that results from uterine operations or uterine infections. Hysteroscopy is considered the gold standard for the diagnosis and treatment of uterine adhesions. Yet, this invasive procedure leads to re-adhesions after hysteroscopic treatment. Hydrogels loading functional additives (e.g., placental mesenchymal stem cells (PC-MSCs)) that can act as physical barriers and promote endometrium regeneration are a good solution. However, traditional hydrogels lack tissue adhesion which makes them unstable under a rapid turnover of the uterus, and PC-MSCs have biosafety risks when used as functional additives.

Methods: In this study, we coupled an adhesive hydrogel with a PC-MSCs conditioned medium (CM) to form a hybrid of gel and functional additives (CM/Gel-MA).

Results and Discussion: Our experiments show that CM/Gel-MA enhances the activity of endometrial stromal cells (ESCs), promotes cell proliferation, and reduces the expression of α-SMA, collagen I, CTGF, E-cadherin, and IL-6, which helps to reduce the inflammatory response and inhibit fibrosis. We conclude that CM/Gel-MA can more potentially prevent IUA by combining the physical barriers from adhesive hydrogel and functional promotion from CM.

KEYWORDS

adhesive hydrogel, stem cell conditional medium, endometrial stromal cell, uterine adhesion, fibrosis

1 Introduction

Intrauterine adhesion (IUA), also known as Asherman Syndrome, is one of the prominent reasons for impaired fertility (March 2011; Dreisler and Kjer, 2019), which is caused by both traumatic and non-traumatic factors. The non-traumatic factors are commonly related to intrauterine infections, while the traumatic factors are iatrogenic, such as pregnancy-related curettage (Dreisler and Kjer, 2019; Rein et al., 2011). IUA shows a variety of symptoms such as uterine amenorrhea, menstrual disorders, pelvic pain, recurrent miscarriage, and even infertility, in clinical diagnosis (Dreisler and Kjer, 2019). The present clinical treatment for uterine adhesions is hysteroscopic adhesion release and postoperative balloon placement with hormonal therapy (AAGL Elevating Gynecologic Surgery, 2017). However, the treatment effect is critically correlated with the degree of adhesions. Especially, for patients with moderate and severe adhesions, the prognosis after hysteroscopic treatment

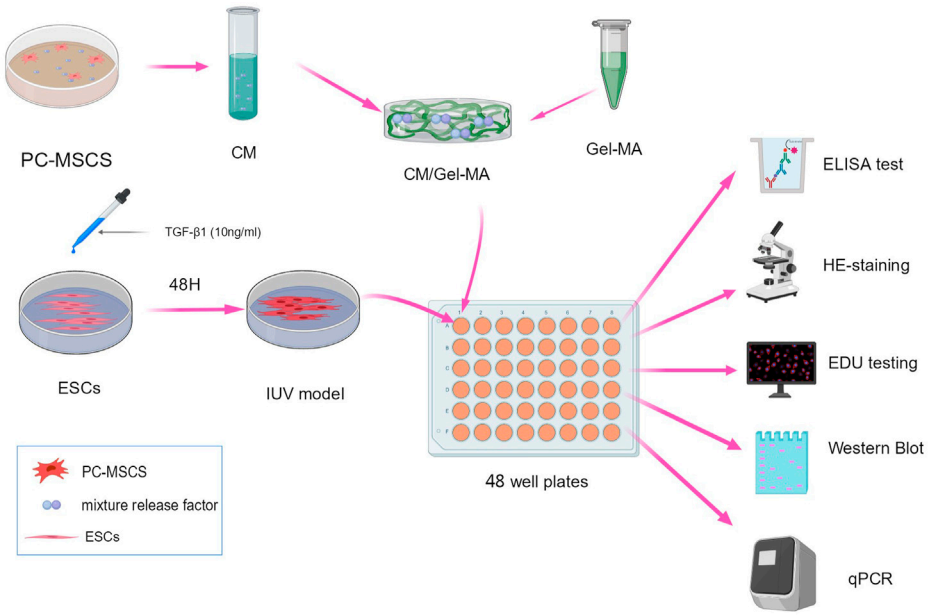

FIGURE 1
Scheme of the experimental procedure. All schematics are drawn using MedPeer (www.medpeer.com).

is poor, and some re-adhesions form to aggravate the initial adhesions (Benor et al., 2020; Johary et al., 2014). The re-adhesion rate after hysteroscopic therapy for patients with severe IUA was high, with a live birth rate of only 29.1% (Chen et al., 2020). The statistics based on the classification system from the European Hysteroscopy Society depicted 21%–25%, 29.1%, 38.5%, and 41.9% of recurrence for patients with grade 1-2, grade 3, grade 4, and grade 5 adhesions, respectively (Dreisler and Kjer, 2019). Therefore, safer and more effective methods must be discovered to avoid adhesion formation and ensure functional recovery.

The treatment of IUA requires individualized therapy to recover physical structure, restore function, and stimulate stromal cell regeneration. A thorough cure is the regeneration of stromal cells (Rodriguez-Fuentes et al., 2021). Stem cells exhibit some regeneration functions (Wang et al., 2020) and can effectively treat a few chronic diseases. At present, the clinical primary stem cells used are mesenchymal stem cells (MSCs). Researchers have demonstrated that MSCs transplantation effectively relieves intrauterine adhesions (Song et al., 2021). But the transplantation of undifferentiated or improperly differentiated stem cells carries a significant risk of tumorigenesis (Sharpe et al., 2012). Stem cells secrete some active substances (Jabbehdari et al., 2020; Sato et al., 2018) with good curative effects that help in repair function (He et al., 2022; Yamashita et al., 2018). The culture medium containing the secretion of MSCs is named as the conditioned medium (CM). CM can be used to promote cell proliferation and damage repair to avoid the ethical and safety issues of stem cells (Sagaradze et al., 2019). However, CM cannot stay in the uterine cavity for a long time. This is because CM easily flows due to its liquidity when the patient's position changes. The short duration of CM in the uterine cavity reduces its therapeutic effect. Moreover, the efflux of CM causes symptoms of vaginal discharge and results in discomfort and vaginitis.

The application of hydrogels to biomedical research is a hot topic. Hydrogels possess good three-dimensional morphology, controlled swelling, biodegradation properties, and excellent cytocompatibility. They can also be modified for additional properties (Tytgat et al., 2019). They are widely used as wound dressings and biological scaffolds to promote tissue regeneration and injury repair (Colangelo et al., 2021; Hu et al., 2023; Tytgat et al., 2019; Wen et al., 2022) because of their superb adjustability. Researchers have found that some hydrogel-derived biological scaffolds not only support endometrial cell attachment and proliferation, but also deliver stem cells or bioactive molecules that promote endometrial regeneration (Li et al., 2021). A CS/Exos structure with a collagen scaffold and UC-MSCS-derived exosomes promotes endometrial regeneration and fertility recovery through macrophage immunomodulation (Xin et al., 2020). However, because of the rapid turnover of the uterus, these gels cannot stay stable when applied. A healthy uterus of women secretes 3-4 g of endometrial mucus every 4 h (Ensign et al., 2012). Hydrogels with adhesion properties can perfectly solve this problem. After application, the adhesion hydrogels can easily stay at the applied surface because of the interaction with tissues. Methacrylate-modified gelatin (Gel-MA) is a biodegradable polymer that can easily form adhesive hydrogels with photo initiation (Liu and Chan-Park, 2010). Gel-MA-based adhesive hydrogels are good scaffolds for wound healing (Stubbe et al., 2021), cartilage regeneration (Shi et al., 2021), and dental repair (Wang et al., 2021) with good adhesion properties (Pirmoradian et al., 2022). Moreover, it can easily load functional additives (Lim et al., 2019). Although the use of Gel-MA adhesive hydrogels in IUA prevention is very promising, few studies have been reported.

In this study, we designed a CM-loaded adhesive hydrogel (CM/Gel-MA) based on Gel-MA. CM/Gel-MA is greatly adhesive which

TABLE 1 Primers utilized in quantitative real-time PCR.

Primer name	Forward primer	Reverse primer
α-SMA	CGTTACTACTGCTGAGCGTG	TGAAGGATGGCTGGAACAGG
collagen I	GGACACAGAGGTTTCAGTGG	CAGTAGCACCATCATTTCCACG
CTGF	CTGGTCCAGACCACAGAGTG	TGCCCTTCTTAATGTTCTCTTCCA
E-cadherin	GCTGGACCGAGAGAGTTTCC	CGACGTTAGCCTCGTTCTCA
IL-6	ACTCACCTCTTCAGAACGAATTG	CCATCTTTGGAAGGTTCAGGTTG

TABLE 2 Antibodies.

Antibody	Source	Cat. no	Brand	Dilution
β-Actin	Rabbit	20536-1-AP	Proteintech	1:1000
α-SMA	Rabbit	14395-1-AP	Proteintech	1:1000
collagen I	Rabbit	14695-1-AP	Proteintech	1:1000
CTGF	Rabbit	25474-1-AP	Proteintech	1:1000
E-cadherin	Rabbit	20874-1-AP	Proteintech	1:20000
IL-6	Rabbit	21865-1-AP	Proteintech	1:500

favors the stable retention of CM. The potential anti-IUA effect of CM/Gel-MA has been tested on the classical uterine adhesion cell model (Figure 1). CM/Gel-MA was found to improve cell viability, promote cell proliferation, and significantly reduce fibrosis, implying its potential for cell adhesion inhibition. This suggests that Gel-MA is a suitable biological scaffold in IUA injury repair and CM/Gel-MA is a potential agent for IUA treatment.

2 Materials and methods

2.1 Experimental materials

TGF-β1 (PEPRO TECH, China, 100-21-10 μg), PC-MSC (Provided by Shenzhen 150 Biomedical Co.,Ltd.), ESC (Provided by ATCC), FITC Mouse IgG1 κ Isotype control (Biolegend, 7313762), PE Mouse IgG1 κ Isotype control (Biolegend, 9217868), APC Mouse IgG1 κ Isotype control (Biolegend, 9282592), PE Mouse Anti-Human CD73 (Biolegend, 8151901), APC Mouse Anti-Human CD105 (Biolegend, 9277133), FITC Mouse IgG2a κ Isotype control (Biolegend, 8241935), FITC Mouse Anti-Human CD14 (Biolegend, 8299630), FITC Mouse Anti-Human CD45 (Biolegend, 8206704), DMEM/F12 medium (Peiyuan, Shanghai, L310 kJ), Fetal bovine serum (Gemini, 900-108), Trypsin digestive fluid (Beyo, C0203), DPBS (Beyo, C0221G), CCK8 (Beyotime, C0039), EDU staining kit (Beyotime, C0081s), Hematoxylin-eosin staining kit (Solarbio, G1120), DEPC-treated water (Solarbio, R1600), trichloromethane (Sinopharm Chemical Reagent Co. LTD., 10006818), GelRed dye (Biotium, #41003), RNA Loading Buffer (TaKaRa, 9168), Tris-Borate-EDTA Buffer (TBE) 10× Powder, pH8.3 (TaKaRa, T9122), RNAsimple Total RNA Kit (TIANGEN, DP419), All-in-One First-Strand Synthesis Master Mix (Yugong Biolabs, EG15133S), SuperReal PreMix Plus (SYBR Green) (TIANGEN, FP205-02), and Methacrylate anhydride (MAA, 0.1 mL/1 g gelatin), ELISA Kit (Solarbio, SEKH-0052), MateRegen® Gel (2104006, BioRegen Biomedical (Changzhou) Co., Ltd.).

2.2 Methods

2.2.1 Establishment of the IUA model

Endometrial stromal cells (ESCs) were first cultured with 80–90% confluence. Then, cells were digested, collected, and dispersed into 6-well cell culture plates with a density of 1.0×10^5 cells/mL for further incubation at 37°C, in a 5% CO_2 cell culture incubator (Thermo Fisher Scientific, Heracell 240i). When the confluence reached approximately 80%, TGF-β1 (10 ng/mL) was added to the plate for another 48 h treatment to induce the IUA model (Liu et al., 2020).

2.2.2 Synthesis of Gel-MA

Gel-MA was prepared according to a previous report (Zhu M. et al., 2019). Gelatin (10 g) was dissolved at 10 (w/v) % in a carbonate–bicarbonate (CB) buffer solution (0.25 M, 100 mL) and heated to 50°C. Methacrylate anhydride (MAA, 0.1 mL/1 g gelatin) was added to the fully dissolved gelatin solution at 500 rpm magnetic stirring, and the reaction pH was adjusted to 9. After 3 h reaction at 50°C, the solution was adjusted to pH 7.4 to stop the reaction. The final solution was purified by dialysis in an aqueous solution at 50°C. Finally, Gel-MA solid products were obtained by freeze-drying.

2.2.3 Acquisition of CM

PC-MSCS (Provided by Shenzhen 150 Life Technology Co., LTD.) were cultured (Source Biologicals, T310JV) and continuously passaged until P3 generation PC-MSC cells were collected. Subsequently, cells were identified by positive (PE-CD73, APC-CD105) and negative (FITC-CD14, FITC-CD45) biomarkers. After confirming the phenotype of the cells, they were continuously cultured to P5 generation. The collected cells were incubated with a serum-free DMEM/F12 (Shanghai Peiyuan, L310 kJ) medium, and were continuously cultivated for 48 h. Finally, the CM supernatant obtained was collected for further use.

2.2.4 *In vitro* lap shear test of Gel-MA and CM/Gel-MA

The shear resistance of Gel-MA ($n = 3$) and CM/Gel-MA ($n = 3$) was tested following the previous report (Annabi et al., 2017) with some modifications. Each sample was examined using two glass slides (25 mm and 75 mm) with the top (25 mm and 10 mm) coated

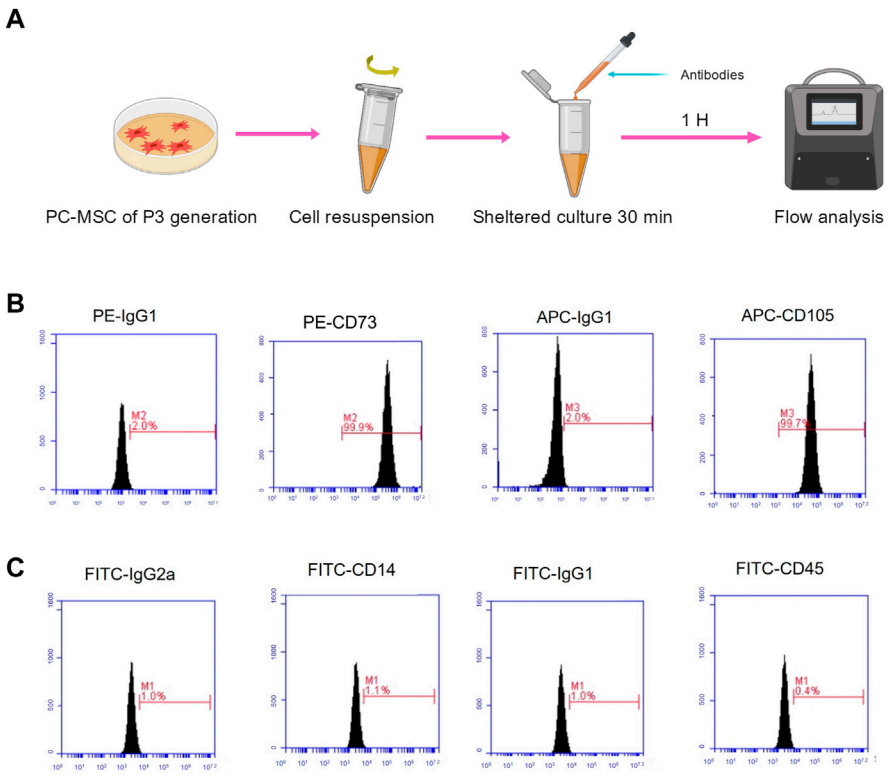

FIGURE 2
PC-MSC immunophenotype identification. **(A)** Schematic diagram of flow analysis. **(B)** Test for CD73 and CD105 expressions. **(C)** Test for CD14 and CD45 expressions.

with gelatin solution. At room temperature, gelatin-coated glass slides were dried. The Gel-MA solution (40 L) and the CM/Gel-MA solution (40 L) were then added to one of the gelatin-coated areas, and the other slide was placed in the solution. Subsequently, UV light irradiation was used to cross-link the hydrogel between the two glass slides. Finally, the shear strength of the hydrogel was determined using an electronic universal testing equipment (CMT1103, Zhuhai Sansi Test Equipment Co., Ltd., China).

2.2.5 *In vitro* wound closure test of Gel-MA and CM/Gel-MA

An *in vitro* wound closure test was conducted in accordance with the grouping of the shear experiment. The test was carried out using sliced, rectangular-shaped pig skin (length 20 mm, width 10 mm). The pig skin was then split along the middle using a knife to imitate an injury. Gel-MA (10 L) and CM/Gel-MA (10 L) solutions were injected into both sides of the wound. The hydrogels were then individually photo-crosslinked on both surfaces using UV light irradiation. Finally, an electronic universal testing machine was used to assess the wound closure strength (CMT1103, Zhuhai Sansi Test Equipment Co., Ltd., China).

2.2.6 Adhesion test

The test was carried out using sliced, rectangular-shaped pig skin (length 30 mm, width 10 mm). To begin, 100 μL of Gel-MA, CM/Gel-MA, and hyaluronic acid hydrogels (HA) (MateRegen® Gel (2104006, BioRegen Biomedical (Changzhou) Co., Ltd.) were applied to rectangular pig skin. The Gel-MA and CM/Gel-MA are then illuminated with UV light. Finally, the gel was rinsed using PBS with a 5 mL pipette at an even rate.

2.2.7 ELISA analysis

The slow release of CM/Gel-MA was investigated by measuring the VEGF content of CM (n = 3). Following the manufacturer's instructions, VEGF levels were measured using an ELISA kit (Solarbio, SEKH-0052).

2.2.8 CCK-8 assays for cell proliferation evaluation

ESCs after TGF-β1 treatment were collected, digested, and made into a single cell suspension at 1×10^4 cells/well (edge wells are filled with sterile PBS to eliminate edge effect). The cells were then incubated for approximately 6 h. After adhering to the plate, Gel and control agents were added. After another 48 h incubation, 250 μL of CCK-8 solution (Beyotime, C0039) was added to each well and again incubated for 2 h. Finally, the OD values at 450 nm were read and recorded by a plate reader (Biotek, Elx808).

2.2.9 H&E staining for pathological check

Each sample was washed with PBS 1–2 times. Then, 200 μL of paraformaldehyde (4%) was added to the samples and incubated for 30 min at room temperature. Subsequently, 200 μL of hematoxylin

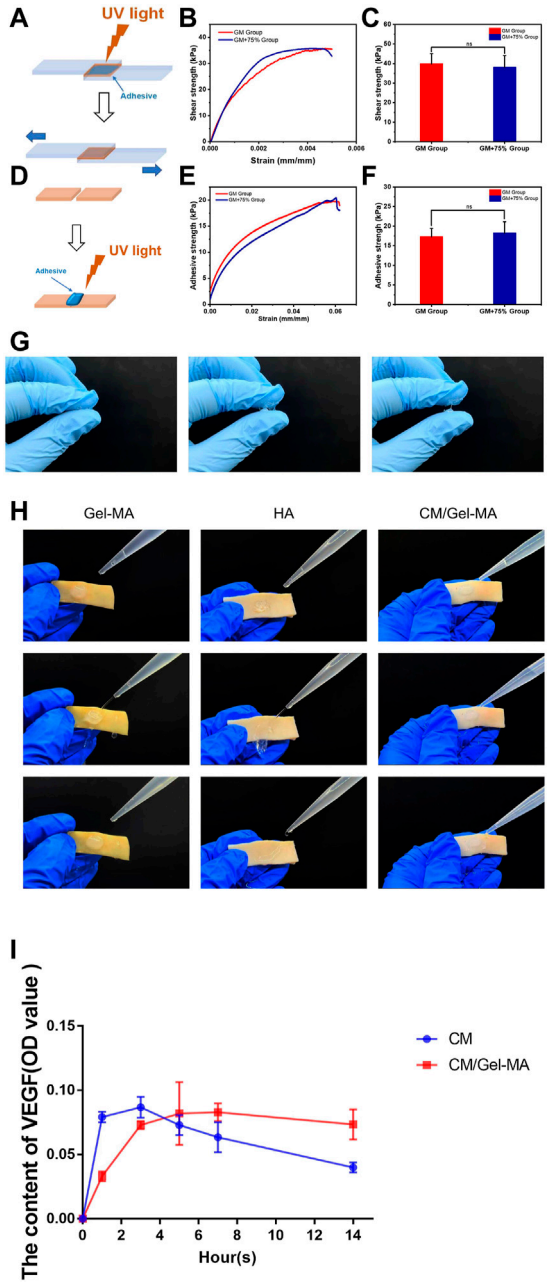

FIGURE 3
Evaluation of gel properties. **(A** and **D)** Schemes showing the lap shear test (A) and wound closure test of Gel-MA and CM/Gel-MA. **(B** and **C)** The shear strength of Gel-MA and CM/Gel-MA (n = 3, mean ± SD, ns: not significant). **(E** and **F)** The wound closure strength of Gel-MA and CM/Gel-MA (n = 3, mean ± SD, ns: not significant). Statistical significance calculated using Student's t-test is given in **C** and **F**. **(G)** The tensile resistance of HA. **(H)** Adhesion test. **(I)** The results of the ELISA. CM/Gel-MA group: Gel containing 75% CM (100 μL) + PBS(800 μL); CM group: 75% CM solution (100 μL) + PBS (800 μL).

staining solution (Solebro, G1120) was added for 25 min incubation at room temperature, followed by 200 μL eosin incubation (Solaibao, G1120) for 1 min. Finally, the stained samples were washed and immediately observed.

2.2.10 EDU assay for cell proliferative capacity evaluation

EDU (Beyotime, C0081s) was first diluted into a DMEM/F12 cell medium at a ratio of 250:1 to reach a concentration level of 40 μM. Then, 100 μL of 40 μM EDU medium was added to each well and incubated for 24 h. After washing with PBS, 200 μL of paraformaldehyde (4%) was added to fix them. Then, they were decolorized and shaken for 5 min, followed by a sequential addition of 200 μL permeabilizer (0.3% Triton-100) and 200 μL 1× click reaction solution. After another 30 min incubation, 100 μL of 1× Hoechst 33342 reaction solution was added to each well and incubated for 10 min at room temperature. After washing with PBS, using the 405 nm channel of a fluorescence microscope, it was observed and photographed.

2.2.11 mRNA level evaluation of α-SMA, collagen I, CTGF, E-cadherin, and IL-6

Total RNA was extracted from cells with an RNAsimple total RNA kit (TIANGEN, DP419), and was stored at −80°C. To quantify the mRNA level of biofactors, the corresponding primer pairs were designed and synthesized, as listed in Table 1. Hsa-β-actin was chosen as the internal reference primer for PCR, whose forward and back sequences were TTCCTTCCTGGGCATGGAGTC and TCTTCATTGTGCTGGGTGCC, respectively.

2.2.12 Western blot (WB) assay

To confirm the protein expression of interest, western blot was carried out as previously descrbied (Ai et al., 2020). The primary antibodies used were listed in Table 2. Amount of the protein of interest was normalized to the densitometric units of β-actin.

2.2.13 Statistical analysis

All experimental results mentioned in this study are expressed as the mean ± SD. Statistical analysis was carried out using GraphPad Prism 9.0 software (GraphPad Software, San Diego, CA, United States) and Origin software (Origin Lab, United States). The t-test was used to compare two conditions. ANOVA with a Bonferroni post-test was used for multiple comparisons. The p-value <0.05 was considered statistically significant.

3 Results and discussion

3.1 Preparation and characterization for CM/Gel-MA

Before preparing the CM, the PC-MSC phenotype was strictly identified. We followed the regular procedure and identified PC-MSCs by flow cytometry (Figure 2A). As shown in Figures 2B, C, the expression of CD73 and CD105 was 99.9%, and 99.7%, respectively, whereas both CD14 and CD45 were expressed at low levels (less than 5%). These results indicated that the cells used were PC-MSCs.

Following a previous report, CM concentrations of 75% were chosen to fabricate CM/Gel-MA for performance evaluation (Zhu H. et al., 2019). Appropriate adhesion favors the retention of hydrogel and increases the duration of loaded factors in the uterus. Gels from Gel-MA have good tissue adhesion (Pirmoradian et al., 2022). However, the influence of CM on Gel-

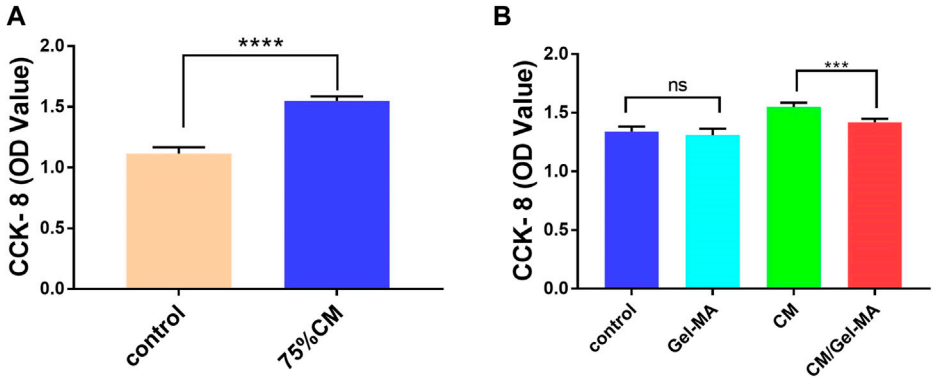

FIGURE 4
CCK-8 assays for cell proliferation. **(A)** 75% CM promotes cell proliferation. Control group: Complete medium (800 μL) + serum-free medium (100 μL); 75% CM group: 75% fresh CM (800 μL) +75% serum-free CM medium (100 μL); **(B)** Proliferation ability of ESCs in different media. All subgroups contain 800 μL of 75% fresh CM as the basic medium. Control group: serum-free medium (100 μL); Gel-MA group: Gel containing serum-free medium (100 μL); CM group: 75% serum-free CM medium (100 μL); CM/Gel-MA group: Gel containing 75% serum-free CM (100 μL). (***: $p < 0.001$; **: $p < 0.01$; *: $p < 0.01$; ns: >0.05).

MA's adhesion performance is unknown. As a result, the adhesion strength of Gel-MA and CM/Gel-MA was evaluated by a lap shear test (ASTM F2255-05) and a wound closure test (ASTM F2458-05). The lap shear tests in Figures 3A–C demonstrate that the lap shear strength of the Gel-MA group is nearly the same as that of the CM/Gel-MA group, without a statistical difference. It indicated that the addition of CM did not change the adhesion performance much. The wound closure tests were carried out further (Figures 3D–F). It still revealed that the wound closure strength of the Gel-MA group was 17.29 ± 2.14 kPa, which was not statistically different from that of CM/Gel-MA (18.23 ± 2.92 kPa). Hence, the addition of PMCSCM to Gel-MA did not significantly reduce the adhesion performance of Gel-MA.

3.2 CM/Gel-MA has better adhesion effect than HA and can gradually release CM

HA, like a gelatin, is now widely used in tissue regeneration and wound healing (Bonafe et al., 2014; Rao et al., 2023). HA can also be used as a transporter in the treatment of intrauterine adhesions (Liu et al., 2019). However the advantage of gelatin over hyaluronic acid is that gelatin can offer tissue adhesiveness through ionic bonding with tissue (Duan et al., 2023; Bu and Pandit, 2022). Here, the commercially available HA hydrogel of IUA prevention was used as control. Figure 3G showed that HA hydrogel didn't show any sign of adhesion. As a result, lap shear and wound closure experiments can't be carried out. To further show the different performance in adhesion, the Gel-MA hydrogels and HA hydrogels were applied on the pig skin. Figure 3H showed that Gel-MA and CM/Gel-MA adhered firmly to pig skin even under water flow while HA hydrogel was quickly washed away. A good tissue adhesion can increase the stability of those functional hydrogels, thus increasing the therapeutic efficacy (Feng et al., 2023).

CM has a complex composition, and studies have revealed that it contains a variety of cytokines of which VEGF is one (Zagoura et al., 2012; Pawitan, 2014). Here to show that after loading CM into Gel-MA, the system can gradually release the bioactive components, VEGF was used as the representive and the release was detected by ELISA. Figure 3I showed that after dissolving CM in the medium, the content of VEGF reached maximum and gradually decreased. The decreased amount might result from the denaturation of VEFG. However, a gradually increased amount of CM was detected in CM/Gel-MA system, which kept stable even after 14 h of release. These experiments showed that after loading CM into Gel-MA, the system achieved a gradually release of CM and might even help prevent the VEGF from denaturation.

3.3 CM/Gel-MA attenuates fibrosis and promotes the proliferation of ESCs

ESCs were closely associated with IUA treatment. As ESCs increased, IUA levels decreased. Thus, we assessed the apparent number of ESCs treated with CM, Gel-MA, or CM/Gel-MA in the IUA model using the CCK-8 assay. The OD value increased as the apparent number of cells increased. First, compared with the control group, there was a significant enhancement in the relative cell numbers of the group with 75% CM treatment (Figure 4A). This indicated that CM addition improved cell proliferation, which was consistent with the previous results (Wei et al., 2022; Zhu H. et al., 2019). Then, we investigated the effect of Gel-MA on ESCs proliferation. No significant difference was observed in cell numbers between the groups with or without Gel-MA treatment. This means Gel-MA is a suitable material for safe application to the endometrium. It was also observed that cells treated with CM/Gel-MA had fewer cell numbers than those treated with CM of the same amount, which is a significant difference (Figure 4B). This is because slowly released CM in Gel-MA could not perform the highest promotion effect in a short time. However, regular therapy needs a longer period to match with the sustained release system. Hence, CM/Gel-MA can be used for long-term therapy.

We then investigated the ESCs proliferation state and evaluated CM/Gel-MA mediated ESCs fibrosis by H&E staining, after different treatments. ESCs are adnexal cells with a morphology similar to

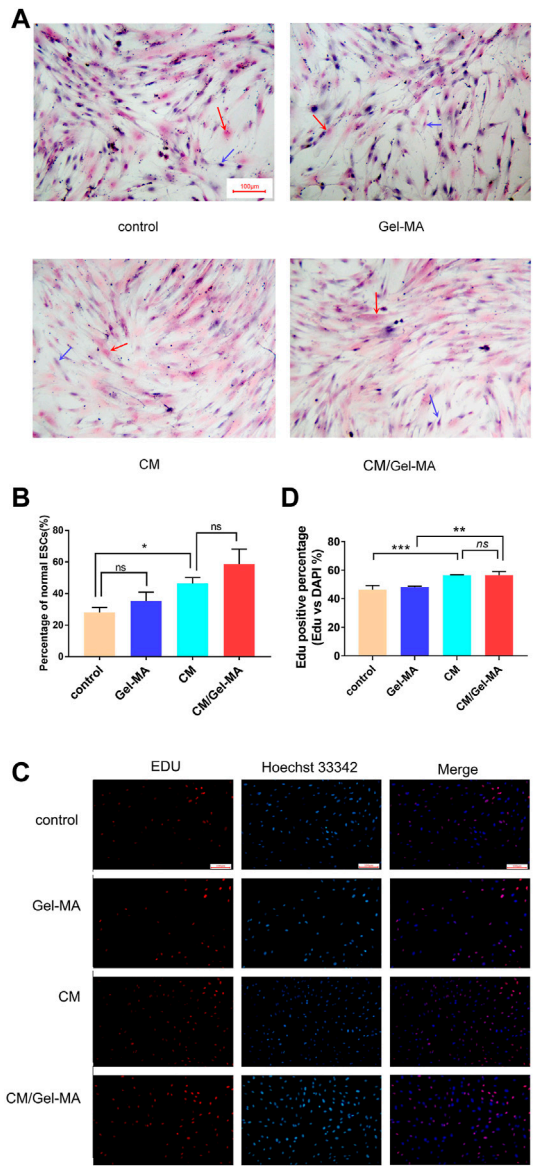

FIGURE 5
CM/Gel-MA enhances cell viability and reduces fibrosis. **(A)** H&E staining (100×). The nucleus is stained blue and the cytoplasm is stained pink. Blue arrows indicate normal ESC and red arrows indicate post-fibrotic ESC. **(B)** Percentage of normal ESCs. **(C)** EDU assay for cell viability, cells in the proliferative phase show strong red fluorescence after EDU staining and blue fluorescence reaction of the nucleus after Hoechst 33324 staining. **(D)** Statistical analysis table of EDU assay for cell viability. (***: $p < 0.001$; **: $p < 0.01$; *: $p < 0.01$; ns:>0.05).

fibroblasts, with a long spindle shape and a large nucleus (Queckborner et al., 2020). In Figure 5A, after TGF-β1 treatment, the morphology of some ESCs changed: cytoplasm, nucleus, and multiple branches on the cell membrane faded, and the original spindle shape was lost. This indicated the occurrence of fibrosis in ESCs. Whereas, after CM or CM/Gel-MA treatment, most cells recovered their original long shuttle shape. We also counted the percentage of normal ESCs in each group, and the results revealed that the percentage of normal ESCs increased after CM or CM/Gel-MA treatment (Figure 5B). Both CM and CM/Gel-MA attenuated fibrosis.

EDU (5-ethynyl-2′deoxyuridine nucleoside) is a thymidine nucleoside analog, which can light on cells in the proliferative phase. As shown in Figures 5C, D, after being stained by EDU, more ESCs are observed in a proliferating state in the groups treated by CM and CM/Gel-MA. These results are consistent with those from Wei's study, which demonstrated the positive effect of CM on IUA (Wei et al., 2022). There was also no significant difference between CM and CM/Gel-MA, which means Gel-MA did not hinder the CM's function of cell growth promotion. In addition, ESCs treated by Gel-MA showed a similar activity with the control group. It solidly implied that Gel-MA was biocompatible. Overall, our result confirmed that CM/Gel-MA significantly promotes ESC proliferation like CM, and also, Gel-MA is safe for use and potentially synergistic for CM application.

3.4 CM/Gel-MA reduces the expression of some pro-fibrotic factors, pro-adhesion molecules, and attenuates fibrosis

The abnormality of the TGF-β/Smad signaling pathway plays an important role in fibrosis. Through Smad2 or Smad3, the α-SMA level can be upregulated, thus promoting fibrosis (Zeisberg and Kalluri, 2013). In accordance with previous reports, α-SMA would be significantly elevated in ESCs after TGF-β1 treatment (Li et al., 2016; Zhu H. et al., 2019). Therefore, it was used as a control group to mimic disease status to investigate CM/Gel-MA's effect. As shown in Figure 6A, the mRNA expression of α-SMA was slightly enhanced by the addition of Gel-MA in the IUA model, while it decreased after being treated with CM. When using CM/Gel-MA, downregulation of mRNA expression is still observed, but the degree of attenuation is less than that of the CM-only group. CM/Gel-MA is advantageous because CM is gradually released and has a durable effect with the degradation of Gel-MA in CM/Gel-MA.

Collagen I is a fibrogenic factor mainly found in the cell stroma (Li et al., 2016). The expression of collagen I significantly increases with fibrosis in endometrial cells (Sun et al., 2019). Our study revealed that CM decreases the mRNA expression of collagen I (Figure 6B), consistent with the previous reports (Yu et al., 2018). Importantly, CM/Gel-MA also downregulated collagen I mRNA expression (Figure 6B). However, the slow-release effect partially decreased CM function in a limited treatment period. This result still indicated the potential applicability of CM/Gel-MA against fibrosis. In addition, the expression of CTGF, another indicator evaluating fibrosis, was tested. CTGF expression increased when IUA occurred (Chen et al., 2021), but it could be significantly decreased by CM or CM/Gel-MA treatment (Figure 6C). In summary, CM/Gel-MA can downregulate the mRNA expression of α-SMA, collagen I, and CTGF, which is its function mechanism to inhibit ESC fibrosis.

E-cadherin is an important factor involved in the intercellular adhesion and maintenance of cytoskeletal integrity (Gumbiner, 2005; Wynn, 2007). Epithelial-mesenchymal transformation (EMT) has been shown to be associated with fibrosis (Marconi et al., 2021), while E-cadherini is essential for EMT (Bure et al., 2019), so E-cadherin may be associated with fibrosis. However, compared with the control group, the mRNA level of E-cadherin is decreased when treated with CM

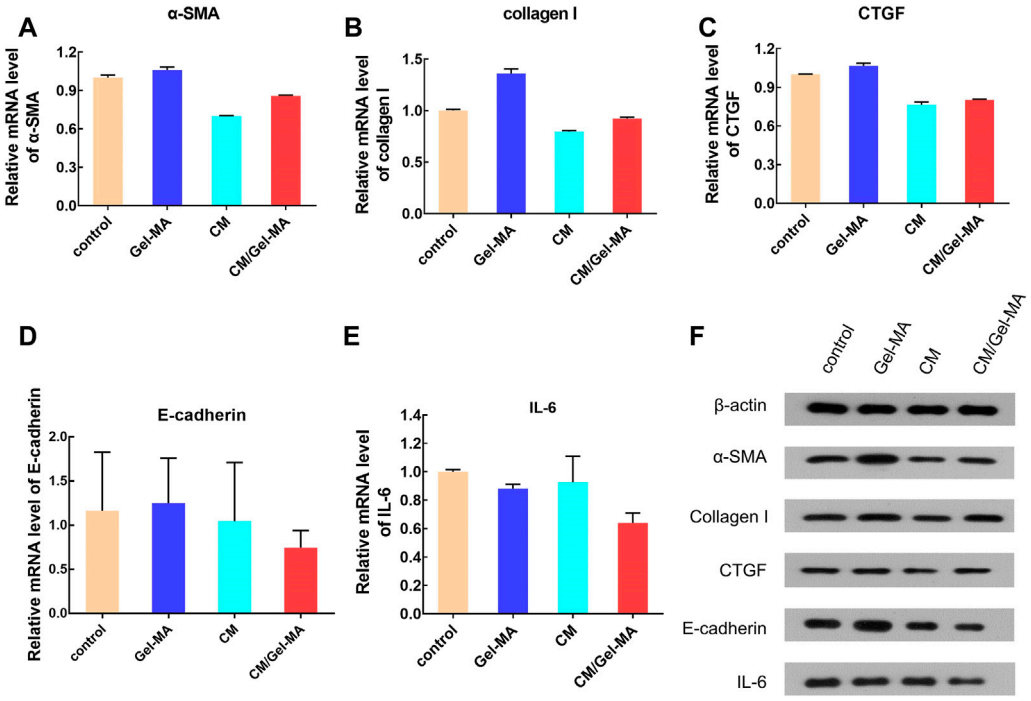

FIGURE 6
Expression level of some bio-factors. **(A)** Relative mRNA level of α-SMA. **(B)** Relative mRNA level of collagen I. **(C)** Relative mRNA level of CTGF. **(D)** Relative mRNA level of E-cadherin. **(E)** Relative mRNA level of IL-6. **(F)** The results of WB.

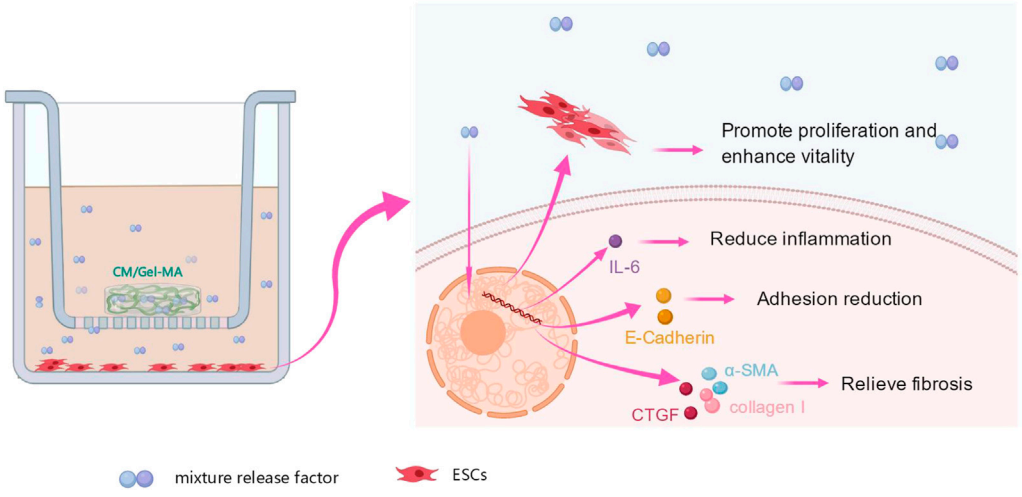

FIGURE 7
Effect of CM/Gel-MA on IUA cell model. The IUA model was induced by adding TGF-β1 into endometrial stromal cells. After treating the model with CM/Gel-MA, the fibrosis was inhibited with decreased the expression of α-SMA, collagen I, CTGF, E-cadherin, and IL-6. At the same time, the cell vitality and proliferation ability were enhanced after treatment.

or CM/Gel-MA, and CM/Gel-MA downregulated E-cadherin better (Figure 6D). Therefore, CM/Gel-MA effectively downregulated mRNA expression of E-cadherin and might prevent endometrial fibrosis. Moreover, both CM and CM/Gel-MA decreased IL-6 expression (Figure 6E), and the effect of CM/Gel-MA was more pronounced. It indicated reduced inflammation which helped fibrosis inhibition (Vahedian et al., 2020). Therefore, the downregulation of E-cadherin and IL-6 mRNA levels supported the conclusion that CM/Gel-MA had the potential to attenuate IUA fibrosis.

Further, the WB experiments were carried out to show the expression of the fibrosis-associated proteins. Figure 6F showed that all trends of those protein expression were basically consistent with

the results of qPCR. As a result of the aforementioned findings, it is summarized that CM/Gel-MA reduces the expression of α-SMA, collagen I, CTGF, E-cadherin, and IL-6. Good CM functions as well as Gel adhesion on the uterine cavity may help CM/Gel-MA to have a long-term curation effect on IUA (Figure 7).

4 Conclusion

In summary, we explore a new method of Gel-MA-assisted CM for uterine adhesion relief. A simple and environmentally friendly procedure is used to create the CM/Gel-MA hybrid. In this hybrid, CM is used to regulate the levels of some biofactors and resist uterine adhesion, whereas Gel-MA is used as a supporter with great adhesive capability to fix CM at the uterine wall and slowly release it. CM addition does not weaken the mechanical properties of Gel-MA. The CM/Gel-MA scaffold efficiently executes CM functions, such as increasing cell survival and proliferation, inhibiting the expression of α-SMA, collagen I, CTGF, E-cadherin, and IL-6, and thereby preventing fibrosis and inflammation. In the next phase, we will conduct experimental studies from the animal level to further explore CM/Gel-MA in IUA.

Data availability statement

The datasets presented in this study can be found in online repositories. The names of the repository/repositories and accession number(s) can be found in the article/supplementary material.

Author contributions

Conceptualization, YZ and Z-ML; methodology, YZ and TW; software, TW and M-JB; validation, YZ, Z-ML, TW, and X-HQ; formal analysis, YZ and TW; investigation, YZ; resources, YZ and Z-ML; data curation, TW; writing—original draft preparation, TW and M-JB; writing—review and editing, YZ; visualization, Z-ML; supervision, Z-ML; project administration, YZ; funding acquisition, YZ. All authors have read and agreed to the published version of the manuscript.

Funding

This research was funded by the National Natural Science Foundation of China (grant no. 81660265), the Natural Science Foundation of Jiangxi Province (grant nos 20224BAB206026 and 20181BAB205015), Key Research and Development Program of Jiangxi Province (grant no. 20202BBGL73065), the Natural Science Foundation of Hunan Province (grant no. 2019JJ50955), and the Science and Technology Program of Jiangxi Healthcare Commission (grant nos 202130758 and 20191104).

Conflict of interest

The authors declare that the research was conducted in the absence of any commercial or financial relationships that could be construed as a potential conflict of interest.

Publisher's note

All claims expressed in this article are solely those of the authors and do not necessarily represent those of their affiliated organizations, or those of the publisher, the editors and the reviewers. Any product that may be evaluated in this article, or claim that may be made by its manufacturer, is not guaranteed or endorsed by the publisher.

References

AAGL Elevating Gynecologic Surgery (2017). AAGL practice report: Practice guidelines on intrauterine adhesions developed in collaboration with the European society of gynaecological endoscopy (ESGE). *Gynecol. Surg.* 14 (1), 6. doi:10.1186/s10397-017-1007-3

Ai, Y., Chen, M., Liu, J., Ren, L., Yan, X., and Feng, Y. (2020). lncRNA TUG1 promotes endometrial fibrosis and inflammation by sponging miR-590-5p to regulate Fasl in intrauterine adhesions. *Int. Immunopharmacol.* 86, 106703. doi:10.1016/j.intimp.2020.106703

Annabi, N., Zhang, Y. N., Assmann, A., Sani, E. S., Cheng, G., Lassaletta, A. D., et al. (2017). Engineering a highly elastic human protein–based sealant for surgical applications. *Sci. Transl. Med.* 9 (410), eaai7466. doi:10.1126/scitranslmed.aai7466

Benor, A., Gay, S., and DeCherney, A. (2020). An update on stem cell therapy for Asherman syndrome. *J. Assist. Reprod. Genet.* 37 (7), 1511–1529. doi:10.1007/s10815-020-01801-x

Bonafe, F., Govoni, M., Giordano, E., Caldarera, C. M., Guarnieri, C., and Muscari, C. (2014). Hyaluronan and cardiac regeneration. *J. Biomed. Sci.* 21, 100. doi:10.1186/s12929-014-0100-4

Bu, Y., and Pandit, A. (2022). Cohesion mechanisms for bioadhesives. *Bioact. Mat.* 13, 105–118. doi:10.1016/j.bioactmat.2021.11.008

Bure, I. V., Nemtsova, M. V., and Zaletaev, D. V. (2019). Roles of E-cadherin and noncoding RNAs in the epithelial–mesenchymal transition and progression in gastric cancer. *Int. J. Mol. Sci.* 20 (12), 2870. doi:10.3390/ijms20122870

Chen, L., Xiao, S., He, S., Tian, Q., and Xue, M. (2020). Factors that impact fertility after hysteroscopic adhesiolysis for intrauterine adhesions and amenorrhea: A retrospective cohort study. *J. Minim. Invasive Gynecol.* 27 (1), 54–59. doi:10.1016/j.jmig.2018.12.023

Chen, X., Zhou, Y., Sun, Y., Ji, T., and Dai, H. (2021). Transplantation of decellularized and lyophilized amniotic membrane inhibits endometrial fibrosis by regulating connective tissue growth factor and tissue inhibitor of matrix metalloproteinase-2. *Exp. Ther. Med.* 22 (3), 968. doi:10.3892/etm.2021.10400

Colangelo, M. T., Govoni, P., Belletti, S., Squadrito, F., Guizzardi, S., and Galli, C. (2021). Polynucleotide biogel enhances tissue repair, matrix deposition and organization. *J. Biol. Regul. Homeost. Agents.* 35 (1), 355–362. doi:10.23812/20-320-L

Dreisler, E., and Kjer, J. J. (2019). Asherman’s syndrome: Current perspectives on diagnosis and management . *Int. J. Womens Health.* 11, 191–198. doi:10.2147/IJWH.S165474

Duan, W. L., Zhang, L. N., Bohara, R., Martin-Saldana, S., Yang, F., Zhao, Y. Y., et al. (2023). Adhesive hydrogels in osteoarthritis: From design to application. *J. Article; Res. Support, Non-U.S. Gov't; Rev. Mil. MED. RES.* 10 (1), 4. doi:10.1186/s40779-022-00439-3

Ensign, L. M., Tang, B. C., Wang, Y. Y., Tse, T. A., Hoen, T., Cone, R., et al. (2012). Mucus-penetrating nanoparticles for vaginal drug delivery protect against herpes simplex virus. *Sci. Transl. Med.* 4 (138), 138ra79–179r. doi:10.1126/scitranslmed.3003453

Feng, L., Wang, L., Ma, Y., Duan, W., Martin-Saldana, S., Zhu, Y., et al. (2023). Engineering self-healing adhesive hydrogels with antioxidant properties for intrauterine adhesion prevention. *J. Artic. Bioact. Mat.* 27, 82–97. doi:10.1016/j.bioactmat.2023.03.013

Gumbiner, B. M. (2005). Regulation of cadherin-mediated adhesion in morphogenesis, *Nat. Rev. Mol. Cell Biol.* 6(8), 622–634. doi:10.1038/nrm1699

He, C., Dai, M., Zhou, X., Long, J., Tian, W., and Yu, M. (2022). Comparison of two cell-free therapeutics derived from adipose tissue: Small extracellular vesicles versus conditioned medium. *J. Artic.*; research support, non-U.S. Gov't]. *Stem Cell Res. Ther.* 13(1), 86. doi:10.1186/s13287-022-02757-8

Hu, J., Jiao, W., Tang, Z., Wang, C., Li, Q., Wei, M., et al. (2023). Quercetin inclusion complex gels ameliorate radiation-induced brain injury by regulating gut microbiota. *J. Artic. Biomed. Pharmacother.* 158, 114142. doi:10.1016/j.biopha.2022.114142

Jabbehdari, S., Yazdanpanah, G., Kanu, L. N., Chen, E., Kang, K., Anwar, K. N., et al. (2020). Therapeutic effects of lyophilized conditioned-medium derived from corneal mesenchymal stromal cells on corneal epithelial wound healing. *Curr. Eye Res.* 45(12), 1490–1496. doi:10.1080/02713683.2020.1762227

Johary, J., Xue, M., Zhu, X., Xu, D., and Velu, P. P. (2014). Efficacy of estrogen therapy in patients with intrauterine adhesions: Systematic review. *J. Minim. Invasive Gynecol.* 21 (1), 44–54. doi:10.1016/j.jmig.2013.07.018

Li, J., Cen, B., Chen, S., and He, Y. (2016). MicroRNA-29b inhibits TGF-β1-induced fibrosis via regulation of the TGF-β1/Smad pathway in primary human endometrial stromal cells. *Mol. Med. Rep.* 13 (5), 4229–4237. doi:10.3892/mmr.2016.5062

Li, X., Lv, H. F., Zhao, R., Ying, M. F., Samuriwo, A. T., and Zhao, Y. Z. (2021). Recent developments in bio-scaffold materials as delivery strategies for therapeutics for endometrium regeneration. *Mat. Today bio.* 11, 100101. doi:10.1016/j.mtbio.2021.100101

Lim, K. S., Klotz, B. J., Lindberg, G., Melchels, F., Hooper, G. J., Malda, J., et al. (2019). Visible light cross-linking of gelatin hydrogels offers an enhanced cell microenvironment with improved light penetration depth. *J. Artic.*; research support, non-U.S. Gov't]. *Macromol. Biosci.* 19(6), e1900098. doi:10.1002/mabi.201900098

Liu, F., Hu, S., Yang, H., Li, Z., Huang, K., Su, T., et al. (2019). Hyaluronic acid hydrogel integrated with mesenchymal stem cell-secretome to treat endometrial injury in a rat model of asherman's syndrome. *Adv. Healthc. Mat.* 8 (14), e1900411. doi:10.1002/adhm.201900411

Liu, L., Chen, G., Chen, T., Shi, W., Hu, H., Song, K., et al. (2020). si-SNHG5-FOXF2 inhibits TGF-β1-induced fibrosis in human primary endometrial stromal cells by the Wnt/β-catenin signalling pathway. *J. Artic.*; Research Support, Non-U.S. Gov't]. *Stem Cell Res. Ther.* 11(1), 479. doi:10.1186/s13287-020-01990-3

Liu, Y., and Chan-Park, M. B. (2010). A biomimetic hydrogel based on methacrylated dextran-graft-lysine and gelatin for 3D smooth muscle cell culture. *J. Artic.*; Research Support, Non-U.S. Gov't]. *Biomaterials.* 31(6), 1158–1170. doi:10.1016/j.biomaterials.2009.10.040

March, C. M. (2011). Asherman's syndrome. *Semin. Reprod. Med.* 29 (2), 083–094. doi:10.1055/s-0031-1272470

Marconi, G. D., Fonticoli, L., Rajan, T. S., Pierdomenico, S. D., Trubiani, O., Pizzicannella, J., et al. (2021). Epithelial-mesenchymal transition (EMT): The type-2 EMT in wound healing, tissue regeneration and organ fibrosis. *Cells.* 10, 1587(7). doi:10.3390/cells10071587

Pawitan, J. A. (2014). Prospect of stem cell conditioned medium in regenerative medicine. *J. Article; Res. Support, Non-U.S. Gov't]. Biomed Res. Int.* 2014, 965849. doi:10.1155/2014/965849

Pirmoradian, M., Hooshmand, T., Najafi, F., Haghbin, N. M., and Davaie, S. (2022). Design, synthesis, and characterization of a novel dual cross-linked gelatin-based bioadhesive for hard and soft tissues adhesion capability. *Biomed. Mat.* 17, 065010(6). doi:10.1088/1748-605X/ac9268

Queckborner, S., Syk, L. E., Gemzell-Danielsson, K., and Davies, L. C. (2020). Endometrial stromal cells exhibit a distinct phenotypic and immunomodulatory profile. *J. Artic.*; Research Support, Non-U.S. Gov't]. *Stem Cell Res. Ther.* 11(1), 15. doi:10.1186/s13287-019-1496-2

Rao, K. M., Kim, E., Kim, H. J., Uthappa, U. T., and Han, S. S. (2023). Hyaluronic acid-quercetin pendant drug conjugate for wound healing applications. *Int. J. Biol. Macromol.* 240, 124336. doi:10.1016/j.ijbiomac.2023.124336

Rein, D. T., Schmidt, T., Hess, A. P., Volkmer, A., Schondorf, T., and Breidenbach, M. (2011). Hysteroscopic management of residual trophoblastic tissue is superior to ultrasound-guided curettage. *J. Minim. Invasive Gynecol.* 18 (6), 774–778. doi:10.1016/j.jmig.2011.08.003

Rodriguez-Fuentes, D. E., Fernandez-Garza, L. E., Samia-Meza, J. A., Barrera-Barrera, S. A., Caplan, A. I., and Barrera-Saldana, H. A. (2021). Mesenchymal stem cells current clinical applications: A systematic review. *J. Artic.*; research support, non-U.S. Gov't; systematic review]. *Arch. Med. Res.* 52(1), 93–101. doi:10.1016/j.arcmed.2020.08.006

Sagaradze, G. D., Basalova, N. A., Kirpatovsky, V. I., Ohobotov, D. A., Grigorieva, O. A., Balabanyan, V. Y., et al. (2019). Application of rat cryptorchidism model for the evaluation of mesenchymal stromal cell secretome regenerative potential. *Biomed. Pharmacother.* 109, 1428–1436. doi:10.1016/j.biopha.2018.10.174

Sato, C., Yamamoto, Y., Funayama, E., Furukawa, H., Oyama, A., Murao, N., et al. (2018). Conditioned medium obtained from amnion-derived mesenchymal stem cell culture prevents activation of keloid fibroblasts. *Plast. Reconstr. Surg.* 141 (2), 390–398. doi:10.1097/PRS.0000000000004068

Sharpe, M. E., Morton, D., and Rossi, A. (2012). Nonclinical safety strategies for stem cell therapies. *Toxicol. Appl. Pharmacol.* 262 (3), 223–231. doi:10.1016/j.taap.2012.05.007

Shi, C., Yao, Y., Wang, L., Sun, P., Feng, J., and Wu, G. (2021). Human salivary histatin-1-functionalized gelatin methacrylate hydrogels promote the regeneration of cartilage and subchondral bone in temporomandibular joints. *J. Artic. Pharm.* 14 (5), 484. doi:10.3390/ph14050484

Song, Y. T., Liu, P. C., Tan, J., Zou, C. Y., Li, Q. J., Li-Ling, J., et al. (2021). Stem cell-based therapy for ameliorating intrauterine adhesion and endometrium injury. *Stem Cell Res. Ther.* 12 (1), 556. doi:10.1186/s13287-021-02620-2

Stubbe, B., Mignon, A., Van Damme, L., Claes, K., Hoeksema, H., Monstrey, S., et al. (2021). Photo-crosslinked gelatin-based hydrogel films to support wound healing. *J. Artic.*; research support, non-U.S. Gov't]. *Macromol. Biosci.* 21(12), e2100246. doi:10.1002/mabi.202100246

Sun, L., Zhang, S., Chang, Q., and Tan, J. (2019). Establishment and comparison of different intrauterine adhesion modelling procedures in rats. *Reprod. Fertil. Dev.* doi:10.1071/RD18397

Tytgat, L., Markovic, M., Qazi, T. H., Vagenende, M., Bray, F., Martins, J. C., et al. (2019). Photo-crosslinkable recombinant collagen mimics for tissue engineering applications. *J. Artic.*; Research Support, Non-U.S. Gov't]. *J. Mat. Chem. B* 7(19), 3100–3108. doi:10.1039/c8tb03308k

Vahedian, V., Asadi, A., Esmaeili, P., Zamani, S., Zamani, R., Hajazimian, S., et al. (2020). Anti-inflammatory activity of emu oil-based nanofibrous scaffold through downregulation of IL-1, IL-6, and TNF-α pro-inflammatory cytokines. *Horm. Mol. Biol. Clin. Investig.* 41 (2). doi:10.1515/hmbci-2019-0052

Wang, L., Fu, H., Wang, W., Liu, Y., Li, X., Yang, J., et al. (2021). Notoginsenoside R1 functionalized gelatin hydrogels to promote reparative dentinogenesis. *J. Artic.*; Research Support, Non-U.S. Gov't]. *Acta Biomater.* 122, 160–171. doi:10.1016/j.actbio.2020.12.031

Wang, L., Yu, C., Chang, T., Zhang, M., Song, S., Xiong, C., et al. (2020). *In situ* repair abilities of human umbilical cord-derived mesenchymal stem cells and autocrosslinked hyaluronic acid gel complex in rhesus monkeys with intrauterine adhesion. *J. Artic.*; Research Support, Non-U.S. Gov't]. *Sci. Adv.* 6(21), a6357. doi:10.1126/sciadv.aba6357

Wei, X., Liu, F., Zhang, S., Xu, X., Li, J., Wang, Q., et al. (2022). Human umbilical cord mesenchymal stem cell-derived conditioned medium promotes human endometrial cell proliferation through wnt/β-catenin signaling. *J. Artic. Biomed. Res. Int.* 2022, 1–10. doi:10.1155/2022/8796093

Wen, Y., Chen, X., Yan, H., and Lin, Q. (2022). Comparative study of physicochemical properties of alginate composite hydrogels prepared by the physical blending and electrostatic assembly methods. *J. Artic. Gels* 8 (12), 799. doi:10.3390/gels8120799

Wynn, T. A. (2007). Common and unique mechanisms regulate fibrosis in various fibroproliferative diseases. *J. Clin. Investig.* 117 (3), 524–529. doi:10.1172/JCI31487

Xin, L., Lin, X., Zhou, F., Li, C., Wang, X., Yu, H., et al. (2020). A scaffold laden with mesenchymal stem cell-derived exosomes for promoting endometrium regeneration and fertility restoration through macrophage immunomodulation. *J. Artic.*; Research Support, Non-U.S. Gov't]. *Acta Biomater.* 113, 252–266. doi:10.1016/j.actbio.2020.06.029

Yamashita, T., Takahashi, Y., and Takakura, Y. (2018). Possibility of exosome-based therapeutics and challenges in production of exosomes eligible for therapeutic application. *Biol. Pharm. Bull.* 41 (6), 835–842. doi:10.1248/bpb.b18-00133

Yu, J., Jiang, L., Gao, Y., Sun, Q., Liu, B., Hu, Y., et al. (2018). Interaction between BMSCs and EPCs promotes IUA angiogenesis via modulating PI3K/Akt/Cox2 axis. *Am. J. Transl. Res.* 10 (12), 4280–4289.

Zagoura, D. S., Roubelakis, M. G., Bitsika, V., Trohatou, O., Pappa, K. I., Kapelouzou, A., et al. (2012). Therapeutic potential of a distinct population of human amniotic fluid mesenchymal stem cells and their secreted molecules in mice with acute hepatic failure. *J. Artic.*; Research Support, Non-U.S. Gov't]. *Gut.* 61(6), 894–906. doi:10.1136/gutjnl-2011-300908

Zeisberg, M., Kalluri, R., and Extramural, N. I. H. (2013). Cellular Mechanisms of Tissue Fibrosis. 1. Common and organ-specific mechanisms associated with tissue fibrosis. *Am. J. Physiol.-Cell Physiol.* 304 (3), C216–C225. doi:10.1152/ajpcell.00328.2012

Zhu, H., Pan, Y., Jiang, Y., Li, J., Zhang, Y., and Zhang, S. (2019a). Activation of the Hippo/TAZ pathway is required for menstrual stem cells to suppress myofibroblast and inhibit transforming growth factor β signaling in human endometrial stromal cells. *J. Artic.*; Research Support, Non-U.S. Gov't]. *Hum. Reprod.* 34(4), 635–645. doi:10.1093/humrep/dez001

Zhu, M., Wang, Y., Ferracci, G., Zheng, J., Cho, N. J., and Lee, B. H. (2019b). Gelatin methacryloyl and its hydrogels with an exceptional degree of controllability and batch-to-batch consistency. *J. Artic.*; Research Support, Non-U.S. Gov't]. *Sci. Rep.* 9(1), 6863. doi:10.1038/s41598-019-42186-x

frontiers | Frontiers in Bioengineering and Biotechnology

TYPE Original Research
PUBLISHED 05 May 2023
DOI 10.3389/fbioe.2023.1203709

OPEN ACCESS

EDITED BY
Yong Liu,
University of Chinese Academy of Sciences, China

REVIEWED BY
Xixi Zhu,
Shandong University of Science and Technology, China
Yuguang Gao,
Binzhou Medical University Hospital, China

*CORRESPONDENCE
Wanchun Wang,
wangwanchun2019@qdu.edu.cn
Yuanping Hao,
yphao@qdu.edu.cn

RECEIVED 11 April 2023
ACCEPTED 24 April 2023
PUBLISHED 05 May 2023

CITATION
Qu X, Guo X, Zhu T, Zhang Z, Wang W and Hao Y (2023), Microneedle patches containing mesoporous polydopamine nanoparticles loaded with triamcinolone acetonide for the treatment of oral mucositis.
Front. Bioeng. Biotechnol. 11:1203709.
doi: 10.3389/fbioe.2023.1203709

Microneedle patches containing mesoporous polydopamine nanoparticles loaded with triamcinolone acetonide for the treatment of oral mucositis

Xiaoying Qu[1], Xiaoli Guo[2], Tingting Zhu[2], Zhe Zhang[2], Wanchun Wang[3]* and Yuanping Hao[3]*

[1]Department of Stomatology, School of Stomatology of Weifang Medical University, Weifang, China, [2]School of Stomatology of Qingdao University, Qingdao, China, [3]Qingdao Stomatological Hospital, Qingdao, China

Oral mucositis (OM) is the most common disease of the oral mucosa, which affects people's daily production and life. Triamcinolone ointment is the common clinical drug for OM treatment. However, the hydrophobic properties of triamcinolone acetonide (TA) and the complex microenvironment of the oral cavity led to its low bioavailability and unstable therapeutic effects on ulcer wounds. Herein, dissolving microneedle patches (MNs) composed of mesoporous polydopamine nanoparticles (MPDA) loaded with TA (TA@MPDA), sodium hyaluronic acid (HA), and *Bletilla striata* polysaccharide (BSP) are prepared as the transmucosal delivery system. The prepared TA@MPDA-HA/BSP MNs exhibit well-arranged microarrays, high mechanical strength and fast solubility (<3 min) properties. In addition, the hybrid structure improves the biocompatibility of TA@MPDA and expedites oral ulcer healing in the SD rat model through the synergistic anti-inflammatory and pro-healing effects of microneedle ingredients (hormones, MPDA and Chinese herbs extracts), with 90% less amount of TA compared with Ning Zhi Zhu®. TA@MPDA-HA/BSP MNs are shown to be their great potential as novel ulcer dressings for OM management.

KEYWORDS

oral mucositis, dissolving microneedle, mesoporous polydopamine nanoparticles, triamcinolone acetonide, oral ulcer

1 Introduction

Oral mucositis (OM) is an inflammatory disease caused by necrosis and shedding of oral mucosal tissue, which can involve the epithelial layer and connective tissue (An et al., 2022). At the stage of the disease's progression, the mucosa will be congested, erosive, prolonged, and may even become oral cancer. Characterized by severe pain, OM affects the patient's eating and speaking functions and reduces the quality of life. OM is closely associated with vitamin or trace element deficiency, genetic and immune factors, local trauma, and allergenic infections, and other systemic diseases such as head and neck chemotherapy (Bilodeau and Lalla, 2019; Elad et al., 2022). These processes lead to cell and microvascular injury, the release and amplification of inflammatory cytokines, the generation of reactive oxygen species (ROS), and the destruction of mucosal epithelial integrity. Tumor necrosis factor-α (TNF-α) plays an important role in the pathogenesis of autoimmune diseases. In response to

the inflammatory response of immune cells, TNF-a is released on a large scale, resulting in oral epithelial damage and eventually the formation of ulcerated surfaces. Platelet endothelial cell adhesion molecule-1 (CD31), a member of the immunoglobulin superfamily, plays an important role in clearing aging neutrophils and is closely related to angiogenesis from the body. During the healing stage, epithelial hyperplasia causes the mucosa to gradually heal. Therefore, inhibiting inflammatory response, clearing ROS and promoting cell proliferation are the key to the treatment of oral mucositis. Triamcinolone acetonide (TA) is commonly used in the treatment of OM as an adrenal glucocorticoid, which has highly effective anti-inflammatory, immunosuppressive and anti-allergic effects (Padula et al., 2018; Seon-Woo et al., 2019). However, TA is currently only produced as a topical formulation (ointment and gel) with poor water solubility and minimal oral bioavailability. Moreover, the oral cavity is a dynamic and moist environment where it is difficult for ointment and gel to exert effects in the lesion area due to saliva flushing, involuntary oral movements and swallowing (Zheng et al., 2021).

Recently, microneedles (MNs), as a highly effective transdermal drug delivery form that can break through the mucosal barrier, have attracted extensive attention in the treatment of oral diseases (Moore et al., 2022). MNs can be classified in a variety of ways. The most common way is to divide microneedles into solid microneedles, coated microneedles, hollow microneedles, soluble microneedles and hydrogel microneedles. Among them, Hydrogel microneedles (HMNs) are prepared from expandable crosslinked polymers. In a transdermal drug delivery system, drugs enter the body through loose apertures to achieve transdermal drug delivery. Compared with other kinds of microneedles, hydrogel microneedles can increase the drug loading of microneedles by setting up a reservoir. However, there are also some problems such as large pores left after the removal of loose hydrogel, long recovery time, and easy infection. Dissolving MNs composed of hydrophilic polymers have become popular biological drugs because of their simple manufacturing process, good biocompatibility, and precise transdermal drug delivery (Bian et al., 2021; Jing et al., 2021; Sartawi et al., 2022). With certain mechanical strength, dissolving MNs can insert into the oral mucosa, form multiple tiny channels, and subsequently dissolve into the liquid to release drug quickly. Therefore, MNs has become one of the most desirable alternatives to traditional local drug for the delivery of small molecules, large molecules and nanoparticles (Hao et al., 2020; Qin et al., 2020; Vora et al., 2020). *Bletilla striata* polysaccharide (BSP) is a kind of natural glucomannan with high biosafety and low price. BSP has anti-inflammatory, pro-coagulant, antibacterial and antioxidant activities, thus promoting wound healing (Wu et al., 2021; Zhang et al., 2022). Hu et al. first prepared MN using BSP in 2018 (Hu et., 2018). The results showed that MNs consisting of 24% BSP could penetrate the skin of rats. Sodium hyaluronic acid (HA) is a substance extracted from cockscomb and can also be prepared by lactic acid fermentation. HA with good biocompatibility has been found extensively used for tissue regeneration (Hemshekhar et al., 2016; Agarwal et al., 2020; Xing et al., 2020). HA in the form of microneedles has been applied in drug transdermal delivery systems for wound dressings and superficial tumor treatment (Hao et al., 2020; Peng et al., 2021; Saha and Rai, 2021). We have recently developed hyaluronic acid microneedle patch to improve the delivery of soluble small-molecule drugs into rat oral mucosa, and to protect the adhesive layer from mouth movement and saliva (Zhu et al., 2022). In this study, we tried to combine HA and BSP to enhance the therapeutic effect. Low molecular weight HA can enhance the mechanical strength of microneedle tip, and cooperate with BSP to give full play to anti-inflammatory and wound healing effects.

So far, many materials have been used as carriers to synthesize composite materials, such as montmorillonite (Li et al., 2022; Zhu et al., 2022), polydopamine (PDA) and so on. PDA is a new nanoscale material that has attracted more attention because of its good biocompatibility, near-infrared absorption, scavenging ability of oxidative free radicals, good antimicrobial properties, and excellent drug carrier (Bao et al., 2018; Wang et al., 2018). Mesoporous polydopamine nanoparticles (MPDA NPs) have a significantly higher drug-loading capacity than conventional PDA. The abundant functional groups and mesoporous structure on its surface enable it to combine with drug molecules through chemical bonding, electrostatic adsorption, π-π stacking and spatial structure (Tang et al., 2015; Zhu et al., 2021).

Here, we may reasonably hypothesize that i) MPDA NPs may be the ideal carrier for TA, both to improve the bioavailability of TA and to exert the anti-inflammatory effects of MPDA NPs; ii) the combination of TA@MPDA NPs with dissolving HA/BSP microneedle may produce synergistic effects in the treatment of OM, reducing the dosage of the hormone administered. To test our hypotheses, TA@MPDA NPs were prepared through π-π stacking and encapsulated in the HA/BSP dissolving microneedle patch *via* a one-casting fabrication process for oral mucositis treatment. The schematic illustration of the TA@MPDA-HA/BSP MN patch is shown in Figure 1. The sharp tips of microneedles penetrated the mucosal barrier and delivered the drug deep without causing adverse reactions. TA could be sustainably released at the lesion, synergistic with MPDA to inhibit ROS-induced inflammation reaction. At the same time, the combination of TA@MPDA and HA/BSP could significantly increase the human oral keratinocytes (HOK) and primary human gingival fibroblasts (hGFs) proliferation and migration. The TA@MPDA-HA/BSP MN patch exhibited excellent treatment effects for accelerating oral ulcer closure. Taken together, the constructed microneedle patch is a promising candidate for oral inflammatory disease.

2 Materials and methods

2.1 Materials

1,3,5-Trimethylbenzene (TMB, Mw 120.19 g/mol, AR, 97%), Tris (hydroxymethyl) aminomethane (TRIS, Mw 121.14 g/mol, ≥99.9%), dopamine hydrochloride (Mw 189.64 g/mol, 98%), Triamcinolone acetonide (TA), Lipopolysaccharides from *Escherichia coli* O55:B5 (LPS) and phenol were purchased from Aladdin (Shanghai, China). Pluronic® F-127 (F127) was purchased from Sigma (Shanghai, China). *Bletilla striata* polysaccharide (BSP, Mw 390–460 kDa, ≥98%) was acquired from Xi'an Zelang Biotechnology (Xi'an, China). Sodium hyaluronic acid (HA, Mw 5–10 kDa) was obtained from Freda Biology Co., Ltd. (Shandong, China). The polydimethylsiloxane mold (PDMS, Shenzhen Thunder

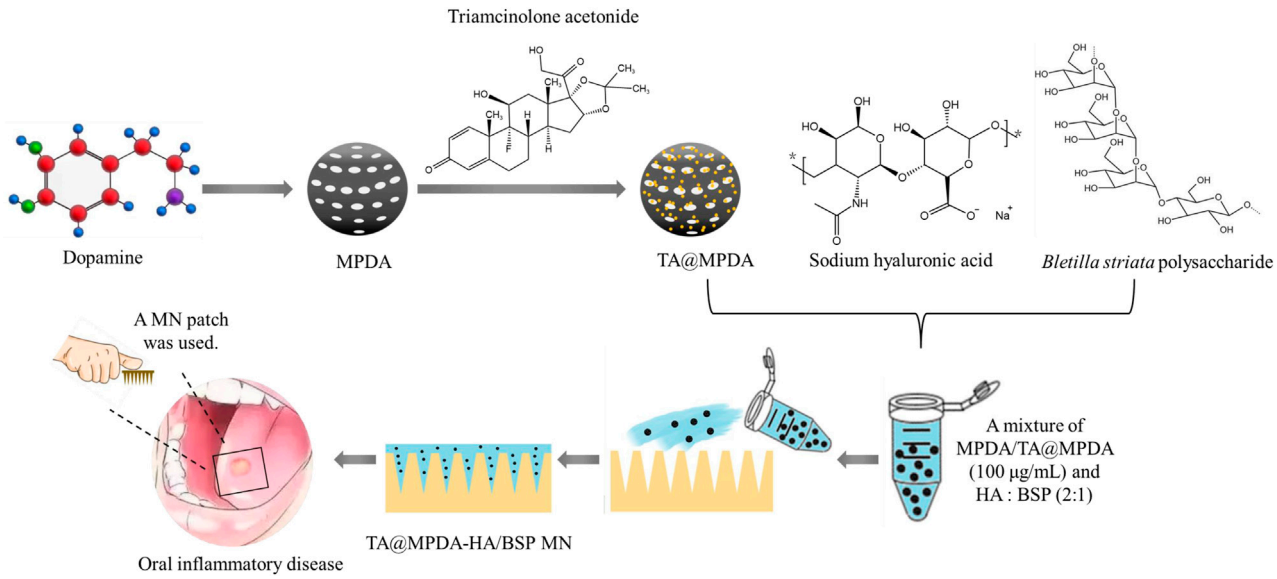

FIGURE 1
Schematic illustrations of the preparation of TA@MPDA-HA/BSP MN patch and its application in oral inflammatory disease.

Cloud Information Technology Co., Ltd., China) had 225 (15 × 15) MNs, and the height and width of each needle were 700 and 300 μm, respectively. The distance among needles was 600 μm. TRITC-Phalloidin, 4′,6-diamidino-2-phenyllindole (DAPI) was purchased from Solarbio. Cell Counting Kit-8 (CCK-8) was purchased from Absin Bioscience Inc (Shanghai, China). Human Tumor Necrosis Factor Alpha (TNF-α) ELISA Kit was purchased from Elabscience Biotechnology Co., Ltd. (Wuhan, China). Methanol was the chromatographic grade for chromatographic analysis when High-performance liquid phase (HPLC) was used, and other chemical reagents were analytical grade, both provided by Sinopharm Chemical Reagent Co., Ltd. (Shanghai, China), and used directly.

2.2 Cell culture and animals

2.2.1 Cell

In a humidified incubator (WIGGENS, Germany) at 37°C with 5% CO_2, Human Oral Keratinocytes (HOK) and Human gingival fibroblasts (hGFs) were cultured using the complete medium. The complete medium includes 90% Dulbecco's Modified Eagle Medium (DMEM, Biological Industries, Israel), 10% fetal bovine serum (FBS, Solarbio, Beijing, China) and 1% penicillin/streptomycin (Biological Industries, Israel).

2.2.2 Animals

We purchased adult Sprague Dawley rats (SD, male, ~150 g) from Jinan Pengyue laboratory animal breeding center (Shandong, China) and maintained them in Qingdao University's Laboratory Animal Center in a specific pathogen-free (SPF) environment. All procedures performed in the study were in accordance with the Ethics Committee of Qingdao Stomatological Hospital Affiliated of Qingdao University Certificate (contract grant 2021KQYX031) and with the National Research Council's Guide for the Care and Use of Laboratory Animals ethical standards.

2.3 Preparation of mesoporous polydopamine nanoparticles (MPDA NPs)

The preparation of MPDA NPs was carried out according to the methods reported in the previous literature (Yuan et al., 2020; Zeng et al., 2022). Briefly, 0.36 g of F127 and 417 μL of TMB solution were added to the mixture of 60 mL of ethanol and 65 mL of deionized water. After stirring on a magnetic stirrer for 30 min at room temperature, 90 mg of TRIS and 60 mg of dopamine hydrochloride were added to the mixture. The reaction was maintained for 24 h. The crude products were collected and washed at least three times with an ethanol/acetone mixture (v/v = 2: 1) to remove the template by centrifugation. Finally, MPDA NPs were obtained and dried in a vacuum drying oven (DZF-6050AB, China, Beijing).

2.4 Preparation of TA-loaded MPDA nanoparticles (TA@MPDA NPs)

Different concentrations of MPDA NPs suspension were prepared by dispersing MPDA NPs (5, 10, and 20 mg) uniformly in 10 mL of methanol under the action of sonication. TA solution (2 mg/mL, dissolved in methanol) was added dropwise to the MPDA NPs dispersion and stirred at 45°C for 3 h. Finally, TA@MPDA NPs were collected by centrifugation, dried by vacuum and stored at 4°C for further use. The amount of TA loaded into MPDA was calculated by subtracting the mass of TA in the supernatant from the total mass of the TA in the initial solution.

2.5 Characterization of MPDA and TA@MPDA NPs

The particle size distribution and surface charge of MPDA and TA-loaded MPDA were detected by dynamic light scattering (DLS, Zetasizer Nano ZS) at 25°C. All the tests were conducted in triplicate, and all the data were expressed as the mean ± standard (SD). The morphology of nanoparticles was observed by a JEM-2100 transmission electron microscopy (TEM, JEOL Ltd., Tokyo, Japan). The functional groups of MPDA and TA@MPDA in the range of 500–4,000 cm^{-1} were characterized using a Nicolet iN10 Fourier transform infrared (FTIR) spectrometer (Thermo Fisher Scientific, Waltham, MA, United States) performed 32 scans with a scan resolution of 2 cm^{-1}. TA was determined by a Shimadzu LC-20A instrument (DGU-20A5R degasser, SIL-20A autosampler, CTO-20A column temperature chamber, SPD-M20A UV detector, LC-20AT infusion pump, and LabSolutions Chemical workstation, Kyoto, Japan) equipped with a SHIMADZU Shim-pack GIST C18 (250 × 4.6 mm, 5 μm) analytical column (P/N: 277-30017-08) using methanol-deionized water (65:35, v/v) as the mobile phases with a flow rate of 1.0 mL/min at 25°C. The regression equation with TA concentration as the independent variable and peak area as the dependent variable is Y = ×27681 − 27556 (r^2 = 0.9979) (Supplementary Figure S1A). The peak areas at 240 nm of the supernatants were collected. The drug loading (DL) and encapsulation efficiency (EE) of TA@MPDA were calculated via Eqs 1, 2, respectively:

$$\mathrm{DL} = \frac{\text{TA loaded (g)}}{\text{TA@MPDA (g)}} \times 100\% \quad (1)$$

$$\mathrm{EE} = \frac{\text{Total TA (g)} - \text{free TA (g)}}{\text{Total TA (g)}} \times 100\% \quad (2)$$

2.6 Fabrication and characterization of dissolvable microneedle patches

2.6.1 Dissolving Microneedle Fabrication

0.1 mg MPDA or TA@MPDA was evenly dispersed in 1 mL deionized water by ultrasonic vibration. Then, HA and BSP were mixed in the ratio of 1:2, 1:1, 2:1, respectively, and dissolved in the above dispersion solution. The final concentration of HA was 30%. The microneedle molds injected with deionized water were placed in a vacuum at 0.08 mPa for 20 min so that each well was filled with deionized water, and the excess deionized water was removed. After that, the MPDA-HA/BSP or TA@MPDA-HA/BSP matrix solution was poured into the microneedle molds and then maintained 30 min under ultrasound until the cavity of the tips was filled with solution. The sample was then left at room temperature for approximately 48 h to dry completely. The corresponding MPDA-HA/BSP MNs or TA@MPDA-HA/BSP MNs were gently separated from the mold and stored in a dryer. In addition, HA/BSP MNs were prepared by the same method with HA/BSP as matrix solution.

2.6.2 Morphology and mechanical property of MNs

The morphology of TA@MPDA-HA/BSP MNs was visualized by a dermoscope (AX-10, KaLanDe). In order to observe the microscopic structure of MNs, they were gilded by sputtering to increase conductivity after the edges of MNs were trimmed properly and then imaged using a scanning electron microscope (SEM, VEGA3, TESCAN, Czech Republic) at an accelerating voltage of 10 kV. The size of MNs was measured by ImageJ. The mechanical properties of MNs were tested by compression method at a temperature of 22°C ± 5°C and relative humidity of 40% ± 10%. TA@MPDA-HA/BSP MNs (array: 15 × 15) were pressed into the pig skin using thumb force. The insertion marks left were observed. In addition, TA@MPDA-HA/BSP MNs were inserted into the mucous membrane of rat tongue with the same force for 3 min, and hematoxylin and eosin (H&E) staining was performed to observe the depth of insertion.

2.6.3 Dissolvability

The dissolution rates of TA@MPDA-HA/BSP MNs were studied on the tongue abdomen of SD rats. At the predetermined time points, MNs were removed from the tongue and observed by a microscope (OLYMPUS, Japan). The size variations of MNs were analyzed by ImageJ.

2.7 Preliminary evaluation of biosafety

2.7.1 Blood compatibility

Citrated whole blood from healthy donors was diluted with normal saline (NS) to 2% (v/v). Then 50 μL of the diluted blood was added into the TA@MPDA-HA/BSP MNs dispersed NS solution with different concentrations (0.5, 1.0, 1.5, 2.0 mg/mL), and kept at 37°C for 1 h. Afterward, the mixtures were centrifuged at 1,500 rpm/min for 5 min. The absorbance of the supernatant was detected at 540 nm by a UV-Vis spectrophotometer (UV-8000, Shanghai Metash Instruments Co., Ltd., China). In addition, deionized water and NS solution were mixed with an equal volume of diluted blood to form the positive and negative control group, respectively. The hemolysis ratio was calculated as the following formula:

$$\text{Hemolysis rate} = \frac{A_{\text{Sample}} - A_{\text{Negative control}}}{A_{\text{Positive control}} - A_{\text{Negative control}}} \times 100\% \quad (3)$$

2.7.2 Cytotoxicity

The cytotoxicity of MPDA, TA@MPDA, MPDA-HA/BSP MNs and TA@MPDA-HA/BSP MNs were evaluated using a standard CCK-8 assay. Human Oral Keratinocytes (HOK) were seeded into 96-well plates at a density of 3 × 10^3 cells per well and incubated in at 37°C with 5% CO_2 using the complete medium for 24 h. The cell culture medium was replaced by the test preparation diluted with culture medium for 24 h. After that, the medium was discarded, and the cells were cultured with 100 μL of CCK-8 reagent (10%) solution per well for 2 h. Subsequently, the optical density (OD) values were read with a microplate reader (800TS, Bio-Tek, China) at a wavelength of 450 nm. Pristine culture medium was used as a control group. Cell viability was calculated according to the formula:

$$\text{Cell viability} = \frac{OD_{\text{Preparation}} - OD_{\text{Blank}}}{OD_{\text{Control}} - OD_{\text{Blank}}} \times 100\% \quad (4)$$

where $OD_{Preparation}$, $OD_{Control}$, and OD_{Blank} refer to the OD values of the test preparation-treated group, pristine medium-treated group, and the culture medium without cells, respectively. Each group was carried out in three replicates.

2.8 Cell Morphology Staining

TRITC-Phalloidin and DAPI staining were used to detect the effect of the MN patches on cell morphology. Human gingival fibroblasts (hGFs) were inoculated into 24-well plates at a density of 5.0×10^4 cells per well. After incubation for 24 h, the original medium of experimental group was replaced by a MN-contained medium (MPDA-HA/BSP MNs or TA@MPDA-HA/BSP MNs, 2 mg/mL) and the control group was replaced by the complete medium. Cells were fixed with 4% (v/v) paraformaldehyde to maintain morphology, and treated with 0.5% (w/v) Triton X-100 for 3 min and 5% bovine serum albumin for 30 min, with phosphate buffered saline (PBS) used for cleaning. Then, cells were stained with TRITC-Phalloidin and DAPI under dark conditions. The morphology of the cells was photographed using a fluorescence microscope (OLYMPUS, Japan).

2.9 Cell scratching assay

The cell scratching assay was performed using hGFs. Briefly, hGFs were seeded on 6 well culture-treated plates with a density of 5×10^5 cells each well and cultured for 24 h. To verify that cell migration was caused by drug action rather than cell proliferation, cells were maintained in a serum-free starvation state for 24 h to minimize proliferation. Then, three straight lines were drawn evenly using a 10 μL tip for the formation of microdamage and the fallen cells were washed and removed with PBS, after which the microneedle-contained medium (2 mg/mL) was then introduced into each well. Wound closure was monitored and imaged using an optical microscope (OLYMPUS, Japan) in 12 h intervals. ImageJ was used to quantify the wound area. The formula is as follows:

$$\text{Degree of wound closure} = \frac{S_0 - S_A}{S_0} \times 100\% \quad (5)$$

where S_0 refers to the initial wound area (0 h), and S_A refers to wound area of 12 and 24 h. Each group was carried out in three replicates.

2.10 Anti-inflammatory test

To verify the anti-inflammatory ability of the prepared microneedle patches, LPS-induced hGFs were used to construct a cell inflammation model. hGFs were inoculated into 96-well plates at a density of 3×10^3 per well for 24 h. After removing the original medium, the cells were co-cultured with LPS and MN patches for 24 h. Only adding medium was used as blank control group. LPS and culture medium were used as the positive control group. The final concentrations of LPS and MN patches were 0.1 and 2 mg/mL, respectively. The level of TNF-α in the supernatant was determined by enzyme-linked immunosorbent assay ($n = 3$).

2.11 Insertion safety of MN patches

To evaluate the safety of TA@MPDA-HA/BSP MNs insertion, the MNs were inserted into the tongue mucosa of rats using thumb force to observe the recovery of the mucosa. After 3 min, the MNs were completely dissolved, and then were removed. Before the insertion of the MNs, immediately and 5, 10, and 30 min after the insertion, photos of the tongue mucosa were recorded. Twenty-4 hours later, the rats were euthanized, and the tongue tissue was removed for pathological section preparation and H&E staining.

2.12 Study of the therapeutic effect of MN patches for ulcer model *in vivo*

The model of oral ulcer was constructed by chemical burning as our previous studies (Zhu et al., 2022). SD rats were anesthetized by intraperitoneal injection of sodium pentobarbital (50.0 mg/kg). A cotton ball immersed in 90% phenol solution was placed at one end of a glass tube and exposed to the mucous membrane of rat tongue abdomen for 60 s. The oral ulcer model was successfully established. On the first day after modeling, the rats were randomly divided into five groups: control, triamcinolone acetonide dental paste (Ning Zhi Zhu®) group, HA/BSP MNs group, MPDA-HA/BSP MNs group, TA@MPDA-HA/BSP MNs group. Three rats were assigned for each group, and the healing of the ulcer was recorded using a digital camera for analysis. On the fifth day after administration, the rats were euthanized, and tongue tissue was excised. H&E staining and Masson's Trichrome staining were used to detect oral ulcer healing degree. The levels of TNF-α and CD31 in each group were observed by immunohistochemistry (IHC) to evaluate the ulcer repair.

2.13 Statistical analysis

All quantified data were presented as mean ± standard deviation (SD). All statistical analysis graphs were drawn using GraphPad Prism 9 or Origin 2021. One-way analysis of variance (ANOVA) with Tukey`s test was used to determine the differences between groups. A value of $p < 0.05$ was considered to be statistically significant.

3 Results and discussion

3.1 Preparation and characterization of MPDA and TA@MPDA NPs

MPDA NPs were synthesized by oxidative self-polymerization and self-assembly of dopamine under alkaline conditions (Yuan et al., 2020). The typical structure of MPDA NPs was observed from transmission electron microscopy (TEM), and their surface had obvious mesoporous structure with an average particle size of 241.97 ± 7.54 nm and a narrow size distribution (Figure 2A). Then, triamcinolone acetonide (TA) was loaded on the surface of MPDA. As shown in Figure 2B, the morphology of TA@MPDA tended to be flat after loading TA and the size of NPs increased to 297.16 ± 8.12 nm. The particle size of nanoparticles subjected to drug loading increased. With decrease of TA/MPDA mass ratio in feed, the drug loading decrease, whereas, the

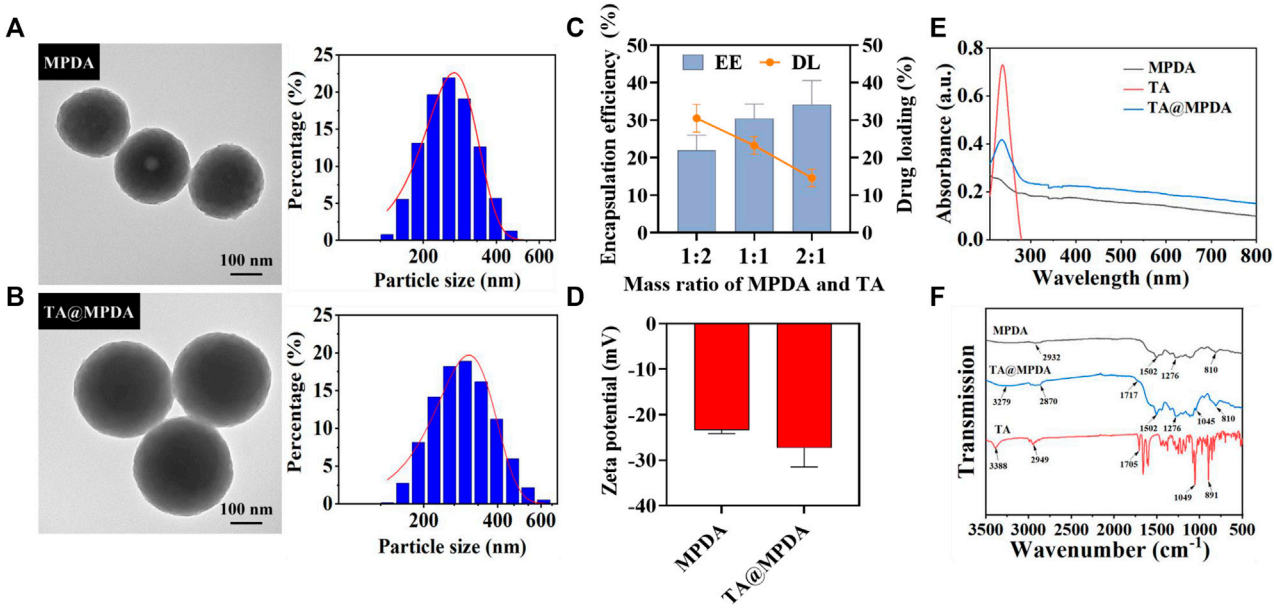

FIGURE 2
Characterization of **(A)** MPDA and **(B)** TA@MPDA TEM Images and particle size distributions. **(C)** The EE (%) and DL (%) of TA and MPDA in different proportions. **(D)** Zeta potential of TA, MPDA and TA@MPDA, respectively. **(E)** UV–Vis absorption spectra of TA, MPDA, and TA@MPDA, respectively. **(F)** The FTIR spectra of TA, MPDA, and TA@MPDA.

encapsulation efficiency and stability increased according. In consideration of drug loading and encapsulation efficiency, 1:1 was selected for further applications and was characterized in detail. The high-performance liquid chromatography was shown in Supplementary Figure S1B. The DL and EE were 23.27% ± 1.91% and 30.43% ± 3.18%, respectively (Figure 2C). The zeta potential of TA@MPDA NPs decreased from −23.37 ± 0.63 mV to −27.30 ± 3.42 mV (Figure 2D). It was demonstrated that the negatively charged NPs had good colloid stability and can be evenly distributed in MNs (Cheng et al., 2020). In the UV-Vis spectrum of TA@MPDA, the new characteristic absorption peak of triamcinolone acetonide shown at ~ 237 nm (λ_{Max}) demonstrated that the successful loading of TA into MPDA NPs (Figure 2E). To investigate the intermolecular interaction between MPDA and TA, FTIR detection was performed. The characteristic peaks of TA skeleton appear at 3,388, 2,949, 1,075, 1,049, and 891 cm^{-1}, which is corresponding to–OH, C–H, C=O and C–C tensile vibration, respectively. The MPDA skeleton has characteristic peaks at 2,932 and 810 cm^{-1}, which is C–H and C–C tensile vibration, respectively. The characteristic peaks of TA@MPDA skeleton at 3,279, 2,870, 1,717, 1,045 and 810 cm^{-1} were the tensile vibration of–OH, C–H, C=O, respectively. In addition, both the MPDA and TA@MPDA skeletons have the characteristic peaks at 1,502 and 1,276 cm^{-1} (Figure 2F). The above experiments proved that TA was successfully loaded.

3.2 Preparation and characterization of the dissolving microneedle patch

As shown in Figure 3A, the microneedles were fabricated by a one-casting fabrication process. The results showed that when the ratio of HA to BSP was 1:2 or 1:1, the demolding time of MNs was longer and the tip was difficult to form. When the ratio was 2:1, the MNs can be completely dried within 2 days and successfully demolded. In the dermoscopy (Figure 3B) and SEM (Figure 3C) images, the microneedle patch consisted of 15 × 15 arrays, which showed a well-arranged regular cone without bubbles and needle breakage. In the process of SEM, a certain Angle was set for the MNs to achieve better imaging, so the size of the MNs presented in the SEM image was smaller than the actual size. After pressing the MNs that have been loaded with TA@MPDA into a pig skin for 3 min, complete dark arrays (15 × 15) were left on the surface of the skin, indicating that the MNs had enough mechanical strength (Figure 3D). The histological section of the MN penetrated oral mucosa also showed a clear shape of microneedle penetration and the insertion depth was 418 ± 2 mm (Figure 3E). The solubility of MNs after puncture of oral mucosa directly affected the release and distribution of their payload. As shown in Figure 3F, the sharp needle of microneedles completely dissolved within 3 min after insertion into the lingual mucosa of rats. The above results manifested that the mechanical strength of the microneedles was sufficient to penetrate and transport the cargo to the interior of the wound site.

3.3 Preliminary evaluation of biosafety

3.3.1 Blood compatibility

The hemocompatibility of microneedles is one of the key factors for the overall success of clinical applications (Zhao et al., 2017; Wu et al., 2021). As described above, we performed hemolysis assays to elucidate their blood compatibility of TA@MPDA-HA/BSP MNs to

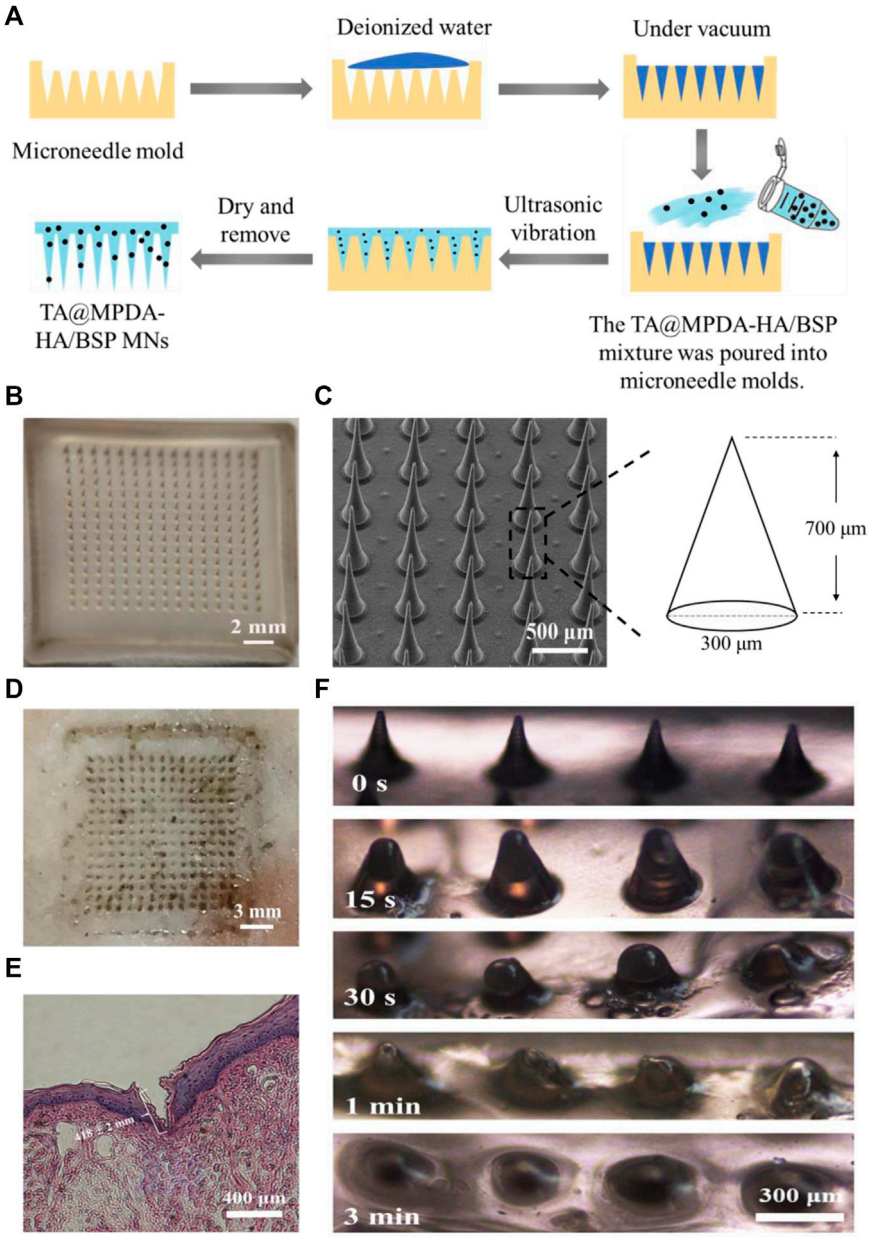

FIGURE 3
Characterization of MN patch. **(A)** One-casting fabrication process of the microneedles. **(B)** Images of TA@MPDA-HA/BSP MNs taken using a microscope. **(C)** SEM image of TA@MPDA-HA/BSP MNs. **(D)** Photo of pig skin after microneedle insertion (15 × 15). **(E)** The image of H&E staining image of the rat tongue mucosa after being treated with MN patch. **(F)** Solubility of TA@MPDA-HA/BSP MN patch inserted into oral mucosa at different times.

whole blood in biological solutions. The illustration in Figure 4A exhibited that the color of the supernatant of the MN groups was similar to that of the negative control group, which was almost colorless, while the distilled water group was distinctly red. According to the authoritative evaluation standard of ASTM F756-17, if the clinic biomedical materials with a hemolysis rate are less than 2%, it can be considered admissible. Quantification demonstrated that the hemolysis ratio of different concentrations (0.5–2.0 mg/mL) was <2%, no hemolysis occurred (Figure 4A). These data indicated that TA@MPDA-HA/BSP MNs have good blood compatibility.

3.3.2 Cytotoxicity

The cytotoxicity of both MPDA and TA@MPDA groups gradually increased as the drug concentration increased in the range of 25–200 μg/mL, showing concentration dependence (Supplementary Figure S2A, B). The cell viability of 25–100 μg/mL MPDA and TA@MPDA were above 58.55% ± 1.58% and 50.84% ± 1.99%, respectively. There were significant differences ($p < 0.05$) in cell viability between 100 μg/mL and 200 μg/mL of the two kinds of particles. The statistical results showed that there was a statistical difference between 0.5 and 2 mg/mL MPDA-HA/BSP MNs groups (Supplementary Figure

10.3389/fbioe.2023.1203709

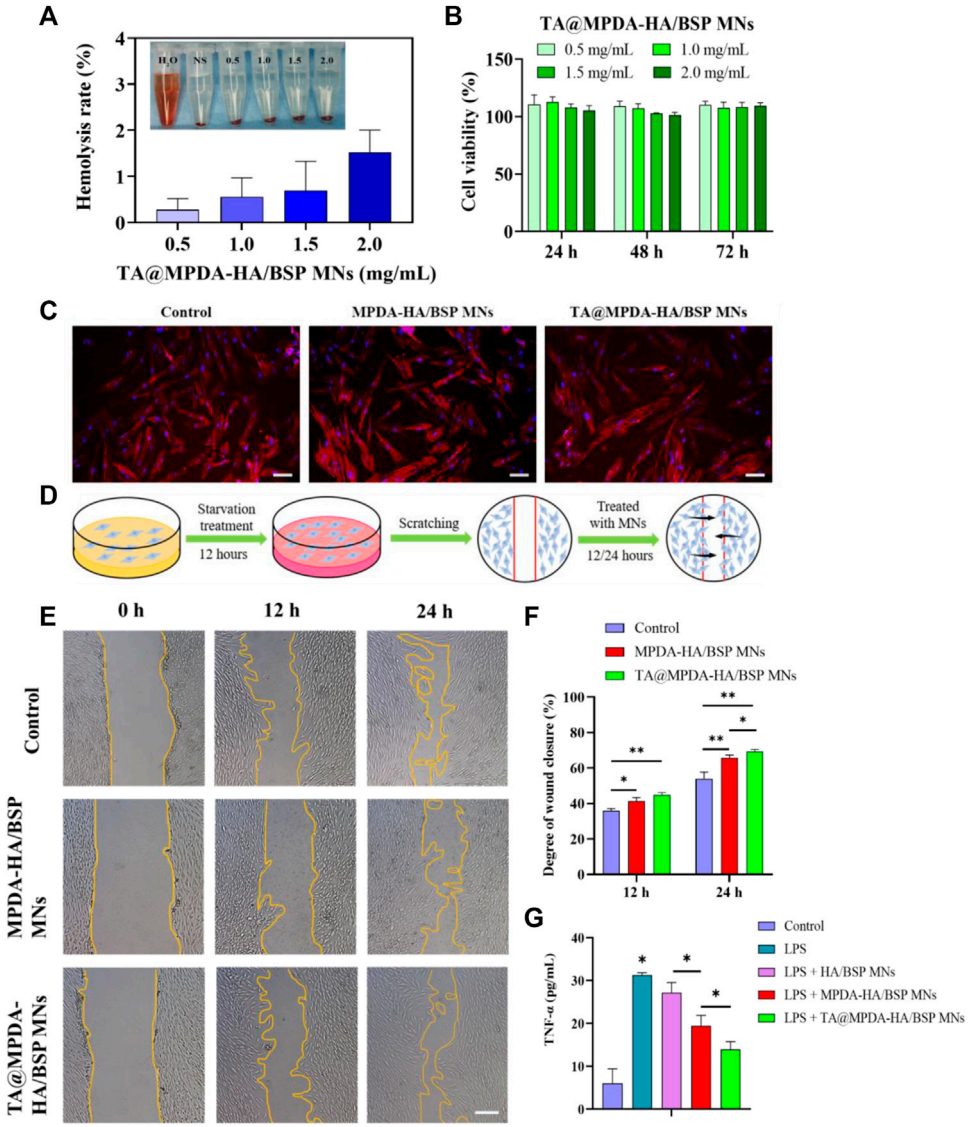

FIGURE 4
(A) Hemolysis ratio of whole blood by TA@MPDA-HA/BSP MNs (0.5, 1.0, 1.5, 2 mg/mL). **(B)** Cell viability of HOK after the incubation with TA@MPDA-HA/BSP MNs. **(C)** Fluorescent images of hGFs treated with blank, MPDA-HA/BSP MNs and TA@MPDA-HA/BSP MNs. The red staining is actin cytoskeleton and the blue staining is the cell nucleus (scale bars: 50 μm). **(D)** Schematic diagram of a cell scratch experiment. **(E)** Typical images show hGFs wound closure treated with blank, MPDA-HA/BSP MNs and TA@MPDA-HA/BSP MNs at 12 and 24 h (scale bars: 200 μm). **(F)** Degree of wound closure in each group of the scratch test. **(G)** To test the anti-inflammatory ability of the MN patches, levels of TNF-α were analyzed by ELISA.

S2C) at 24 h ($p < 0.05$) and there were no statistical differences between TA@MPDA-HA/BSP MNs groups ($p > 0.05$) (Figure 4B). Two kinds of MNs had cell viability above 101.55% ± 1.77%. These results indicated that HA and BSP may have the effect of promoting cell proliferation. The above experiments proved that the drug-loaded MNs had good biocompatibility, providing a reliable guarantee for use as oral mucosal patches.

3.3.3 Cell Morphology Staining

The cytoskeleton was stained with TRITC-Phalloidin and DAPI to observe the effect of microtargeting on cell morphology. After staining, the cell membrane of hGFs showed red spindle shapes, and the cell nucleus was filled, and the nucleus showed blue round shapes, which corresponded to the cell membrane one by one (Figure 4C). The results showed that the morphology of hGFs in the experimental group did not change significantly compared with the control group.

3.4 Cell scratching assay

The process of wound-scratch testing was shown in Figure 4D. Upon quantification, the MPDA-HA/BSP, TA@

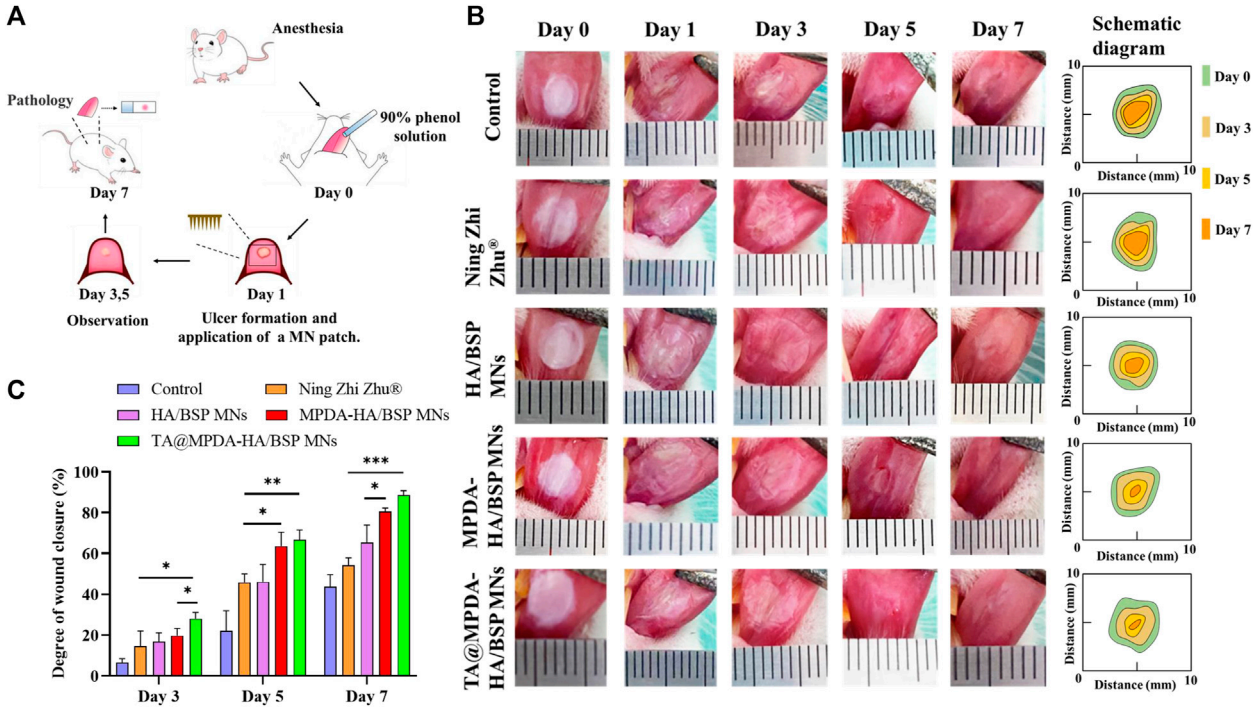

FIGURE 5
(A) A schematic modeling and treatment process of rat oral ulcer. **(B)** Photos and diagrammatic drawing of oral ulcer changes in each group on the day of ulcer formation, before treatment, and on day three, five, and seven after treatment. **(C)** Degree of wound closure at day three, five, and seven of each group.

MPDA-HA/BSP MNs and the control group displayed scratch closures of 65.83% ± 1.24%, 69.40% ± 0.93%, and 54.01% ± 3.05% after 24 h, respectively ($p < 0.05$, Figure 4F). These data showed that the migration rate of hGFs treated with MPDA-HA/BSP MNs solution was significantly faster than that of the control group, and the migration rate of hGFs treated with TA@MPDA-HA/BSP solution was the fastest (Figure 4E). These results indicated that the MPDA-HA/BSP, TA@MPDA-HA/BSP MNs had the ability to promote wound repair and thus promote the healing of oral ulcer.

3.5 Anti-inflammatory test

To our knowledge, MPDA and Chinese herbs extract BSP have been widely explored in the treatment of inflammatory diseases (Zhang et al., 2010; Chen et al., 2021). To verify the synergistic anti-inflammatory effect of TA@MPDA-HA/BSP MNs, we investigated tumor necrosis factor (TNF-α) levels in the supernatant of hGFs after induction by lipopolysaccharides (LPS). As shown in Figure 4G, the TNF-α level in MPDA-HA/BSP MNs group was significantly lower than that in HA/BSP MNs group ($p < 0.05$), and remarkably, the TA@MPDA-HA/BSP MNs group exhibited the lowest TNF-α concentration. From these data we conclude that the superimposition of multiple components of the microneedles enhance their anti-inflammatory effect, which may achieve the goal of low-dose hormones for suppression of inflammation.

3.6 Insertion safety of MN patches

The safety of TA@MPDA-HA/BSP MNs was evaluated by inserting MNs into the tongue mucosa of rats and observing the inflammatory response of the mucosa. Normal SD rats tongue mucosa were selected for the experiment. As was shown in Supplementary Figures S3A–E, immediately after insertion, the pores left by the needle array can be seen in the lingual mucosa. After 5 min, the pore scope was significantly reduced. After 10 min, the pores basically disappeared. 30 min after insertion, the lingual mucosa returned to the normal state before insertion. No obvious hyperemia was observed in the mucosa during the whole process. H&E staining was performed on tongue tissue 24 h after MN application. The results showed that the pathological images of the TA@MPDA-HA/BSP MNs group and the control group were basically the same, and no obvious inflammatory cell infiltration was observed (Supplementary Figures S3E, F). The above phenomenon proved that MNs have good insertion safety, which provides an important basis for clinical application.

3.7 *In vivo* animal experiments

In this study, the ability of MNs to promote oral ulcer wound healing was evaluated by establishing and treating oral ulcer models in SD rats (Figure 5A). The photographic images of the oral ulcer modeling and after treatment with Ning Zhi Zhu® and microneedle samples were shown in Figure 5B. On the first day, oval or round ulcers

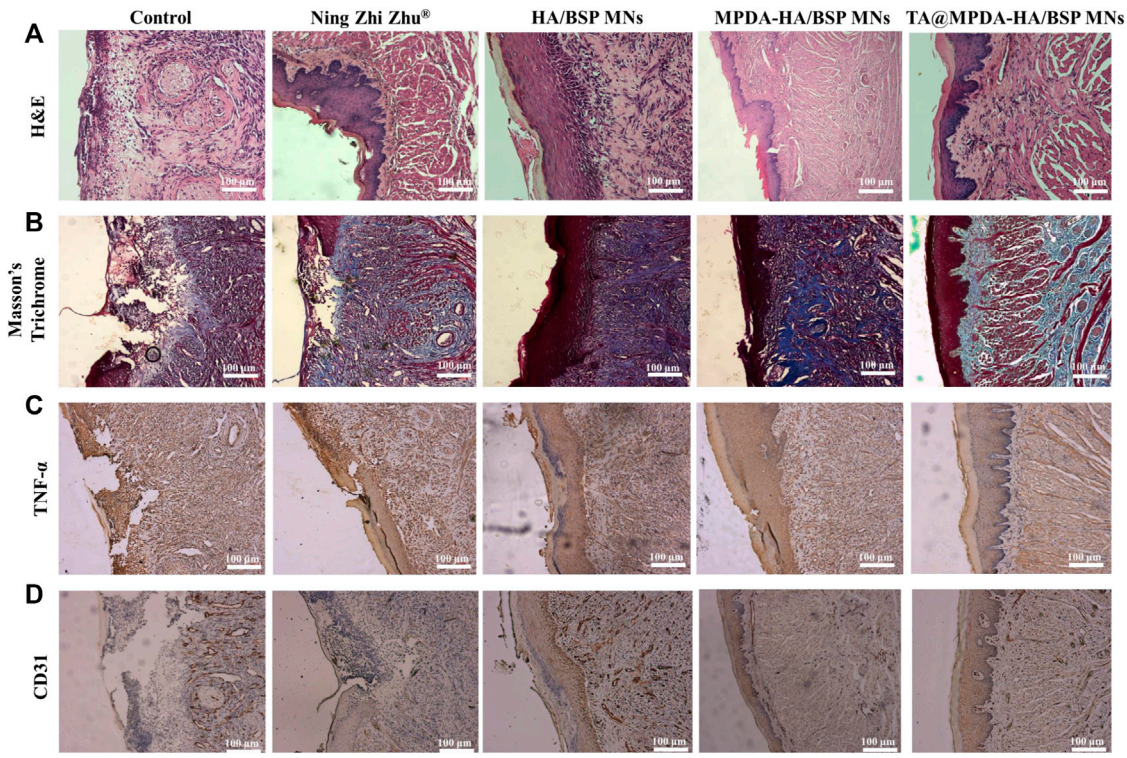

FIGURE 6
(A) H&E staining and **(B)** Masson's Trichrome staining of rat tongue ulcers in each group after treatment. **(C)** TNF-α and **(D)** CD31 IHC after treatment.

with a diameter of approximately 5 mm were formed. The established ulcer models appeared to be hollow in the center, covered with a yellow and white pseudomembrane, and congested and swollen at the edges. Through quantization, as shown in Figure 5C, the TA@MPDA-HA/BSP MNs and MPDA-HA/BSP MNs treated wounds closed faster from the third day compared to Ning Zhi Zhu® and nontreated groups ($p < 0.05$). Moreover, the MPDA-HA/BSP MNs group showed better therapeutic effects than the HA/BSP MNs ($p < 0.05$), suggesting that MPDA NPs are effective in treating oral ulcers (Fu et al., 2021; Zhang et al., 2021). On day seven, the degree of wound closure was 43.59% in the control group, 54.31% in the Ning Zhi Zhu® group, 65.27% in the HA/BSP MNs group, 80.60% in the MPDA-HA/BSP MNs group, and 88.57% in the TA@MPDA-HA/BSP MNs group. Remarkably, the dose of TA in the TA@MPDA-HA/BSP MNs group was only 10% of that in the clinic ointment Ning Zhi Zhu®, however, its therapeutic effect was equal to or better than the latter, which realized the original intention of reducing the dosage of glucocorticoid hormone. In addition, due to the anesthetic effect, the rats could not chew for a certain period of time, increasing the residence time of Ning Zhi Zhu® on the mucosa. However, when the rats were in normal activity, the mastication was more frequent, which made it more difficult for the ointment to stay on the mucous and take effect. The microneedle drug delivery system, on the other hand, could break the mucosal barrier and deliver the drug quickly and give full effect due to its transmucosal delivery ability and adsorption capacity.

To further detect the degree of ulcer healing, H&E staining (Figure 6A) and Masson's Trichrome staining (Figure 6B) had been used to evaluate the quality of oral regenerated tissue in each group. In the control group, a large number of inflammatory cells were infiltrated in the submucosa, including neutrophils and plasma cells, and the upper cortex was shed. The damaged area was in direct contact with the fibrin layer, and the healing was slow. The epithelial tissues of Ning Zhi Zhu® group and HA/BSP MNs group were discontinuous, with inflammatory cells in the submucosa, thickened basement membrane and irregular connective tissue hyperplasia. In the MPDA-HA/BSP MNs group, the stratum corneum was still missing, epithelial cells were edematous, and new connective tissue formed under the basement membrane. The epithelium of TA@MPDA-HA/BSP MNs group was basically intact without obvious inflammatory cells. By observing the blue trend of Masson's Trichrome staining, it can be seen that MPDA-HA/BSP MNs group and TA@MPDA-HA/BSP MNs group both showed good collagen regeneration. Collagen production plays an important role in oral mucosal tissue repair (Wu et al., 2016). TNF-α is a pro-inflammatory cytokine produced primarily by macrophages and monocytes, and is involved in normal inflammatory and immune responses. The results showed that the TA@MPDA-HA/BSP MNs group had significantly lower levels of inflammation than the other groups (Figure 6C). CD31 may be involved in leukocyte migration, angiogenesis and integrin activation. As can be seen from Figure 6D, the number of new blood vessels in the TA@MPDA-HA/BSP MNs group was the highest. Experimental results suggest that TA@MPDA-HA/BSP MNs may accelerate oral ulcer healing by promoting collagen and neovascularization and reducing inflammation levels in tissues.

4 Conclusion

A HA/BSP-based dissolving microneedle was developed to mediate mesoporous polydopamine nanoparticles (MPDA) loaded with Triamcinolone acetonide (TA) for the treatment of oral mucositis (OM). TA can be successfully loaded into MPDA, thus improving bioavailability of TA. TA@MPDA-HA/BSP MNs had well-arranged microneedles array, high penetration efficiency, rapid dissolution in 3 min, excellent biocompatibility and anti-inflammatory properties. When TA@MPDA-HA/BSP MNs were used to treat oral ulcers, the area of oral ulcers and inflammatory factor level such as TNF-α and CD31 were significantly reduced. TA@MPDA-HA/BSP MNs can not only improve the bioavailability of TA, but also play the role of MPDA, BSP and HA in the combination treatment of OM, becoming a new clinical comfortable and effective alternative for the treatment of OM.

Data availability statement

The original contributions presented in the study are included in the article/Supplementary Material, further inquiries can be directed to the corresponding authors.

Ethics statement

The animal study was reviewed and approved by the ethics committee of Qingdao Stomatological Hospital affiliated with Qingdao University.

Author contributions

YH: supervision, conceptualization, resources, funding acquisition, methodology, writing-review and editing; XQ: methodology, investigation, software, writing-original draft; XG, TZ, and ZZ: methodology; WW: funding acquisition, supervision. All authors have read and agreed to the published version of the manuscript.

Conflict of interest

The authors declare that the research was conducted in the absence of any commercial or financial relationships that could be construed as a potential conflict of interest.

Publisher's note

All claims expressed in this article are solely those of the authors and do not necessarily represent those of their affiliated organizations, or those of the publisher, the editors and the reviewers. Any product that may be evaluated in this article, or claim that may be made by its manufacturer, is not guaranteed or endorsed by the publisher.

Supplementary material

The Supplementary Material for this article can be found online at: https://www.frontiersin.org/articles/10.3389/fbioe.2023.1203709/full#supplementary-material

References

Agarwal, G., Agiwal, S., and Srivastava, A. (2020). Hyaluronic acid containing scaffolds ameliorate stem cell function for tissue repair and regeneration. *Int. J. Biol. Macromol.* 165, 388–401. doi:10.1016/j.ijbiomac.2020.09.107

An, H., Gu, Z., Zhou, L., Liu, S., Li, C., Zhang, M., et al. (2022). Janus mucosal dressing with a tough and adhesive hydrogel based on synergistic effects of gelatin, polydopamine, and nano-clay. *Acta Biomater.* 149, 126–138. doi:10.1016/j.actbio.2022.07.016

Bao, X., Zhao, J., Sun, J., Hu, M., and Yang, X. (2018). Polydopamine nanoparticles as efficient scavengers for reactive oxygen species in periodontal disease. *ACS Nano* 12, 8882–8892. doi:10.1021/acsnano.8b04022

Bian, Q., Huang, L., Xu, Y., Wang, R., Gu, Y., Yuan, A., et al. (2021). A facile low-dose photosensitizer-incorporated dissolving microneedles-based composite system for eliciting antitumor immunity and the abscopal effect. *ACS Nano* 15, 19468–19479. doi:10.1021/acsnano.1c06225

Bilodeau, E. A., and Lalla, R. V. (2019). Recurrent oral ulceration: Etiology, classification, management, and diagnostic algorithm. *Periodontol* 80, 49–60. doi:10.1111/prd.12262

Chen, H., Zeng, J., Wang, B., Cheng, Z., Xu, J., Gao, W., et al. (2021). Structural characterization and antioxidant activities of Bletilla striata polysaccharide extracted by different methods. *Carbohydr. Polym.* 266, 118149. doi:10.1016/j.carbpol.2021.118149

Cheng, Z., Lin, H., Wang, Z., Yang, X., Zhang, M., Liu, X., et al. (2020). Preparation and characterization of dissolving hyaluronic acid composite microneedles loaded micelles for delivery of curcumin. *Drug Deliv. Transl. Res.* 10, 1520–1530. doi:10.1007/s13346-020-00735-2

Elad, S., Yarom, N., Zadik, Y., Kuten-Shorrer, M., and Sonis, S. T. (2022). The broadening scope of oral mucositis and oral ulcerative mucosal toxicities of anticancer therapies. *CA Cancer J. Clin.* 72, 57–77. doi:10.3322/caac.21704

Fu, Y., Zhang, J., Wang, Y., Li, J., Bao, J., Xu, X., et al. (2021). Reduced polydopamine nanoparticles incorporated oxidized dextran/chitosan hybrid hydrogels with enhanced antioxidative and antibacterial properties for accelerated wound healing. *Carbohydr. Polym.* 257, 117598. doi:10.1016/j.carbpol.2020.117598

Hao, Y., Chen, Y., He, X., Yang, F., Han, R., Yang, C., et al. (2020). Near-infrared responsive 5-fluorouracil and indocyanine green loaded MPEG-PCL nanoparticle integrated with dissolvable microneedle for skin cancer therapy. *Bioact. Mater* 5, 542–552. doi:10.1016/j.bioactmat.2020.04.002

Hemshekhar, M., Thushara, R. M., Chandranayaka, S., Sherman, L. S., Kemparaju, K., and Girish, K. S. (2016). Emerging roles of hyaluronic acid bioscaffolds in tissue engineering and regenerative medicine. *Int. J. Biol. Macromol.* 86, 917–928. doi:10.1016/j.ijbiomac.2016.02.032

Hu, L., Liao, Z., Hu, Q., Maffucci, K. G., and Qu, Y. (2018). Novel Bletilla striata polysaccharide microneedles: Fabrication, characterization, and *in vitro* transcutaneous drug delivery. *Int. J. Biol. Macromol.* 117, 928–936. doi:10.1016/j.ijbiomac.2018.05.097

Jing, Q., Ruan, H., Li, J., Wang, Z., Pei, L., Hu, H., et al. (2021). Keratinocyte membrane-mediated nanodelivery system with dissolving microneedles for targeted therapy of skin diseases. *Biomaterials* 278, 121142. doi:10.1016/j.biomaterials.2021.121142

Li, H., Song, P., Wu, T., Zhao, H., Liu, Q., and Zhu, X. (2022). *In situ* decorating of montmorillonite with ZnMn2O4 nanoparticles with enhanced oxidase-like activity and its application in constructing GSH colorimetric platform. *Appl. Clay Sci.* 229, 106656. doi:10.1016/j.clay.2022.106656

Moore, L. E., Vucen, S., and Moore, A. C. (2022). Trends in drug- and vaccine-based dissolvable microneedle materials and methods of fabrication. *Eur. J. Pharm. Biopharm.* 173, 54–72. doi:10.1016/j.ejpb.2022.02.013

Padula, C., Telo, I., Di Ianni, A., Pescina, S., Nicoli, S., and Santi, P. (2018). Microemulsion containing triamcinolone acetonide for buccal administration. *Eur. J. Pharm. Sci.* 115, 233–239. doi:10.1016/j.ejps.2018.01.031

Peng, T., Huang, Y., Feng, X., Zhu, C., Yin, S., Wang, X., et al. (2021). TPGS/hyaluronic acid dual-functionalized PLGA nanoparticles delivered through dissolving

microneedles for markedly improved chemo-photothermal combined therapy of superficial tumor. *Acta Pharm. Sin. B* 11, 3297–3309. doi:10.1016/j.apsb.2020.11.013

Qin, W., Quan, G., Sun, Y., Chen, M., Yang, P., Feng, D., et al. (2020). Dissolving microneedles with spatiotemporally controlled pulsatile release nanosystem for synergistic chemo-photothermal therapy of melanoma. *Theranostics* 10, 8179–8196. doi:10.7150/thno.44194

Saha, I., and Rai, V. K. (2021). Hyaluronic acid based microneedle array: Recent applications in drug delivery and cosmetology. *Carbohydr. Polym.* 267, 118168. doi:10.1016/j.carbpol.2021.118168

Sartawi, Z., Blackshields, C., and Faisal, W. (2022). Dissolving microneedles: Applications and growing therapeutic potential. *J. Control Release* 348, 186–205. doi:10.1016/j.jconrel.2022.05.045

Seon-Woo, H.-S., Kim, H. J., Roh, J. Y., and Park, J.-H. (2019). Dissolving microneedle systems for the oral mucosal delivery of triamcinolone acetonide to treat aphthous stomatitis. *Macromol. Res.* 27, 282–289. doi:10.1007/s13233-019-7031-6

Tang, J., Liu, J., Li, C., Li, Y., Tade, M. O., Dai, S., et al. (2015). Synthesis of nitrogen-doped mesoporous carbon spheres with extra-large pores through assembly of diblock copolymer micelles. *Angew. Chem. Int. Ed. Engl.* 54, 588–593. doi:10.1002/anie.201407629

Vora, L. K., Courtenay, A. J., Tekko, I. A., Larraneta, E., and Donnelly, R. F. (2020). Pullulan-based dissolving microneedle arrays for enhanced transdermal delivery of small and large biomolecules. *Int. J. Biol. Macromol.* 146, 290–298. doi:10.1016/j.ijbiomac.2019.12.184

Wang, Z., Duan, Y., and Duan, Y. (2018). Application of polydopamine in tumor targeted drug delivery system and its drug release behavior. *J. Control Release* 290, 56–74. doi:10.1016/j.jconrel.2018.10.009

Wu, J., Zhu, J., He, C., Xiao, Z., Ye, J., Li, Y., et al. (2016). Comparative study of heparin-poloxamer hydrogel modified bFGF and aFGF for *in vivo* wound healing efficiency. *ACS Appl. Mater. Interfaces* 8, 18710–18721. doi:10.1021/acsami.6b06047

Wu, T., Hou, X., Li, J., Ruan, H., Pei, L., Guo, T., et al. (2021). Microneedle-Mediated biomimetic cyclodextrin metal organic frameworks for active targeting and treatment of hypertrophic scars. *ACS Nano* 15, 20087–20104. doi:10.1021/acsnano.1c07829

Xing, F., Zhou, C., Hui, D., Du, C., Wu, L., Wang, L., et al. (2020). Hyaluronic acid as a bioactive component for bone tissue regeneration: Fabrication, modification, properties, and biological functions. *Nanotechnol. Rev.* 9, 1059–1079. doi:10.1515/ntrev-2020-0084

Yuan, Z., Lin, C., He, Y., Tao, B., Chen, M., Zhang, J., et al. (2020). Near-infrared light-triggered nitric-oxide-enhanced photodynamic therapy and low-temperature photothermal therapy for biofilm elimination. *ACS Nano* 14, 3546–3562. doi:10.1021/acsnano.9b09871

Zeng, W. N., Wang, D., Yu, Q. P., Yu, Z. P., Wang, H. Y., Wu, C. Y., et al. (2022). Near-infrared light-controllable multifunction mesoporous polydopamine nanocomposites for promoting infected wound healing. *ACS Appl. Mater Interfaces* 14, 2534–2550. doi:10.1021/acsami.1c19209

Zhang, H., Ye, L., and Wang, K. (2010). Structural characterization and anti-inflammatory activity of two water-soluble polysaccharides from Bellamya purificata. *Carbohydr. Polym.* 81, 953–960. doi:10.1016/j.carbpol.2010.04.011

Zhang, M., Huang, Y., Pan, W., Tong, X., Zeng, Q., Su, T., et al. (2021). Polydopamine-incorporated dextran hydrogel drug carrier with tailorable structure for wound healing. *Carbohydr. Polym.* 253, 117213. doi:10.1016/j.carbpol.2020.117213

Zhang, N., Xue, L., Younas, A., Liu, F., Sun, J., Dong, Z., et al. (2022). Co-delivery of triamcinolone acetonide and verapamil for synergistic treatment of hypertrophic scars via carboxymethyl chitosan and Bletilla striata polysaccharide-based microneedles. *Carbohydr. Polym.* 284, 119219. doi:10.1016/j.carbpol.2022.119219

Zhao, J. H., Zhang, Q. B., Liu, B., Piao, X. H., Yan, Y. L., Hu, X. G., et al. (2017). Enhanced immunization via dissolving microneedle array-based delivery system incorporating subunit vaccine and saponin adjuvant. *Int. J. Nanomedicine* 12, 4763–4772. doi:10.2147/IJN.S132456

Zheng, W., Hao, Y., Wang, D., Huang, H., Guo, F., Sun, Z., et al. (2021). Preparation of triamcinolone acetonide-loaded chitosan/fucoidan hydrogel and its potential application as an oral mucosa patch. *Carbohydr. Polym.* 272, 118493. doi:10.1016/j.carbpol.2021.118493

Zhu, M., Shi, Y., Shan, Y., Guo, J., Song, X., Wu, Y., et al. (2021). Recent developments in mesoporous polydopamine-derived nanoplatforms for cancer theranostics. *J. Nanobiotechnology* 19, 387. doi:10.1186/s12951-021-01131-9

Zhu, T., Yu, X., Yi, X., Guo, X., Li, L., Hao, Y., et al. (2022a). Lidocaine-loaded hyaluronic acid adhesive microneedle patch for oral mucosal topical anesthesia. *Pharmaceutics* 14, 686. doi:10.3390/pharmaceutics14040686

Zhu, X., Li, H., Wu, T., Zhao, H., Wu, K., Xu, W., et al. (2022). *In situ* decorating the surface and interlayer of montmorillonite with Co0.5Ni0.5Fe2O4 nanoparticles: A sustainable, biocompatible colorimetric platform for H2O2 and acetylcholine. *Nano Res.* 15, 9319–9326. doi:10.1007/s12274-022-4594-x

frontiers | Frontiers in Bioengineering and Biotechnology

TYPE Original Research
PUBLISHED 06 June 2023
DOI 10.3389/fbioe.2023.1194704

OPEN ACCESS

EDITED BY
Tengbo Yu,
Qingdao Municipal Hospital, China

REVIEWED BY
Xiaohong Huang,
The Affiliated Hospital of Qingdao University, China
Tsan-Yu Chiu,
Beijing Genomics Institute (BGI), China

*CORRESPONDENCE
Tiemei Liu,
ltm@jlu.edu.cn

†These authors have contributed equally to this work and share first authorship

RECEIVED 27 March 2023
ACCEPTED 17 May 2023
PUBLISHED 06 June 2023

CITATION
Li X, Yin M, Wang H, Duan S, Wang H, Li Y and Liu T (2023), Prenatal diagnosis of fetomaternal hemorrhage by a novel hydrogel fluoroimmunoassay that accurately quantifies fetal haemoglobin. *Front. Bioeng. Biotechnol.* 11:1194704. doi: 10.3389/fbioe.2023.1194704

Prenatal diagnosis of fetomaternal hemorrhage by a novel hydrogel fluoroimmunoassay that accurately quantifies fetal haemoglobin

Xinyang Li[1†], Moli Yin[2†], Hongmei Wang[3], Shengbao Duan[3], Huiyan Wang[2], Yong Li[3] and Tiemei Liu[1*]

[1]Blood Transfusion Department, China-Japan Union Hospital of Jilin University, Changchun, Jilin, China, [2]Jilin Collaborative Innovation Center for Antibody Engineering, Jilin Medical University, Jilin City, Jilin, China, [3]CAS Key Lab of Bio-Medical Diagnostics, Suzhou Institute of Biomedical Engineering and Technology, Chinese Academy of Sciences, Suzhou, Jiangsu, China

Objective: Fetomaternal hemorrhage (FMH) is an alloimmunization resulting caused by the incompatibility between fetal and maternal blood. For the prevention of newborn haemolytic disease (HDN), it is crucial to quantify the amount of fetomaternal hemorrhage. However, the classical Kleihauer–Betke test (K-B test) for detecting fetomaternal hemorrhage is limited by experimental tools and conditions and is not suitable for routine clinical use. Consequently, the method of prenatal diagnosis of fetomaternal hemorrhage applicable to the clinic is a topic worthy of further study. Therefore, it is worthwhile to further investigation on the clinically applicable prenatal diagnosis method for fetomaternal hemorrhage.

Methods: This experiment demonstrates hydrogel's ability to separate sensitized red blood cells from soluble antibodies. Using flow cytometry the fluorescence values of sensitized red blood cells and fluorophore-labeled antibodies were measured, and the testing steps for the detection products of a novel technology were determined. The properties of a hydrogel fluoroimmunoassay were evaluated by distinguishing between the amounts of fetal and adult haemoglobin. The precision of this technology is evaluated using the Kleihauer–Betke test as a comparison.

Results: This experiment compared the detection of haemoglobin fluorescence in adults (n = 2) and fetuses (n = 6). At the same time, the fluorescence intensity of different fetal haemoglobin (HbF) in adult haemoglobin (HbA) was calculated. The fluorescence value is 1.6% when the fetal hemoglobin concentration is 0.1%.

Conclusion: The novel hydrogel fluoroimmunoassay can accurately determine the fluorescence intensity by flow cytometry to differentiate fetal haemoglobin from adult haemoglobin, quantitatively prenatally diagnose fetal haemoglobin, address the incompatibility between fetal and maternal blood types, and prevent alloimmunization.

KEYWORDS

fluoroimmunoassay, adult haemoglobin, hydrogel medium, fetal haemoglobin, fetomaternal hemorrhage

Introduction

Evaluation of fetal red blood cells (RBCs) in the peripheral blood of pregnant women is used to detect fetomaternal hemorrhage (FMH) (Minuk et al., 2020). In order to address the incompatibility of fetal and maternal blood, it is essential to accurately quantify FMH. The number of fetal RBCs transferred to the mother determines the amount of immunoglobulin administered to prevent future Rhesus D (Rh D) alloimmunization (Glazebrook et al., 2020; Ayenew, 2021).

Fetomaternal hemorrhage is the entry of fetal red blood cells (RBCs) into the maternal circulation due to placental rupture or injury during puncture, trauma, abortion, or delivery. When the blood type of the fetus is incompatible with that of the mother, antibodies against fetal RBCs are produced in the mother. These antibodies pass through the placenta and cause the destruction of fetal RBCs (Troia et al., 2019; Hookins and Vatsayan, 2020; Monteiro et al., 2021). 16 weeks is the earliest placenta rupture, so pregnant women at 16 weeks are at risk for FMH (Akorsu et al., 2019; Athiel et al., 2020). David M conducts the Kleihauer–Betke test (K–B test) and concludes that 22.5% of Rh D-negative pregnant women carry Rh D-positive fetuses, resulting in FMH (David et al., 2004). When D-negative pregnant women have D-positive fetal RBCs, the fetal RBCs stimulate the mother to produce anti-D IgG antibody, which can enter the fetus through the placenta and produce alloimmunity (Tneh et al., 2021). Additionally, anti-Kell, anti-E, and anti-C IgG antibodies may also induce allogeneic immunity via the placenta (Erhabor et al., 2020). Alloimmunization following FMH can cause anemia, edema, jaundice, and even death in fetuses and newborns (Christino Luiz et al., 2019; Fan et al., 2021). Statistics indicate that fetal mortality due to FMH can reach 10% (Bowman, 2010). Failure to detect FMH early and treat with anti-D immunoglobulin are the leading causes of perinatal fetal morbidity and mortality (Carr et al., 2022). Therefore, prenatal diagnosis and quantification of FMH can ensure that high-risk pregnant women receive appropriate treatment and the care of experienced obstetricians. Accurate perinatal quantification of FMH and corresponding treatment are the key to addressing the incompatibility of fetal and maternal blood types and are essential for the management of obstetrics and blood transfusion departments (Pahuja et al., 2011).

The purpose of the Kleihauer–Betke test, also known as the acid elution test, is to differentiate fetal RBCs from adult RBCs (Kim and Makar, 2012) based on the difference in acid-resistance between fetal haemoglobin (HbF) and adult haemoglobin (HbA). After acid treatment, fetal RBCs appear pink and adult RBCs appear "ghost-like." The difficulty of manually counting is the primary reason why the K-B test has not yet been implemented in the clinic (Lemaitre et al., 2020; Ficarola et al., 2022). Workers need to quickly distinguish fetal RBCs from adult RBCs according to their colour, size and texture. Usually, the staff need to count 2,000 RBCs within 20 min, and the slide contains neutrophils, overlapping cells and impurities, which makes it more difficult and subjective for the staff to count. Therefore, high labour intensity, strong subjectivity and poor accuracy have become the shortcomings of K-B test (Zhang et al., 2021). Melanie C compared the K-B test to the flow cytometry test and discovered that the K-B test yielded positive results, whereas the flow cytometry test yielded negative results. This circumstance constitutes 94% (Audette et al., 2022).

Hydrogel fluoroimmunoassay combines accurate flow cytometry (FCM) with high-sensitivity microcolumn gel technology, and further develops hydrogel immunoagglutination test into hydrogel fluoroimmunoassay technology, which improves the sensitivity and accuracy of detection technology and can be mass-produced. This technology uses a medium ($1.14\ g\ m^{-1}$) with a higher density than the majority of cells, i.e., the hydrogel medium's separation properties (Wang et al., 2015). The hydrogel medium is in a flowing state at room temperature. Under the influence of centrifugal force, high-density RBCs and low-density small molecule antibodies can be directly separated, and then complicated steps such as washing can be omitted, making the procedure simple, quick, and convenient (Wu et al., 2022). The hydrogel fluoroimmunoassay uses the combination of sensitized indicator RBCs and fluorescently labelled anti-HbF antibody, and determines the fluorescence value by flow cytometry. This method is accurate and reliable in determining the quantity of fetal RBCs. Due to the fact that this method can distinguish HbF from adult haemoglobin, it can be used to detect fetal hemorrhage prenatally. This study's objective is to evaluate the ability of hydrogel fluoroimmunoassay to diagnose FMH at a critical level of 0.1%, which is within the standard range of clinical treatment of FMH with anti-D immunoglobulin (Simes et al., 2022) and can prevent homologous immunity caused by blood group incompatibility between fetus and mother.

Materials and methods

Reagents, instruments and blood samples

The anti-mouse IgG (fab specific)-FITC antibody produced in goal was acquired from Sigma (F5387). All chemical reagents were acquired from Sinopharm Chemical Reagents Co., Ltd., (China). Alexa Fluor TM 647 Carboxylic Acid, Succinimidyl Ester was purchased from Thermo Fisher scientific (United States). Flow cytometer (z2010-254, BD LSRFortessa). In our laboratory, 0.01M PBS (pH 7.2) and hydrogel were prepared. Two lymphocyte hybridoma cells produce the monoclonal antibody against HbF (15-G4, 9-F10). The sample of whole blood was supplied by China-Japan Union Hospital of Jilin University. The blood sample stored at 4°C has been approved by the China-Japan Union Hospital's Ethics Committee (Approval number: 20220425009).

Blood sample preparation and extraction of haemoglobin

Blood from healthy adults and umbilical cord blood from newborn fetal umbilical cords were collected and washed three times with saline. Then, added twice volume of distilled water, which is erythrocyte lysate, centrifuged at 10,000 r.p.m for 20 min, collected the supernatant, which was haemoglobin, and determined its concentration. The same concentration of fetal hemoglobin was then mixed with adult hemoglobin in volumes of 1: 1,000, 3: 1,000, and 5: 1,000 to produce fetal hemoglobin with proportions of 0.1%, 0.3%, and 0.5% in the mixed hemoglobin.

Separation of indicator RBCs from small molecular dyes by hydrogel

Wang's article described the use of hydrogel to separate small molecular dyes from indicator RBCs. The characteristics of methylene blue and the reaction time of the reactants differed between this experiment and Wang's. In this experiment, methylene blue (Mw373.90,0.8%), indicator RBCs, and additional reactants were placed on top of hydrogel, incubated, and centrifuged at 285 g for 3 min.

The preparation of indicator RBCs

Randomly collected "O" type Rh-positive RBCs, thoroughly washed them, treated them with 0.5% GA-PBS solution at room temperature for 30 min, centrifuged and washed them, then added 0.5% PA-PBS solution to water bath at 37°C for 1 h, centrifuged and washed them, then added 1% PFA-PBS solution to water bath at 37°C for 5 h, and shook them every 30 min. After washing and centrifuging, a 10% suspension of RBCs was made and stored at 4°C for future use.

The method of coating indicator RBCs with antibodies

Chromium trichloride solution ($CrCl3.6H_2O$) in saline had a concentration of 1.51%. Adjust the pH to 5.0 using 1 mol/L sodium hydroxide prior to use. By using the metal cation immunoglobulin tannic acid method, aldehyde-modified RBCs were made sensitive. In other words, chromium trichloride solution was added to anti-HbF antibody diluted with acetate buffer (0.175 M pH6.4) to achieve a final concentration of 120 μg/mL. After mixing, water-bathing at 37°C for 10 min. To the anti-HbF antibody and 1 mL of hematocrit that had been incubated, 1:2,000 tannic acid solution was added immediately. It is necessary to ensure that the volume ratio of the mixed solution to the tannic acid solution is 3:1, and to incubate the solution in a 37°C water bath for 15 min. After six times of washing, 2% BSA-PBS was added to a 37°C water bath for 2 hours, and a storage suspension was subsequently prepared.

Verification of binding of indicator cell and anti-HbF antibody

As the second antibody, sheep anti-mouse IgG FITC was used to detect mouse anti-HbF antibody. After 30 min in a 37°C water bath, the cells were washed once and centrifuged before being collected. The hematocrit was then diluted in PBS-BSA at 1%. Using FCM, the fluorescence intensity of negative and positive samples was measured.

Method of labeling antibody with fluorescein

Thermo Fisher Scientific Company's Alexa Fluor TM 647 Carboxylic Acid, Succinimidyl Ester reagent was used to label anti-HbF antibody with F647. Among them, the goat anti-mouse IgG antibody concentration was 16.544 mg, and the labeling time of F647 for goat anti-mouse IgG antibody was 4 h at room temperature, followed by an overnight treatment at 4°C.

Hydrogel fluoroimmunoassay for HbF detection

The haemoglobin (Hb), fluorescence-labeled antibody, and sensitized indicator RBCs were added to the hydrogel-filled card and centrifuged at a low speed until the immune complex in the positive result and the indicator RBCs in the negative result sank, while the fluorescence-labeled antibody remained on the hydrogel in the negative result (Figure 1).

Analysis of fetal red blood cells in hydrogel fluoroimmunoassay

The hydrogel fluoroimmunoassay substances were detected by flow cytometry calibrated with standard fluorescent microspheres, and the fluorescence intensity of 50,000 cells was determined. The operation steps strictly adhere to the BD LSRFortessa flow cytometry instructions. The flowchart is examined with Flowjo 10.8.1. The distinction between fetal and adult red blood cells is based on the fact that their peaks are distinct (Figure 4). Even though the negative control has only one peak (0.0% fetal hemoglobin), this experiment distinguishes it using the abscissa value of 10^3 as the boundary. Flow cytometry values with 0.1%, 0.3%, and 0.5% of fetal hemoglobin are subtracted from negative control values greater than 10^3 according to the principle of data processing.

Analysis of the sensitivity of the K-B test and hydrogel fluoroimmunoassay

The preceding analysis method was used to analyse and compare the K-B test. The K-B test was conducted in accordance with the AABB technical manual. The experiment involved the observation of 10,000 cells and the counting of fetal RBCs (Athiel et al., 2020). This experiment was repeated three times, and the results were statistically analyzed using GraphPad Prism 9.4.1 to determine if there was a statistically significant difference between the hydrogel fluoroimmunoassay and K-B test for detecting different fetal red blood cells produced by 0.0%, 0.1%, 0.3%, and 0.5% cord bloods.

Results

Effect of hydrogel medium on the separation of small molecular dyes and indicator RBCs

To demonstrate that the hydrogel is capable of separating indicator RBCs from small molecular proteins not bound to RBCs, we compared the distribution of small molecular substances, RBCs, and immune complexes in the hydrogel medium under different conditions. The substances with the higher density sank to the bottom of the hydrogel medium, whereas the substances with the lower density remained on top of the hydrogel. Figure 2D indicated that 1 h of incubation had no

10.3389/fbioe.2023.1194704

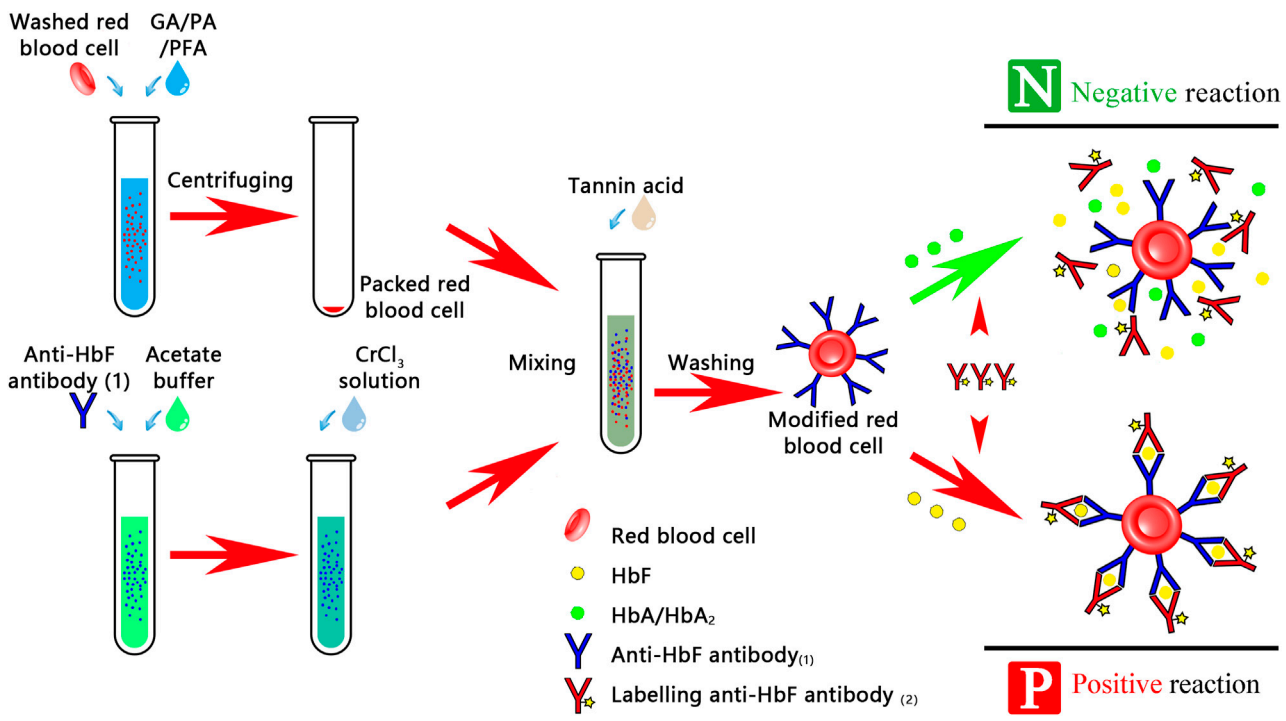

FIGURE 1
Procedure for detecting FMH using a hydrogel fluoroimmunoassay technique. This experiment was divided into two stages: the first stage was prepared by research units, which includes fluorescently labeled antibody, indicator RBCs-coated antibody, and RBC lysis; the second stage was prepared by hospital transfusion departments.

effect on the diffusion of small molecules or RBCs. In Figure 2, $(A)_1$ and 2 $(B)_1$ remained unchanged, indicating that methylene blue was not centrifuged to the card's bottom. Red indicator red blood cells coated with an antibody were added to the top of the 2 $(A)_2$ card. The top of the card in 2 $(B)_2$ changed from red to white after centrifugation, and red (indicator RBC-coated antibodies) appeared at the bottom of the card, indicating that the antibody-coated indicator red blood cells were centrifuged to the bottom of the card. The 2 $(A)_3$ card turns red when the immune complex (indicator RBC-coated antibodies, fluorescently labeled antibodies, and excessive hemoglobin to be detected) is added. The immune complex formed by indicator RBC-coated antibodies—HbF—fluorescently labeled antibodies is centrifuged to the bottom of the card to form red, while hemoglobin at the top of the card is not bound to form an immune complex and is therefore still red. The experimental findings were consistent with Wang's perspective (Wang et al., 2015). The results demonstrated that hydrogel medium could indeed separate soluble antigens, soluble antibodies, granular substances, and other macromolecules. The centrifugal force of RBCs and small molecules sinking in this experiment was 285 g.

Analysis of the binding of indicator cells to antibodies

Figure 3A's objective is to determine if the indicator cells were bound to anti-HbF antibody. In comparison to the red line (negative sample), the light blue line (positive sample) is clearly shifted to the right, and the fluorescence value is clearly elevated. The outcomes demonstrated that the anti-HbF antibody was successfully coupled with indicator RBCs, which could be used in the subsequent experiment.

Immune complex detection with fluorescent-labeled antibodies

Figure 3B demonstrated that F647-labeled antibody and antibody modification indicated that RBCs could indeed recognise HbF specifically, indicating that the experimental steps had been established successfully. Compared to the red line (negative sample), the light blue line (positive sample) was clearly shifted to the right, and the fluorescence value was clearly increased, indicating that this experiment was able to distinguish between fetal and HbA. As depicted in Figure 5C, this experiment was repeated three times with negative and positive controls. The Hb concentration used in this experiment was 0.608 mg/mL (0.60–0.62 mg/mL). In the traditional FCM detection method, the incubated reactants were required to be washed a minimum of three times; if the washing times were insufficient, the false positive rate would increase, and if they were excessive, fetal RBCs would be lost. It had been reported in the literature that washing times should be minimised as much as possible when detecting fetal bleeding with FCM (Wiley Online Library, 1999). Figure 3B depicted the detection

10.3389/fbioe.2023.1194704

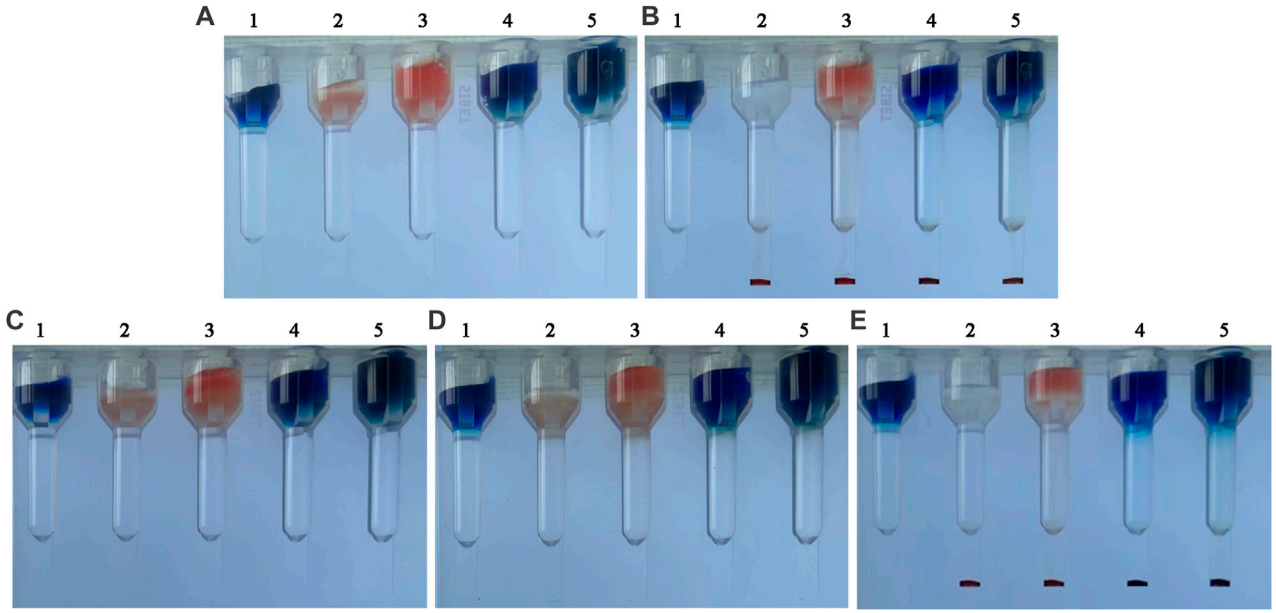

FIGURE 2
Separation results of small molecule dyes and indicator RBCs using a hydrogel medium. **(A)** before centrifugation, from left to right: $(A)_1$ Methylene blue, $(A)_2$ indicator RBC-coated antibodies $(A)_3$ immune complex components, $(A)_4$ indicator RBC-coated antibodies and methylene blue, and $(A)_5$ immune complex components and methylene blue. **(B)** after centrifugation. **(C)** before incubation. **(D)** 1-h incubation. **(E)** centrifugation immediately following incubation.

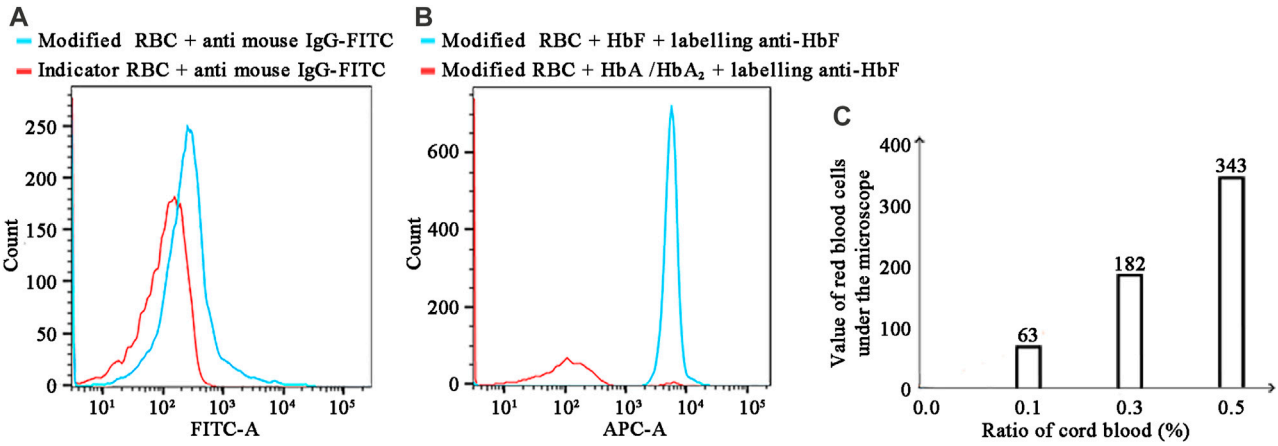

FIGURE 3
(A) Detection results of bound antibodies using FITC-conjugated goat anti-mouse IgG. **(B)** FCM detection of hemoglobin using Alexa Fluor™ 647-conjugated anti-HbF. **(C)** The K–B test results for various cord blood ratios in the mode of FMH.

results obtained after a single washing, while Figure 4depicted the separation results obtained using a hydrogel medium. It was discovered that the fluorescence intensity of washing once was demonstrably higher than that of hydrogel separation, indicating that the separation effect of hydrogel was demonstrably more effective than that of washing once. Consequently, the use of hydrogel medium can reduce washing steps, save time, and ensure the accuracy of experimental results.

Hydrogel fluoroimmunoassay and K-B test sensitivity

Figure 4 depicts the detection of mixed haemoglobin in various proportions (the ratio of HbF to HbA) via hydrogel fluoroimmunoassay. In this experiment, 50,000 cells were counted. Figure 4B depicted the global distribution of HbF concentrations of 0.0%, 0.1%, 0.3%, and 0.5%. The fluorescence intensity increased as the ratio of fetal RBCs increased. As shown in

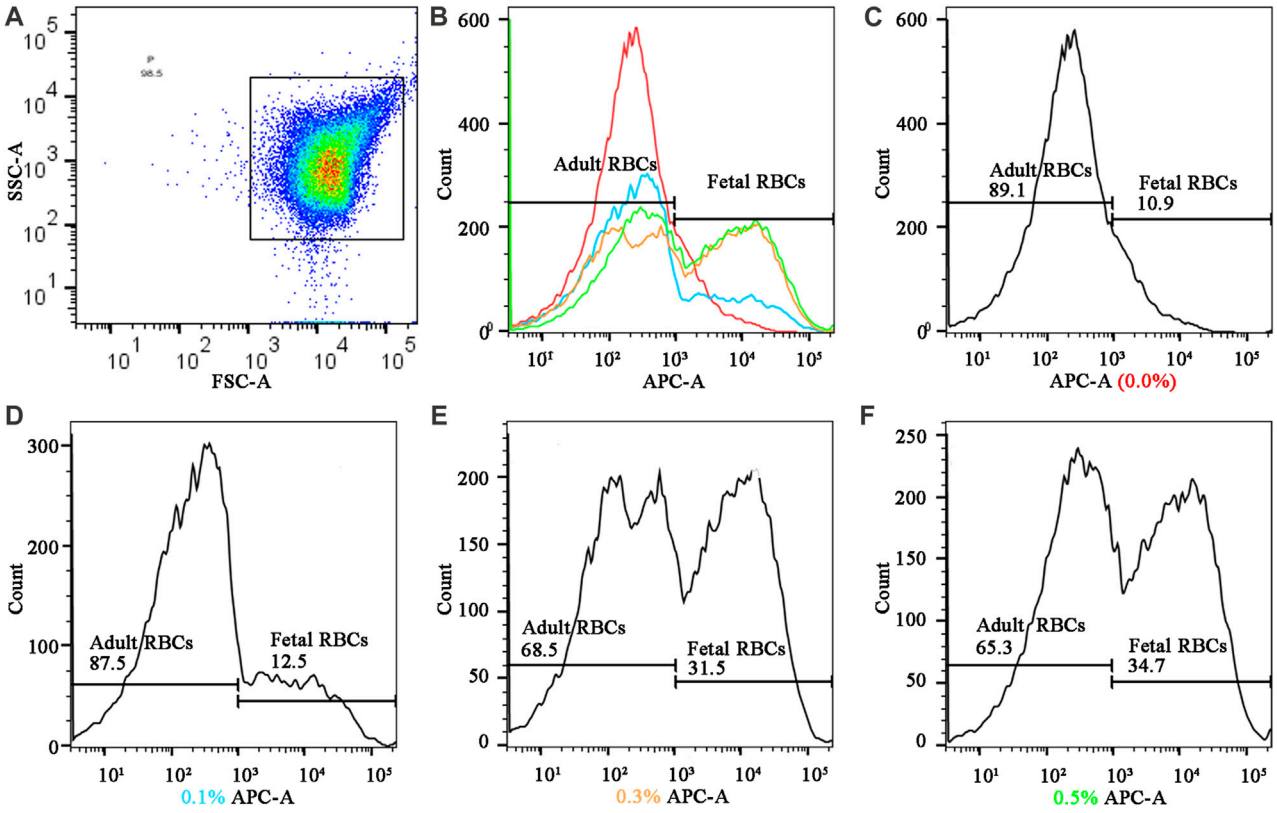

FIGURE 4
Fluorescence quantification results of different cord blood ratios in the mode of FMH by hydrogel fluoroimmunoassay technique **(A)** Gating strategy: The fetal RBCs gate was defined using a positive control fetal control and a negative adult control. **(B)** the summarized figures obtained by superimposing the **(C)** **(D)**, **(E)**, and **(F)** figures, differentiated by line colors; **(C)**, **(D)** **(E)**, and **(F)**, and f represented the fluorescence intensities of various proportions of fetal hemoglobin in mixed hemoglobin, respectively (0.0%, 0.1%, 0.3%, and 0.5%).

the image, the negative result (0.0%) had a peak that represented HbA; there were two peaks with varying proportions of HbF (0.1%, 0.3%, and 0.5%). HbA was represented by the peak on the left, while HbF was represented by the peak on the right. As the fetal RBC ratio increased, the height of the left peak decreased, while the height of the right peak increased. Positive APC-A values for 0.1% HbF were found to be 1.6%, 0.3% HbF was 20.6%, and 0.5% HbF was 23.8%. As the fetal RBC ratio increased, the APC-A positive value increased dramatically. Figures 4C–F represented sub-graphs for HbF concentrations of 0.0%, 0.1%, 0.3%, and 0.5%, respectively. Figure 3C depicted the outcomes of the K-B test on blood samples with varying proportions. Using electron microscopy, 10,000 cells were tallied; Figure 3C displays an upward trend in the proportion of fetal RBCs within adult RBCs. The K-B test and the hydrogel fluoroimmunoassay exhibited a strong correlation. Both were able to reliably and accurately detect the amount of FMH, and their sensitivity can reach 0.1%, which is in line with the clinical treatment standard for 2 mL of FMH. On the basis of these results, a critical concentration of 0.1% is determined. The conclusion reached by Davis is consistent with this one (Davis et al., 2010). Figure 5 was a bar graph of repeated hydrogel fluoroimmunoassay and K-B tests for different hemoglobin concentrations. $p < 0.0001$ indicated that the fluorescence values of 0.0%, 0.1%, 0.3%, and 0.5% of fetal hemoglobin detected by hydrogel fluoroimmunoassay were statistically significant. Figure 5B demonstrates that the K-B test was statistically significant for detecting fetal red blood cells in 0.1%, 0.3%, and 0.5% of mixed blood ($p < 0.0001$).

Discussion

In this study, fetal hemorrhage was diagnosed quantitatively using the hydrogel fluoroimmunoassay. It is believed that this is the first time the combination of hydrogel medium and fluoroimmunoassay have been combined to diagnose FMH. This experiment also assessed the precision of FMH and compared it to the K-B test. By employing this technique, the risk of alloimmunization due to maternal and fetal blood group incompatibility can be reduced. Consequently, hydrogel fluoroimmunoassay technology may be advantageous for the diagnosis and prevention of FMH. Evaluation of FMH using hydrogel fluoroimmunoassay required minimal blood (approximately 10 μL), minimal dependence on manual operation.

Inability to distinguish between HbF and F cells is a common source of false-positive results in K-B tests (Flynn et al., 2022). F cells refer to normal RBCs (Alter, 1984; Fabry et al., 2001; Corcoran et al., 2014) that contain a small amount of HbF (1%–2% in adults) (Cormack et al., 2019). Nonetheless, certain inherited or acquired

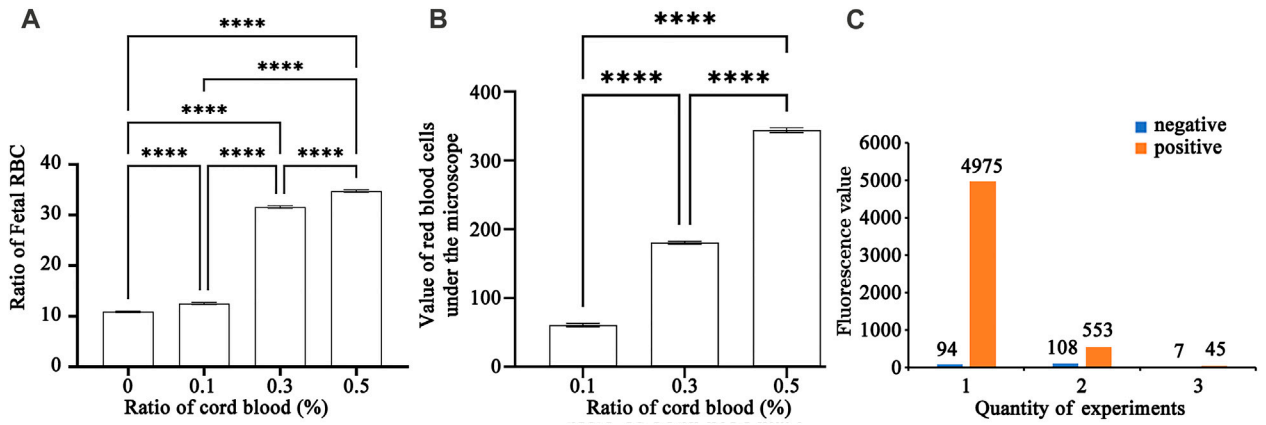

FIGURE 5
(A) A bar chart of repeated experiments using hydrogel fluoroimmunoassay to detect various cord blood ratios. ✳: The magnitude of differences between the various percentages of umbilical cord blood (0.0%, 0.1%, 0.3%, and 0.5%).**(B)** A bar chart of repeated experiments using K-B test to detect various cord blood ratios. ✳: The magnitude of differences between the various percentages of umbilical cord blood (0.1%, 0.3%, and 0.5%).**(C)** Diagram of negative and positive control in a repeated experiment.

haemoglobin disorders, such as sickle cell anaemia and -thalassemia, result in a substantial increase in HbF levels. In addition, F cells will physiologically increase during pregnancy. Hemoglobin in F cells and fetal RBCs has different antigen specificity to support the distinct differentiation of fetal RBCs and adult RBCs, resulting in different fluorescence intensities (Cardoso et al., 2019; Stanic et al., 2020). The anti-HbF antibody used in this experiment is a specific antibody against two distinct epitopes of HbF, and the adult HbF sample, which is the negative control, is used as the negative control. The fluorescence value of fetal hemorrhage minus the fluorescence value of the negative control is the final fluorescence result produced by different proportions of HbF in order to avoid the influence of the increase of HbF in F cells on the detection results (Hsia et al., 2019). In addition, the results were confirmed by repeating experiments with three adult erythrocytes and three fetal erythrocytes (Figure 5C). Therefore, the anti-fetal haemoglobin antibody fluorescence value calculated by the hydrogel fluoroimmunoassay will not prompt patients to take additional anti-D immunoglobulin. In addition, compared to the article by Agaylan, A. and Kumpel, B., this technique has the advantages of not requiring washing, high efficiency, loss-free separation of antigen-antibody complexes, higher sensitivity, simple and rapid operation, reduced fibrinogen interference, and elimination of false positives (Agaylan et al., 2007; Kumpel et al., 2014). FCM is more advantageous in this study for detecting fetal RBCs and F cells in blood samples, consistent with Marcella R's report (Cardoso et al., 2019). In this experiment, the centrifugal force that causes red blood cells sensitized with anti-HbF to sink is 285 g. The article by Wang demonstrates that the minimum centrifugal force required for red blood cells to sink is less than 100 g, whereas the minimum centrifugal force required for proteins to sink is 3,000 g. In this experiment, the centrifugal force is greater than in Wang's article. The primary cause may be that the red blood cells in this experiment have been sensitized by anti-HbF and their molecular weight is greater than that of red blood cells.

Preventing and treating fetal hemorrhage requires not only prenatal and perinatal diagnosis, but also monitoring of pregnant women and newborns after delivery. Hydrogel fluoroimmunoassay can monitor the concentration of HbF, which can determine the drug dosage and disease severity (Garner et al., 2000; Franco et al., 2006). This method is expected to be used to diagnose various obstetric diseases, including placental intervillous thrombosis, due to its simplicity, speed, and efficacy (Sukhanova et al., 2022).

Nonetheless, this experiment has some restrictions. In the experiment, the sensitized RBCs at the bottom of the hydrogel medium are extracted using a needle and then detected using FCM. Due to the complexity of this step and the high cost of FCM, hospitals with small sample sizes are unable to run FCM continuously (Kim and Makar, 2012). The development of a small analyzer that can quantitatively detect the fluorescence intensity at the bottom of a hydrogel medium warrants further study.

Data availability statement

The raw data supporting the conclusions of this article will be made available by the authors, without undue reservation.

Ethics statement

The studies involving human participants were reviewed and approved by the China-Japan Union Hospital's Ethics Committee (Approval number: 20220425009). Written informed consent from the participants' legal guardian/next of kin was not required to participate in this study in accordance with the national legislation and the institutional requirements.

Author contributions

XL and MY: Conceptualization, Methodology, Investigation, Writing—original draft, Writing—review and editing, Visualization.

HoW and SD: Conceptualization, Methodology, Investigation, Writing - original draft, Writing—review and editing, Visualization. HuW: Visualization. YL: Project administration. TL: Conceptualization, Supervision, Project administration, Writing—original draft, Writing—review and editing. All authors contributed to the article and approved the submitted version.

Funding

This work was supported by Department of Science and Technology of Jilin Province under Grant number 20200708105YY; Department of Finance of Jilin Province under Grant number 202201RK; Department of Science and technology of Jilin Province under Grant number 20230508069RC.

Acknowledgments

We thank all the study participants for their time and support. Antibody center of Jilin medical college deserves special thanks for her contribution in antibody. The authors also thank CAS Key Lab of Bio-Medical Diagnostics, Suzhou Institute of Biomedical Engineering and Technology, Chinese Academy of Sciences to support technique.

Conflict of interest

The authors declare that the research was conducted in the absence of any commercial or financial relationships that could be construed as a potential conflict of interest.

Publisher's note

References

Agaylan, A., Meyer, O., Ahrens, N., Dudenhausen, J., Bombard, S., and Salama, A. (2007). A rapid gel agglutination test for the determination of fetomaternal haemorrhage. *Transfus. Med.* 17 (5), 395–398. doi:10.1111/j.1365-3148.2007.00763.x

Akorsu, E. E., Acquaye, J. K., Benneh, A. A., Oppong, S. A., and Olayemi, E. (2019). Fetomaternal hemorrhage among pregnant women in Accra, Ghana. *Int. J. Gynaecol. Obstet.* 146 (3), 333–338. doi:10.1002/ijgo.12890

Alter, B. P. (1984). Advances in the prenatal diagnosis of hematologic diseases. *Blood* 64 (2), 329–340. doi:10.1182/blood.v64.2.329.bloodjournal642329

Athiel, Y., Maisonneuve, E., Bleas, C., Maurice, P., Cortey, A., Toly-Ndour, C., et al. (2020). Reduced fetal movement during pregnancy: Is the Kleihauer-Betke test really useful? *J. Gynecol. Obstet. Hum. Reprod.* 49, 101748. doi:10.1016/j.jogoh.2020.101748

Audette, M. C., McLean, K., Malkani, N., Kingdom, J., and Sobel, M. (2022). Diagnostic accuracy of kleihauer-betke (kb) testing to predict fetal outcomes associated with fetomaternal hemorrhage: A retrospective cohort study. *J. Perinatol.* 42 (1), 91–96. doi:10.1038/s41372-021-01185-5

Ayenew, A. A. (2021). Prevalence of rhesus D-negative blood type and the challenges of rhesus D immunoprophylaxis among obstetric population in Ethiopia: A systematic review and meta-analysis. *Matern. Health Neonatol. Perinatol.* 7 (1), 8. doi:10.1186/s40748-021-00129-3

Bowman, J. (2010). Thirty-five years of Rh prophylaxis. *Transfusion* 43 (12), 1661–1666. doi:10.1111/j.0041-1132.2003.00632.x

Cardoso, M. R., de Souza-Araujo, C. N., Talarico, M. C. R., Heinrich-Moucoucah, J., Guimaraes, F., and Barini, R. (2019). Evaluation of automatic blood analyzer as screening method in fetomaternal hemorrhage. *Biomed. Res. Int.* 2019, 6481654. doi:10.1155/2019/6481654

Carr, N. R., Henry, E., Bahr, T. M., Ohls, R. K., Page, J. M., Ilstrup, S. J., et al. (2022). Fetomaternal hemorrhage: Evidence from a multihospital healthcare system that up to 40% of severe cases are missed. *Transfusion* 62 (1), 60–70. doi:10.1111/trf.16710

Christino Luiz, M. F., Baschat, A. A., Delp, C., and Miller, J. L. (2019). Massive fetomaternal hemorrhage remote from term: Favorable outcome after fetal resuscitation and conservative management. *Fetal Diagn Ther.* 45 (5), 361–364. doi:10.1159/000492750

Corcoran, D., Murphy, D., Donnelly, J. C., and Ainle, F. N. (2014). The prevalence of maternal F cells in a pregnant population and potential overestimation of foeto-maternal haemorrhage as a consequence. *Blood Transfus.* 12 (4), 570–574. doi:10.2450/2014.0297-13

Cormack, O. M., Guilfoyle, F., and Flynn, C. M. (2019). The prevalence of an elevated F cell population in a maternal and gynaecology cohort. *Transfus. Med.* 29 (5), 369–373. doi:10.1111/tme.12625

David, M., Smidt, J., Chen, F., Stein, U., and Dudenhausen, J. W. (2004). Risk factors for fetal-to-maternal transfusion in Rh D-negative women--results of a prospective study on 942 pregnant women. *J. Perinat. Med.* 32 (3), 254–257. doi:10.1515/jpm.2004.047

Davis, B. H., Olsen, S., Bigelow, N. C., and Chen, J. C. (2010). Detection of fetal red cells in fetomaternal hemorrhage using a fetal hemoglobin monoclonal antibody by flow cytometry. *Transfusion* 38 (8), 749–756. doi:10.1046/j.1537-2995.1998.38898375514.x

Erhabor, O., Azachi, W. B., and Tosan, E. (2020). A case report of haemolytic disease of the foetus and newborn caused by Alloantibody D and Jka in a Rhesus D negative Nigerian woman: Justification for the implementation of universal access to prophylaxis and evidenced-based best practices. *Hum. Antibodies* 28 (3), 245–252. doi:10.3233/hab-200414

Fabry, M. E., Suzuka, S., Weinberg, R. S., Lawrence, C., Factor, S. M., Gilman, J. G., et al. (2001). Second generation knockout sickle mice: The effect of HbF. *Blood* 97 (2), 410–418. doi:10.1182/blood.v97.2.410

Fan, K., Wang, Y. J., Bu, Y. H., and Zhang, N. J. (2021). Maternal ABO discrepancy caused by massive fetomaternal hemorrhage: A case report. *Clin. Lab.* 67 (6). doi:10.7754/clin.lab.2020.201107

Ficarola, F., Svelato, A., Angioli, R., Rossi, R., D'Avino, S., Luca, C. D., et al. (2022). Reduced fetal movements: The case of fetomaternal hemorrhage case series and proposal of a management protocol. *Minerva obstetrics Gynecol.* 74 (4), 386–392. doi:10.23736/s2724-606x.21.04972-1

Flynn, A. N., Hoffman, E., Murphy, C., Jen, A., Schreiber, C. A., and Roe, A. H. (2022). Fetomaternal hemorrhage assessment in Rh-negative patients undergoing dilation and evacuation between 20 and 24 weeks' gestational age: A retrospective cohort study. *Contraception* 110, 27–29. doi:10.1016/j.contraception.2022.02.001

Franco, R. S., Yasin, Z., Palascak, M. B., Ciraolo, P., and Rucknagel, D. L. (2006). The effect of fetal hemoglobin on the survival characteristics of sickle cells. *Blood* 108 (3), 1073–1076. doi:10.1182/blood-2005-09-008318

Garner, C., Tatu, T., Reittie, J. E., Littlewood, T., Darley, J., Cervino, S., et al. (2000). Genetic influences on F cells and other hematologic variables: A twin heritability study. *Blood* 95 (1), 342–346. doi:10.1182/blood.v95.1.342.001k33_342_346

Glazebrook, B., Akers, C., Bielby, L., Bastin, K., Von Wielligh, K., and Daly, J. (2020). Quality audit of the guidelines for the use of RhD immunoglobulin in obstetrics: Are we getting it right? *Aust. N. Z. J. Obstet. Gynaecol.* 60 (4), 504–508. doi:10.1111/ajo.13177

Hookins, B., and Vatsayan, A. (2020). Intraplacental choriocarcinoma and fetomaternal haemorrhage and maternal disseminated intravascular coagulopathy in a term pregnancy: A case report. *Case Rep. Womens Health* 27, e00216. doi:10.1016/j.crwh.2020.e00216

Hsia, J. K., Schimmoeller, N. R., Cansino, C. D., Hou, M. Y., Jensen, H. M., and Creinin, M. D. (2019). Prospective quantification of fetomaternal hemorrhage with dilation and evacuation procedures. *Contraception* 99 (5), 281–284. doi:10.1016/j.contraception.2018.11.015

Kim, Y. A., and Makar, R. S. (2012). Detection of fetomaternal hemorrhage. *Am. J. Hematol.* 87 (4), 417–423. doi:10.1002/ajh.22255

Kumpel, B., Hazell, M., Guest, A., Dixey, J., Mushens, R., Bishop, D., et al. (2014). Accurate quantitation of D+ fetomaternal hemorrhage by flow cytometry using a novel

reagent to eliminate granulocytes from analysis. *Transfusion* 54 (5), 1305–1316. doi:10.1111/trf.12484

Lemaitre, J., Planche, L., and Ducarme, G. (2020). Systematic kleihauer-betke test after external cephalic version for breech presentation: Is it useful? *J. Clin. Med.* 9 (7), 2053. doi:10.3390/jcm9072053

Minuk, L., Clarke, G., and Lieberman, L. (2020). Approach to red blood cell antibody testing during pregnancy: Answers to commonly asked questions. *Can. Fam. Physician* 66 (7), 491–498.

Monteiro, S., Burling, M., and Doyle, H. (2021). Late diagnosis of intraplacental choriocarcinoma co-existing with fetomaternal haemorrhage causing fetal demise: A case report. *Case Rep. Womens Health* 31, e00341. doi:10.1016/j.crwh.2021.e00341

Pahuja, S., Gupta, S. K., Pujani, M., and Jain, M. (2011). The prevalence of irregular erythrocyte antibodies among antenatal women in Delhi. *Blood Transfus.* 9 (4), 388–393. doi:10.2450/2011.0050-10

Simes, M., Vale, G., Lacerda, C., Pais, P., and Pignatelli, D. (2022). Fetomaternal hemorrhage: A clue to intraplacental choriocarcinoma and neonatal malignancy. *J. Matern. Fetal Neonatal Med.* 35 (25), 6615–6617. doi:10.1080/14767058.2021.1918665

Stanic, Z., Stanisic, L., Fure, R., Persec, Z., Dapic, K., and Hrgovic, Z. (2020). Fetomaternal hemorrhage: Can we use hemoglobin electrophoresis as a diagnostic tool? *Z. für Geburtshilfe Neonatologie* 224 (03), 150–152. doi:10.1055/a-1041-3443

Sukhanova, M., Mithal, L. B., Otero, S., Azad, H. A., Miller, E. S., Jennings, L. J., et al. (2022). Maternal vs fetal origin of placental intervillous thrombi. *Am. J. Clin. Pathol.* 157 (3), 365–373. doi:10.1093/ajcp/aqab139

Tneh, S. Y., Baidya, S., and Daly, J. (2021). Clinical practices and outcomes of RhD immunoglobulin prophylaxis following large-volume fetomaternal haemorrhage in Queensland, Australia. *Aust. N. Z. J. Obstet. Gynaecol.* 61 (2), 205–212. doi:10.1111/ajo.13226

Troia, L., Al-Kouatly, H. B., McCurdy, R., Konchak, P. S., Weiner, S., and Berghella, V. (2019). The recurrence risk of fetomaternal hemorrhage. *Fetal Diagn Ther.* 45 (1), 1–12. doi:10.1159/000491788

Wang, H., Chen, Y., Ding, S., Duan, S., Tian, J., Meng, Q., et al. (2015). A new approach to detection of incomplete antibodies using hydrogel chromatography medium. *Transfus. Apher. Sci.* 53 (3), 337–341. doi:10.1016/j.transci.2015.06.003

Wiley Online Library (1999). The estimation of fetomaternal haemorrhage. *Transfus. Med.* 9 (1), 87–92. doi:10.1046/j.1365-3148.1999.009001087.x

Wu, K., Duan, S., Wang, Y., Wang, H., and Gao, X. (2022). Convolutional neural network-based automatic classification for incomplete antibody reaction intensity in solid phase anti-human globulin test image. *Med. Biol. Eng. Comput.* 60 (4), 1211–1222. doi:10.1007/s11517-022-02523-1

Zhang, Z., Ge, J., Gong, Z., Chen, J., Wang, C., and Sun, Y. (2021). Evaluation of machine learning–driven automated kleihauer-betke counting: A method comparison study. *Int. J. Laboratory Hematol.* 43, 372–377. doi:10.1111/ijlh.13380

Frontiers in
Bioengineering and Biotechnology

Accelerates the development of therapies, devices, and technologies to improve our lives

A multidisciplinary journal that accelerates the development of biological therapies, devices, processes and technologies to improve our lives by bridging the gap between discoveries and their application.

Discover the latest Research Topics

See more →

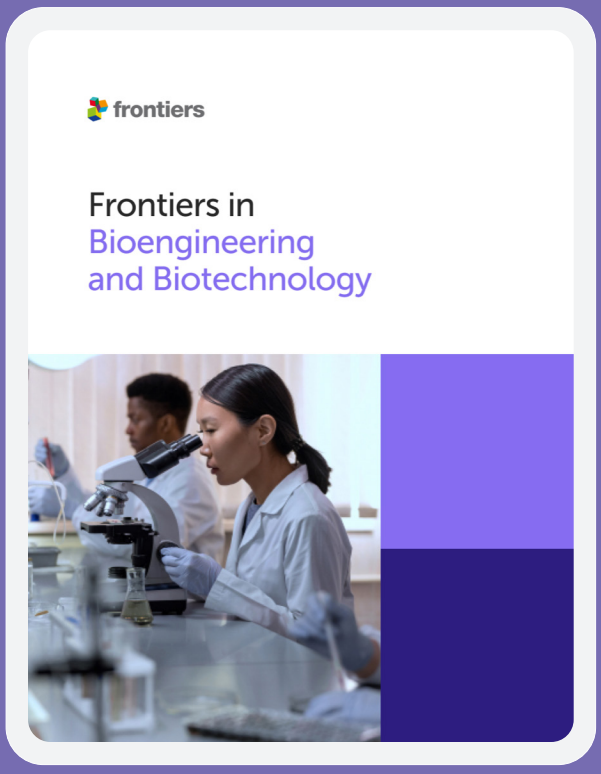

Frontiers

Avenue du Tribunal-Fédéral 34
1005 Lausanne, Switzerland
frontiersin.org

Contact us

+41 (0)21 510 17 00
frontiersin.org/about/contact